Identification of Active Galactic Nuclei through different selection techniques

Ektoras Pouliasis

HELLENIC REPUBLIC
National and Kapodistrian University of Athens

Identification of Active Galactic Nuclei through different selection techniques

A dissertation presented

by

Ektoras Pouliasis

to

The Faculty of Physics,

Department of Astrophysics, Astronomy and Mechanics

in partial fulfillment of the requirements

for the degree of

Doctor of Philosophy

in the subject of

Astronomy & Astrophysics

National and Kapodistrian University of Athens,

Greece

February 2020

Cover page image credit: DESY / Science Communication Lab.

Evaluation Committee:
Dr. Ioannis Georgantopoulos
Dr. Alceste Z. Bonanos
Prof. Kanaris Tsinganos
Prof. Apostolos Mastichiadis
Prof. Nektarios Vlahakis
Prof. Despina Hatzidimitriou
Prof. Kalliopi Dasyra

Diss. Advisors: Dr. I. Georgantopoulos, Dr. A.Z. Bonanos & Prof. K. Tsinganos

Identification of Active Galactic Nuclei through different selection techniques

Abstract

The most recent studies suggest that almost all galaxies in the Local Universe host Super-Massive Black Holes (SMBHs) in their center. SMBHs are responsible for the most powerful phenomena in the Universe, the Active Galactic Nuclei (AGN). When SMBHs accrete matter, strong radiation is emitted at all wavelengths of the electromagnetic field. The complete census of the various populations of AGN and the construction of samples with high statistical significance are essential to understand the evolution of the SMBHs and the host galaxies in the history of the Universe. The present doctoral thesis focused on comparing different AGN detection techniques. In particular, AGN selection techniques based on photometric and spectroscopic data were used from different wavelength regimes of the electromagnetic spectrum (optical, infrared, X-rays) as well as techniques that are based on flux variability. Comparing the methods with each other, the observational and physical AGN properties were studied. The main conclusion is that the different methods used to identify AGN are complementary to each other and equally important in building the whole picture of the AGN population. This doctoral thesis is divided into three distinct parts according to the fields studied and the techniques applied:

A. Robust identification of Active Galactic Nuclei through HST optical variability in GOODS-S: Comparison with the X-ray and mid-IR selected samples

Identifying AGN through their X-ray emission is efficient, but necessarily biased against X-ray-faint objects. In order to characterize this bias, we compare the X-ray-selected AGN to the ones identified through optical variability and mid-IR colours. We present a catalogue of AGN selected through optical variability using all publicly available z-band *Hubble* Space Telescope images in the GOODS-South field. For all objects in the catalogue, we compute X-ray upper limits or discuss detections in the deepest available ∼7 Ms *Chandra* Deep Field South images and present the *Spitzer*/IRAC mid-IR colours. For the variability study, we consider only sources observed over at least five epochs and over a time baseline of up to ten years. We adopt

the elevated median absolute deviation as a variability indicator robust against individual outlier measurements and identify 113 variability-selected AGN candidates. Among these, 26 have an X-ray counterpart and lie within the conventional AGN area in the F_X/F_{opt} diagram. The candidates with X-ray upper limits are on average optically fainter, have higher redshifts compared to the X-ray detected ones and are consistent with low luminosity AGN. Out of 41 variable optical sources with IR detections, 13 fulfill the IR AGN colour selection criteria. Our work emphasizes the importance of optical variability surveys for constructing complete samples of AGN including the ones that remain undetected even by the deepest X-ray and IR surveys. The results in this field were published in the journal Monthly Notices of the Royal Astronomical Society (MNRAS) as Pouliasis et al. (2019).

B. The "Hubble Catalog of Variables": AGN identification in CANDELS and Frontier Fields

Within the framework of the "Hubble Catalog of Variables" (HCV) project, AGN candidates were selected through variability. The purpose of the HCV program is to detect variable point-like sources as well as extended sources using data from the Hubble Source Catalog. In particular for the AGN detection, fields that have deep observations with long exposure times and have also been observed many times are necessary using all the available filters. Such are the CANDELS and Frontiers fields. The results in the GOODS-South field were used as a keystone in the selection process and confirmation and verification of the results in the latter fields. Depending on the available data from the entire electromagnetic spectrum in each field, different AGN selection methods were used to compare the results. Part of the results in the CANDELS fields were included in the publication of Bonanos et al. (2019) in the journal Astronomy & Astrophysics.

C. An obscured AGN population hidden in the VIPERS galaxies: identification through spectral energy distribution decomposition

The X-ray emission constitutes a reliable and efficient tool for the selection of Active Galactic Nuclei (AGN) although, it may be biased against the most heavily obscured AGN. Simple mid-IR broad-band selection criteria could identify a large number of luminous and absorbed AGN yet again host contamination could lead to non-uniform and incomplete samples. The Spectral Energy Distribution (SED) decomposition could decouple the emission from the AGN and that from star-forming regions revealing weaker AGN components. We aim to identify an obscured AGN population through SED modelling among galaxies in the VIPERS survey in the CFHTLS W1

field. We construct SEDs for 6,860 sources and identify 160 AGN at a high confidence level using a Bayesian approach. Using optical spectroscopy, we confirm the nature of ∼85% of the AGN. Our AGN sample is highly complete (∼92%) compared to mid-IR colour AGN, but also includes a significant number of galaxy-dominated systems with lower luminosities. In addition to lack of X-ray emission (80%), the SED fitting results suggest that the majority of the sources are obscured. We use a number of diagnostic criteria in the optical, infrared and X-ray regime to verify these results. Interestingly, only 35% of the most luminous mid-IR selected AGN have X-ray counterparts suggesting strong obscuration. Our work emphasizes the importance of using SED decomposition techniques to select a population of type II AGN, which may remain undetected by either X-ray or IR colour surveys. The results in this field have been submitted in the journal MNRAS.

The conclusions derived from this thesis are that the different methods used to detect AGN are complementary to each other and equally important in determining the full picture of the AGN demographics. Each method selects AGN samples with different physical and observational properties. Mid-IR identification selects AGN with large amounts of dust around the black hole, which may obscure some or all of the X-ray emission. On the other hand, the X-ray selected AGN could not be selected in the infrared regime, as they may contain less amount of dust and often be contaminated by the host galaxy. Furthermore, the optical variability is able to identify a large number of low-luminosity AGN, especially at high redshifts, including those that remain undetectable even at the deeper observations in the X-rays or the infrared. This population is critical for studying the faint end of the AGN luminosity function and may be the key between normal galaxies and AGN. In addition, the importance of using SED decomposition techniques to detect less luminous AGN of high absorption of radiation at optical wavelengths and X-rays is emphasized, which other methods may not be as effective.

Τριμ. επιτροπή: Δρ. Ι. Γεωργαντόπουλος, Δρ. Α.Ζ. Μπονάνου & Καθ. Κ. Τσίγκανος

Ανίχνευση ενεργών γαλαξιακών πυρήνων χρησιμοποιώντας και συγκρίνοντας διαφορετικές μεθόδους

Περίληψη

Οι πιο πρόσφατες μελέτες δείχνουν ότι σχεδόν όλοι οι γαλαξίες στο κοντινό Σύμπαν περιέχουν Υπέρ-Μεγέθεις Μελανές Οπές (ΥΜΜΟ) στο κέντρο τους. Οι ΥΜΜΟ είναι υπεύθυνες για τα πιο δυναμικά φαινόμενα στο Σύμπαν, τους Ενεργούς Γαλαξιακούς Πυρήνες (ΕΓΠ). Όταν ύλη πέφτει στις ΥΜΜΟ, εκλύεται ισχυρή ακτινοβολία σε όλα τα μήκη κύματος του ηλεκτρομαγνητικού φάσματος. Η πλήρης καταγραφή των διάφορων πληθυσμών των ΕΓΠ και η κατασκευή δειγμάτων με μεγάλη στατιστική πληρότητα είναι απαραίτητα στην κατανόηση της εξέλιξης των μελανών οπών και των γαλαξιών στην ιστορία του Σύμπαντος. Η παρούσα διδακτορική διατριβή επικεντρώθηκε στην σύγκριση διαφορετικών τεχνικών ανίχνευσης ΕΓΠ. Πιο συγκεκριμένα, χρησιμοποιήθηκαν τεχνικές ανίχνευσης ΕΓΠ βασισμένες σε φωτομετρικά και φασματοσκοπικά δεδομένα, που προέρχονται από διαφορετικές περιοχές του ηλεκτρομαγνητικού φάσματος (οπτικό, υπέρυθρο, ακτίνες Χ), καθώς και τεχνικές που βασίζονται στην μεταβολή της ροής. Συγκρίνοντας όλες τις μεθόδους μεταξύ τους, μελετήθηκαν οι παρατηρησιακές και φυσικές ιδιότητες των ΕΓΠ. Το συμπέρασμα που απορρέει είναι ότι οι διαφορετικές μέθοδοι που χρησιμοποιούνται για τον προσδιορισμό των ΕΓΠ είναι συμπληρωματικές μεταξύ τους και εξίσου σημαντικές για τον σχηματισμό της πλήρους εικόνας των δημογραφικών στοιχείων των ΕΓΠ. Η διδακτορική διατριβή χωρίζεται σε τρία διακριτά μέρη ανάλογα με τα πεδία που μελετήθηκαν και τις τεχνικές που εφαρμόστηκαν:

Α. Ανίχνευση ΕΓΠ με τη μέθοδο μεταβολής της ροής στο οπτικό φίλτρο z στο πεδίο GOODS-South: Σύγκριση με τα επιλεγμένα ΕΓΠ στο υπέρυθρο και τις ακτίνες Χ

Η ανίχνευση των ΕΓΠ μέσω της εκπομπής τους στις ακτίνες Χ είναι αποτελεσματική για την εύρεση ενός μεγάλου δείγματος ΕΓΠ. Όμως, υπάρχει η δυνατότητα μη εντοπισμού των πιο αμυδρών πηγών. Ένας εναλλακτικός τρόπος είναι η μεταβλητότητα της ροής τους

σε όλα τα μήκη κύματος, η οποία αποτελεί βασική ιδιότητα των ΕΓΠ και έχει αποδειχθεί ότι είναι μια αξιόπιστη μέθοδος για την εύρεσή τους, περιλαμβανομένων των ΕΓΠ μικρής φωτεινότητας. Στο πεδίο GOODS-South ανιχνεύθηκαν όλες οι μεταβλητές πηγές χρησιμοποιώντας έναν νέο δείκτη μεταβλητότητας (μέση τυπική απόκλιση) των καμπυλών φωτός όλων των πηγών στο πεδίο. Για την κατασκευή των καμπυλών φωτός χρησιμοποιήθηκαν παρατηρήσεις από το διαστημικό τηλεσκόπιο Hubble . Για την διαχείριση και ανάλυση των εικόνων, δημιουργήθηκε ένα πρόγραμμα, το όποιο αυτόματα καθαρίζει τις εικόνες από κοσμικές ακτίνες, κάνει φωτομετρία, βρίσκει αστρομετρική λύση και, τελικά, μέσω του δείκτη μεταβλητότητας δίνει έναν κατάλογο με τις μεταβλητές πηγές. Καθώς οι μεταβλητές πηγές μπορεί να περιέχουν ακόμη μεταβλητούς αστέρες ή υπέρκαινοφανείς, για να επιλεγεί ένα καθαρό δείγμα ΕΓΠ, οι παραπάνω πηγές διαχωρίστηκαν μέσω οπτικών και υπέρυθρων δεικτών χρώματος ή μέσω των χαρακτηριστικών των καμπυλών φωτός, αντίστοιχα. Τα αποτελέσματα συγκρίθηκαν με ΕΓΠ που επιλέχτηκαν μέσω ακτινοβολίας στις ακτίνες X (Chandra X-ray Telescope) και μέσω δεικτών χρώματος στο υπέρυθρο (Spitzer-IRAC) . Με την μέθοδο μεταβλητότητας στο οπτικό φάσμα, ανιχνεύονται χαμηλής φωτεινότητας ΕΓΠ, οι οποίοι είναι οπτικά αμυδρότεροι και έχουν υψηλότερες ερυθρό-μετατοπίσεις από τους αντίστοιχους ΕΓΠ με ακτίνες X. Επίσης, ο πληθυσμός αυτός είναι πιο ασθενής στις ακτίνες X και έχει παρόμοια φωτεινότητα με αντίστοιχους ΕΓΠ χαμηλής φωτεινότητας στο κοντινό Σύμπαν, αλλά βρίσκεται σε πολύ μακρύτερη απόσταση. Τα αποτελέσματα στο συγκεκριμένο πεδίο δημοσιεύτηκαν στο επιστημονικό περιοδικό Monthly Notices of the Royal Astronomical Society, MNRAS, ως Pouliasis et al. (2019).

Β. Ο κατάλογος μεταβλητών του Hubble: ανίχνευση ΕΓΠ στα CANDELS και Frontier πεδία

Στα πλαίσια του προγράμματος "Hubble Catalog of Variables" (HCV), πραγματοποιήθηκε η ανίχνευση ΕΓΠ. Σκοπός του προγράμματος HCV είναι η ανίχνευση μεταβλητών σημειακών, αλλά και εκτεταμένων πηγών, χρησιμοποιώντας δεδομένα από τον κατάλογο πηγών του Hubble (Hubble Source Catalog). Πιο συγκεκριμένα, για την ανίχνευση ΕΓΠ χρησιμοποιήθηκαν πεδία τα οποία έχουν βαθιές παρατηρήσεις με μεγάλους χρόνους έκθεσης και επίσης έχουν παρατηρηθεί πολλές φορές χρησιμοποιώντας όλα τα διαθέσιμα φίλτρα. Τέτοια είναι τα CANDELS και Frontiers πεδία. Τα αποτελέσματα στο πεδίο GOODS-South χρησιμοποιήθηκαν ως άξονας όσον αφορά την επιλογή της διαδικασίας και την επιβεβαίωση και επαλήθευση των αποτελεσμάτων στα παραπάνω πεδία. Ανάλογα με τα διαθέσιμα δεδομένα από όλο το ηλεκτρομαγνητικό φάσμα σε κάθε πεδίο, διαφορετικές μέθοδοι ανίχνευσης των ΕΓΠ χρησιμοποιήθηκαν για σύγκριση αποτελεσμάτων. Μέρος των αποτελεσμάτων στα CANDELS πεδία, περιλήφθηκαν στην δημοσίευση Bonanos et al. (2019) στο επιστημονικό περιοδικό Astronomy & Astrophysics.

Γ. Ένας πληθυσμός ΕΓΠ μεγάλης απορρόφησης στις ακτίνες X και το οπτικό φάσμα, κρυμμένος στους γαλαξίες VIPERS: ανίχνευση μέσω ανάλυσης των φασματικών ενεργειακών κατανομών.

Η εκπομπή ακτινών Χ ως μέθοδος ανίχνευσης των ΕΓΠ αποτελεί ένα αξιόπιστο και αποτελεσματικό εργαλείο, όμως μπορεί να μεροληπτεί έναντι των πηγών με μεγάλη απορρόφηση στις ακτίνες Χ και το οπτικό μέρος του ηλεκτρ/κού φάσματος. Απλά κριτήρια επιλογής ΕΓΠ με ευρείες μπάντες στην μεσαία υπέρυθρη ακτινοβολία θα μπορούσαν να αναγνωρίσουν έναν μεγάλο αριθμό φωτεινών και με μεγάλη απορρόφηση ΕΓΠ, αν και η σύγχυση με τους γαλαξίες που τα περιέχουν θα μπορούσε να οδηγήσει σε μη ομοιόμορφα και ελλιπή δείγματα. Η ανάλυση των φασματικών ενεργειακών κατανομών (ΦΕΚ) μπορεί να διαχωρίσει την μεσαία υπέρυθρη εκπομπή που προέρχεται από τους ΕΓΠ από εκείνη των περιοχών όπου ο ρυθμός σχηματισμού αστέρων είναι υψηλός και να αποκαλύψει τέτοιου είδους ΕΓΠ με ακόμη μικρότερη συνιστώσα. 'Ενας μεγάλος πληθυσμός ΕΓΠ μεγάλης απορρόφησης εντοπίστηκε χρησιμοποιώντας την ανάλυση ΦΕΚ σε ένα δείγμα γαλαξιών από το πρόγραμμα VIPERS στο πεδίο CFHTLS W1, όπου υπάρχει πληθώρα φωτομετρικών και φασματοσκοπικών δεδομένων. Κατασκευάστηκαν οι ΦΕΚ 6,860 πηγών με δεδομένα στο οπτικό (CFHTLS) και το υπέρυθρο (WISE και VHS) και με αξιόπιστες ερυθρό-μετατοπίσεις. Επίσης, χρησιμοποιήθηκαν μοντέλα μόνο γαλαξιών και, στη συνέχεια, διερευνήθηκε κατά πόσο ο έλεγχος καλής προσαρμογής μεταβάλλεται με την προσθήκη μοντέλων ΕΓΠ. Με τον συγκεκριμένο τρόπο, επιλέχθηκαν 160 ΕΓΠ χρησιμοποιώντας Μπαεσιανή προσέγγιση με υψηλό διάστημα εμπιστοσύνης (99.3%). Μελετώντας τα οπτικά φάσματα (VIPERS) και τις αντίστοιχες τεχνικές ανίχνευσης ΕΓΠ, 85% του δείγματος είναι επιβεβαιωμένοι ΕΓΠ. Το δείγμα ΕΓΠ είναι εξαιρετικά πλήρες (∼92%) σε σύγκριση με τους ΕΓΠ που έχουν επιλεχθεί στο υπέρυθρο, αλλά περιλαμβάνει επίσης έναν σημαντικό αριθμό πηγών χαμηλής φωτεινότητας με συστήματα που κυριαρχεί η ακτινοβολία του γαλαξία έναντι του ΕΓΠ. Εκτός από την έλλειψη εκπομπής ακτίνων Χ (80%), τα αποτελέσματα των ΦΕΚ υποδηλώνουν ότι η πλειοψηφία των πηγών τυγχάνει απορρόφησης μεσαίας κλίμακας στα οπτικά μήκη κύματος. Χρησιμοποιώντας ορισμένα διαγνωστικά κριτήρια στο οπτικό, υπέρυθρο και τις ακτίνες Χ, τα αποτελέσματα αυτά επαληθεύονται. Είναι ενδιαφέρον ότι μόνο το 35% των πλέον φωτεινών ΕΓΠ που έχουν επιλεχθεί στο υπέρυθρο εκπέμπουν στις ακτίνες Χ, γεγονός που υποδηλώνει ισχυρή απορρόφηση. Η γραπτή δημοσίευση για τα παραπάνω αποτελέσματα έχει ήδη κατατεθεί στο περιοδικό MNRAS ως Pouliasis et al.

Τα συμπεράσματα που απορρέουν από την συγκεκριμένη διδακτορική διατριβή είναι ότι οι διαφορετικές μέθοδοι που χρησιμοποιούνται για την ανίχνευση των ΕΓΠ είναι συμπληρωματικές μεταξύ τους και εξίσου σημαντικές για τον προσδιορισμό της πλήρους εικόνας των δημογραφικών στοιχείων των ΕΓΠ. Η κάθε μέθοδος επιλέγει δείγματα ΕΓΠ με διαφορετικές φυσικές και παρατηρησιακές ιδιότητες. Η ανίχνευση στην μεσαία υπέρυ-

θρη ακτινοβολία προτιμάει ΕΓΠ με μεγάλα ποσά σκόνης γύρω από την μαύρη τρύπα, τα οποία μπορεί να αποκρύψουν μερικά ή ολικά την εκπομπή στις ακτίνες Χ. Στην αντίθετη περίπτωση, οι ΕΓΠ επιλεγμένοι στις ακτίνες Χ δύνανται να μην επιλεχθούν στην υπέρυθρη ακτινοβολία, καθώς εμπεριέχουν μικρότερα ποσά σκόνης και συχνά συγχέονται με την ακτινοβολία από τον γαλαξία που τα φιλοξενεί. Η μεταβλητότητα της ροής στο οπτικό μπορεί να αναγνωρίσει ένα μεγάλο αριθμό ΕΓΠ μικρής φωτεινότητας, ειδικότερα σε υψηλές ερυθρό-μετατοπίσεις, συμπεριλαμβανομένων εκείνων που παραμένουν μη ανιχνεύσιμοι ακόμα και στις βαθύτερες παρατηρήσεις στις ακτίνες Χ και στο υπέρυθρο. Ο πληθυσμός αυτός είναι κρίσιμος για τη μελέτη της αμυδρής περιοχής της συνάρτησης φωτεινότητας των ΕΓΠ και μπορεί να είναι το κλειδί μεταξύ των κανονικών γαλαξιών και των ΕΓΠ. Επιπρόσθετα, υπογραμμίζεται η σημασία της χρήσης τεχνικών ανάλυσης ΦΕΚ για την ανίχνευση λιγότερο φωτεινών πηγών μεγάλης απορρόφησης της ακτινοβολίας στα οπτικά μήκη κύματος και τις ακτίνες Χ, που άλλες μέθοδοι μπορεί να μην είναι τόσο αποτελεσματικές.

Contents

Abstract vii

Περίληψη xi

Contents xv

List of Figures xix

List of Tables xxii

Acknowledgments xxv

1 Introduction 1

1.1 The signs of the times 2

1.2 AGN taxonomy and classification 7

1.3 The Unified Model 12

1.4 AGN structure 16

1.4.1 Super massive black holes 16

1.4.2 Energy produced through accretion 19

1.4.3 Growth of SMBHs 20

1.4.4 Accretion disc 21

1.4.5 Emission Line Regions 23

1.4.6 The Dusty Torus 26

1.4.7 The Hot Corona . . . 27
1.4.8 Relativistic Jets and Lobes . . . 30
1.5 AGN selection techniques . . . 32
1.5.1 X-ray regime . . . 32
1.5.2 UV-optical-NIR regime . . . 33
1.5.3 Mid-IR regime . . . 35
1.5.4 AGN variability . . . 37
1.6 Scope of this thesis . . . 38

2 Telescopes Overview 41
2.1 Optical Telescopes . . . 41
2.1.1 Hubble Space Telescope . . . 41
2.1.2 The Canadian-French-Hawaiian Telescope . . . 42
2.2 Infrared Telescopes . . . 43
2.2.1 The Spitzer Space Telescope . . . 43
2.2.2 WISE . . . 45
2.3 X-ray Telescopes . . . 45
2.3.1 XMM-Newton Telescope . . . 45
2.3.2 Chandra X-ray Observatory . . . 47

3 Robust Identification of Active Galactic Nuclei through *HST* Optical Variability in GOODS-S: Comparison with the X-ray and mid-IR Selected Samples 49
3.1 Data Reduction . . . 51
3.1.1 Optical HST data . . . 51
3.1.2 X-ray and IR data sets . . . 56
3.2 AGN selection based on optical variability . . . 62
3.2.1 Variability detection in the presence of outlier measurements . 63

3.2.2 Variability algorithm 65
3.2.3 Stars and supernovae 70
3.3 Properties of the AGN candidates 73
3.3.1 X-ray detections & upper limits 73
3.3.2 Mid-infrared selected AGN 81
3.4 Discussion 83
3.4.1 Comparison with previous variability studies 83
3.4.2 X-ray, mid-IR and optical variability selected AGNs 85

4 Hubble Catalogue of Variables: identification of AGN candidates in the CANDELS and Frontier Fields 89
4.1 Hubble catalogue of variables 90
4.1.1 Data processing & Variability Analysis 91
4.1.2 Validation algorithm 92
4.1.3 HCV main results 93
4.2 Results 93
4.2.1 CANDELS fields 93
4.2.2 Frontier Fields 97

5 An obscured AGN population hidden in the VIPERS field: identification through SED decomposition 105
5.1 Data 106
5.1.1 VIPERS 106
5.1.2 VISTA-VHS 107
5.1.3 AIIWISE 107
5.1.4 XMM-XXL 108
5.1.5 Final sample 108
5.2 Analysis 110

5.2.1 SED analysis with CIGALE 111
5.2.2 Best model selection - Bayesian factor 113
5.3 Results 116
5.3.1 SED selected AGNs 116
5.3.2 X-ray detections and upper limits 122
5.3.3 Mid-IR selected AGNs 123
5.3.4 Optical spectroscopy 126
5.3.5 Intrinsic absorption estimation 131
5.4 Discussion 135

6 Summary & Conclusions **145**

A Additional Figures & Tables - Frontier Fields **151**

B Miscellaneous **177**
B.1 List of publications 177
B.2 List of Conferences/Workshops attended 178
B.3 Other activities 178

References **181**

List of Figures

1.1 A sketch of the galaxy M51 by Lord Rosse (Rosse 1850). 3

1.2 Image comparison of an AGN and a normal galaxy. 9

1.3 Typical spectra of different AGN classes. 10

1.4 The AGN unified model scheme. 14

1.5 A quantitative criterion for AGN radio-loudness transition 15

1.6 A schematic view of the multi-wavelength SED of AGN. 17

1.7 The first image of the SMBH in M87. 18

1.8 Multi-colour black body SED emitted by a standard accretion disc . . 22

1.9 A schematic view of the AGN components 24

1.10 The inner structure of Cygnus A in radio. 27

1.11 Typical AGN X-ray spectrum with varied N_H. 28

1.12 The structure of the radio galaxy M87 in different scales. 31

1.13 BPT and MEx diagrams. 34

1.14 SEDs of the ionizing radiation in AGN and SF models 35

3.1 Magnitude error vs. magnitude. 53

3.2 Normalized measurement error distribution. 54

3.3 magnitude distribution & completeness curves. 56

3.4 Number of epochs vs. time baseline. 58

3.5 Magnitude comparison with HSCv2. 59

3.6 CI distribution vs. magnitude. 60
3.7 Colour composite image of the 7 Ms CDF-S. 61
3.8 Simulated SNR vs. n_{LC} for MAD, $1/\eta$ & σ 64
3.9 MAD vs. magnitude distribution in GOODS-S 66
3.10 MAD vs. magnitude with variability thresholds. 67
3.11 Cumulative distributions of the normalized significance. 69
3.12 The $J-K$ *vs.* $3.6\mu m$ and the $3.6\mu m/r$ flux ratio vs. $r-i$ diagrams. 71
3.13 Example light curves of SNe. 72
3.14 Spatial distribution of the AGN candidates. 73
3.15 Example light curves of the AGN candidates 76
3.16 X-ray vs. optical flux 78
3.17 Redshift distribution for the candidate AGN 78
3.18 F850LP magnitude distribution for the candidate AGN 79
3.19 Comparison of X-ray luminosities 80
3.20 IRAC colour-colour diagram in GOOD-S 82
3.21 Recovery rates of variable sources 84
3.22 Venn diagram for different AGN samples 86
3.23 X-ray AGN recovery fraction 87

4.1 Location of the CANDELS and Frontier fields 90
4.2 Example light curves of variables in the CANDELS fields. 96
4.3 MAD vs. magnitude in ABELL 2744 cluster field 98
4.4 CI distribution (point-like and extended) 99
4.5 IRAC colour-colour diagram in Abell 370. 102
4.6 IRAC colour-colour diagram in Abell 2744. 103
4.7 IRAC colour-colour diagram in Abell s1063. 104

5.1 The optical near-IR and mid-IR magnitude distributions 109

5.2 Redshift distributions of the AGN candidates 110
5.3 The distribution of ΔBIC 120
5.4 Example SEDs with & without AGN templates 121
5.5 *WISE* magnitude-colour (W2, W1–W2) diagram 125
5.6 *WISE* colour-colour (W2–W3, W1–W2) diagram 126
5.7 Venn diagram - comparing mid-IR selection methods 127
5.8 The mass Excitation diagram (MEx) 129
5.9 The TBT diagram 130
5.10 The r–W2 colour distribution 132
5.11 Optical-IR colour diagram 133
5.12 The X-ray luminosity vs. the IR luminosity 134
5.13 Example SEDs of CT candidate AGN 136
5.14 Venn diagram for different AGN selection methods 137
5.15 W2, W1–W2 diagram for different AGN probabilities 138
5.16 W2–W3, W1–W2 diagram for different AGN probabilities 139
5.17 (W2, W1–W2) diagram - luminosity/redness dependence 140
5.18 Stacked AGN SEDs selected via different methods 142
5.19 Example SEDs for luminous AGNs with X-ray detections 143
5.20 Example SEDs for luminous AGNs without X-ray detections 144

A.1 MAD vs. magnitude in ABELL 2744 parallel field. 152
A.2 MAD vs. magnitude in ABELL S1063 parallel field. 156
A.3 MAD vs. magnitude in the combined MACS 0717 fields. 157
A.4 MAD vs. magnitude in the combined MACS 1149 fields. 158
A.5 MAD vs. magnitude in the MACS 0717 cluster fields 159
A.6 MAD vs. magnitude in the MACS 0717 parallel fields 160

List of Tables

3.1 The HST Treasury programs included in this study 52

3.2 Summary of the basic information of the CDF-S X-ray catalogues. . . 57

3.3 Catalogue of confirmed SNe identified in our survey. 70

3.4 Catalogue of the variable AGN candidates. 74

4.1 HCV variables in the CANDELS fields. 95

4.2 HCV variables in the Frontier Fields. 100

5.1 X-CIGALE model parameters 112

5.2 Comparison of different AGN samples 114

5.3 Catalogue of the 160 SED selected AGNs. 117

A.1 HCV variables in the Abell 2744 cluster field. 161

A.2 HCV variables in the Abell 2744 parallel field. 162

A.3 HCV variables in the Abell s1063 cluster field. 163

A.4 HCV variables in the Abell s1063 parallel field. 165

A.5 HCV variables in the Abell 370 cluster field. 166

A.6 HCV variables in the Abell 370 parallel field. 168

A.7 HCV variables in the MACS 0416 cluster field. 169

A.8 HCV variables in the MACS 0416 parallel field. 171

A.9 HCV variables in the MACS 1149 cluster field. 172

A.10 HCV variables in the MACS 1149 parallel field. 173
A.11 HCV variables in the MACS 0717 cluster field. 174
A.12 HCV variables in the MACS 0717 parallel field. 176

Acknowledgments

I wish to express my sincere appreciation to my supervisors, Dr. Ioannis Georgantopoulos, who has the attitude and the substance of a genius: he continually and convincingly conveyed a spirit of excitement and adventure in regard to research, Dr. Alceste Bonanos, who guided and encouraged me to be professional and do the right thing even when the road got tough, and Prof. Kanaris Tsinganos, who has been tremendous mentor and guidance for me with his professional experience and knowledge. Their important suggestions and advice were priceless and without their persistent help, the goal of this project would not have been realized.

I wish to show my gratitude to the other evaluation committee members of this thesis, Prof. Apostolos Mastichiadis, Prof. Nektarios Vlahakis, Prof. Despina Hatzidimitriou and Prof. Kalliopi Dasyra for taking their precious time to consider my work and provide to me their invaluable insights and suggestions.

I would also like to thank my fellow doctoral students and my colleagues, who always support and give full attention for me to solve any problem. They always help me in exchanging any ideas and give the enjoyable working environment. They made my life at NOA a truly memorable experience and their friendships are invaluable to me. A big thank you to Georgios Mountrichas, Ming Yang, Panos Gavras, Angel Ruiz, Antonis Georgakakis, Vassilis Charmandaris, Letizia P. Cassarà, Maria Ida Moretti, Marina Vika, Ioannis Bellas-Velidis, Manolis Xilouris, Panagiotis Boumis, Tasos Dapergolas, Kirill Sokolovsky, Elias Koulouridis, Lazaros Koutoulidis, Ioanna Leonidaki, Zoi Spetsieri, Michalis Kourniotis, Alexandros Psychogios, Stella Boula, Nikolay Britavskiy, Emmy Paraskeva, Maria Chira, Angelos Nersersian, Vaggelis Paspaliaris, Sophia Derlopa, Vasileia Masoura, Georgios Dimopoulos, Frank Tramper, Stephan de Wit, Alexandros Chiotellis, Alexis Liakos and Grigoris Maravelias.

I wish to acknowledge the support and great love of my family, my father, Panagiotis; my mother, Elsa; and my brother, Miltos. They kept me going on and this work would not have been possible without their input. Last but not least, I would like to thank my friends, Athina Vareli, Periklis Peteinatos, Stavros Satolias and Stavroula Papatheochari for their great support to me and understanding throughout the whole time.

"Everybody is a Genius. But if you judge a fish by its ability to climb a tree, it will live its whole life believing that it is stupid."

Albert Einstein

Chapter 1

Introduction

It is widely accepted that massive galaxies and a fraction of lower mass galaxies in the Local Universe host a super massive black hole (SMBH) in their centre (Magorrian et al. 1998; Kormendy & Kennicutt 2004; Filippenko & Ho 2003; Barth et al. 2004; Greene & Ho 2004, 2007; Dong et al. 2007; Greene et al. 2008). Their mass ranges between 10^6 and 10^{10} solar masses (Lynden-Bell 1969; Lauer et al. 2007; Koss et al. 2017). When matter from the galaxies starts to accrete into the SMBH, an enormous amount of energy is released across the electromagnetic spectrum (from radio emission up to X- and γ- rays). This constitutes the characteristic signature of the class of Active Galactic Nuclei (AGN). In many cases, the power of a single AGN with a size that is similar to our Solar System is higher than the power emitted by the stellar population of its host galaxy. Recent studies suggest a close interaction between the creation and evolution of galaxies and that of SMBHs (e.g. Silk & Rees 1998; Granato et al. 2004; Di Matteo et al. 2005; Croton 2006; Hopkins et al. 2006, 2008; Menci et al. 2008), though the physical processes governing this relationship are not yet fully understood. Moreover, there is a correlation between the mass of the black holes and the properties of their host galaxies (Kormendy & Ho 2013), such as the luminosity, the stellar mass, the velocity dispersion or the bulge rotational velocity (Dressler 1989; Kormendy & Richstone 1995; Magorrian et al. 1998; Ferrarese & Merritt 2000; Gebhardt et al. 2000; Tremaine et al. 2002; Marconi & Hunt 2003; Häring & Rix 2004; Ferrarese & Ford 2005; Graham & Driver 2007; Gültekin et al. 2009). Hence, either the processes that take place in AGN play an important role in star formation and shaping of the galaxy structure, or vice versa the galaxy evolution directly affects the mass and spin of the central black hole.

To better understand the relations between the central black hole and its host galaxy, it is necessary to have complete samples of AGN, not biased against redshift,

obscuration, luminosity, etc. The detection and study of AGN is one of the most active fields of extra-galactic astrophysics today. Their demographics (e.g. space density), their distribution on the cosmic web (e.g. two-point auto-correlation function) and their physical properties (e.g. luminosity, black hole mass, accretion rate, absorption) play an important role in understanding the evolutionary models of black holes and whether the AGN affect their host galaxy properties (e.g. star formation rate). The main purpose of this thesis is to enhance the reliability and completeness of the different AGN selection techniques, but also to apply and test new methods. Through comparison of the methods in different observational windows and fields with different depths and areas, it is possible to constrain their limitations and find ways to reveal AGN populations that are missed. In this Chapter, some historical facts and an introduction will be given in the observational properties and the physics lying behind the AGN, while I will focus on the selection methods ending with the analytical purpose of this thesis.

1.1 The signs of the times

In this section, a brief history is given concerning the birth of the extra-galactic astronomy and the definition of the AGN. The first AGN observations are presented in different parts of the electromagnetic spectrum and the connection between them. Furthermore, all the signs and theories are summarized that led to the interpretation of the physical mechanisms lying behind AGN and the beginning of a new era of multi-wavelength technological excess.

The beginning of extra-galactic astronomy: The idea of some distant nebulae that do not belong to our Galaxy and represent further Milky Ways was given, firstly, in the 18$^{\text{th}}$ century (Wright 1750) and, later, Kant (1755) called them "Welteninslen" that means "island Universes". Then, William Herschel built a large catalogue of around 5,000 nebulae (Herschel 1786, 1789, 1800, 1802) and some years later Lord Rosse by constructing a 72" telescope was the first to draw a sketch (Fig. 1.1) of the spiral arms in the "nebula" M51 (Whirpool galaxy, for the Advancement of Science. 1845) and later on he gave the term "spiral" to other nebulae (Rosse 1850). In these nebulae, he identified some point-like sources inside them indicating that they are not just clouds of gas. At the end of the 19$^{\text{th}}$ century the director of the Lick Observatory, James E. Keeler, with a catalogue of 120,000 nebulae found that the majority of them had spiral structures supporting that they originated outside of our own galaxy (Keeler 1900). Some years later, Edward A. Fath during his PhD in the Lick Observatory using the Lick reflector gathered many spectra from these spiral

nebulae and none had continuous spectra. The only explanation was that the spiral nebulae had to be a gathering of stars (clusters) and should be really far away from the Milky Way (Fath 1909a,b,c, 1913).

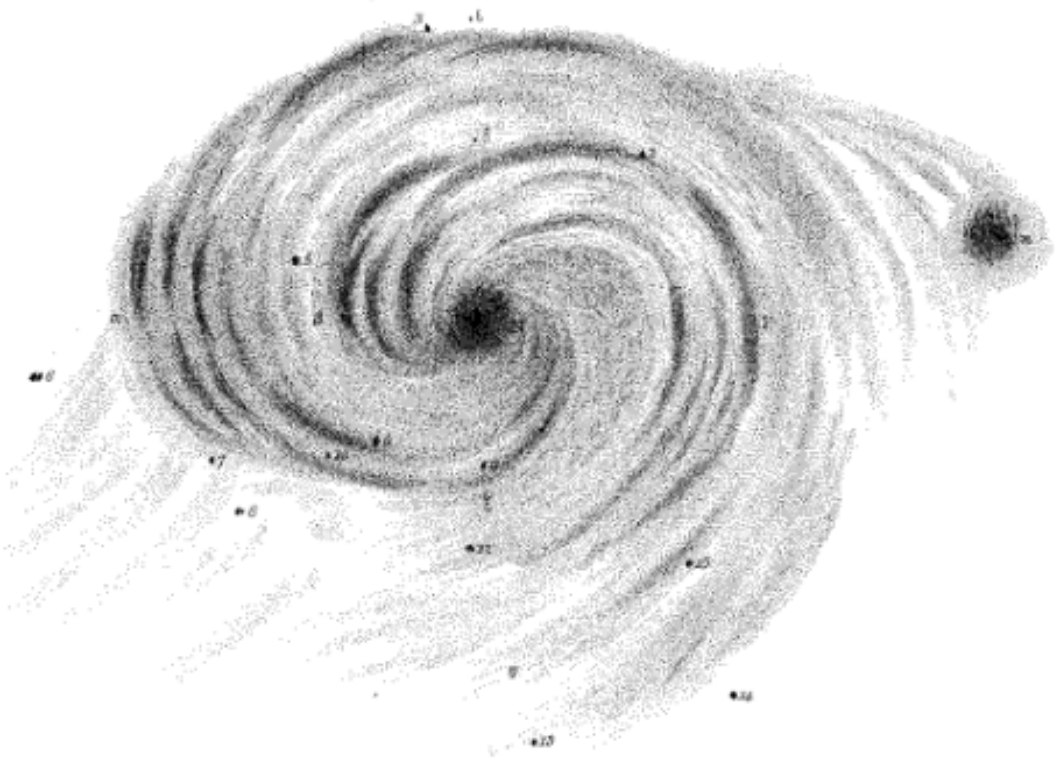

Figure 1.1: A sketch of the galaxy M51 by Lord Rosse (Rosse 1850).

Discovery of Seyfert galaxies: E. Fath was the first to notice some strong emission lines (H, O, Ne) in the spectrum in the center of the NGC 1068 (Fath 1909a). With more extensive observations resulting in higher resolution spectra, E. Fath in collaboration with Vesto Slipher (Lowell Observatory) found signs of unusually broad emission lines with velocities of several hundreds of km/s (Slipher 1917). In 1918, Herber Curtis observed also the first optical jet that is connected with the nucleus in the M87 and noticed "a curious straight ray....apparently connected with the nucleus by a thin line of matter" (Curtis 1918). In 1926, E. Hubble retrieved along with the spectrum of NGC 1068, two more spectra for the nebulae NGC 4051 and NGC 4151 and found also broad emission lines (Hubble 1926). With the general relativity theory established in 1915 (published in Einstein 1916), he concluded that these "nebulae" are extra-galactic. A couple of decades later, Seyfert (1943) found a large number of galaxies (NGC 1275, 3516, 4051, 4151, and 7469) similar to NGC 1068 separating them from the others as a new distinct class. These galaxies with very bright point-

like nuclei and high-excitation nuclear emission lines (broad lines up to 8500 km s-1) were named after him as "Seyfert galaxies". Seyfert galaxies remained in the dark for a couple of decades until two radio sources were associated with NGC 1068 and NGC 1275 (1955) and Schmidt (1963) realized that the radio source 3C 273 had an optical counterpart with a redshift at z=0.158. But how a radio source could be associated with an astronomical object?

Discovery of radio galaxies: Radio astronomy started at the end of 19th century with the James Clerk Maxwell's equations showing that the electromagnetic radiation could have any frequency. A little bit later, Heinrich Hertz showed that these electromagnetic fields, indeed, exist by constructing the first radio wave transmitter (LC oscillator) that transmits and receives electromagnetic waves of about 5 m wavelength and he, further, confirmed the predicted polarization. Efforts at that time to detect a radio signal coming from the Sun were unsuccessful, since the antennas constructed were technically limited. In 1932, when Karl Jansky was working for a company in detecting static from the vehicles, he detected an unusual radio signal with a constant cycle of approximately 24 hours (Jansky 1932). His initial thoughts were that this radio emission comes from the Sun. However, by comparing sky maps in different wavelengths, he concluded that this radio source is coming from the Milky Way and, especially, from the constellation of Sagittarius (Jansky 1933). Grote Reber, in 1939, inspired by the work of K. Jansky, built his own parabolic reflector (∼9.5 m) in the back yard of his home in Chicago. He aimed to observe the full sky during the nights to avoid the sparks from the vehicles that induced large noise. His first two attempts to receive a signal at 3300 MHz and 900 MHz did not have any results. His trial at 160 MHz (corresponding wavelength at 1.9 m) was successful, since he found a signal from the central part of the Milky Way (1938) confirming the discovery of K. Jansky. The next years, he focused in building a full sky map in 160 MHz that published in the year 1944 (Reber 1944). This catalogue included a radio source in Cygnus constellation (the second brightest object) that was a precursor of what followed in the AGN interpretation, while it motivated the scientists to turn their interest in constructing radio catalogues starting the era of radio astronomy. Such surveys with radio catalogues were conducted by different institutes around the world. The early radio surveys included the 3C, 3CR and 4C Cambridge catalogs (Edge et al. 1959; Pilkington & Scott 1965; Gower et al. 1967) at 158 and 178 MHz, the PKS survey (Ekers 1969) at Parkes in Australia that observed the southern sky at 408 and 1410 MHz, the Arebico Occultation survey (Hazard et al. 1967) giving high precision positions and the Ohio radio survey (Ehman et al. 1970) at 1415 MHz. Some of the early radio discoveries included the detailed studies of the Cygnus region from 1946 Stanley Hey that found rapidly variation in a source that called Cygnus A and concluded that the variations could be explained only with a small number of

discrete sources. (Ryle et al. 1950), with the detection of similar sources categorized them as a new type of stars with bright radio emission, but invisible in the optical light, the radio stars.

Discovery of Quasars: Minkowski (1960) was the first to identify an optical counterpart of the radio source 3C 295 that has a redshift of z=0.46. After this discovery, Allan Sandage and Schmidt started the quest of optical identifications and redshifts of radio galaxies. Both of them worked in collaboration with Matthews that used the interferometry in Caltech to derive accurate positions. In 1960, A. Sandage took an optical photograph of the radio source 3C 48 and he found a source with 16 magnitude, stellar-like object showing variability. Furthermore, this source had an excess in the UV regime and also had broad emission lines in not familiar wavelengths in its spectrum. This result was presented in a conference and was published in the proceedings by Matthews et al. (1961). Next, the discovery of many other objects similar to 3C 48 were found (e.g. Matthews & Sandage 1963), and the number of these objects was high enough to categorize them as a new class of objects giving them the name Quasi-Stellar Radio Sources (QSRSs), Quasi-stellar sources (QSS) or quasars. In the same year, (Hazard et al. 1963) found an accurate position of the brightest radio source, 3C 273, using the technique of lunar occultations. Maarten Schmidt then identified the optical counterpart of this radio source and surprisingly this point-like "star" had a very bright magnitude (13^{th} mag). With further examination of its spectrum, M. Schmidt found a peculiar compared to that of 3C 48 spectrum with very broad lines. He also surprised recognised the Hydrogen Balmer emission lines, though redshifted at 16% (Schmidt 1963). This meant that this source with the huge energy emitted is at a distance 770 Mpc (redshift z=0.16). The same year, Greenstein (1963) and Oke & Schmidt (1963) found the optical spectra from the radio sources 3C 48 and 3C 273, respectively and identified similar emission lines if redshift was taken into account. After that it was clear that these object belonged in the same AGN family. Sandage (1965) identified more objects similar to the previous but without radio emission. He called them as quasi stellar galaxies. Since then the radio was not included in the definition of these objects.

Towards super-massive black holes: After all this progress the previous years in identifying AGN, the idea of SMBHs being in the center of the AGN has started to be dominant. It was clear at that time that a super massive and compact source should explain all these observations. Furthermore, this object should be responsible for the powerful energy emitted and be capable of forming collimated jets. Woltjer (1959) was the first to list some basic properties of the Seyfert galaxies: a) unresolved nuclei with size less than 100 pc, b) nuclear activity should last more than 10^8 years (this is a result of the fraction of spiral galaxies hosting an AGN), c) if material is

bound gravitationally to very high mass, then from the virial argument the velocity dispersion of the emission lines is about 1000 km/s and the nuclear size (<100 pc) could give an upper limit in the mass. So the mass should be in the order of 10^8-10^{10}. Hoyle & Fowler (1963) was the first to claim that in the center of the AGN lies a stellar type object with huge mass and that emits a large amount of radiation by accreting mass from the surrounding environment. The idea of a black hole that replaces this hyper-massive star was given by Salpeter (1964) and Zel'dovich (1964). However, black holes as objects were not something new. Even though, (Wheeler 1968) gave the term "black holes" to gravitational singularities, the theoretical studies have began almost two centuries ago with Michell (1784) supporting the existence of objects with sufficient gravitational energy that could be capable to trap the light. Independently, Laplace (1796) introduced the concept of "dark stars" that represented the most massive stars in the Universe that are invisible in the optical light due to the gravitational potential. With the General relativity replacing the Newtonian, (Schwarzschild 1916) solved the Einstein's equations and gave the black hole solution. After several works later on white dwarf (Chandrasekhar 1931) and neutron stars (Oppenheimer & Volkoff 1939), Oppenheimer & Snyder (1939) suggested that massive stars when reaching a critical gravitational radius could collapse into black holes formatting an event horizon. So in 1970's, the black hole paradigm as the intrinsic mechanism of the AGN could explain the huge energy output of the AGN as the gravitational energy is converted into accretion energy and could explain also the short-scale variability of the center of these galaxies that should be very small (Salpeter 1964; Zel'dovich 1964; Lynden-Bell 1969; Rees 1984).

X-ray revolution: After the discovery of quasars, in the mid-1960s the X-ray astronomy started and was important to understand better the nature and the properties of the AGN, as the X-ray emission seemed to occur in the majority of the them. The first X-ray detected emission of AGN was that of M87 and 3C 273 in a survey of the Virgo region (Giacconi et al. 1962) with a proportional counter (Geiger counter) on board an Aerobee rocket (Friedman & Byram 1967). Later, Uhuru, the first X-ray satellite launched in 1970 was responsible for the first detection of a Seyfert galaxy (Gursky et al. 1971), while Ariel V, a British-USA collaboration satellite launched in 1974, mended to monitor the X-ray sky. Results of Ariel V data included the confirmation of the X-ray variability in the center of AGN (Ives et al. 1976; Marshall et al. 1981) and strong X-ray emission in Seyfert galaxies (Elvis et al. 1978) with typical luminosities of $10^{42.5}$-$10^{44.5}$ erg s^{-1}. Also, Elvis et al. (1978) claimed that not all QSOs have the basic properties defined by Schmidt, but the majority of them have X-ray emission. The next generation X-ray telescopes included in addition to proportional counters, scintillation detectors. These are a) the NASA's High Energy Astronomy Observatory (HEAO 1) that was launched in 1977 and carried the first

complete X-ray sky survey, especially towards high Galactic amplitudes (Piccinotti et al. 1982) and b) the Einstein Observatory satellite launched in 1978 that was the first telescope with focusing optics and capable of producing images. The advanced astronomical findings of the latter led to surveys with many X-ray point-like sources and also diffuse sources with very high spatial resolution of a few arcseconds (Tananbaum et al. 1979). Furthermore, it was the first time that the power-law was observed in the 3-50 keV regime characteristic feature of AGN, the very first discovery of the soft X-ray (<1 keV) bump in the Seyfert galaxies (Singh et al. 1985), a good spectral characterization of the X-ray cosmic background (Marshall et al. 1980) and studies of X-ray spectra and time variability (Mushotzky et al. 1980; Dower et al. 1980). At that time, the X-ray emission has become basic and main characteristic of the AGN and in the decades after, many other X-ray telescopes were launched with match higher spatial resolution and with much larger collective areas. Some examples of those are: a) the European EXOSAT and the Japanese Ginga satellites in 1980's with results confirming the soft bump in X-ray spectra (Turner & Pounds 1989) and showing the flattening of hard X-ray spectra, a strong indicator of X-ray reflection (Pounds et al. 1990; Singh et al. 1990), b) the ROSAT satellite operating in energies smaller than 2 keV that mapped the whole sky with very high spatial resolution and resulted in more than hundred thousands of AGN (Voges et al. 1999) and ultra deep observations that resolved the soft X-ray spectrum (Lehmann et al. 2001), c) the Japanese ASCA (Tanaka et al. 1994), the Italian BeppoSAX (Boella et al. 1997) and the Rossi X-ray Timing Explorer (RXTE) (McHardy 2010) in the late 1990's and d) the more recent Chandra X-ray Telescope and the XMM-Newton Telescope that provided many scientific results with their high spatial resolution and large collective areas along with the NuSTAR telescope (Harrison et al. 2013) and eRosita (Cappelluti et al. 2011).

1.2 AGN taxonomy and classification

The classification of the AGN is empirical and is based on their different observational properties. Some are only based on the orientation and some others reflect real internal physical characteristics. First, they can be categorized according to the radio emission and the presence or not of jets: a) the radio-quiet AGN with negligible or very weak jets in the radio wavelengths and, b) the radio-loud AGN with very strong jets. Usually, the host galaxies of the first class are spiral galaxies, while in the case of radio-loud AGN, the galaxies underneath are elliptical galaxies (Marziani et al. 1997). Another criterion to separate the two classes is based on the angle between the SMBH spin and the vector of the angular momentum of the accretion disc. In this manner, radio loud AGN have large (>60 degrees) angles, while in radio-quiet

AGN the level of the accretion disc is almost parallel to the equatorial surface of the SMBH. Also, according to their optical spectra they could be of type 1 or type 2. Type 1 AGN spectra show both narrow and broad emission lines, while type 2 AGNs have only narrow emission lines. Further, depending of their luminosity there are Seyfert galaxies and quasars with the latter lying in the bright end of the luminosity range. Moreover, there are some special types of AGN, such as blazars that belong to the radio loud class, but they have relativistic jets with the direction of the observer showing very strong variability. More recently, Padovani et al. (2017) reviewed the different AGN types and classes with different morphological and spectral features and resulted in more than 50 different AGN types with specific features each. They concluded that the unification between those should be in terms of the efficiency of the radiation and also of the presence or absence of relativistic jets. Below, some of the basic and more common AGN classes are described in more detail along with their properties to give an idea of the diversity but also the similarities of the AGN zoo terminology.

Seyfert galaxies are lower-luminosity AGN. They have very luminous point-like nuclei in the center of the galaxies and in the optical bands they are very similar to bright stars. A comparison of an AGN to a normal galaxy is given in the Figure 1.2. Seyfert galaxies have lower luminosities that the QSOs and they are predominately found in early-type spiral galaxies (up to 10% of Sa and Sb's), but a much higher fraction is expected. Initially, they were categorized as Type I and Type II depending on the presence or not of broad Balmer emission lines in their spectra (Osterbrock 1977). Though, after the Unification model (Antonucci 1993; Urry & Padovani 1995), the best criterion should be the viewing angle. This angle is defined as the angle between the line of sight and the perpendicular line to the equatorial axis of the accretion disc. For small angles, the observations are edge-on (Type II) and only the NLR are present, while for large angles the AGN is shown face-on (Type I) and the observer sees both the BLR and NLR and also the central engine of the AGN, such as the accretion disc. Considering their spectrum could be categorized as type 1 or type 2 with type 1 having broad allowed emission lines (e.g. Balmer series) and FWHM up to 10^4 km/s, while those of type 2 lack broad lines and they have weak absorption lines coming from the underlying galaxy (usually late-type galaxy). There are also intermediate classes, such as Sy 1.5, 1.7, 1.9 with decreasing widths of the Balmer lines Osterbrock (1981). In Figure 1.3, example spectra are shown for a classic type 1 and type 2 Seyfert galaxy along with the typical spectra of quasars, LINERS and normal galaxies.

QSOs (quasi-stellar objects) are characterized as the luminous version of Seyfert galaxies with nuclear magnitudes higher than $M_B > -21.51 + 5log(H_o)$ (Schmidt &

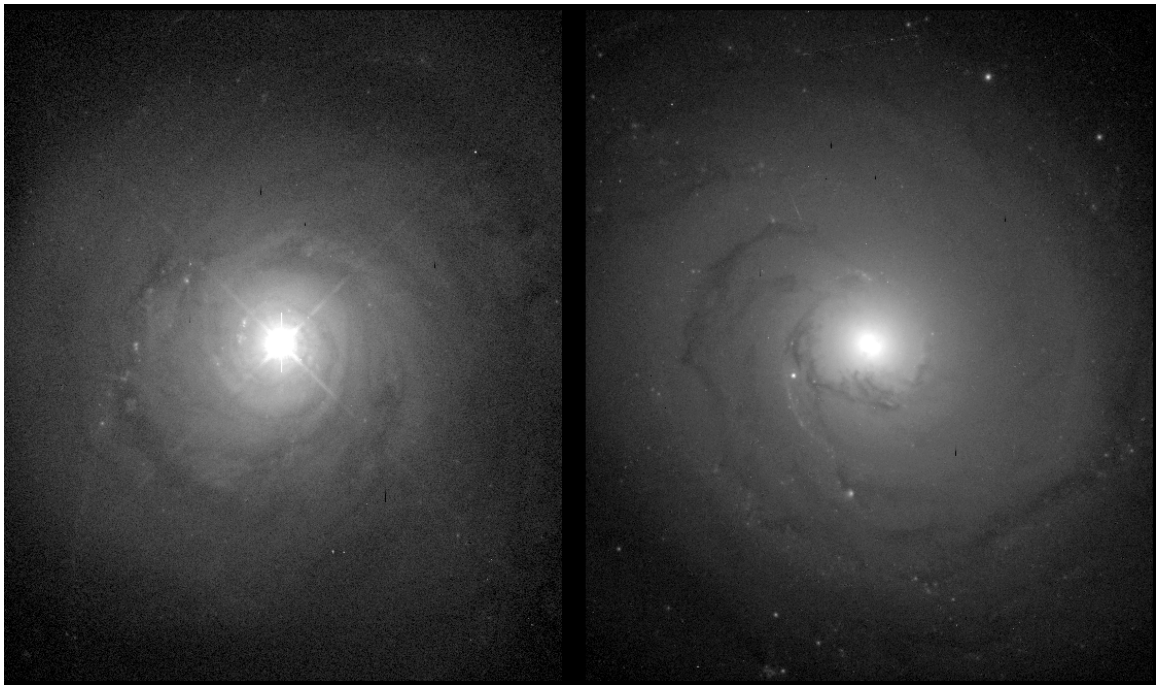

Figure 1.2: Image of a Seyfert galaxy type I, NGC 5548 (left) and a normal galaxy, NGC 3277 (right). The nucleus of the AGN is much brighter than that of a normal galaxy and its brightness has saturated the detector resulting in the diffraction spikes seen. Image credit: https://pages.astronomy.ua.edu/gifimages/ngc5548.html.

Green 1983), where the H_o is the Hubble constant. They are AGN that have very high luminosities ($\sim 10^{46} - 10^{48} ergs^{-1}$) and usually are found in greater distances than Seyferts, but they have similar spectra with them. The difference between them is that their nuclei is so bright that totally outshine their host galaxies by a factor of a thousand and thus, it is difficult to observe the hosts even with high resolution imaging, such as HST, and the absorption line features. The separation is empirical and some times it is difficult to separate high luminosity Seyfert galaxies from low luminosity QSO. A historical division between them is at i=23 mag. Similarly to Seyferts, QSO are divided into type I and type II according to the appearance or not of broad emission lines. The latter sub-class was recently discovered (Stern et al. 2002; Norman et al. 2002) compared to the discovery of quasars.

LINERs stands for Low-Ionization Nuclear Emission Line Regions and they are sources with strong forbidden narrow emission lines ([OI]λ6300, [NII]$\lambda\lambda$6548,6583 and [SII]$\lambda\lambda$6716,6731) in their optical spectra similar to AGN, however they display weaker [OIII]λ5007 emission lines (Fig. 1.3). They first defined as a distinct class by Heckman (1980) that pointed out that these source have spectra that are very different than the classic AGN or H II regions. Interestingly, the majority of nearby AGN are

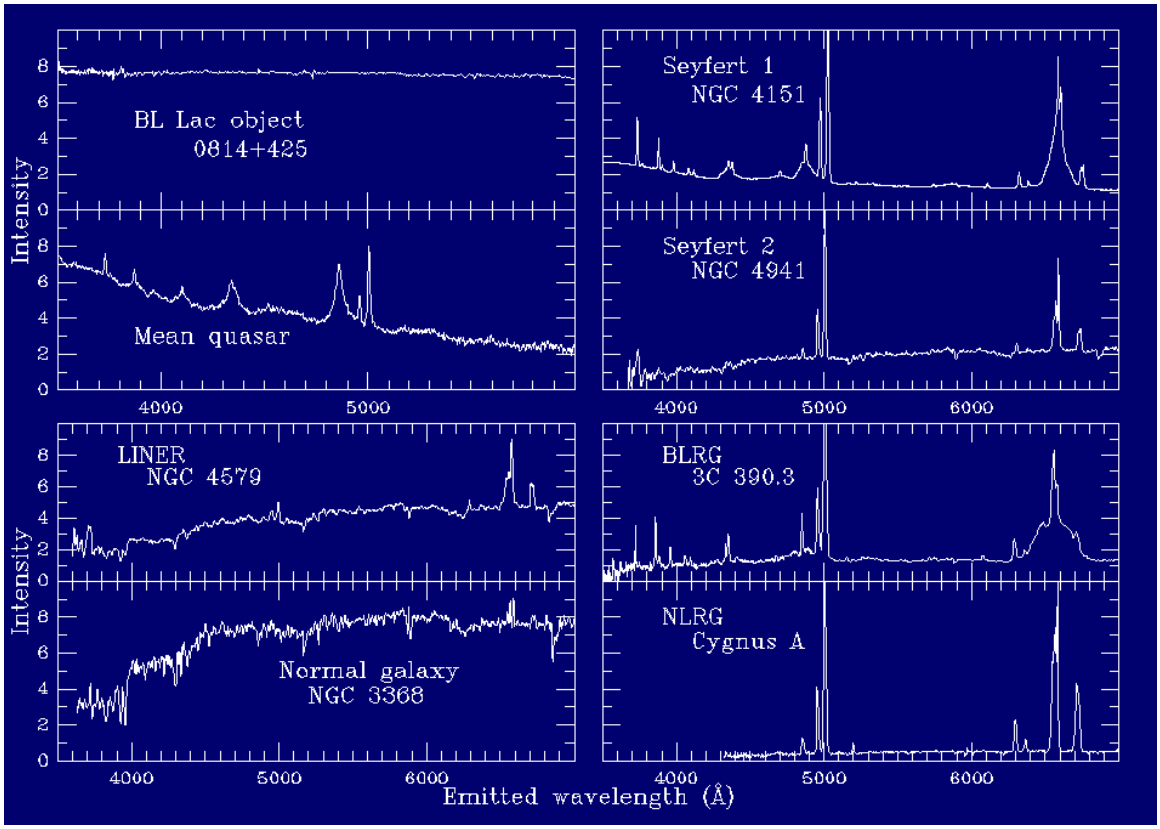

Figure 1.3: Typical spectra of different classes of AGN as indicated. Image credit: https://pages.astronomy.ua.edu/keel/agn/spectra.html.

dominated by emission lines of low ionization, such as [OI]λ6300, [OII]$\lambda\lambda$3726,9 and [SI]$\lambda\lambda$6717,31 (Ho et al. 1997). Also, one third of the galaxies in the Local Universe and, especially, in early-type galaxies has spectra similar to LINERS (Heckman 1980; Ho et al. 1995, 1997). In principle, LINERs are less luminous than Seyfert galaxies or quasars and some times they are synonymous to low luminosity AGN, though there are some exceptions in this rule (e.g. Filippenko 1993) and thus low luminosity AGN are not all LINERs. LINERs may have weak broad lines ($\sim$20%), and by analogy to Seyfert galaxies they are divided into LINERs type I and type II in the presence or not of broad emission lines. Furthermore, when comparing the strength of the X-ray and radio emission, LINERs tend to be radio-loud (Terashima & Wilson 2003). This agrees well with the work of Ho (1999, 2002) that showed that radio-loudness is a common feature in nearby accreting AGN. LINERS are usualy defined by one or two line intensity ratios. The most common ratios are [OII]/[OIII]>1 or/and [OI]/[OIII]>1/3 and NII/Ha>0.6 or [OIII]/Hb$\leq$3 (Veilleux & Osterbrock 1987; Kewley et al. 2006). The true nature of LINERS is debated as their power source is still unclear. There are many evidences indicating that an AGN is responsible for the low ionization emission

lines, but with lower ionization parameters than Seyfert galaxies (Heckman 1980; Ho et al. 1993). Some of them a) have double-peakes broad Balmer lines (Bower et al. 1996; Storchi-Bergmann et al. 1997; Eracleous & Halpern 2001), b) have compact radio cores (Falcke et al. 2000; Ulvestad & Ho 2001; Filho et al. 2002, 2004; Anderson et al. 2004), c) have evidence of hard X-ray spectra (Terashima et al. 2000; Ho et al. 2001) and/or d) show UV variability (Maoz et al. 2005). On the other hand, there are some different interpretation of the emission of LINERs, such as fast socks (Heckman 1980; Dopita & Sutherland 1995; Lípari et al. 2004), photoionization by hot stars (Filippenko & Terlevich 1992; Shields 1992; Maoz et al. 1998; Barth & Shields 2000) or photoionization by an old, metal-rich stellar population (Taniguchi et al. 2000; Alonso-Herrero et al. 2000). Concerning the low ionization region, it is observed in extra-nuclear regions and it is though that is connected with large-scale outflows and related shocks (Lípari et al. 2004) or with regions shocked by radio-jets (Cecil et al. 2000).

Blazars are characterized by non-thermal emission and rapid high amplitude variability from minutes to years and the emission in almost all band (optical, radio, X-rays) is polarized. The strong radio emission originates in the jets that have direction towards the observer and outshine the rest of the central engine and the host galaxy that are usually giant elliptical galaxies. The main categories of blazars are a) the Flat Spectrum Radio Quasars (FSRQs), b) the BL Lac objects and, c) the Steep Spectrum Radio quasars (SSRQs) with very steep spectra, while there are plenty of other sub-classes (LPQs or lobe-dominated SSRQs, OVVQs and core-dominated, etc.). Efforts to understand the physical processes that differentiate the classes of BL Lacs and FSRQs have been made from many authors. For example, in Boula et al. (2019) they used a one-zone leptonic model with only one free parameter, the mass accretion rate, to reproduce the blazar sequence observed for the different classes.

Radio galaxies are characterized by extended radio emission and could be split into Fanaroff-Riley I (FR Is) and Fanaroff-Riley II (FR IIs) based on differences in the jets (morphology) and the power of the radio-waves (Fanaroff & Riley 1974). **FR Is**: a) usually have jets that do not have hot spots, b) areas of increased brightness are those located near the central core while brightness is reduced in the outermost regions, c) there is no need of any obscurial material, such as the torus component, that would hide the central engine in the direction of the observer (Chiaberge 2004), d) do not have emission lines and, in general, are considered as low-brightness AGN, and, e) may have jet in one direction only (one-sided) or in both directions (double sided). **FR IIs**: a) display aligned jets with prominent hot spots on the edges of the lobes, b) unlike FR Is, the presence of material with high optically depth (optically thick) is generally acceptable that conceals the central area of teh AGN, c) areas of

high brightness are those considered to be far from the center (e.g. edge brightened).

1.3 The Unified Model

As discussed in the previous section, there is a big variety of AGN classes that arises from the different detection criteria and the wavelengths AGN are observed. Though, despite the differences between the AGN classes, there were some common characteristic that led to the idea of a unique and simple model that would explain physically or observationally the distinct AGN classes. Such unification theories were initially appeared in 1970's with the idea that inside the Seyfert galaxies exceeds faint quasars (Weedman 1973; Penston et al. 1974). This was in agreement with the work of Kristian (1973) that found quasars with extended host galaxies and not being point-like sources. Rowan-Robinson (1977) was the first trying to unify the Seyfert galaxies and the radio sources and he made the assumption of an obscuring by dust material that attenuates the broad line emission and it is responsible for the type I and type II classification. Even though, he was correct partially, he did not take into account the beaming effect. The latter was approached by Blandford & Rees (1978) doing a beaming unification in which for example the blazars have its beaming axis toward the observer. Scheuer & Readhead (1979) further tried to unify the the radio-quiet and the radio-loud AGN. Later on, the idea was extended to radio-lobe and radio-core dominated galaxies Orr & Browne (1982); Kapahi & Saikia (1982) and the radio-loud galaxies and the quasars (Barthel 1989). In many studies (Antonucci 1984; Antonucci & Miller 1985; Miller et al. 1991), the search for a connection between Seyfert galaxies of type I and type II led to the first evidence that there is an anisotropic obscuring material (mainly dust) in AGN. In particular, using spectropalrimetry in the prototype of Seyfert type II galaxy, NGC 1068, they found broad permitted lines that appear usually in Seyfert type I galaxies. Thus, in type II AGN there is an optically thick obscuring material that hides the BLR.

With the reviews of Antonucci (1993) and Urry & Padovani (1995), the Unified model became very shortly broadly accepted. In this scheme, there are two different types of AGN, the radio-quiet and the radio-loud AGN, and the variety of all the AGN classes observed is due to an obscuring material between the central engine and the observer, while the different classes could be explained in terms of the viewing angle. In Figure 1.4, an artistic view of the Unified model is shown by Beckmann & Shrader (2012). The different components that are included in the current picture of the AGN will be discussed in detail in the next section, while they can be summarized as follows:

- A super-massive black hole in the nucleus with mass in the order of 10^6-10^9 Mo and size $R_s << 10^{-3}$ pc.
- An accretion disc that sourounds the SMBH ($r_{disc} << 0.1$ pc) constituted by hot (10^4-10^6 K) and optically thick ionized gas.
- The Broad Line Region (0.01-0.1 pc) with dense, ionized by the accretion disc gas clouds with very high velocities producing the broad emission lines observed in spectra.
- A dust molecular torus that hides the central engine of the AGN (1-10 pc) with the inner border set by the dust sublimation temperature (T_{sub}=1500 K).
- A hot corona near the central engine that emits in the X-ray regime.
- In larger distances (10-100 pc) there are less dense gas clouds of lower velocities responsible for permitted and forbidden narrow emission lines
- Relativistic jets that are created at 100*Rg from the SMBH with sizes of 0.01-10^6 pc.

Other evidences that both types of Seyfert galaxies have the same central engine was through X-ray and IR observations. Lawrence & Elvis (1982) found higher column densities of absorbed gas in Seyferts II galaxies compared to those of type I and Goodrich et al. (1994); Ruiz et al. (1994) using near-infrared observations where the opacity is much lower than the optical regime identified broad permitted emission lines in a sample of Seyfert type II galaxies. Moreover, in Page et al. (1997) and Hasinger et al. (1998) the majority of AGN with broad emission lines are unobscured in the X-ray regime. Another strong argument supporting the Unified model is the existence of the torus itself. From the late 1990's Gallimore et al. (1997); Jaffe et al. (2004); Capetti et al. (2005) up to more recent observations (García-Burillo et al. 2016a; Carilli et al. 2019) the structure of the torus can be observable.

One of the main difference between the AGN sub-classes is the presence or not of broad emission lines in the optical spectra. The Unified model suggests that all sources have the same intrinsic mechanism, but their observational properties are different. Since, the broad and narrow regions lie in different regions, this could be imprinted in the spectra. For example, for small viewing angles where the AGN is seen edge-on, the NLR is observable but not the BLR, because the NLR is more extended than the BLR and the obscuration torus hides the central components, such as the accretion disc and the BLR. In this case, the spectrum of a source would have only narrow lines indicating a Seyfert galaxy or a quasar of type II. On the other hand, large

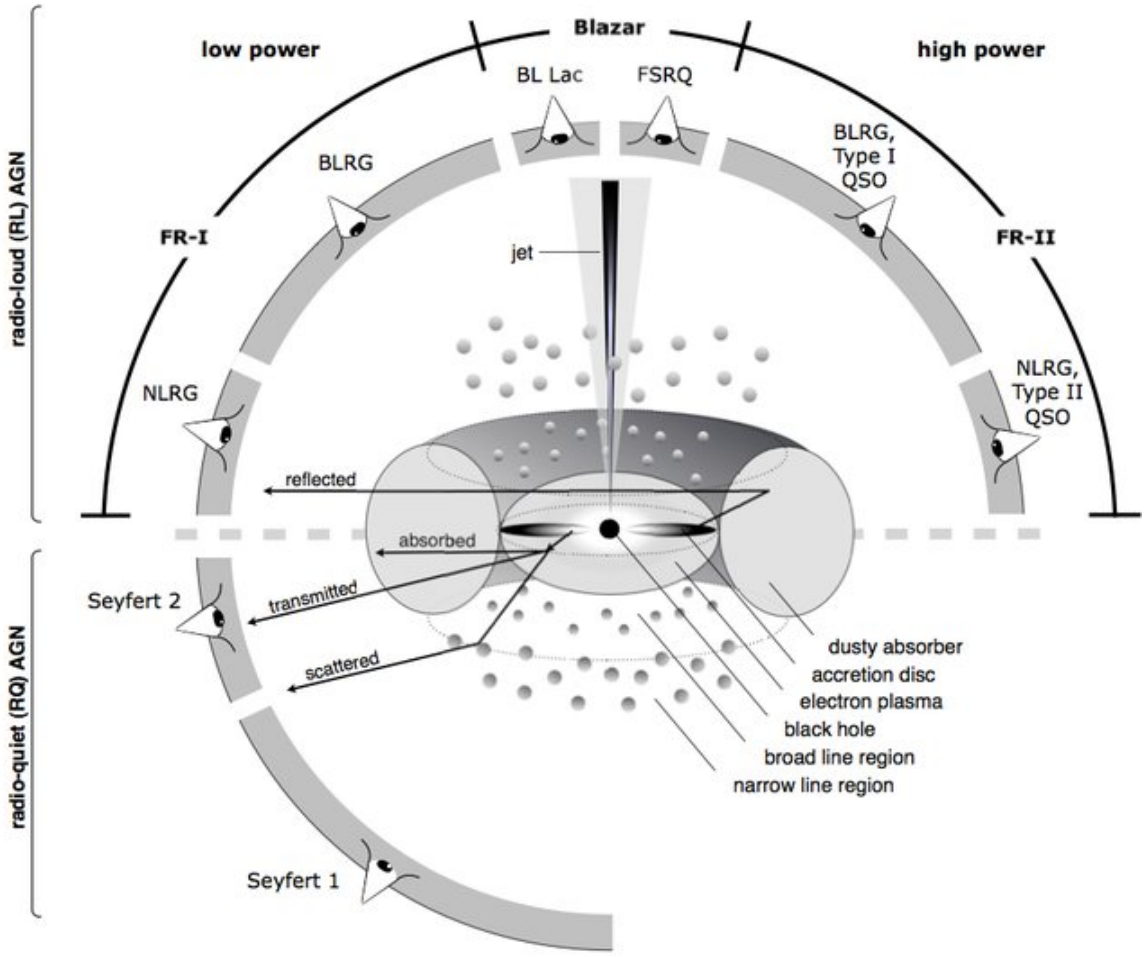

Figure 1.4: A schematic view of the AGN Unified model by Beckmann & Shrader (2012).

viewing angles allow the observation inside the torus of both the broad and narrow line regions and also the accretion disc, thus in the spectra there is a superposition of broad and narrow lines similar to Seyfert galaxies of type I. Following the same logic in the X-ray regime, for small viewing angles the X-ray radiation from the central engine is absorbed and this can be interpreted with high column densities ($N_H > 10^{22}$) of the torus (type II AGN), while for large viewing angles the X-ray emitting region is observable and thus there is no obscuration ($N_H < 10^{22}$), such in type I AGN.

As the majority of the different AGN classes could be explained with the orientation effect, many studies have tried to understand the transition from the radio-quiet (non- or sub- relativistic radial outflows) to radio-loud AGN (relativistic jets). For example, this difference in outflows was suggested to be attributed to the BH spin

(Blandford 1990; Wilson & Colbert 1995), to the host galaxy type and properties (Smith et al. 1986) or to the mass accretion rate (Rees et al. 1982). Though, in Tsinganos et al. (2001), it was the first time that a quantitative physical criterion was proposed to explain the differences in the radio-loudness based on analytical model of Magneto-Hydro-Dynamic (MHD) outflows from a magnetic and rotating BH. In particular, they introduced the magnetic rotator parameter, ϵ, that depends on the efficiency of the magnetic rotator and the pressure gradient inside the streamlines of the jets that is affected by the environment the jet propagates. Previous works in MHD analytical solutions and the formation and morphology of collimated jets included Sauty & Tsinganos (1994) and Sauty et al. (1999). This magnetic rotator could explain the different class of AGN in addition to the viewing angle. Figure 1.5 presents a unified scheme including this parameter (vertical axis). Thus, the transition from radio-quiet (upper) to FRI and further to FRII could be explained with the efficiency of the magnetic rotator and also the environment.

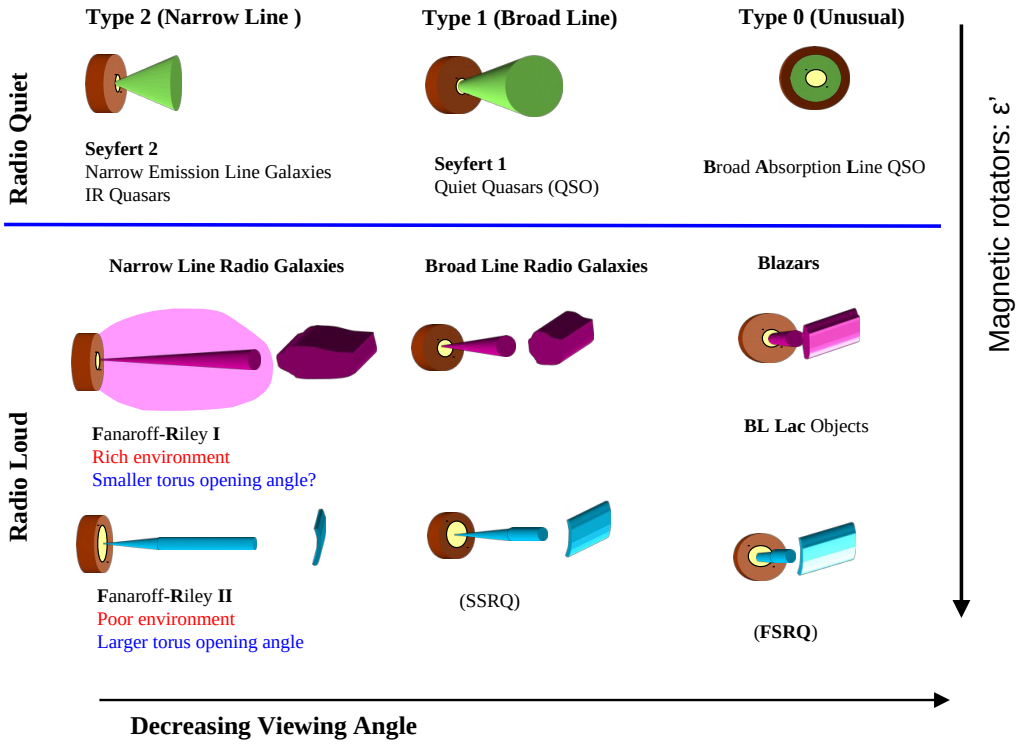

Figure 1.5: The AGN unification scheme proposed by Tsinganos et al. (2001) that includes a quantitative physical criterion to explain the radio-loudness transition. Image credits: Prof. K. Tsinganos.

However, the Unified model does not seem to be applied in all the cases. For example, Tran (2001) studied Seyfert galaxies of type II and they found a high fraction of sources with no polarization as expected, so the orientation effect was not consistent in these galaxies and other, probably intrinsic mechanisms, should be taken into account. Netzer (2015) claimed that this fraction is around 30% in the Local Universe. Moreover, the recent years, there are many studies showing that some AGN change spectral types within a few years, the so-called Changing-look AGN. For example, an initially type 1.5 Seyfert galaxy could change to type 1 and later on in type 2, such as the Mrk 590 (Denney et al. 2014). Such a behaviour would result in a variable obscuration material or an accretion rate that varies with time. Mateos et al. (2016) also supported that the Unified model cannot explain different covering factors measured in type I and type II AGN in terms only of the orientation and the nature of the obscuring torus should be further investigated.

1.4 AGN structure

Nowadays, the paradigm responsible for the huge amount of energy released from the AGN is the presence of a central engine composed of a super massive black hole and a accretion disc from which matter falls inwards the SMBH. Other components of the AGN structure are the broad and narrow emission line regions, the dusty torus, a hot corona and/or relativistic jets. Behind these structures, different physical phenomena occur resulting in a multi-wavelength emission. The energy emitted from the different components covers the full electromagnetic spectrum from γ-rays to radio wavelengths. In Figure 1.6, a typical spectral energy distribution (SED) of AGN is shown. In this section, the structure of the AGN will be presented with the corresponding emission features after a brief introduction in the power that could be produced by accretion.

1.4.1 Super massive black holes

The black holes are region in space-time with such a high gravitational potential that even the light cannot escape and they are surrounded by the event horizon in which the escape velocity is higher than the speed of light. BH can characterized only by three parameters: the mass, the spin and the charge. Applying the General Relativity theory (Einstein 1916) and taking into account the influence of the matter on the geometry of the space-time, Schwarzschild (1916) gave the solution for a neutral, non-rotating black hole with the event horizon radius given by $Rg = 2GM/c^2$, where g is

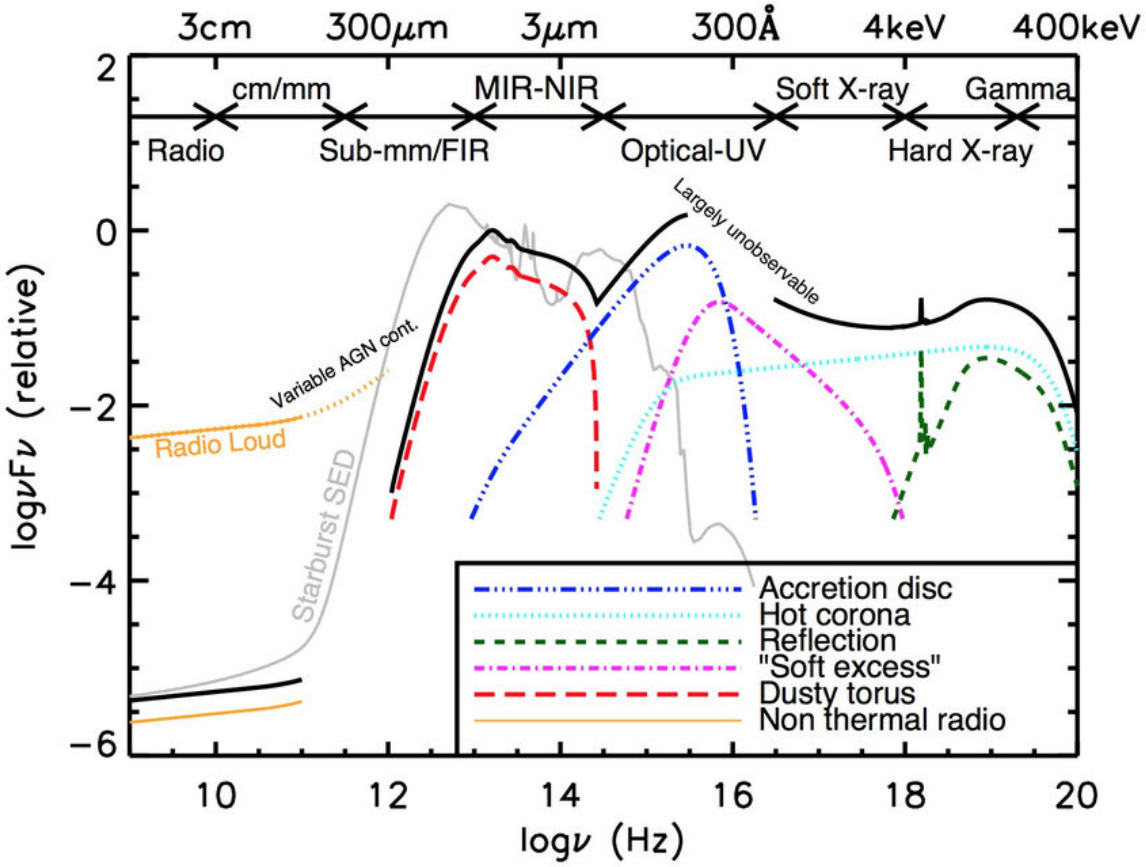

Figure 1.6: A schematic view of a multi-wavelength SED of AGN from radio to γ-rays. The different colours represent different components of the AGN structure as indicated. The image was taken from Harrison (2014).

the Gravitational constant, M the mass of the black hole and c the speed of light. The solution for rotational black holes was given by (Kerr 1963). Rees (1978) gave three possible scenarios for the formations of black holes: a) gravitationally collapse of many stars or of massive primordial clouds (Dokuchaev et al. 2007), remnant of population III stars, c) formation of dense cluster and runaway collisions. None of these can be ruled out nowadays, since there are limitations in the high-redshift observations (Volonteri 2010). Then, these stellar BHs become the seeds of the SMBHs in the center of galaxies (Lynden-Bell 1969; Rees & Volonteri 2007) as they grow by accretion matter or by merging with other stars or black holes. The SMBH mass ranges between $10^6-10^9 M_o$ (Lynden-Bell 1969; Lauer et al. 2007). The most extreme cases were found at redshift higher than six when the Universe was less than 700 Myr old with masses exceeding $10^9 M_o$ (Mortlock et al. 2011; Bañados et al. 2016; Mazzucchelli et al. 2017). The big question raised from these observations and it is still unclear was how these BHs formed in the early Universe (Volonteri 2014; Bañados et al. 2018). Moreover, the

SMBHs evolve slowly with time (Vika et al. 2009) and, thus, the accretion process may not explain the most extreme cases of black hole masses (Mayer et al. 2010). Finally, there are correlations between the black hole mass with the host galaxy properties, such as the bulge mass and the velocity dispersion (Kormendy & Ho 2013).

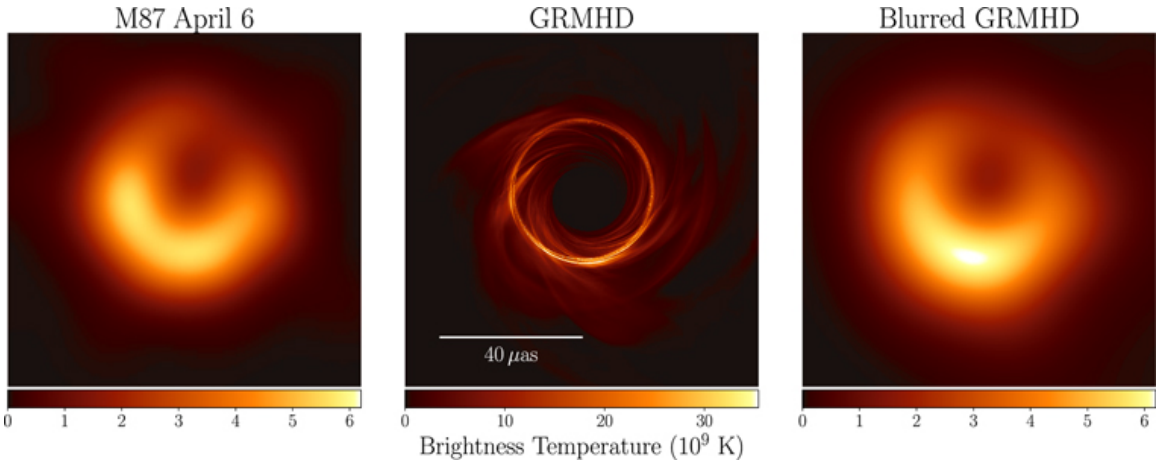

Figure 1.7: The first image of a SMBH in M87 (left), the image expected from General relativity and Magneto-Hydro-Dynamics simulations (right) and the expected image with the telescope biases. The image was taken from Event Horizon Telescope Collaboration et al. (2019).

The first evidence of the BH existence found in IR observations. In Genzel et al. (1996); Ghez et al. (1998), stars orbit around an invisible object in the center of the Milky Way suggesting a heavy and compact object. The mass of Sgr A* was estimated equal to $4.4 \times 10^6 M_\odot$. Other methods for finding BH masses relies on: a) the broadening of several emission lines, such as broad Ha (Greene & Ho 2005b) and Hb (Trakhtenbrot & Netzer 2012) emission lines, b) reverberation mapping with Bentz & Katz (2015) providing an AGN catalogue with the majority of them having BH masses between $10^6 - 10^9 M_o$ (Koss et al. 2017) consistent with the theoretically models and c) stellar velocity dispersion (Greene & Ho 2005a; Dasyra et al. 2008, 2010, 2011). The latter indicates that the accretion history of the BHs are linked with the evolution of the galaxy in the Local Universe (Ferrarese & Ford 2005). Another evidence of the existence of the BHs can be given by the Soltan argument. The cosmic X-ray background that is observed in the X-ray spectrum peaking at ∼30 keV consists of the emission of AGN and a small fraction of small X-ray clusters or/and starbusrts galaxies (Gilli et al. 2007). Assuming a specific radiative efficiency and the fact that SMBHs grow in time, the SMBH density can be derived by the radiation density from the AGN. The initial idea of this argument was given by Soltan (1982) and it provides an observational limit of the BH density in the Universe. The latter was

measured by Marconi et al. (2004) and found values equal to $\rho = 4 \times 10^5 M_\odot Mpc^{-3}$. The first direct view of a SMBH was observed with the Event Horizon Telescope (EHT) in M87 (Event Horizon Telescope Collaboration et al. 2019). EHT linking telescopes at millimetre wavelengths around the world reached spatial resolution up to 25 mas that corresponds to 0.035 pc in the case of M87. In Figure 1.7, it is shown the first image of a SMBH in M87 (left), the image expected from General relativity and Magneto-Hydro-Dynamics simulations (right) and the expected image with the telescope biases.

1.4.2 Energy produced through accretion

One main characteristic of the AGN that separates them from the other galactic and extra-galactic sources is the release of huge amount of energy with luminosities up to 10^{46} ergs s^{-1}. Nowadays, it is commonly accepted that inside the AGN there is a super-massive black hole that accretes mater from a disc around it. In this picture, the energy released is due to the conversion of gravitational energy into heat and radiation. Assuming a particle with mass dm originally located very far from the black hole (for simplicity in the infinity) is captured by the accretion disc in a circular orbit with radius r around the black hole. Then, the centripetal equilibrium balance for the mass particle dm gives:

$$\frac{dmv^2}{r} = \frac{GMdm}{r^2}, \tag{1.1}$$

where M is the mass of the black hole. In the circular orbit, the particle has negative total energy. As the initial energy, E_∞, in its original position, was zero, the release of the extra energy, dE_{acc}, should be due to viscosity in the accretion disc:

$$dE_{acc} = E_\infty - E_r = 0 - \left(\frac{1}{2}dmv^2 - \frac{GMdm}{r}\right). \tag{1.2}$$

From the equations 1.1 and 1.2 there is:

$$dE_{acc} = \frac{1}{2}\frac{GMdmv^2}{r}. \tag{1.3}$$

Considering the Schwarzschild radius of the black hole ($R_s = 2GM/c^2$), the previous equation gives:

$$dE_{acc} = \frac{1}{4}\frac{R_s dmc^2}{r}. \tag{1.4}$$

The luminosity, L_{acc}, produced by this accretion is:

$$L_{acc} = \frac{dE_{acc}}{dt} = \frac{1}{4}\frac{R_s}{r}\dot{m}c^2, \tag{1.5}$$

where $\dot{m} = dm/dt$ is the accretion rate of the material into the black hole. The latter equation, further, can be written as:

$$L_{acc} = \eta \dot{m} c^2, \tag{1.6}$$

where $\eta = (R_s/4r)$ denotes the efficiency factor that converts the potential energy to radiation. The efficiency factor may vary in the range between 6 and 42% (Krolik 1999), as the accretion rate depends on the mass of the black hole and the distance (compactness of the source). The maximum value can be reached by a maximally spinning black hole (Novikov & Thorne 1973; Fanidakis et al. 2011). Typical values for AGN are close to $\eta = 10\%$, such as in the case of 3C 273 (Marconi et al. 2004; Merloni 2004). These values are in agreement with observations of quasars with values $\eta \sim 6 - 30\%$ (Davis & Laor 2011). For comparison, the efficiency of hydrogen fusion into helium during the thermonuclear reactions occurring in the core of the stars is equal to $\eta = 0.007$. Therefore, the accretion matter is a very efficient way of producing the huge amounts of radiation produced in the center of the AGN. This could not be explained just by nuclear reactions inside the stars. Finally, the efficiency factor depends strongly on the spin of the black hole and in this case, the energy released will be much larger (Shapiro & Teukolsky 1983). In the case of the Milky way, the equation 1.6 could explain its low luminosity compared to that of AGN as the accretion rate is too low or its efficiency process is very small.

1.4.3 Growth of SMBHs

Assuming a steady, spherically symmetric and non-rotating accretion of a fully ionized gas (e.g. hydrogen), there is a maximum luminosity that can be reached from the accreting object that depends only from its mass (Eddington 1916). According to the hydro-static equilibrium, the Eddington luminosity (or Eddington limit) could be defined when the gravitational force is equal to the radiation pressure. The radial component of the gravitational force onto an electron-proton pair (electromagnetically coupled), with masses me and mp respectively, is:

$$F_{grav} = \frac{GM(m_p + m_e)}{r^2} == \frac{GMm_p}{r^2}, \tag{1.7}$$

where G is the gravitational constant, M is the mass of the accreting object and assuming the mass of the electron negligible compared to that of the proton ($m_p = 2000 m_e$). On the other hand, a photon with energy $h\nu$ and luminosity L has flux $L/4\pi r^2$, thus the number of the photons will be:

$$N_{phot} = \frac{L}{4\pi r^2 h\nu}. \tag{1.8}$$

The radiation pressure related to the momentum transferred from photons to electrons is:

$$F_{rad} = \sigma_T N_{phot} p = \frac{\sigma_T L h\nu}{c 4\pi r^2 h\nu}, \tag{1.9}$$

where $\sigma_T = 6.65 \times 10^{-25} cm^2$ is the Thomson scattering cross-section and the momentum is defines as $p = hv$. Satisfying the condition of the energy production, the radiation power should be lower than the gravitational force:

$$F_{rad} \leq F_{gran}, \tag{1.10}$$

thus by replacing these quantities with equations 1.7 and 1.9 the Eddington luminosity, L_{EDD}, can be given by:

$$\frac{\sigma_T L}{c 4\pi r^2} \leq \frac{G M m_p}{r^2} ==> L_{EDD} \leq \frac{4\pi G M m_p c}{\sigma_T} = 1.26 \times 10^{38} \left(\frac{M}{M_o}\right) \quad ergs^{-1} \tag{1.11}$$

So, the L_{EDD} is depending only from the mass of the accreting object. Theoretically, if the luminosity is higher than the L_{EDD}, then the ionized gas is expelled by the radiation pressure and the accretion will be halted resulting in a natural feedback process with a limiting accretion rate. This accretion rate, the Eddington accretion rate $\dot{M}_{EDD}$ can be inferred by setting the accretion luminosity (eq. 1.6) equal to the Eddington luminosity (eq. 1.11):

$$\dot{M}_{EDD} = \frac{L_{EDD}}{\eta c^2} \sim 2.2 \left(\frac{M_{BH}}{10^8 M_o}\right) \left(\frac{\eta}{0.1}\right)^{-1} [M_o yr^{-1}]. \tag{1.12}$$

Further, the Eddington ratio defined as $\lambda_{Edd} = L_{Bol}/L_{Edd}$ should be less than one (for larger luminosities than L_{Edd} the accretion stops) and is thought to regulate the SMBH growth over cosmic time being valid for both low and high redshifts (Schulze & Wisotzki 2010; Nobuta et al. 2012; Suh et al. 2015). In reality, though, the geometry of the accretion is rather axially than spherical symmetric as assumed here and there could be luminosities higher than the L_{EDD} with Super-Eddington accretion rates. Indeed, Super-Eddington accretion periods are believed to be plausible (Zubovas & King 2013) and may even be necessary to explain the fast growth of the first SMBHs (Volonteri 2012).

1.4.4 Accretion disc

The simplest case of accretion onto a black hole is the spherical accretion (Bondi 1952) where the motion is steady and spherically symmetrical with the gas being at rest. In this case, the accretion rate can be given by:

$$\dot{M}_{Bondi} = 4\pi R_{BA}^2 \rho_{BA} c_s, \tag{1.13}$$

where $R_{BA} = 2GM/c^2$ is the radius in which the escape velocity is equal to the speed of sound (c_s) and ρ_{AB} is the gas density at this radius. Though, in this case the efficiency of producing such high energies observed in AGN is too low. The solution given was an optically thick geometrically thin accretion disc introduced by Shakura (1972) and developed by Shakura & Sunyaev (1973), in which the accretion disc transfers angular momentum outward and track the gas inward onto the black hole maximizing the efficiency. The loss of the angular momentum is due to viscosity driven by magnetic instabilities (Balbus & Hawley 1991) or due to mass and momentum loss through winds (Ostriker et al. 2010) or both. The relativistic version of this standard model of accretion disc was given by Novikov & Thorne (1973). In the standard

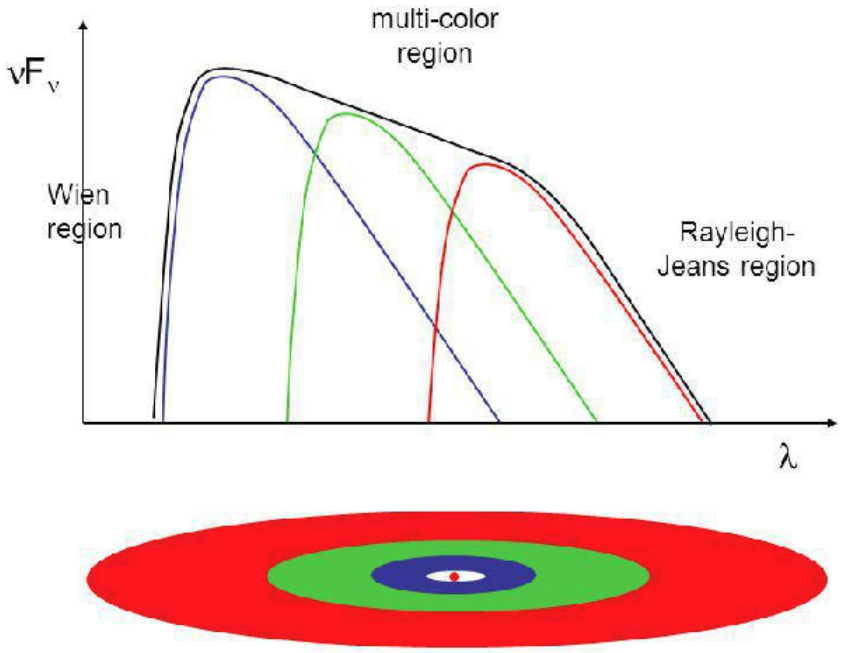

Figure 1.8: Multi-colour black body SED emitted by a standard accretion disc. Image credit: Lecture by D.P. Dullemond.

model, the radial profile of the gas temperature is:

$$T(R) = T * \left(\frac{R}{R*}\right)^{-3/4}. \tag{1.14}$$

The total radiation coming from the accretion disc can be interpreted as a multi-colour black body emission (Fig. 1.8) with the super-imposition of different Planck curves. Each part of the disc has a given temperature at a specific radius from the black hole and the monochromatic surface brightness of such independent black bodies is given

by Rybicki & Lightman (1986) equation:

$$Bv(T(R)) = \frac{2hv^3}{c^2} \frac{1}{e^{\frac{hv}{\kappa_B T(R)}} - 1}, \tag{1.15}$$

It can be shown that the spectrum is proportional to $\nu^{1/3}$ between frequencies corresponding to the minimum and maximum distance from the black hole. In the case of low frequencies, the spectrum follows a Rayleigh-Jeans relation ($I \propto \nu^2$), while for $h\nu \gg kt(R_{in})$ the thermal emission is represented by the Wien law with a cut-off in the inner part. Thus, the maximum temperature of the accretion disc is found in the inner part of the disc at the Schwarzschild radius of the BH:

$$T_{max} = 1.4 \times 10^5 \left(\frac{\dot{M}}{0.1\dot{M}_{Edd}} \right)^{1/4} \left(\frac{\eta}{0.08} \right)^{-1/4} \left(\frac{M}{10^7 M_\odot} \right)^{-1/4} K. \tag{1.16}$$

In the case of Seyfert 1, the maximum temperature is $T_{max} = 10^5$ K that corresponds to $kT = 12$ ev. Thus the emission of the accretion disc is prominent in the UV area and cannot account for the X-ray emission.

Other models similar to the optically thick geometrically thin accretion disc model has been proposed in the literature and include a) the SLE (Shapiro, Lightman & Eardly) solution where there are two temperature optically thin plasma accreting at the Eddington rate (Shapiro et al. 1976), b) The Advection-Dominated Accretion Flow (ADAF) model with a an optically thick for Super-Eddington accretion rates (Katz 1977; Abramowicz et al. 1988) or an optically thin disc for sub-Eddington accretion rates (Narayan & Yi 1994) and, c) more lately, a model that instead of an accretion disc, there is accretion of matter in clumps (Courvoisier & Türler 2005; Ishibashi & Courvoisier 2009).

1.4.5 Emission Line Regions

As mentioned in previous sections, the spectral observations of AGN resulted into division of broad and narrow line regions as independent components of the central engine with the narrow line region being much more extended, since there is no variable features in objects with large continuum variations. These regions are very distinct with each other in terms of velocity, density and geometry. In Figure 1.9 there is schematic view of these regions. Lately, though, an intermediate component found indicating the existence of an intermediate line region. In the following, the physical properties of these regions are given.

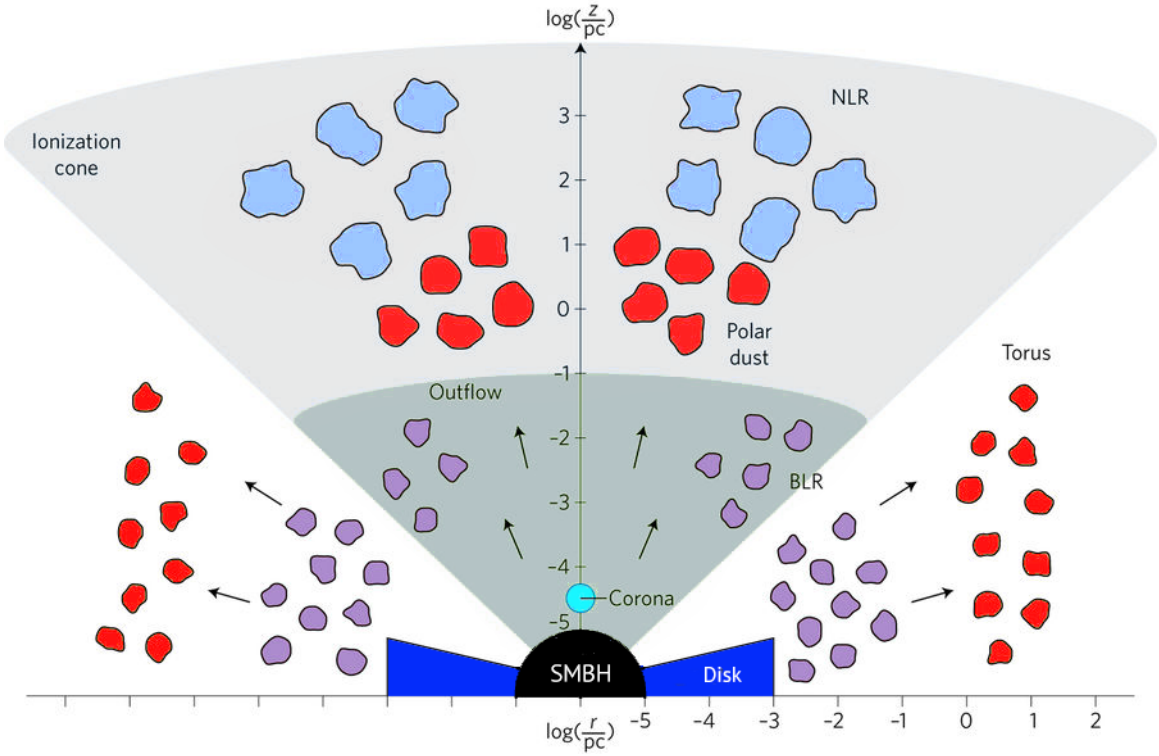

Figure 1.9: A schematic view of the AGN components. The image was taken from Ramos Almeida & Ricci (2017)

The Broad Line Region (BLR) constitutes of gaseous clouds very close to the actively accreting SMBH that produce broad emission lines, such as the Hydrogen Balmer lines and the lyman Series. Responsible for these lines is the photo-ionization of gas by far/extreme UV continuum radiation originated in the accretion disc (Bahcall et al. 1972; Davidson & Netzer 1979). Recombination by de-excitation and cascade emission is followed (Netzer 2013). These lines are broad with the widths corresponding to thousand of km/s (Peterson 2006) caused by the Doppler broadening due to Keplerian bulk motions of the gas around the SMBH (Clavel et al. 1991). The size of the BLR is a few light days for Seyfert galaxies, while it can be extended from tens up to hundreds light days in the case of quasars (Kaspi et al. 2000; Bentz et al. 2013; Hoormann et al. 2019). The temperature of the ionized gas is around 10^4 K (Popović 2003) and its density is at least 10^8 cm^{-3}. The observed broad line profiles are not yet fully understood and there are many physical explanations for its structure. These include streaming of gas in a bi-conical structure (Corbett et al. 2000), spherical distribution clouds around the SMBH (Goad & Wanders 1996), two-component model or relativistic Keplerian disc (Strateva et al. 2003). Though, more recently, Gravity Collaboration et al. (2018) spatially resolved the BLR of 3C 273 AGN in sub-pc scale

and the BLR seems to be located close to the illuminated side of the dusty torus with a disc-like geometry (Baskin & Laor 2018).

The Narrow Line Region (NLR) is a gaseous region much further than the BLR and constitutes a natural continuation of the polar winds. The gas is ionized by radiation originate in the central region of the AGN (e.g. accretion disc, corona) or by socks due to interactions between outflows and interstellar medium (Afanasiev et al. 2007; King & Pounds 2015). The size of the NLR correlates with the luminosity of some emission lines (O III) and it usually is 100-1000 pc long, but it may reach up to a few kpc in the case of the most luminous AGN (Netzer 2013). Because of its size, NLR is resolved in optical or infrared images and its bi-conical nature can be revealed (Tadhunter & Tsvetanov 1989) that agrees well with the Unified model. Progress in the NLR structure has been achieved with using integral field spectroscopy creating a de-projected 2D-map with the inferred velocities of the ionized gas. Further, some observations showed in addition to a rotational structure also outflows with rate 2-3 orders higher than the accretion rate, indicating that these outflows are loaded by mass in the surrounding interstellar medium (Müller-Sánchez et al. 2011). Unlike BLR, the NLR lack broad emission lines in their spectra and instead there are permitted and forbidden narrow emission lines similar to H II regions or the planetary nebula, but the range of the ionization parameter is much more wider (Osterbrock & Ferland 2006). The spectra of this ionized gas include some narrow permitted lines, such as the Hydrogen Balmer lines (H I, He I, He II), and also some forbidden lines. The most prominent and strong lines though are [OIII]λ λ 4959,5007, [NII]λ λ6548,6583, [OII]λ λ6300,6364, [SII]λ λ6716,6731, [NeIII]λ3869, [NeV]λ3426, and some times the [FeVII]λ6087 and [FeX]λ6375. The forbidden lines are indicative for the electron low density, as they may be formed due to collisional excitation of electron to a meta-stable state that the following de-excitation can produce radiation. The widths of the lines varies between 200 and 1000 km s-1 and by using line diagnostic ratios (e.g. [OIII] or [NII]), it is possible to derive the physical properties of the NLR, such as the temperature (10^4 K) or the electron concentration ($10^2 - 10^4 cm^{-3}$) that is much lower compared to BLR (Osterbrock & Ferland 2006).

The Intermediate Line Region (ILR) is thought to located between the BLR and NLR and constituted by gas clouds with intermediate density that is imprinted as an extra component in the spectra. Initially, it was too difficult to explain the significant suppression of the emission lines in the region between the BLR and NLR in the majority of the AGN (Osterbrock & Ferland 2006; Boroson & Green 1992). Netzer & Laor (1993) suggested that responsible is the dust suppression. Though, there are some observations that favor the existence of an intermediate line region. Brotherton et al. (1994); Mason et al. (1996); Crenshaw & Kraemer (2007) found

emission lines with velocities near 1000 kms-1. Then, spectral analysis showed the existence of intermediate width components in the spectra of some AGN located in the inner 3 pc (Hu et al. 2008; Crenshaw et al. 2009; Li et al. 2015). Though, there is need for more observations with high spatial resolution to securely define an intermediate region.

1.4.6 The Dusty Torus

As already mentioned, the AGN Unified model suggested that the central engine is surrounded by a geometrically thick dusty torus (Antonucci 1993; Urry & Padovani 1995). The existence of such a toroidal structure blocks the direct emission from the central engine of the AGN (accretion disc, BLR, corona) by reprocessing the UV and optical photons and re-emitting in the IR wavelengths (Rees et al. 1969). Furthermore, it collimates the emission and, thus, it is responsible for the bi-conical shape of the ionization cone (Kishimoto et al. 2011). The parameter that describes this cone is the opening angle and it has be shown that correlates with luminosity and most probably with the Eddington accretion rate (Lawrence 1991; Simpson 2005; Oh et al. 2015). This toroidal structure is different for different sources and through sub-mm (Imanishi et al. 2016; García-Burillo et al. 2016b; Gallimore et al. 2016) and MIR imaging (Packham et al. 2005; Radomski et al. 2008) and interferometry (Burtscher et al. 2013) its size is constraint between 0.1 and 10 pc. The outer radius of the torus can be defined from the gravitational sphere influence of the SMBHs at ∼10 pc (Alexander & Hickox 2012). The inner region of the torus is thought to be less than 1 pc and it is limited by the dust sublimation temperature that depends on the luminosity, $r^{1/4}$ (Barvainis 1987; Suganuma et al. 2006; Kishimoto et al. 2011). In Figure 1.10, the most recent view of the torus in Cygnus A is shown in the radio (Carilli et al. 2019) in addition to an artistic view.

Initially, a very simplified torus model was considered with a smooth and homogeneous dust density distribution (Krolik 1992; Efstathiou & Rowan-Robinson 1995; Efstathiou et al. 2013; Fritz et al. 2006). Though, Krolik & Begelman (1988) and many studies after started to reconsider the torus structure inclining in a clumpy distribution rather than homogeneous. The first observational evidences from Tristram et al. (2007); Burtscher et al. (2009) supported this idea. Further advance in computational capabilities allowed simulations of clumpy models (Nenkova et al. 2001, 2008b; Hönig et al. 2006; Hönig & Kishimoto 2010; Schartmann et al. 2008; Stalevski et al. 2012) with results in agreement with the observations and they could explain the differences in the silicate strength of type 1 and type II AGN (Nikutta et al. 2009). More recent observations with high angular resolution (Hönig et al.

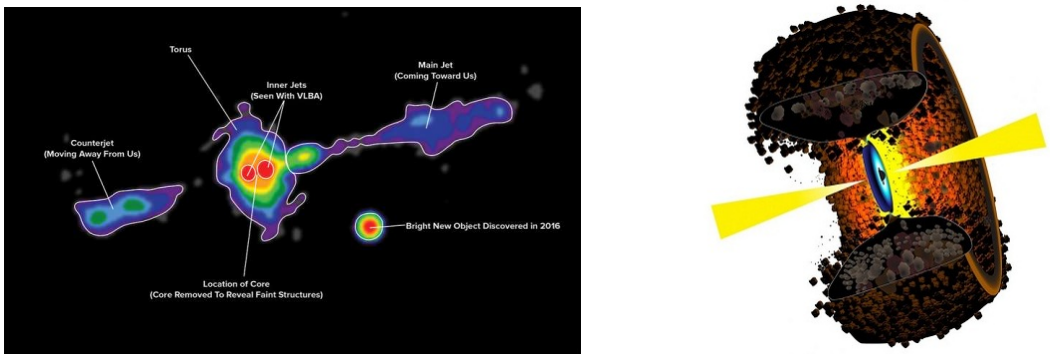

Figure 1.10: An artistic view of the torus of Cugnus A (right), while in the left panel the real image in radio is shown from Carilli et al. (2019).

2012, 2013; Tristram et al. 2014; López-Gonzaga et al. 2016; Leftley et al. 2018) are inconsistent with the radiative transfer models from IR interferometry or the IR SED fitting results. The inferred structure of the torus included two components rather that a single torus classical smooth or clumpy one. The elements of this new picture constitutes of an equatorial thin disc with a polar extended feature originated in the dust winds forming a hollow cone and defining the NLR edges (Hönig & Kishimoto 2017; Stalevski et al. 2017; Hönig 2019).

1.4.7 The Hot Corona

The hot corona is composed by a hot cloud of electrons located very close to the center of the accretion disc (Haardt & Maraschi 1993). The hot plasma probably is analogous to the solar corona, hence this name was given by Galeev et al. (1979). Reverbaration mapping of prominent emission lines and micro-lensing analysis suggest that the corona is relatively small and has a radius, R_c<10*R_g, where R_g is the gravitational radius of the black hole (Fabian et al. 2009; Chartas et al. 2009). Many studies suggested different models for the corona geometry. Some of those are: a) a hot sphere around the SMBH (Zdziarski et al. 1994), b) the hot planes parallel covering the cold accretion disc (Haardt & Maraschi 1991; Haardt et al. 1994), c) an inner hot sphere plus an inner warm disc (Kubota & Done 2018), d) a "lamp-post" corona (Matt et al. 1991; Miniutti & Fabian 2004; Petrucci & Henri 1997) or more extended filling the inner part of the accretion disc. Furthermore, nowadays, it is still unclear whether the coronal plasma is a continuous or it is a patchy medium (Petrucci et al. 2013).

The shape of the spectral energy distribution of the corona could be represented by a power-law continuum. In addition to this, there is a reprocessed radiation by the

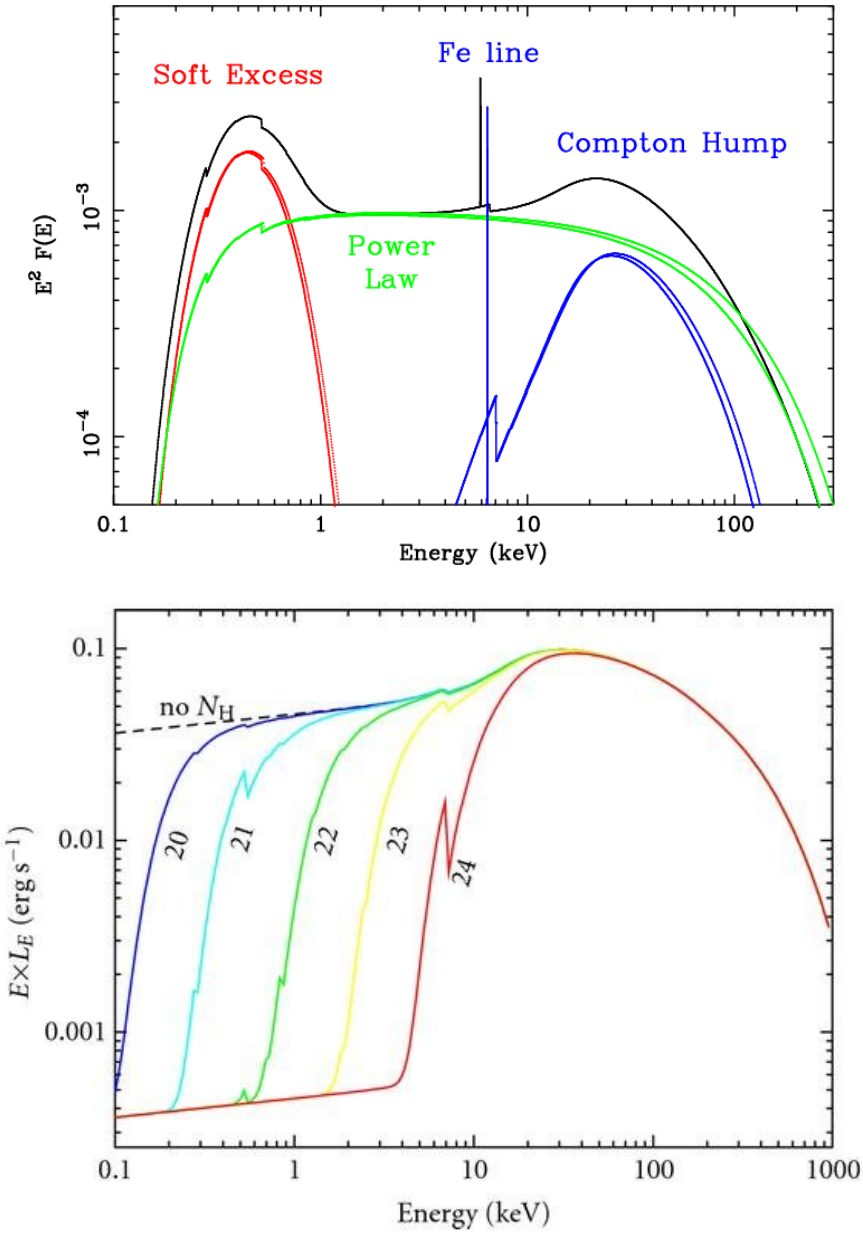

Figure 1.11: Upper: The typical X-ray spectrum of AGN with its main components, the primary continuum (yellow), the Compton hump, the soft excess and the absorption Fe Ka line. Image credits: Fabian (2006). Lower: The effect of the absorption on the X-ray spectrum (Treister & Urry 2012). The different spectra correspond to different values of the hydrogen column densities, N_H, as indicated.

other elements of the AGN, such as the torus, the BLR region and the accretion disc. This is reflected in the X-ray spectrum imprinting some characteristic features as the iron Ka emission line, the soft excess or/and the Compton hump. In Figure 1.11

(upper), the SED of the X-ray spectrum is shown with its different components:

The power-law continuum has a very high-energy turn-over (a few hundreds of keV) and it is suggestive of Comptonization of thermal electrons (Haardt & Maraschi 1991). Optical and UV photons from the accretion disc are efficiently up-scattered by the relative electrons in the corona and produce the X-ray emission. The energy cut-off is dependent only on the temperature of the electrons (Shapiro et al. 1976; Rybicki & Lightman 1979) and different studies used hard X-ray spectroscopy observations (with the BeppSAX, INTEGRAL and Swift/BAT) found that it varies from 50 up to 300 keV (Dadina 2007; de Rosa et al. 2012; Ricci et al. 2018). In Seyfert galaxies, this cut-off ranges between 100-300 keV. The primary X-ray continuum was given by Elvis et al. (1978):

$$F(E) = kE^{-\Gamma}\, photons\, cm^{-2}\, s^{-1}\, keV^{-1}, \tag{1.17}$$

where k is a normalization factor of the power-law at 1 keV and Γ is the photon index. The slope of the power-law spectra in the X-ray band ranges between gamma 1.6 and 2.2 (Bianchi et al. 2009; Sobolewska & Papadakis 2009) and depends on the optical depth and the temperature of the scattered medium. For radio-quiet galaxies it is equal to Gamma=1.8-2 (Dadina 2008; Beckmann et al. 2009), while for type I and type II AGN it has values of 1.83 and 1.90, respectively (Brightman & Nandra 2011). In the case of radio-loud AGN the spectrum is more flat. Furthermore, there is a debate if there is a correlation between the physical parameters (optical depth, temperature, cut-off) of the corona and the SMBH properties. In particular, Tortosa et al. (2018) found an anti-correlation between the optical depth and the temperature and no correlation between these parameters and the BH mass, the accretion rate or the intrinsic spectral slope, while Ricci et al. (2018) found that the cut-off is depended on the Eddington ratio.

The iron Ka line is present in almost all AGN. Part of the radiation coming from the accretion disc and corona interacts with the BLR and the result is the Fe Ka emission line at l=6.4 keV. This is a fluorescence line of an L to K shell electron transition. This is happened when X-ray photons ionize the atom from the L shell and then an outer electron fills the energy state and emits to the transition energy from the electron (Barr et al. 1985). In reality, the Fe Ka complex consists of multiple lines, though higher resolution in spectrometers is needed to distinguish them. The dominant component of the Fe Ka complex has typical values of 1,000-17,000 kms-1 (Yaqoob & Padmanabhan 2004), while it can be distorted due to gravitational redshifting, Doppler boosting and broadening.

The Compton hump is the second reflection component observed at 30-40 keV (George & Fabian 1991; Ross & Fabian 2005; García & Kallman 2010; Fabian &

Ross 2010) and this is believed to come from the super-position of two components: a) reflection from the inner part of the accretion flow and b) reflection by material located further away, such as the BLR and/or the torus. The emission of the Compton hump consists of a few percent of the primary X-ray emission in the 2-10 keV band (Comastri et al. 2010; Baloković et al. 2014; Ricci et al. 2017), while in many studies it appears mostly in mildly obscured AGN with column densities $N_H = 10^{23-24}\ cm^{-2}$ (Ricci et al. 2011; Esposito & Walter 2016; Zappacosta et al. 2018). Panagiotou & Walter (2019) showed that the main reflection of unobsured and obscured sources comes from the accretion disc and the clumpy torus, respectively.

The soft excess is present in the majority of Seyfert 1 galaxies at energies below 1-2 keV (Pravdo et al. 1981; Singh et al. 1985; Arnaud et al. 1985). Its origin is still a matter of debate (Petrucci et al. 2018; García et al. 2019; Middei et al. 2019). It may have different origin for the absorbed and unabsorbed AGN. In the second case, it may come from blurred reflection from the disc, smeared absorption by ionized winds or a second cooler corona.

Absorption The X-ray emission may be affected by absorption mainly due to two processes. The first one is the photoelectric absorption that depends strongly on the energy of the X-ray photon, especially on energies below 10 keV. In higher energies, the absorption is not significant for column densities lower than $N_H < 10^{24}\ cm^{-2}$. For different column densities, the energy cut-off of the primary power-law emission is different as shown in Figure 1.11 (lower panel). The column density is the key factor to characterize the type of AGN in the X-ray regime. Below the threshold $N_H = 10^{22}$ cm^{-2} (Ricci et al. 2017), the absorption does not affect the X-ray spectrum and the AGN are characterized as unabsorbed or type I AGN, while for values higher than this threshold the AGN are obscured or type II AGN. The second process that affect the observed X-ray emission is the Compton Scattering.

1.4.8 Relativistic Jets and Lobes

As mentioned in the previous sections, around 10% of the AGN have relativistic outflows (jets) at which plasma moves with incredibly high velocities reaching the speed of light. The material of the accretion disc is highly conducting and it produces a magnetic field as it rotates around the black hole. The changing magnetic field creates strong electric field capable of accelerating charged particles and boost them from the central engine creating two jets vertical to the equatorial axis of the accretion disc at two opposite directions. The particles spin around the dynamical lines of the magnetic field accelerating and reaching relativistic velocities. This process produces the Synchrotron radiation. The magnetic torques push away the angular momentum

from the disc as the magnetic field of the disc is paired with the relativistic particle flow, so the accreting matter moves toward the inner parts of the disc. Another theory responsible for the accelerating particles comes from angular kinetic energy of the black hole, the so-called Blandford-Znajck for rotating black hole (Blandford & Znajek 1977).

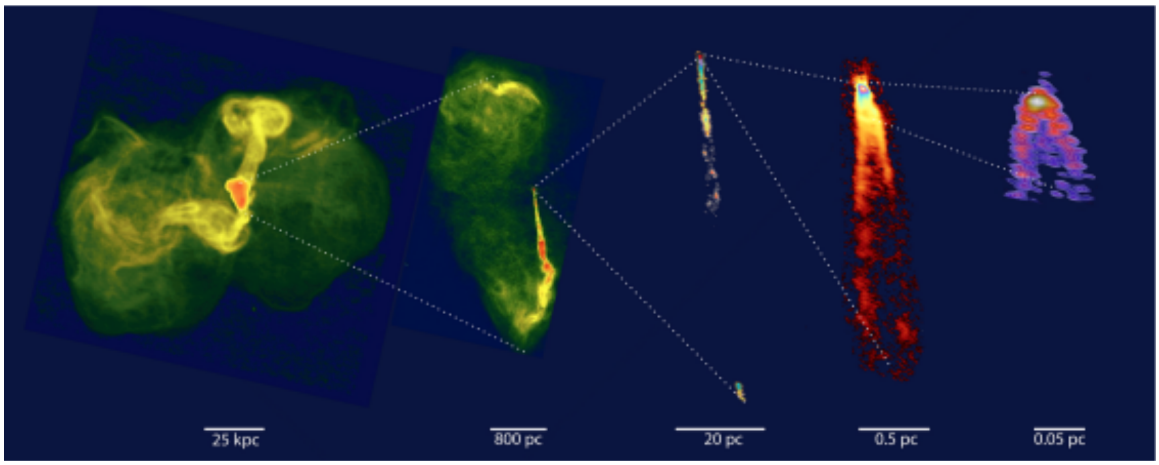

Figure 1.12: The structure of the radio galaxy M87 in different scales. All the components, such as the jets, the lobes and the knots are resolved. This image was taken from Blandford et al. (2019).

The two jets usually have different brightness and in some cases only one jet is visible. This is due to the frame of the special relativity theory, the relativistic projection and also due to orientation effects. These are also responsible for the apparent super-luminal motions of bright spots inside the jets that move away from the center of the jets with velocities that appear to be higher than the speed of light (Whitney et al. 1971; Zensus 1997). Usually, the jets have lengths from kpc to Mpc scales, while they could be continuous or forming dense and bright regions (knots). The lobes are created as the matter in jets moves outwards the AGN. Its energy constitutes only of kinetic energy. Though, as the jets move, the matter in the front of the jets interacts with the interstellar and/or intergalactic medium and create shock waves (Begelman & Cioffi 1989; Kaiser & Alexander 1997). The accumulation and deceleration of the matter form the shape of these lobes. In Figure 1.12, the structure of the M87 radio galaxy is shown in scales from kpc to sub-pc, where all its components (jets, lobes, knots) are resolved with radio interferometry observations. More details on the structure, the physics and the formation of the relativistic jets can be found in the recent review of Blandford et al. (2019).

The spectrum of the emission produced in the jets consists of two basic components, one in low frequencies from radio to X-rays and one in high frequencies

(X-ray to γ-rays). Many models have been suggested in order to reproduce these SEDs. When considering leptonic models, the energy emitted produced through Synchrotron radiation and also from the Inverse Compton scattering. The Compton scattering could be due to photon produced by the Synchrotron radiation (Self-Compton, Maraschi et al. 1992; Bloom & Marscher 1996) or from external photon fields (Dermer & Schlickeiser 1993; Finke 2013). In the case of lepto-hadronic models, the photo-hadronic interactions are taken into account (Petropoulou & Mastichiadis 2012; Mastichiadis 2016; Cerruti et al. 2015).

1.5 AGN selection techniques

In this section, different AGN selection methods will be described in the X-ray , optical and infrared regimes, as they will be used for the analysis and the interpretation of the results of this thesis.

1.5.1 X-ray regime

X-ray emission is nearly a Universal property of all AGN and it is associated with the accretion disc having a tight relation with the UV and optical emission (Lusso & Risaliti 2016). X-ray selection provides clean and reliable samples of AGN, as the continuum of the host galaxy is very low and the contrast is very high (Brandt & Alexander 2015). Also, the penetrating power of X-ray emission (above 2 keV) allows low amount of absorption by the host ($N_H = 10^{22}$cm^{-2}). Usually, the AGN are selected as those having hard X-ray luminosity higher than $L_X = 10^{42}$ ergs s^{-1}. Below this limit, there is a high contamination by stellar processes originate in the host galaxy. In particular, X-ray binaries or Ultra luminous X-ray sources (ULXs) can have luminosities up to $L_X = 10^{41}$ ergs s^{-1}. Using the most sensitive observations of XMM-Newton and Chandra X-ray telescopes in the energy regime E<10 keV in the deep fields, a large sample of AGN was produced with a wide range of redshifts and luminosities with density up to 23,900 deg^2 (Alexander et al. 2003; Luo et al. 2008; Brandt & Alexander 2010; Xue et al. 2011; Luo et al. 2017). The latter is an order of magnitude larger than in the optical selection techniques. On the other hand, the AGN selection below 10 keV is biased against the most heavily obscured AGN due to the high absorption of the X-ray emission from the torus. The most recent observatories Swiftand Nustar was meant to provide cleaner and more complete AGN samples in this manner. Though, the Compton Thick AGN with column densities higher than $N_H = 10^{25}$cm^{-2} would be still difficult to detect. Another way to identify

AGN in the X-ray regime is to use high resolution images (mainly from nearby sources) of the nucleus and find a point-like X-ray source near the central engine. This demands attention for a probably contamination from X-ray binaries (Gallo et al. 2010; She et al. 2017).

1.5.2 UV-optical-NIR regime

One of the first and pioneer method to identify AGN is through optical and UV colours. The accretion disc has overall higher temperatures than that of the stars resulting in an excess in the blue and UV spectrum and thus it could distinguish them from the stellar emission. The only exception is the white dwarfs with very strong emission in UV light only when they are young. So, looking for point-sources brighter in the UV than the normal stars is very efficient up to z=2-2.5. Beyond this redshift, it becomes challenging, since there is a lot of inter-galactic absorption and the quasars are very red in the blue part of the spectrum. Colour-colour diagrams have been used extensively in the literature to provide a large sample of AGN. In these diagrams the AGN have a different location from the stellar locus and by combining many colours the separation is quite easy at least for the unobsorbed sources. In the case of obscured AGN where there is a large amount of dust that absorbed the UV and optical light, this method is not that efficient. Another disadvantage concerns the low luminosity AGN, since the host galaxy is the dominant emission and the colours are strongly affected.

Spectroscopic techniques to identify AGN in the optical/UV regime rely on the high ratio of high-ionization to low-ionization emission lines and on the presence of very high ionization emission lines. The very first diagnostic diagram proposed by Baldwin et al. (1981). According to this, the so-called BPT diagram, the different population of AGN, LINERS, star-forming galaxies or composite galaxies can be distinguished by the ratio of high to low ionization ratios (Fig. 1.13, left panel) based on the [OIII], ha, Hb and [NII] emission lines. Other studies include SII or OI instead of NII lines or a combination of all diagrams (Veilleux & Osterbrock 1987; Kewley et al. 2006, 2013). These work very well in the Local Universe. As going to higher redshifts, the standard emission lines used in BPT lie outside the wavelength coverage of optical spectrographs. For example, for redshifts higher than z=0.5 the NII and Hα lines are redshifted to the observed NIR regime. Therefore, other indicators are needed to replace this ratio. In the literature, alternatives indicators have been proposed, such as the rest-frame Bessel U-B galaxy colour (Yan et al. 2011, Colour Excitation diagram), H band absolute magnitude (Weiner et al. 2006), OII/Hb (Lamareille 2010), Dn4000 break (Marocco et al. 2011) or stellar mass (Juneau et al. 2011, 2014,

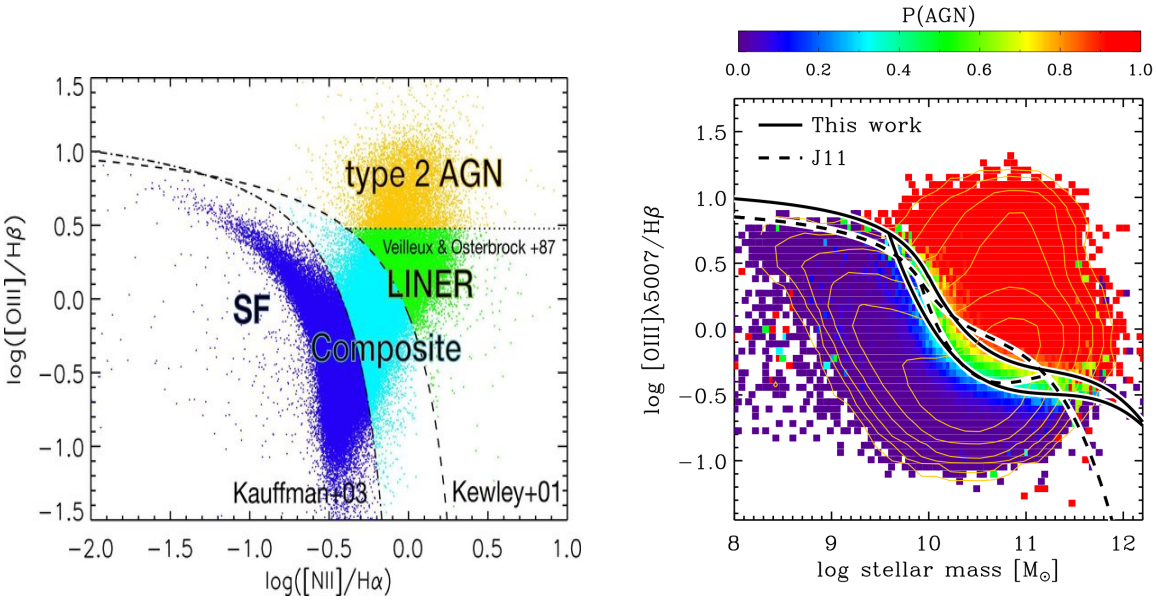

Figure 1.13: Left: BPT diagram from Toba et al. (2014). Right: Mass Excitation diagram from Juneau et al. (2014).

Mass excitation, MeX, diagram). In Figure 1.13 (right panel), the MeX diagram is shown colour-coded with the AGN probability (high probability with red colour). All these replacements of the [NII]/Halpha ratio are based on the correlation between the galaxy stellar mass and the gas phase metallicity or the rest-frame (depended on stellar mass) Kauffmann et al. (2003).

In the second case, high ionization narrow lines produced in scales of 0.1 to few kpc from the central BH are free from nuclear obscuration. Such lines are the [OIV]λ26μm and [OIII]λ5007$\AA$ forbidden lines and in combination with hard X-rays could identify heavily obscured AGN (Maiolino et al. 1998; Panessa et al. 2006). However, they are applicable to the low redshift regime, since for high redshifts (z>0.8), they move out from the optical spectral window. Another such line is the [NeV] at $\lambda = 3426\AA$ and $\lambda = 3346\AA$ and they could be used up to z=1.5. Even though, these lines are very weak compared to [OIII], their presence indicates strong AGN activity, since high energy photons (>97 eV) are required for ionization (Schmidt et al. 1998), while the maximum energy potential from stellar emission reaches up to 55 eV (Haehnelt et al. 2001). In Figure 1.14, the SEDs for different models of star-forming galaxies (low and high metallicities) and AGN are shown taken from Feltre et al. (2016). For low energy ($\sim$20 eV) the AGN and SF galaxies are very similar, while for energy potentials greater than 50 eV the SF SEDs are dropping dramatically and thus the emission lines are very prominent for AGN activity.

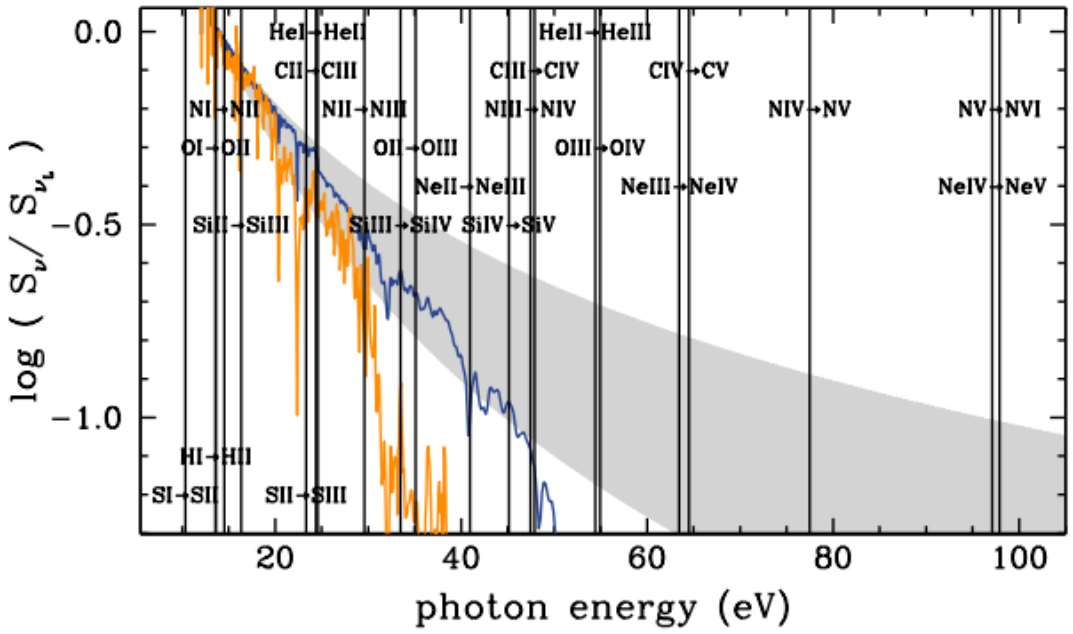

Figure 1.14: SEDs of the incident ionizing radiation in AGN and Star-forming models. The shaded area indicates the location of AGN spectra, while the blue/orange lines indicate the spectra for stellar population with Z = 0.001/0.03. Image credit: Feltre et al. (2016)]

1.5.3 Mid-IR regime

The mid-IR emission from AGNs, in particular after the advent of sensitive spectrographs in space telescopes such as *ISO* and *Spitzer*, has proven extremely useful in revealing the presence of an AGN and characterising whether it is of type I or type II (Clavel et al. 2000; Verma et al. 2005; Weedman et al. 2005; Wu et al. 2009; Alonso-Herrero et al. 2016). It is now widely accepted that the AGN continuum emission appears as a power law from the 3 to 10 μm range, since the strong UV and X-ray radiation destroys the molecules responsible for the Polycyclic Aromatic Hydrocarbon (PAH) emission, while heating the surrounding dust particles in thermal equilibrium to near dust sublimation temperatures. The mid-IR AGN spectrum may also display absorption features with variable strength (due to astronomical silicates at 9.7 and 18μm) depending on the geometry of the obscuring dust as well as the luminosity of the active nucleus compared with the host galaxy (Nenkova et al. 2008a,b).

Even when mid-IR spectra are not available, one may use mid-IR broad-band colours to trace this slope. These criteria are based on the power-law that appears in the mid-IR bands (5-10 μm) when AGN luminosity is at least comparable with

that of its host. A number of such diagnostics have been proposed using the IRAC instrument (Fazio et al. 2004) on board the *Spitzer* Space Telescope (Werner et al. 2004) which provided imaging at 3.6, 4.5, 5.8 and 8.0 μm for a large sample of galaxies. These include the "Lacy wedge" (Lacy et al. 2004, 2007; Sajina et al. 2005), the "Stern wedge" (Stern et al. 2005) and more recently the "Donley wedge" (Donley et al. 2007, 2012). Below, the AGN selection criteria by Donley et al. (2012) and Lacy et al. (2007) are presented, as they were used in the analysis of this thesis. The criteria by Donley et al. (2012) are:

$x > 0.08$ and $y > 0.15$

$y > (1.21 * x) - 0.27$ and $y < (1.21 * x) + 0.27$

$f[4.5] > f[3.6]$ and $f[5.8] > f[4.5]$ and $f[8.0] > f[5.8]$,

where x=log(f[5.8]/f[3.6]), y=log(f[8.0]/f[4.5]) and f[band] is the flux of the corresponding band.

Lacy et al. (2007) used a similar mid-IR colour-colour diagram with somewhat relaxed limits and without the power law condition:

$x > -0.1$ and $y > -0.2$

$y > (0.8 * x) - 0.5$.

Furthermore, a number of similar diagnostics have been proposed using *WISE* data that provides imaging at 3.4, 4.6, 12 and 22μm for a large sample of galaxies. These include a simple colour W1–W2 cut-off defined by Stern et al. (2012), a more refined magnitude-dependent cut-off taking into account faint sources in the W2 band by Assef et al. (2013) and two wedges in W1–W2 vs. W2–W3 and W1–W2 vs. W3–W4 colour-colour diagrams suggested by Mateos et al. (2012) using three and four *WISE* bands, respectively. The AGN selection criteria by Assef et al. (2013) are:

$$y > \alpha_r * exp(\beta_r * (x - \gamma_r)^2), \quad \text{if } x > \gamma_r \quad \text{and} \tag{1}$$

$$y > \alpha_r, \quad \text{if } x \leq \gamma_r, \tag{2}$$

where $x = W2$ and $y = W1 - W2$ and the revised constant values of $(\alpha_r, \beta_r, \gamma_r)$ given by Assef et al. (2018) are equal to $(0.650, 0.153, 13.86)$ and $(0.486, 0.092, 13.07)$. reliability++++. Moreover, the Mateos et al. (2012) colour selection criteria use the colours (W2–W3) and (W1–W2):

$$W1 - W2 < 0.315 \times (W2 - W3) + 0.796, \quad (1)$$

$$W1 - W2 > -3.1725 \times (W2 - W3) + 7.624 \text{ and} \quad (2)$$

$$W1 - W2 > 0.315 \times (W2 - W3) - 0.222. \quad (3)$$

In this thesis, the WISE AGN selection diagnostics by Assef et al. (2013) and Mateos et al. (2012) were used in the Chapter 2.

1.5.4 AGN variability

An alternative method to identify AGNs is based on the detection of variability at any wavelengths on timescales from hours to years (Ulrich et al. 1997; Kawaguchi et al. 1998; Paolillo et al. 2004; García-González et al. 2014). There is a correlation between the amplitude of the AGN variability and the timescale of variation (Hook et al. 1994; Trevese et al. 1994; Cristiani et al. 1997; di Clemente et al. 1996; Vanden Berk et al. 2004; Kelly et al. 2009; Bauer et al. 2009; Middei et al. 2017), the redshift and the black hole mass (for timescales longer than 100 days; Cristiani et al. 1990; Hook et al. 1994; Trevese et al. 1994; Vanden Berk et al. 2004). On the other hand, the variability amplitude is anticorrelated with the rest-frame wavelength (di Clemente et al. 1996; Cristiani et al. 1997; Giveon et al. 1999; Helfand et al. 2001; Vanden Berk et al. 2004; Zuo et al. 2012) and the nuclear luminosity (Trevese et al. 1994; Vagnetti et al. 2016). The latter suggests that low-luminosity AGNs (LLAGNs) will dominate a variability survey compared to more luminous AGNs.

Several theories and mechanisms have been proposed to explain the variability. For example, Rees (1984) and Kawaguchi et al. (1998) proposed that AGN variability may be due to the fact that accretion disks are vulnerable to dynamical instabilities, while Li & Cao (2008) and Zuo et al. (2012) attributed the variability to fluctuations in the accretion rate. In the extreme case of blazars (the most luminous class of AGNs possessing a relativistic jet pointing towards the observer), the variability is modulated by changes in the accretion disk, but also by non-thermal power-law emission from the jets and the (not fully explored) connection between them (Gu & Li 2013; Finke & Becker 2014; Chatterjee et al. 2018). Other interpretations of AGN variability include gravitational microlensing effects (Hawkins 1993; Alexander 1995), tidal disruption events (Komossa 2015) and multiple explosions of supernovae (SNe) near the nuclei (Kawaguchi et al. 1998; Terlevich et al. 1992).

In the last several years, AGN variability has been used in many studies. In the X-ray region, Young et al. (2012) and Ding et al. (2018) selected LLAGNs in

the 4 and 7 Ms *Chandra* Deep Field South (CDF-S), respectively. In the optical and near IR bands, Sarajedini et al. (2003, 2011); Trevese et al. (2008); Villforth et al. (2010); Simm et al. (2015); Falocco et al. (2015); Graham et al. (2014); De Cicco et al. (2015); Baldassare et al. (2018); Kim et al. (2018) identified a large sample of AGNs, suggesting that the search for variability at short time scales is efficient in selecting LLAGNs that would have been missed by X-ray surveys. As AGNs exhibit a red-noise behaviour (Lawrence & Papadakis 1993; Park & Trippe 2017; i.e. they have more power at low frequencies in the Fourier space), De Cicco et al. (2015) and Paolillo et al. (2017) pointed out that the longer the time baseline (e.g. greater than few years), the larger the variability amplitude and the more complete is the AGN selection. Indeed, De Cicco et al. (2019) used longer time baseline in the Cosmic Evolution Survey (COSMOS) field achieving giher reliability (86%) and completeness (60%) compared to previous works.

However, while blazars tend to show variability at all timescales, the power spectrum and structure function analysis of light curves of many radio-quiet AGNs suggest that their variability amplitude does not rise indefinitely with longer timescales. Their power spectrum flattens below some frequency. Such power spectra were modeled with a damped random walk and continuous auto-regressive moving average models (de Vries et al. 2005; Kelly et al. 2009; MacLeod et al. 2010; MacLeod et al. 2012; Kelly et al. 2014; Kasliwal et al. 2015; Kozlowski 2016; Simm et al. 2016).

1.6 Scope of this thesis

The main purpose of this thesis is to enhance the reliability and completeness of the different AGN selection techniques, but also to apply and test new methods. Through comparison of the methods in different observational windows and fields with different depths and areas, it is possible to constrain their limitations and find ways to reveal AGN populations that are missed. An outline of the content of each chapter in this thesis follows:

Chapter 2: The main results of this thesis are based on the data in different fields and in different wavelength regimes. Thus, in the first Chapter, an overview and a brief description of the telescopes and instruments used is given.

Chapter 3: In this Chapter, data from the Hubble Space telescope were used to identify AGN through optical variability in the GOODS-South field. Comparing to previous HST-based studies, in this work the time baseline of the light curves was expanded up to 10 years using the latest HST data, while a new method, the Median

Absolute deviation, was used as a variability indicator that is more robust than the classic indicators, such as σ, and returns cleaner samples of variable sources. The AGN candidates were compared with the AGN selected by the deepest ($\sim$7 Ms) X-ray data and also the mid-IR colour diagnostics. The main result of this study is the advance of the optical variability method to detect low luminosity AGN at high redshifts that may be missed from the other methods. This work was published in Pouliasis et al. (2019).

Chapter 4: In this chapter, firstly, the "Hubble Catalog of Variables" (HCV) project is presented that aimed to identify all the variables sources from the Hubble Source Catalog. Furthermore, with the constraints derived from the results in the GOODS-South field, a demonstration of the HCV power in identifying AGN through variability is given in the CANDELS and Frontier Fields listing the optically variable AGN candidates. The results in CANDELS fields were included in Bonanos et al. (2019).

Chapter 5: In this chapter, the AGN identification is done through SED decomposition using a Bayesian statistical method. In particular, we use data from optical to mid-IR to construct the SEDs of a sample of $\sim$7,000 sources. After, by comparing the statistical significance when adding to the parameter space AGN templates, we identify 160 AGN with high confidence. These results are compared to the X-ray, infrared and optically spectroscopical AGN. The results of this study have been submitted in MNRAS as Pouliasis et al.

Chapter 6: This chapter summarizes the results of this thesis for all the fields and presents the main conclusions derived.

Chapter 2

Telescopes Overview

In this chapter, a description is given of the different telescopes used in this thesis and of their main instruments. In particular, there is an overview of the XMM-Newton and Chandra X-ray telescopes, the Spitzer and WISE telescopes in the infrared regime and also the optical Hubble Space telescope and the Canadian French Hawaiian Telescope. Since the analysis and the results of this thesis were produced in different fields (GOODS-S, CANDELS, Frontier fields and XMM-XXL), the data reduction and the databases or catalogues used will be described in detail independently for each field in the corresponded chapters.

2.1 Optical Telescopes

2.1.1 Hubble Space Telescope

The Hubble Space Telescope (HST) named after the astronomer Edwin P. Hubble is the first of the NASA's Great Observatories and is dedicated to provide deep images from the ultra-violet to near-infrared spectral range. It was launched in 1990 into a low-earth (∼550 km) orbit with an inclination of 28.5 degrees to the equator and a period of 95 minutes. The HST has size 13.2 m in length and weights almost 10 tonnes. It carries a Cassegrain reflector telescope with a 2.4 m in diameter primary mirror and a 0.3 m secondary mirror. Its advance compared to the other ground-based observatories is its high angular resolution that is 0.05". The observation of the HST helped to make incredible discoveries and promote scientific results in all fields from the physics of stellar population to very faint early-Universe galaxies and AGN. The HST includes two main sets of instruments, imaging cameras and spectrographs. The

instruments can be replaced or fixed with small space missions. Below, I will describe the basic instruments on board HST. In this thesis, data from the ACS camera were used in Chapter 3 in GOODS-S field, while the HCV catalogue in Chapter 4 was based on observation fro all three camera (ACS, WFC3 and WFPC2).

ACS (Ford et al. 1998), the Advanced Camera for Surveys, is a third-generation camera for imaging using two types of detectors, the Charged-Coupled Device (CCD) for near-UV up to near-IR and the Multi-Anode Micro-channel Array detector (MAMA) for observation in the UV. In particular, there are three channels: a) The Wide Field Channel (WFC) that provides imaging between 350 and 1100 nm with a Field Of View (FOV) of 202"×202" and a spatial resolution 0.04", b) the High Resolution Channel (HRC) with FOV 29"×26" and 0.028"/pixel for the 170-1100 nm regime and, c) the Solar Blind Channel (SBC) with a FOV 34.6"×30.8" designated for observation in UV (115-170 nm). Since 2007, HRC is not operational due to an electrical failure.

WFC3, the Wide-Field Camera 3, provides imaging from UV to IR. There are two channels: the UVIS channel that observes in the UV and optical (200-1000 nm) with a FOV of 162"×162" and spatial resolution 0.04" and also the IR channel for IR imaging (900-1700 nm) with FOV 123"×136" and 0.13"/pixel. In total, WFC3 has 80 filters, 63 in UV-optical and 17 in IR.

WFPC2, the Wide Field/Planetary Camera 2, was removed in 2009 from HST and it was the predecessor of WFC3. It was designed for high resolution images in 115-1100 nm regime. It had four detectors, three (WF2,3,4) with FOV 80"×80" and one (PC1) with 36"×36".

Furthermore, there are two instruments for spectroscopy: The Cosmic origins Spectrograph (**COS**) that provides high sensitivity moderate and low resolution spectroscopy in the far-UV to near-UV regime, and the Space Telescope Imaging Spectrograph (**STIS**) designated for spectroscopy in the 115-1000 nm wavelngth regime (UV-NIR).

2.1.2 The Canadian-French-Hawaiian Telescope

The Canadian-French-Hawaiian Telescope (CFHT) as indicated by its name is a joint science facility between the National Research Council of Canada, the Centre National de la Research Scientifique of France and the the University of Hawaii. The 3.6 m telescope is located at Mauna Kea in Hawaii at a height of 4,200 m and it started operating in 1979. All the observational data are archived and handled by the Canadian Astronomy Data Centre (CADC). The CFHT mainly consists of five different scientific instruments:

The MegaCam (Boulade et al. 2000), a wide field optical and near-IR imager. The MegaCam has a field of view almost one square degrees with a resolution 0.18" per pixel. It consists of 36 E2V CCD camera with a size 2048×4612 each resulting in a total 340 millions pixels. The prime focus of the telescope, MegaPrime, is equipped with five broad-band filters (u, g, r, i and z) with a spectral coverage from 3500 to 9400. It started operating in 2002. In this thesis, data from the MegaCam were used in Section 5 in the XMM-XXL field.

The WIRCam (Puget et al. 2004), a wide-field infrared camera. WIRcam started operating in 2006 and mainly aimed to produce infrared complementary images to MegaCam. It is made of four HgCdTe HAWWAII-RG detectors that each has 2048×2048 pixels with a sampling of 0.3" per pixel. The detectors are arranged in 2×2 grid providing a 20 square minutes field of view. The broad-band infrared filters correspond to the Y, J, H and K_s bands.

The ESPaDOnS (Donati 2003), an Echelle Spectropolarimetric Device for the Observations of Stars that provides high resolution spectroscopy and polarimetry since 2005. It was designed to obtain in a single exposure the full spectrum in the 370-1,050 nm regime with a resolving power that can reach even 81,000.

The SITELLE (Drissen et al. 2019), an optical imaging Fourier transform spectrometer (IFTS). This integral field unit (IFU) spectrometer has a field of view approximately 120 square arcminutes that is 100 to 1000 larger that the other traditional IFU spectrometers, such as the MUSE in the Very Large Telescope. Its spectral resolution can be adjusted from R=2 up to R>10^4, while its spatial resolution is 0.32"/pixel. It comprises of two cameras that each has four 2048×2048 E2V CCD's.

The SPIRou (Donati et al. 2018), a near-infrared spectropolarimeter and velocimeter with high radial-velocity precision and accuracy that can reach a meter/second over a period of several years. Its main scientific purposes are the search of habitable exoplanets and also the study of forming sun-like stars and their planetary system.

2.2 Infrared Telescopes

2.2.1 The Spitzer Space Telescope

The Spitzer Space Telescope (Werner et al. 2004) is the fourth of the NASA's Great Observatories and is dedicated to infrared observations of the full sky. It was launched in August 25th in 2003 into an Earth trailing heliocentric orbit. Spitzer carries a cryogenic telescope (85 cm in diameter) with three cryogenic science instruments attached

in the focal plane: The Infrared Array Camera (IRAC), the Ingrared Spectrograph (IRS) and the Multiband Imaging Photometer for Spitzer (MIPS). The cryostat uses liquid helium to keep the temperature at 1.4 K in order to avoid heat biases in the observations. The short expected life (2.5 years) actually was extended to 5.5 years and the cool mode depleted in 2009. At that moment, with a temperature at 28 K (warm mode), only the two short-wavelength channels (3.6 and 4.5 μm) of the IRAC camera are operating very well. Below, it is given a brief description of each instrument:

IRAC (Fazio et al. 2004) is a four-channel camera with four different detectors each one having 256x256 pixel size with a field of views over a 53.2x5.2 squared arcminutes. IRAC is capable of simultaneously observing four mid infrared bands at 3.6, 4.5, 5.8 and 8.0 m and producing images. The detector of the two shortest bands was made of indium and antimony, while the one of 4.5 and 8.0 m bands consists of arsenic. The angular resolution of the four detectors is 1.5 arcsecond while the sensitivity achieved (1 sigma) in each IRAC channel is 0.60 Jy, 1.2 Jy, 8.0 Jy and 9.8 Jy, respectively for 100 seconds of integration and low background. In this thesis, Spitzer/IRAC photometry was used in the analysis of the GOODS-South Field (Chap. 3) and also the Frontier Fields (Chap. 4).

IRS (Houck et al. 2004) provides high and low resolution spectra in the range 5-40 m in addition to 16mm imaging with four different modules: two low (R$\sim$60-130) and high (R 600) resolution at short wavelengths (5.3-20 m) and two more at long wavelengths (14-40mm). The low resolution modules use long-slits that allow simultaneously both spectroscopic data and one-dimension spatial information. Each module is divided into two in-line sub-slits. The high-resolution modules use single slits and a cross-dispersed echelle design to provide broad spectral coverage in a single exposure. Furthermore, IRS with its peak-up arrays provides imaging in two further bands (13-18 and 18-26) between 8 and 24 m completing the spectral gap from the other Spitzer instruments. The sensitivity (the median 1sigma continuum) reached in the IRS low- and high- resolution modules is about 0.05 mJy and about 2 mJy, respectively in 512 seconds of integration with low background.

MIPS (Rieke et al. 2004) provides imaging and photometry in three broad spectral bands at 24, 70 and 160 m in addition to low-resolution spectroscopy in 55-95 m. MIPS consists of three detector arrays that operate simultaneously with an angular resolution of 6, 18 and 40 arcseconds with corresponding low-background sensitivity of 16.1, 5.15, and 6.53 MJy/ster at 24, 70 and 160 m, respectively. The 24 m camera provides roughly a 5 arcmin square FOV, the 70 micron camera provides a FOV that is roughly 2.5 by 5 arcmin, while the 160 m array projects to the equivalent of a 0.5 by 5 arcmin FOV.

2.2.2 WISE

The NASA's Wide-field Infrared Survey Explorer (WISE Wright et al. 2010) launched in December 14th in 2009 aimed to map for the first time the entire infrared sky. The telescope with a weight of ∼650 kg set in a polar circling orbit at ∼525 km above the Earth. It carried a 40 cm diameter telescope with four infrared detector arrays on its focal plane. Each of the detectors has over a million pixels providing imaging photometry at 3.4, 4.6, 12 and 22 m. The entire telescope is placed in a tank of frozen hydrogen (cryostat) that keeps the temperature of the telescope at 12 K, while that of the detectors at 32 K for the 3.4 and 4.6 m and less than 8 K for the 12 and 22 m bands. The primary mission was mended to last 10 months until the tank of the hydrogen was depleted. After that, since two of the infrared detectors could not operate without coulant, the NEOWISE Post-Cryogenic mission began with the two left detectors aimed to observe the near-Earth objects, such as comets and asteroids. NEOWISE's decommission happened in February of 2011. However, the NEOWISE was re-activated two years later in 2013 and since then it operates till today normally.

The angular resolution of the WISE detectors is 6.1", 6.4", 6.5" and 12" for the 3.4, 4.6, 12 and 22 m bands, respectively, with a FOV of ∼47 square arcminutes (three times the dimension of the full Moon). The corresponding achieved 5-sigma sensitivity for point sources is 0.08, 0.11, 1.0 and 6.0 mJy, respectively, in low-background regions on the ecliptic which improves toward the ecliptic poles. Furthermore, the astrometric precision id better than 0.15" for sources with high signal-to-noise ratio. WISE data were used in Chapter 5 to construct the SEDs of the VIPERS field and also to apply AGN selection criteria.

2.3 X-ray Telescopes

2.3.1 XMM-Newton Telescope

XMM-Newton is an European Space Agency X-ray satellite launched in December 10th of 1999. The mission was initially planned for two years but has been extended several times till today operating already 20 years. Initially, it was named X-ray Multi-Mirror Mission, though the name XMM-Newton was given in honor of Sir Isaac Newton. Its main objective is to observe and explore the soft X-ray regime (0.2-15 keV) of distant X-ray sources for long time periods. The satellite with a weight of almost four tons is orbiting the Earth in an elliptical orbit (eccentricity is e=0.68) with a period of 48 hours. The apogee and the perigee of the orbit are at 114,000 and 7,000

km, respectively. It is characterized by a high position accuracy and stability, since the control of its orientation is handled precisely with two sets of four small thruster and four momentum wheels. XMM-Newton constitutes of three X-ray co-aligned telescopes (each one is made up with 58 nested Wolter type-1 mirrors), an optical telescope and, in total, three instruments that provide high sensitivity and good angular and spectral resolution with a moderate energy resolution ($E/\Delta E \sim 20-50$). These are: a) the European Photon Imaging Camera (EPIC), for X-ray imaging and moderate resolution spectroscopy b) the Reflection Grating Spectrometer (RGS), for high-resolution X-ray spectroscopy in the 0.35 2.5 keV range and, c) the Optical Monitor (OM), for optical/UV imaging and spectroscopy. The description of each instrument is summarized below. In this thesis, the analysis of the VIPERS field was based partially on X-ray photometric data from the EPIC camera.

EPIC consists of three CCD detector arrays, two Metal Oxide Semi-conductors (MOS 1 and MOS 2, Turner et al. 2001) and one pn CCD camera (Strüder et al. 2001). Both MOS cameras are equipped with a RGS, thus 44% of the incoming flux goes to MOS cameras in the primary focus, 40% to the RGS detector in the secondary focus, while the rest is absorbed. The pn camera receive the full flux of the third telescope. The EPIC FOV is 30' in the energy range 0.15-15 keV and has spectral resolution of $E/\Delta E$ ∼20-50 and angular resolution PSF 6" FWHM. Furthermore, the pn camera has readout noise much faster compared to MOS cameras and it has very high time resolution equal to 0.03 ms for the "timing" mode and 0.007 ms in the "burst" mode. One main difference is that the MOS cameras (7 CCD's) are front-illuminated, while the pn camera (12 CCD's) is back-illuminated, so they have different quantum efficiency.

RGS (Brinkman et al. 1998; den Herder et al. 2001) are placed in the secondary focus of the two X-ray telescopes and provide high resolution spectra and spectral photometry for bright sources in the soft X-ray band. Each of the RGS consists of an array of reflection gratings which diffracts the X-rays to a CCD array detector. The resolving power is 150-800 in the energy between 0.33 and 2.5 keV (5-35). The effective area for both spectrometers peaks at ∼0.83 keV at about 150 cm2.

OM (Mason et al. 2001) is mounted on the mirror support platform alongside the X-ray telescopes and aimed to provide simultaneously with the X-ray observations also optical and UV imaging and spectrometry with a coverage from 170 to 650 nm. The FOV of OM is 17 square arcminites centred in the FOV of the X-ray images. The 30 cm Ritchey-Chretien telescope has a focal length 3.8 m and the light is reflected to two (redundant) detectors where there is a filter wheel that further provides grism and magnifier.

2.3.2 Chandra X-ray Observatory

The Chandra X-ray Observatory (Weisskopf et al. 2000) launched in July 23th in 1999 at a high-Earth orbit with a period of ∼64 hrs. Its mission was to detect X-ray emission in the 0.3-10 keV regime from very hot regions in the Universe, such as Supernovae, clusters of galaxies and matter sound black holes. The Chandra's telescope system has four nested Wolter-type mirrors with focal length of 10 m and an effective area 800 cm2 at 0.25 keV, while it has very high spatial resolution (PSF∼0.2" FWHM) compared to the XMM-Newton. In the focal plane there are two instruments, the Advanced CCD Imaging Spectrometer (ACIS) and the High Resolution Camera (HRC), that provide sharp images with information on counts, position, energy and time of arrival. In addition there are two more instruments, the High Energy Transmission Grating (HETG) and the Low Energy Transmission Grating (LETG), for high resolution spectroscopy with detailed information about the X-ray emission. Below, a description of these instruments is given. In this thesis, data from ACIS detector were used in the analysis of the GOODS-South field (Chap. 3).

ACIS (Garmire et al. 2003) has two arrays with different configurations. The first one, ACIS-I, is the main imaging (0.2-10 keV) square detector that includes four front illuminated (FI) chips with a field of view 16'×16', while the second one, ACIS-S, is a rectangular array of 6 chips. Four of those are FI and two are back illuminated (BI) resulting in a field of view 8'×48'. ACIS-S is used mainly for the readout of the HETG. All the chips have effective area 340 cm2, while the energy resolution, $E/\Delta E$, is 20-50 and 9-35 at 1 and 6 keV for the FI and BI, respectively.

HRC (Murray et al. 2000) consists of two micro-channel plate detectors and provides imaging and spectroscopy in the 0.1-10 keV regime, while it has very high time resolution of 16 microseconds. The first one, HRC-I has a large field of view of 30'×30' but a smaller energy resolution than the ACIS cameras. Its spatial resolution is 0.5" and its effective area is 225 cm2 at 1 keV. The second, HRC-S has field of view 7'×97' and it serves the LETG mainly for readout of the diffraction grating.

HETG (Canizares et al. 2005) and **LETG** (Brinkman et al. 2000) are diffraction gratings that are located into the path of the X-ray photons and provide high and low resolution spectroscopy, respectively. Both gratings are used in complement with the imaging detectors, ACIS-S and HRC-S, respectively. HETG is sensitive in the 0.5-8 keV (1.6-6) and has spectral resolution power of $E/\Delta E$ ∼60-1000, while LETG is sensitive in the 0.05-2 keV band with $E/\Delta E$ ∼30-2000.

Chapter 3

Robust Identification of Active Galactic Nuclei through *HST* Optical Variability in GOODS-S: Comparison with the X-ray and mid-IR Selected Samples

In order to study AGN variability over cosmic time one needs a deep field observed multiple times. The Great Observatories Origins Deep Survey Southern field (GOODS-S Giavalisco et al. 2004) centered at α =3h32m30s $\delta = -27°48'20''$ J2000, covers an area of $10' \times 16'$. It is the most data-rich area of the sky in terms of depth and wavelength coverage and as it has been observed by the *Hubble* Space Telescope (HST) multiple times, it perfectly satisfies the requirements of our study. Variability studies in this field based on HST multi-epoch data have been performed by Sarajedini et al. (2011) and Villforth et al. (2010, 2012). Sarajedini et al. (2011) used the V-band (F606W) images over five epochs spanning almost seven months and the standard deviation, σ, as the statistical variability indicator to identify 42 variable sources. The authors compared their results with the mid-IR and the 2Ms *Chandra* X-ray data. Villforth et al. (2010) identified 88 variable sources (out of ∼6,000 sources) using the C-statistic (the ratio of the measured standard deviation, σ, to the expected one $\sigma_{\rm exp}$, in this case scaled from the estimated photometric errors; de Diego 2010) on z-band data with the same epochs and time baseline as in Sarajedini et al. (2011). The authors, after removing the false positive detections and the stellar population, validated the AGN nature of 55/88 variable sources through spectral en-

ergy distribution fitting, the identification of X-ray counterparts in the CDF-S 4Ms catalogue and auxiliary radio and IR data (Villforth et al. 2012).

The field was also targeted in ground-based optical variability studies. Trevese et al. (2008) studied the variability of sources in AXAF, a larger field that includes GOODS-S. They analysed V-band images taken from ground-based telescopes and used magnitude differences between eight epochs over two years of observations to identify 132 variable AGN candidates. Similarly, Falocco et al. (2015) applied a multi-epoch variability search spanning six months with the SUDARE-VOICE survey dataset obtained with the VLT Survey Telescope. They selected 175 variable sources over an area of $2\,deg^2$ around CDF-S using σ as the variability index. They compared the optical variable sample with AGNs selected through optical-NIR and IR colour diagnostics and AGNs with X-ray counterparts in the 4Ms CDF-S catalogue.

We extend the previous HST-based studies of Sarajedini et al. (2011) and Villforth et al. (2010, 2012) by using the latest data, variability detection and IR-colour-based AGN selection techniques. We construct a new catalogue of optically variable AGNs based on HST z-band observations and comparing it with other selection techniques. We highlight the following novel aspects of this study:

- We expand the time baseline of the deep HST observations of GOODS-S up to ten years, which should result in a more complete AGN selection.
- We use the Median Absolute Deviation (MAD) as the variability-detection statistic, which, unlike σ, is robust against individual outlier measurements (Sokolovsky et al. 2017). We expect MAD to yield a cleaner sample of variable sources compared to the previous studies.
- We use the new deepest available 7 Ms *Chandra* image to constrain the X-ray brightness of the variability-selected AGNs.
- We compare our variable sample with AGN selected in the mid-IR using the Lacy et al. (2007) and Donley et al. (2012) criteria.

The HST optical observations and the data reduction (astrometry and photometry) along with ancillary data used in this work are presented in Section 3.1, while in Section 3.2, we describe the method we used to create the list of variable sources. We also exclude stars and supernovae from the sample of the AGN candidates. In Section 3.3, we demonstrate the properties of the AGN candidates (e.g. magnitude and redshift distributions or X-ray luminosities) and construct the mid-IR AGN samples. In Section 3.4, we compare our results with other variability studies and we discuss the differences between optically variable, mid-IR and X-ray selected AGNs.

3.1 Data Reduction

3.1.1 Optical HST data

We analyze all publicly available images of the GOODS-S region obtained with the Wide Field Channel of the HST Advanced Camera for Surveys (ACS, Ford et al. 1998) in the F850LP filter (z-band). The images are collected from the Hubble *Legacy Archive (HLA) Data Release 10*[1]. Each image corresponds to an individual HST visit and results from a combination of three or more individual exposures with the purpose of rejecting the cosmic rays. The observations were collected in the framework of the observing programs listed in Table 5.1. We analyze totally 437 individual images spanning up to 10 years in some regions.

We used the code developed by M. Tewes[2] which is based on P. G. van Dokkum's `L.A.Cosmic` algorithm (van Dokkum 2001) to further reduce the cosmic-ray contamination of the visit-combined images, especially on the edges of the combined frames. This algorithm is based on variations of the Laplacian edge detection and is capable of rejecting any cosmic ray, regardless of its shape and size, keeping at the same time the faint point-like sources untouched.

Source detection and photometry was performed using SExtractor (Bertin & Arnouts 1996a, 2010). We applied the *mexican hat* spatial filter for detection and set the minimum contrast parameter for deblending (`deblend_mincont`) to 0.0075 in order to avoid multiple detections for individual extended sources. This did not affect the unresolved sources, since the GOODS-S field is not crowded. For the photometry and the variability analysis, we used a circular aperture with a radius of 0.36″. This was the radius used by Villforth et al. (2010) as for smaller radii the photometry is affected by changes in the point-spread function and aperture centring issues. In addition, we measured the magnitudes for two more radii (0.05″ and 0.15″), which correspond to the ones used for the *Hubble* Source Catalogue (HSC, Whitmore et al. 2016) apertures (`MagAper1` and `MagAper2`). The latter were used to compute the concentration index (`CI`) and to validate our photometry against the HSC. `CI` is an indicator of the extension of a source and is described below.

After visually inspecting images associated with outlier points appearing in many light curves, we noticed that many outliers were situated near the frame edge or the gap between CCD chips in these images. This is related to the background estimation,

[1] http://hla.stsci.edu/

[2] http://obswww.unige.ch/~tewes/cosmics_dot_py/

Table 3.1:: The HST Treasury programs included in this study

Prop. ID	PI Name	Cycle	N_{img} [a]	N_{exp} [b]	Exp. Time (s)	Start_Obs[c]	End_Obs[c]
9352	A. Riess	11	12	4	1880-4800	2002-10	2003-02
9425	M. Giavalisco	11	78	4	2040-2120	2003-02	2003-02
9488	K. Ratnatunga	11	2	3	1800	2002-09	2003-02
9500	H-W. Rix	11	58	3	2160-2286	2002-09	2003-02
9803	R. Thompson	12	18	6	6900	2003-08	2003-11
9978	S. Beckwith	12	68	4	4660-4860	2003-09	2004-01
10086	S. Beckwith	12	3	4	4660	2003-12	2003-12
10189	A. Riess	13	23	3-4	1200-2000	2004-09	2005-01
10258	C. Kretchmer	13	20	4	3034	2004-10	2006-09
10340	A. Riess	13	75	4	1440-1600	2004-07	2005-02
11144	R. Bouwens	16	1	4	2046	2009-10	2009-10
11563	G. Illingworth	17	31	4	5102-5332	2009-08	2010-08
12060	S. Faber	18	15	4	2046-2330	2011-03	2011-11
12061	S. Faber	18	11	5	1836-2086	2010-11	2011-06
12062	S. Faber	18	15	5	1886-1986	2011-07	2011-12
12099	A. Riess	18	4	4-5	1886-2070	2010-12	2011-08
12461	A. Riess	19	2	4	1943-1992	2012-02	2012-03
12534	H. Teplitz	19	1	4	5000	2012-05	2012-05

Note. – (a): Number of combined (level 2) images. (b): Number of single exposure images. (c): Starting and ending time of the observations.

which is essential for aperture photometry. Because the images have been resampled to a north-up east-left orientation, blank areas appear around the actual image (e.g. CCD gaps and image edges). SExtractor uses these blank areas and gets incorrect background estimates. To avoid this effect and, consequently, outliers and false-positive variable sources, we used the weight images provided by HLA and excluded all detections located within 10 pixels, or $\sim$0.5″, from the edges ($\sim$1% of all the detections).

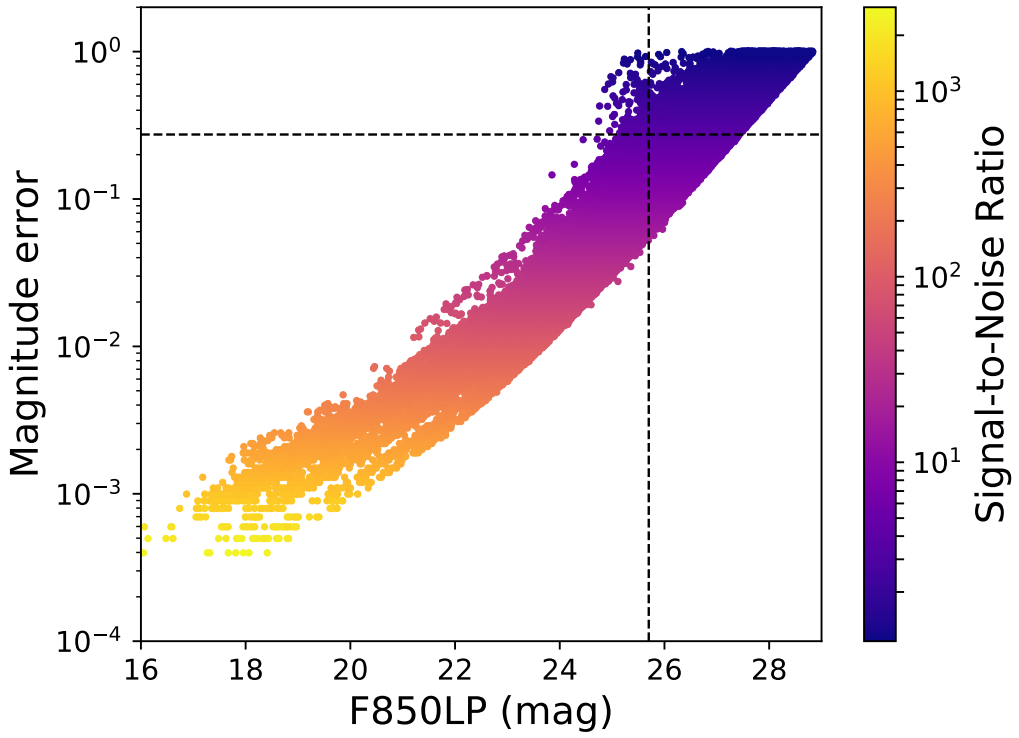

Figure 3.1: The magnitude errors as a function of the magnitude for each detection. The measurements are colour coded by the SNR. The vertical and horizontal lines represent the limits in magnitude and magnitude error, respectively, after the SNR filtering.

To ensure the quality of the data but also enable the search for small amplitude variations, we selected measurements with a signal-to-noise ratio (SNR) greater than five. The SNR was calculated for each of the detections for all images using the fluxes and the corresponding flux errors derived with SExtractor. In Figure 3.1, we plot the magnitude error as a function of the magnitude, colour-coded with SNR. The relation between magnitude and magnitude error is approximately linear as expected if the errors are mainly statistical at the faint end. After applying the SNR cut-off,

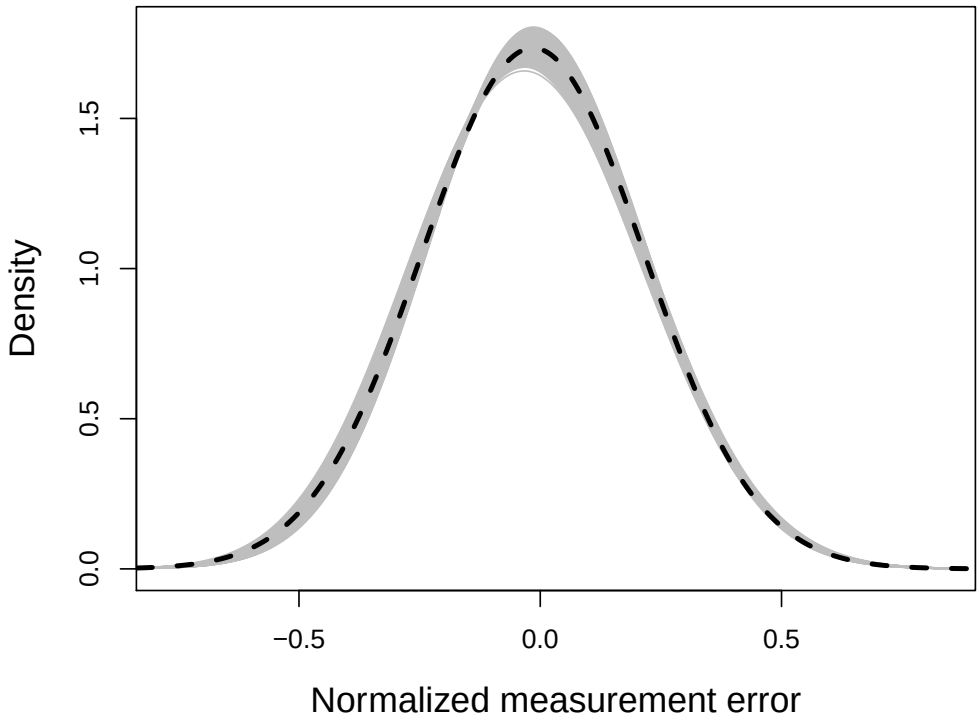

Figure 3.2: The distributions of the normalized measurement errors for each magnitude bin (gray). The black dashed line represent the Gaussian fit to the data. The units are given in magnitudes.

the faintest sources have an average error of about 0.25 mag.

We also divided all the detections into magnitude bins and over-plotted the distributions of the normalized magnitude errors (after subtracting the median) for each of the magnitude bins in order to check if all detections of the same magnitude have similar errors. Figure 3.2 shows that these distributions are approximately Gaussian. The distribution would have been skewed, if there was a group of sources measured with systematically larger uncertainties (e.g. due to bright local background).

Since the astrometric accuracy of the HST is limited by the positional accuracy of individual Guide Star Catalogue stars (Lasker et al. 2008), we applied a triangle matching technique based on the Valdes et al. (1995) algorithm to find the astrometric

solution. We used the `match_v1` program by M. W. Richmond[3] to automatically determine the coordinate system corrections using the 50 brightest sources in each source list. We used the second version of HSC (HSCv2) as the reference catalogue for the astrometry and the resulting positional errors are less than 0.1".

We then cross-matched the coordinates-corrected source lists with each other to construct a light curve for each source. We kept only sources with at least five measurements. Figure 3.3 presents the histogram of the median magnitude, <F850LP>, of all the sources after the SNR filtering. Due to the drop-off of detected sources beyond 25.7 mag, our sample is photometrically complete down to this magnitude. Since the images used to derive the source lists have different depth (Table 5.1), we over-plot in Figure 3.3 the completeness curves of different images with extreme exposure times. We summed the detections of images with exposure times of ∼2000 s (Prop. ID: 12062) and ∼5000 s (Prop. ID: 11563), respectively. For both data sets, the number counts of detections decline at magnitudes fainter than the magnitude completeness limit of this work. Thus, the variable depth of the images did not affect our results. The resulting catalogue consists of 21,647 sources. Figure 3.4 presents the distribution of the number of data points in the light curve, N_p, as a function of the time baseline, T_{bas}, which is defined as the time difference between the first and the last observation of a source. A large fraction of sources (∼ 80%) has been observed for more than two and up to ten years with a median time baseline of 8.5 years. The average and median number of data points in the light curves are 15 and 12, respectively.

The photometric accuracy was tested by comparing our `MagAper2` magnitudes to those in HSCv2. First, we cross-matched all the sources with HSCv2 using a radius of 1″, resulting in 7245 matches out of 21,647 final sources (our source list is much deeper than HSCv2 in this region). In Figure 3.5, we plotted the difference in magnitude, $<F850LP>_{\text{this work}}-<F850LP>_{\text{HSCv2}}$ as a function of magnitude between this study and HSCv2 and find the values to be comparable. The relation is linear through the full magnitude range as expected. We visually inspected the images and the light curves of the outliers (marked with black filled circles on Figure 3.5) and attributed the magnitude discrepancies to multiple detections of the same extended source in the HSCv2.

The separation of the extended and point-like sources was performed using `CI` as defined in the HSC, `CI=MagAper1−MagAper2` (Whitmore et al. 2016). The `CI` histogram reveals two well-defined areas (Figure 3.6, top panel). We fitted two Gaussians to the two populations (point-like and extended) and the point where these two

[3] http://spiff.rit.edu/match/match-1.0/

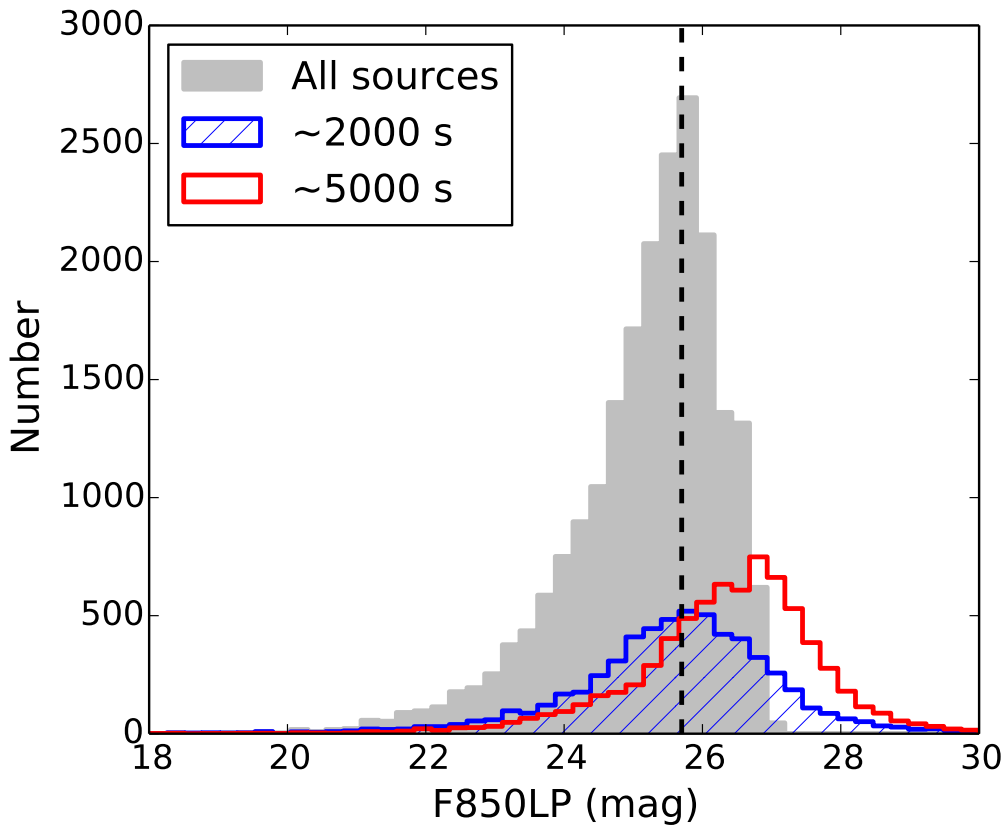

Figure 3.3: The distribution of the median magnitude, <F850LP>, of all the sources (gray shaded histogram) along with the completeness curves for images with exposure times of 2000 s (blue hatched) and 5000 s (red), respectively. The dashed line indicates the completeness limit of our final sample.

fits come across is at CI=1.33 mag. Adopting it as the separation threshold results in 21,022 extended and 625 point-like sources. Figure 3.6 (bottom panel) shows the CI as a function of magnitude, where the two populations are plotted using different colours.

3.1.2 X-ray and IR data sets

GOODS-S is among the deepest and best studied fields in the sky and over the last decades there is a variety of imaging and spectroscopic data available from radio to X-ray wavelengths. In this study, apart from the HST optical observations, we utilize X-ray and IR catalogues and, also, photometric or spectroscopic data when available to validate the nature of the variable sources.

Table 3.2:: Summary of the basic information of the CDF-S X-ray catalogues.

X-ray catalogue	Number of observations	Observation dates	# sources CDF-S	$F_{0.5\text{-}8\ keV}$ (ergs cm^{-2} s^{-1})	$F_{0.5\text{-}2\ keV}$ (ergs cm^{-2} s^{-1})	$F_{2\text{-}8\ keV}$ (ergs cm^{-2} s^{-1})	# matches optical	# matches variable
250 ks ECDF-S	9	2004	430	$> 3.5 \times 10^{-16}$	$> 1.1 \times 10^{-16}$	$> 6.7 \times 10^{-16}$	144	14
2 Ms CDF-S	23	1999 - 2000	578	$> 7.1 \times 10^{-17}$	$> 1.9 \times 10^{-17}$	$> 1.3 \times 10^{-16}$	298	16
4 Ms CDF-S	54	1999 - 2010	776	$> 3.2 \times 10^{-17}$	$> 9.1 \times 10^{-18}$	$> 5.5 \times 10^{-17}$	464	21
7 Ms CDF-S	102	1999 - 2016	1055	$> 1.9 \times 10^{-17}$	$> 6.4 \times 10^{-18}$	$> 2.7 \times 10^{-17}$	621	24

Note. – The flux limits of the 7 Ms CDF-S catalogue in the broad and the hard band are derived up to 7 keV.

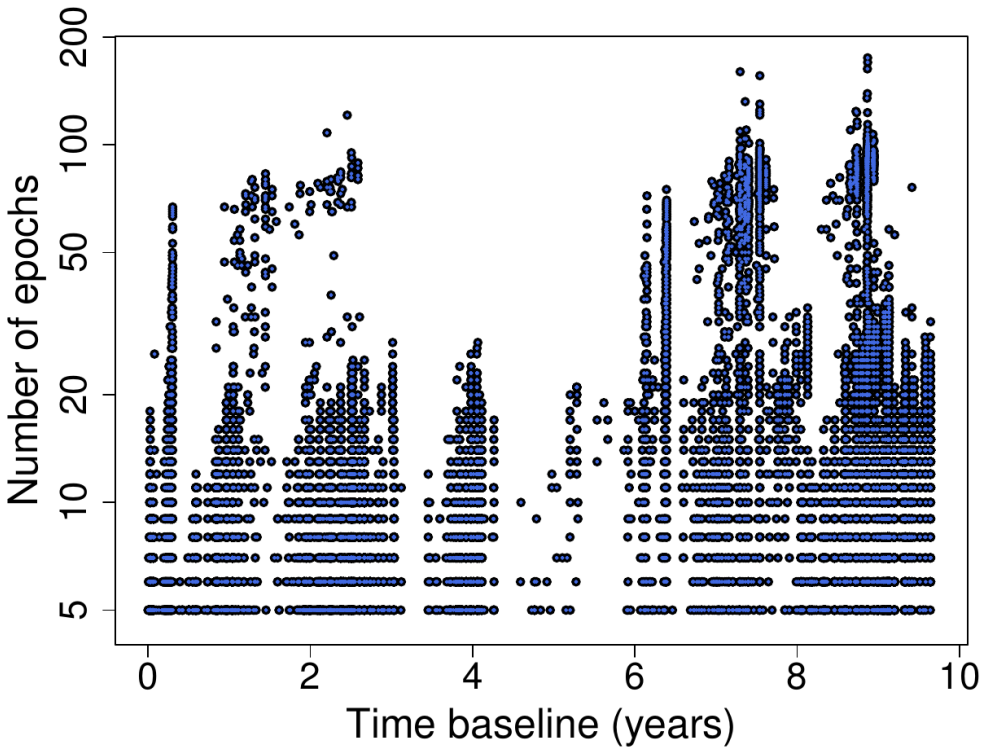

Figure 3.4: The number of data points as a function of the maximum time baseline covered by the light curve.

We use four X-ray catalogues from CDF-S and the Extended Chandra Deep field South (ECDF-S) with different depths: 250 ks (Xue et al. 2016), 2 Ms (Luo et al. 2008), 4 Ms (Xue et al. 2011) & 7 Ms (Luo et al. 2017). The area studied in this work partly overlaps with CDF-S, which is centered at α =3h32m28.06s and δ = $-27°48'26.4''$ (J2000) and covers an area of $\sim$464.5 arcmin^2. ECDF-S covers an area of 0.54 deg^2 in the sky centered at α =3h32m24.0s δ = $-27°48'47.0''$ (J2000). Figure 3.7 shows CDF-S and GOODS-S projected on the sky. The catalogues are produced from the X-ray images taken by the Advanced CCD Imaging Spectrometer camera (ACIS, Garmire et al. 2003) aboard the *Chandra X-Ray Observatory*. We also used these four catalogues to test the dependence of the number of optical counterparts on the depth of the X-ray image.

Table 3.2 presents the number of sources detected in at least one band (the supplementary sources – lower significance X-ray sources with bright IR counterparts – of each catalogue are also included), the number of observations and the observation dates with the on-axis sensitivity limits in the soft (0.5−2 keV), hard (2−8 keV) and

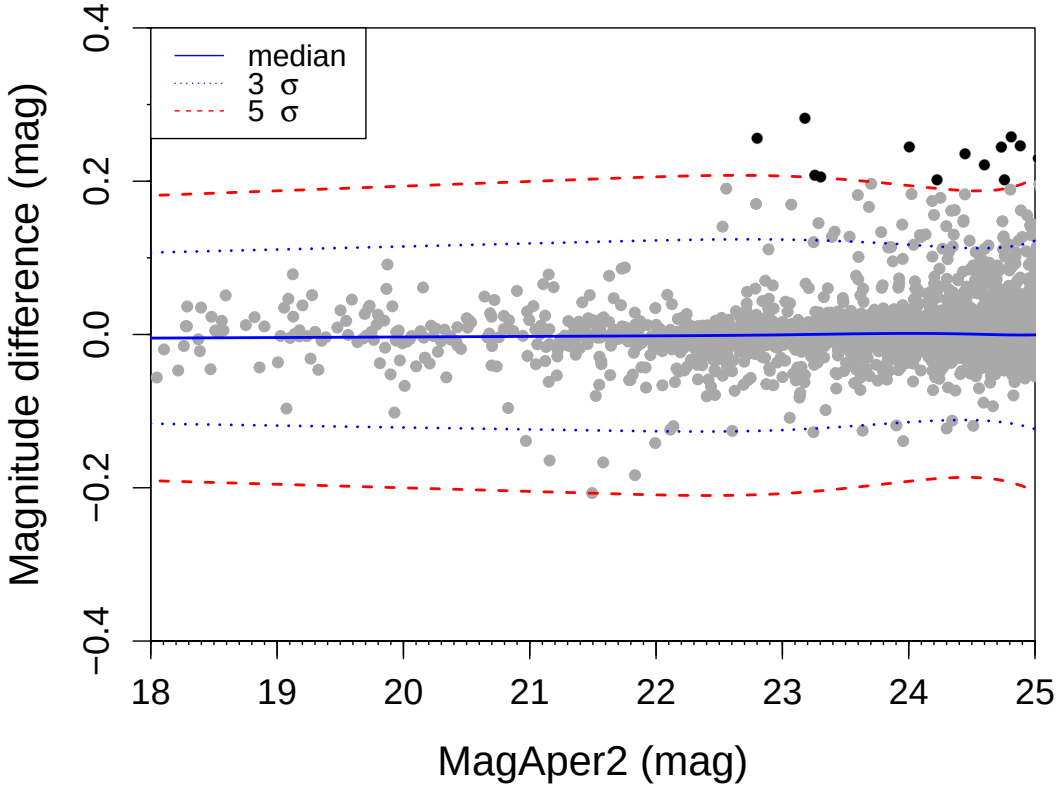

Figure 3.5: A comparison between the <F850LP> magnitude of our photometry and HSCv2. The grey points represent all the sources in common. The blue solid line shows the median, while the blue dotted and red dashed lines represent the 3σ and 5σ values of the magnitude difference, respectively. Sources exceeding the 5σ value are highlighted in black.

broad (0.5−8 keV) bands of the catalogues. The 250 ks catalogue is from ECDF-S, which covers a much larger region, but here we only present the sources that lie within CDF-S. The 7 Ms CDF-S catalogue extends up to 7 keV to avoid the background noise present at higher energies. The full list of the observations of each catalogue and the detailed description of the data reduction can be found in the aforementioned papers and the references therein. All published catalogues include additional information on the sources, such as X-ray properties, multi-wavelength counterparts and redshifts.

For the variable optical sources identified in Sec. 3.2 that have no X-ray counter-

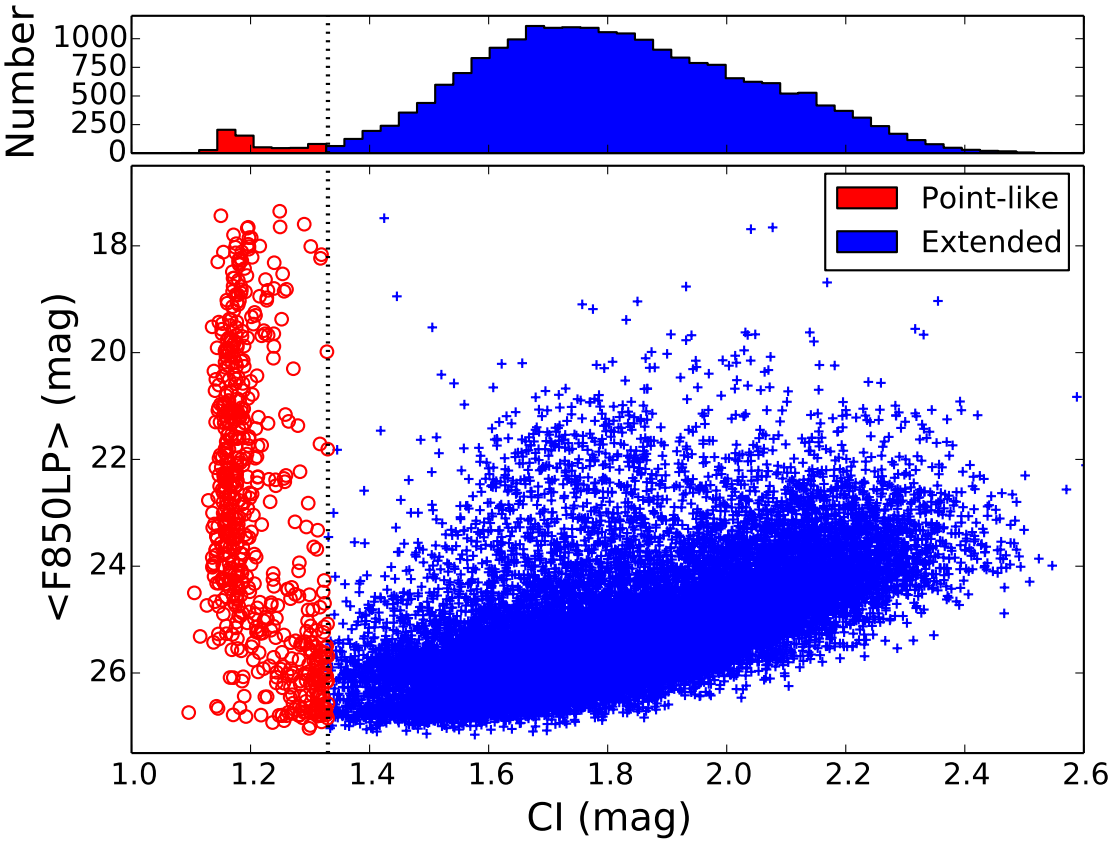

Figure 3.6: The median magnitude, <F850LP>, as a function of the CI for point-like (red circles) and extended sources (blue crosses). The dashed line represents the chosen threshold at $CI = 1.33$ mag that separates the two populations. The upper panel shows the histogram of the CI.

parts, we independently reduced the *Chandra* images using the `CIAO` software v2.0.1[4] to construct the 7 Ms image and calculated the X-ray flux upper-limits. First, we created the 7 Ms co-added images in the three bands – broad, soft and hard, starting with the level 2 event files. We used 99 observations taken from October 1999 to March 2016. We kept only the central CCD chips (`ccd_id`=0,1,2,3) and filtered out flares affecting the background in the light curve of each observation by masking the sources and using the `deflare` tool with the `clean_lc` option. For each observation, we ran the `wavedetect` tool to create source catalogues, so we could reproject the images at the same reference point in the sky to achieve a good absolute astrometric solution. The final step was to combine the event files with the `dmmerge` tool and create images and exposure maps for all the bands.

[4] http://cxc.harvard.edu/ciao

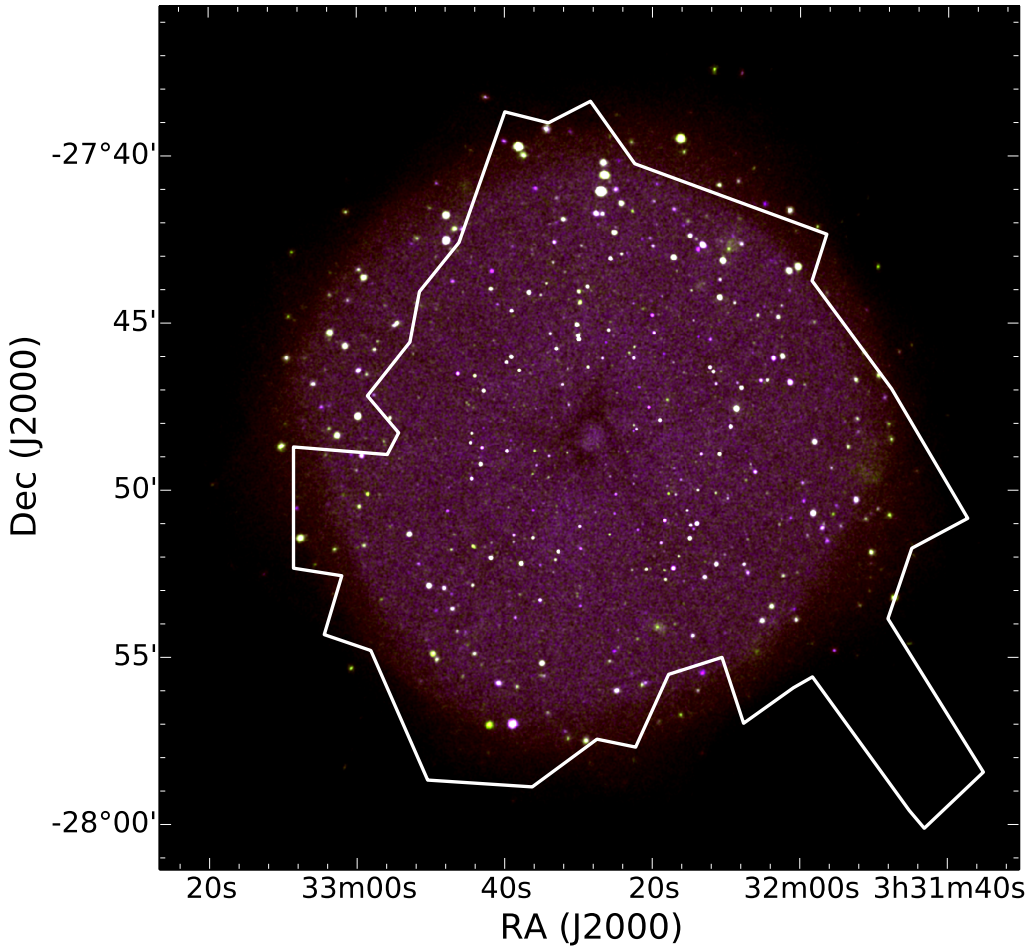

Figure 3.7: Colour composite image of the exposure corrected and smoothed 7 Ms CDF-S. The white polygon represents the GOODS-S footprint.

The smoothed image including all three bands is shown in Figure 3.7. For the non-detected sources in the X-rays, we measured the counts and the exposure effective areas in a circular region centered on the position of the optical counterparts. The radius, r_i, used for each optical source was calculated in a way that to enclose a specified fraction of the point spread function. The fraction adopted here decreases from the on-axis (0.95) to off-axis sources (0.5). The background was extracted from 500 circular regions (with aperture half of r_i) at random positions around the optical source (within a distance from 1.5 to 5 times of r_i) that do not overlap with other X-ray or the optical variable sources. We derived the count rate for each background region and finally normalized the mean value of all of them to the area of the source. Then we derived the upper limits with a confidence interval of 99.7%. The count rates were converted to fluxes, using an energy conversion factor equal to 2.8×10^{-9},

1.5×10^{-9} and 6.2×10^{-9} ergs photon^{-1} for the broad, soft and hard band, respectively by assuming a power-law model with photon index of $\Gamma = 1.7$.

GOODS-S overlaps, also, with the Spitzer IRAC/MUSYC Public Legacy Survey in the Extended Chandra Deep Field South (PI: Pieter van Dokkum, SIMPLE). SIMPLE covers an area of $\sim$ 1,600 arcmin^2 surrounding GOODS-S and contains photometry for $\sim$45,000 sources from deep Spitzer/IRAC (Fazio et al. 2004) observations combined with other UV to mid-IR data from the Multiwavelength Survey by Yale-Chile (MUSYC). In this work, we use the four IRAC bands (3.6 μm, 4.5 μm, 5.8 μm and 8.0 μm) to construct the IR selected AGN sample (Section 3.3.2), while the r, J, K and 3.6 μm bands from the same catalogue were used to separate the stellar from the extra-galactic objects in Section 3.2.3. The full description of these data can be found in Damen et al. (2011).

3.2 AGN selection based on optical variability

Sokolovsky et al. (2017) discussed two classes of statistical methods that quantify variability of a source. The first class quantifies the scatter of the magnitudes within a light curve, while the methods of the second class quantify the smoothness of a light curve by taking into account the order and time at which the magnitude measurements were obtained. Regular variability can be detected that way too, if the observing cadence is shorter than the variability timescale (Ferreira Lopes & Cross 2016), or, if the scatter is higher than what is expected from noise (Ferreira Lopes & Cross 2017). Light curve simulations by Sokolovsky et al. (2017) suggest that the scatter-based methods are more suitable for detection of variability in light curves having a small number of points compared to the methods that characterize the light curve smoothness. Median Absolute Deviation[5] (Rousseeuw & Croux 1993, MAD) belongs to the first class of methods and it is the most robust to outliers among the variability indices discussed by Sokolovsky et al. (2017). MAD is defined as the median value of the absolute deviations of the measurements, m_j, from the median:

$$\mathrm{MAD} = b \times (|m_j - (m_j)|), \tag{3.1}$$

where $b = 1/(\sqrt{2}^{-1}(1/2)) \simeq 1.4826$ is the factor scaling the median absolute deviation to the standard deviation (assuming the normal distribution of m_j); $^{-1}$ is the inverse error function. In the next section, we compare the performance of various variability-detection statistics in the presence of photometric outliers to verify the reliability of MAD.

[5] https://en.wikipedia.org/wiki/Median_absolute_deviation

3.2.1 Variability detection in the presence of outlier measurements

For all but the faintest optical sources, the accuracy of their brightness measurements is limited by the poorly constrained systematic effects rather than the number of collected photons ("shot noise") and uncertainties in the background level estimations. This means we typically do not have a reliable error bar attached to a photometric measurement. Of a particular concern in the context of HST photometry are the residual cosmic rays that were not cleaned-out perfectly in the process of image stacking ("drizzling"; Fruchter & Hook 2002) that overlap with the measured image of the object. To circumvent the above issues, we may *1)* assume that in a non-crowded field like GOODS-S objects of similar brightness will have similar measurement errors and the majority of objects are non-variable; *2)* employ a variability detection statistic that is robust against individual outlier measurements (similar to those caused by cosmic ray hits).

We perform Monte-Carlo modeling to characterize the performance of various variability-detection statistics in the presence of photometric outliers. First, we model $i = 1...10000$ light curves each containing N points randomly distributed in time. At each point in the model light curve we assigned a brightness value drawn from the Gaussian distribution characterized by the variance e^2. In addition, 1% of the points get a "cosmic ray hit" modeled by the additional increase in brightness by a value drawn from a uniform distribution between 0 and $100e$. We, then, compute the median value, $I^{\rm non-var}$ and the standard deviation $\sigma(I^{\rm non-var})$ scaled from the median absolute deviation of $I_{\rm non-var}$ values for each of the tested variability indices:

$$\sigma(I^{\rm non-var}) = 1.4826 \times (|I_i^{\rm non-var} - (I_i^{\rm non-var})|).$$

After that, we add to each light curve an aperiodic variation characterized by a power-law power spectral density with a slope of -1 and amplitude e (equal to the noise level). We use these lightcurves to compute the median value of the variability index:

$$I^{\rm var} = (I_i^{\rm var})$$

and the typical Signal-to-Noise ratio , SNR, of variability detection (among all the realizations of the noise and variability patterns):

$$\mathrm{SNR} = (I^{\rm var} - I^{\rm non-var})/\sigma(I^{\rm non-var}).$$

The resulting values of SNR as a function of N are presented in Figure 3.8 for the three variability indices: the standard deviation σ, the MAD that characterize the scatter of measurements in a light curve and the $1/\eta$ that quantifies the smoothness

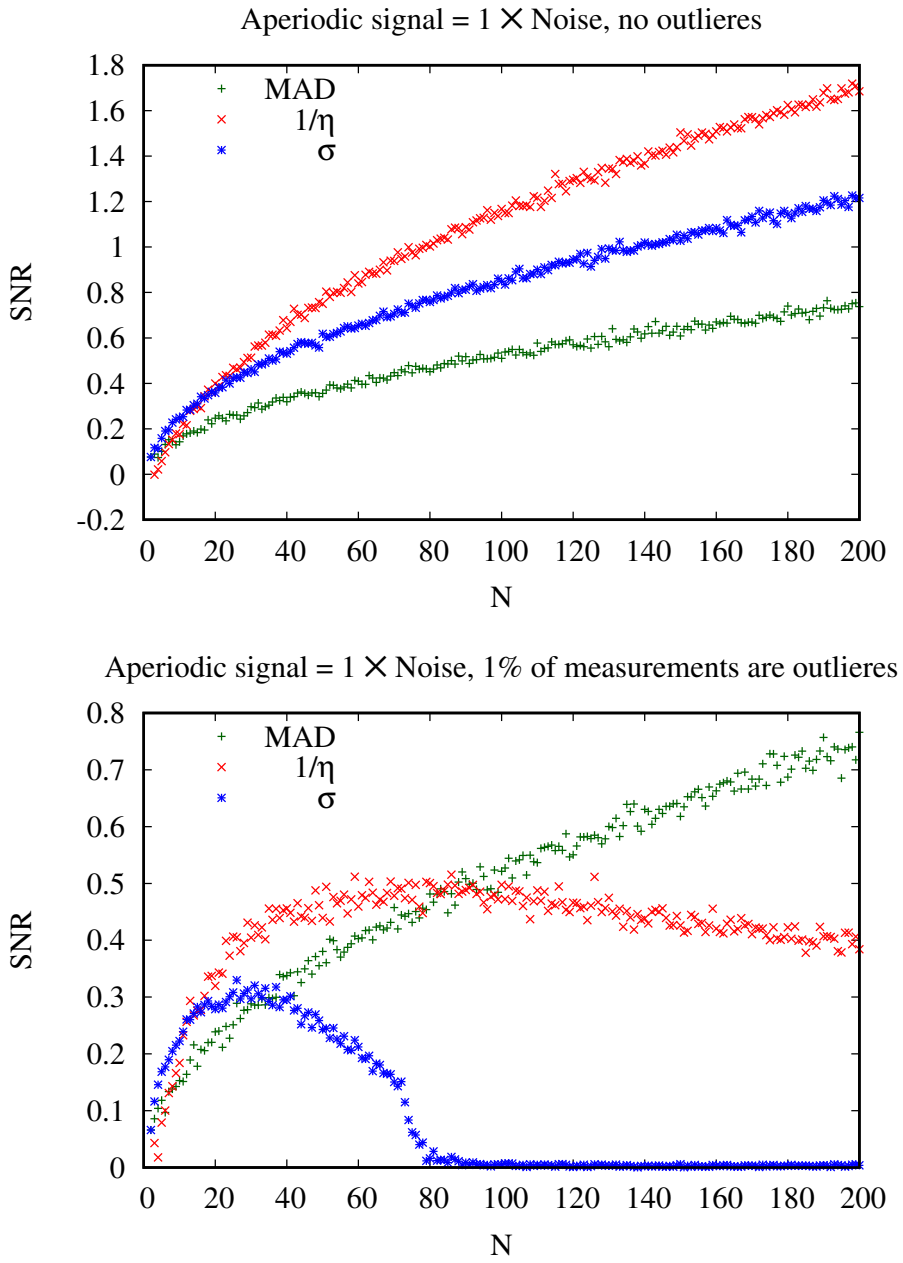

Figure 3.8: The simulated median signal to noise ratio of variability detection as a function of the number of light curve points with no outlier measurements (top panel) and in the presence of outliers (bottom panel).

of a lightcurve. A detailed discussion of these variability indicators can be found in Sokolovsky et al. (2017).

Figure 3.8 highlights that in the absence of outlier measurements (i.e. non-

periodic variability is being detected over a pure Gaussian noise) σ and $1/\eta$ typically provide a higher SNR detection for a given number of light curve points than MAD. If outlier measurements are present in light curves, they dramatically affect the efficiency of σ as a variability indicator rendering its useless as soon as each light curve has so many points that it is likely to contain at least one outlier (recall, that in our model the variability amplitude is lower than the amplitude of outliers). The ability of $1/\eta$ to identify smooth variability is also reduced considerably by outliers, while MAD maintains the SNR that is steadily increasing with N.

The simulations described above confirm that MAD may serve as a variability indicator resistant to individual outlier measurements. It is also apparent that σ is on average a more sensitive variability indicator than MAD as long as N is sufficiently low that each individual lightcurve is unlikely to contain even one outlier. However, if outliers are present in the data set, the light curves that contain outliers will predominantly be selected with σ as candidate variables. The use of MAD is still preferred to select a clean sample of variable objects, even at the cost of a slightly lower detection efficiency compared to σ.

3.2.2 Variability algorithm

Our variability detection algorithm works as follows: we divided the sources into magnitude bins and by assuming a Gaussian distribution, we calculated for each bin the median magnitude, the median MAD and the standard deviation (σ) of MAD. The bin size is adjusted so as to have at least 50 sources in each bin. To get a smooth magnitude dependence, we fitted a cubic spline to the median and the threshold values. We, also, extrapolated toward fainter magnitudes to account for the completeness limit (Section 3.1). Taking into account that the majority of the sources are normal galaxies and no variations are expected, the variable sources are those that exceed a cut-off above the median. We note that Sarajedini et al. (2011) rely on the same critical assumptions as we do here: that the majority of sources are non-variable and that sources of similar brightness have similar photometric errors. Villforth et al. (2010) also rely on this assumption indirectly when they derive the scaling factors for the estimated photometric errors that they use to compute the C-statistic.

Following Bershady et al. (1998), or more recently Sarajedini et al. (2011), we determine the threshold separately for the point-like and the extended sources (except we determine the threshold in MAD scaled to σ rather than in σ as Sarajedini et al. 2011). Figure 3.9 (upper panels) shows the variability index, MAD, as a function of the median magnitude, <F850LP> for the extended (left) and point-

like (right) sources. We also calculated the normalized significance, MAD*, for each source through the following formula:

$$\mathrm{MAD}_i^* = \frac{\mathrm{MAD}_i - (\mathrm{MAD})_b}{\sigma(\mathrm{MAD})_b}, \tag{3.2}$$

where MAD_i is the MAD for the i^{th} source and b the corresponding magnitude bin. The significance has units of σ. The plots of MAD* as a function of magnitude are shown in the lower panels of Figure A.6.

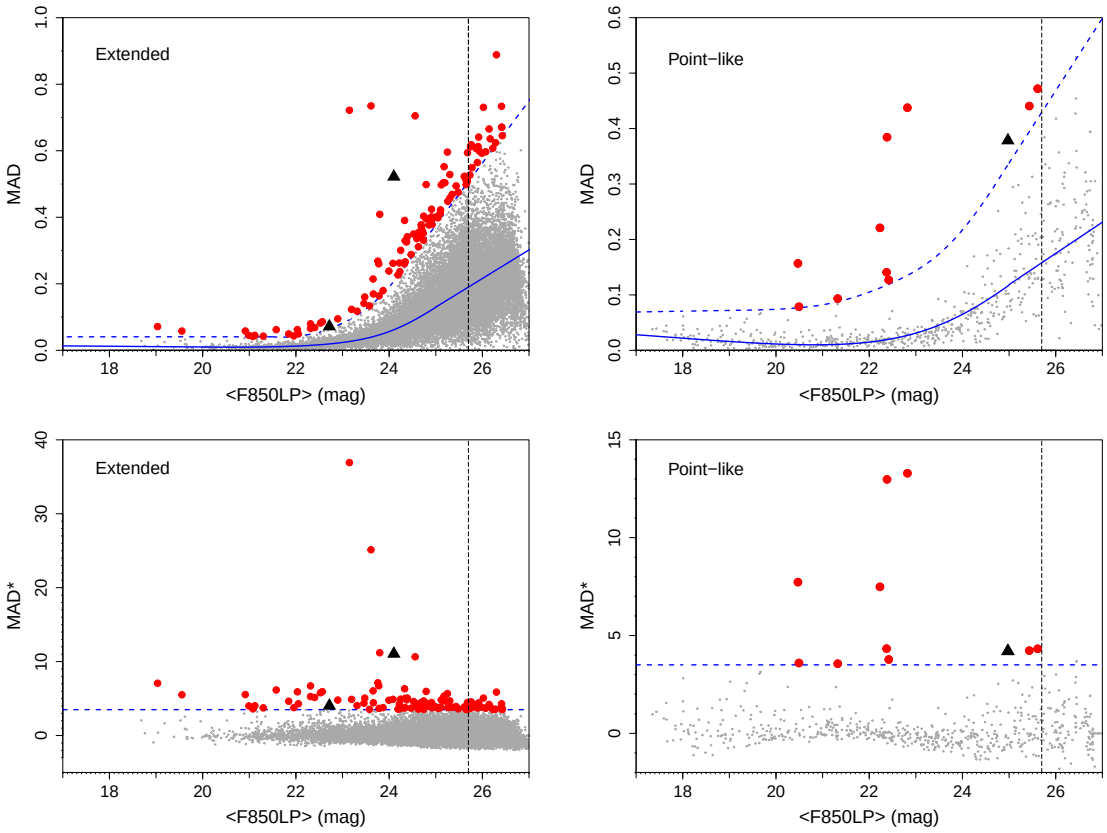

Figure 3.9: The MAD (upper panels) and normalized significance MAD* (lower panels) as a function of the median magnitude (<F850LP>) for the extended (left) and point-like sources (right). All the sources in our survey are shown with grey points, while the AGN candidates are shown with red circles, and the confirmed SNe with black triangles. The blue solid and dashed lines represent the median and the threshold, while the vertical black dashed line the completeness limit of our sample.

We set the threshold of 3.5σ in MAD* above which we consider the sources to be variable. Assuming the normal distribution of MAD* we estimate the fraction of

sources that are expected to have the value of MAD* above the threshold, i.e. the false positive rate, as:

$$\mathrm{FP_{rate}} = 1 - \frac{1}{2}(1 + (\frac{3.5}{\sqrt{2}})) \simeq 2.3 \times 10^{-4}, \tag{3.3}$$

so out of 21,022 extended and 625 point-like sources of the initial sample we expect 5 and < 1 false positives among the extended and point-like candidate variable sources, respectively. This corresponds to $\sim$3.2% of the total number of 187 variable candidates. The false positives are expected to have magnitudes near the completeness limit where the majority of sources are found (Fig. 3.3).

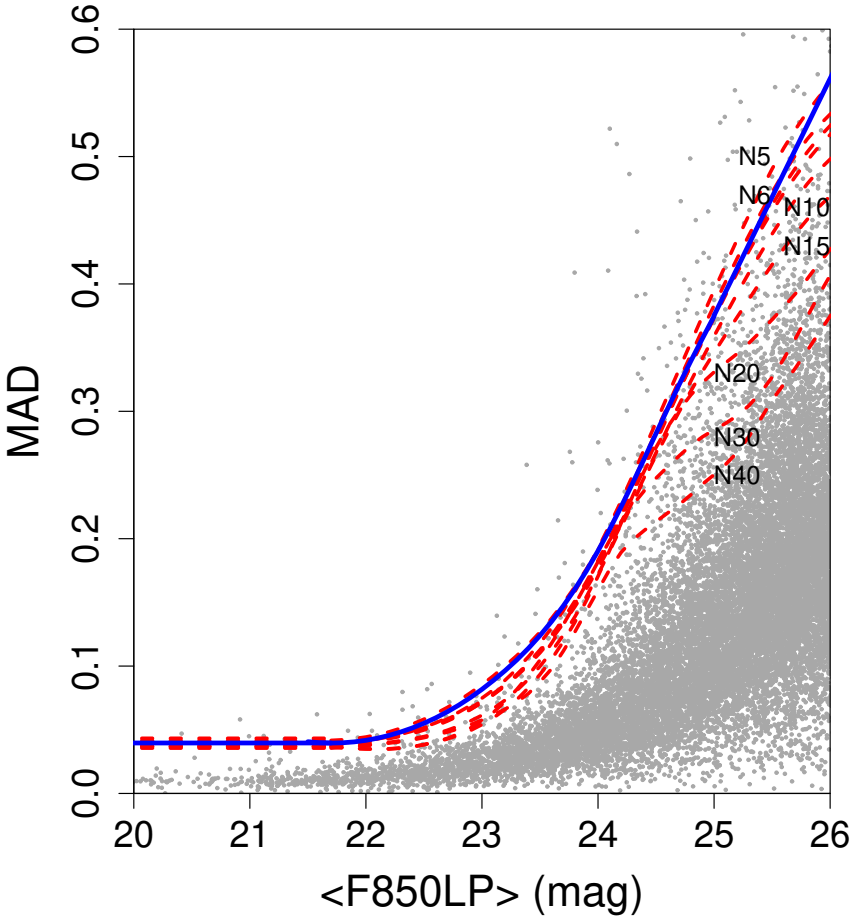

Figure 3.10: MAD as a function of magnitude of all sources in our initial sample. The blue solid line represents the adopted variability threshold of 3.5σ, while the red dashed lines represent the thresholds for the median under-sampled sets for different number of data points in the light curves, N.

Furthermore, as our sample is not homogeneous concerning the number of data points in their light curves, in order to test if the 3.5σ threshold will be at a different level if we consider only light curves with a specific number of data points, we used simulations and checked if the thresholds derived from under-sampled data is lower than the adopted threshold in this work. If this is the case, then the sample of variable sources derived from applying the same threshold to all light curves (irrespective of the number of points in them) will not be affected.

We simulated ten sets of under-sampled data with the sets differing in the number of data points in the light curves (N=5, 6, 7, 8, 9, 10, 15, 20, 30 & 40). The number of sources of the under-sampled data are 21022, 19346, 17428, 15891, 14207, 13128, 6790, 3677, 1769 & 1350, respectively. For each set, we performed 1000 iterations and at each time, we randomly selected N data points for all the sources of our initial sample. We then calculated the MAD values and followed the procedure described in previous section to find the 3.5σ thresholds. We took the median values of the thresholds with N data points in the light curve and we compared the results with different N. In Figure 3.10, we plot the MAD as a function of magnitude for all the sources of our sample and the 3.5σ threshold adopted in this work (solid blue line). We over-plot the median values of 3.5σ thresholds for different number of data points in the light curve, N (dashed black lines).

We find no extreme differences between the thresholds derived from different N. From the bright end of the magnitude distribution up to $\sim$24 mag, the thresholds follow the same trend with small scatter with each other. Above $\sim$24 mag, the scheme changes as the simulated thresholds are getting lower for increasing N. The adopted threshold in this work is above all the simulated ones but the set with N=5 above 24 mag that has slightly higher values. As long as the number of sources that have only five data points in their light curves is small, and the differences in the thresholds is not significant, we expect no false variability induced by the different number of data points in the light curves.

Moreover, to further explore the genuine statistical significance of our threshold, we calculated the cumulative distributions of the normalized MAD for several magnitude bins with different number of data points (N=5, 6, 7, 8, 9, 10, 20, 30 & 40). In Figure 3.11, we show the median cumulative distributions for different number of data points as long as with the real distribution of our sample. The average statistical significance of the 3.5σ thresholds is 99.65%. However, the true significance should be greater than this value, since the distribution also includes the variable sources. We visually inspected the light curves of all the candidate variable sources and the associated images. We checked for diffraction spikes from nearby foreground stars, close neighbors, poorly removed cosmic rays, proximity to a frame edge and satura-

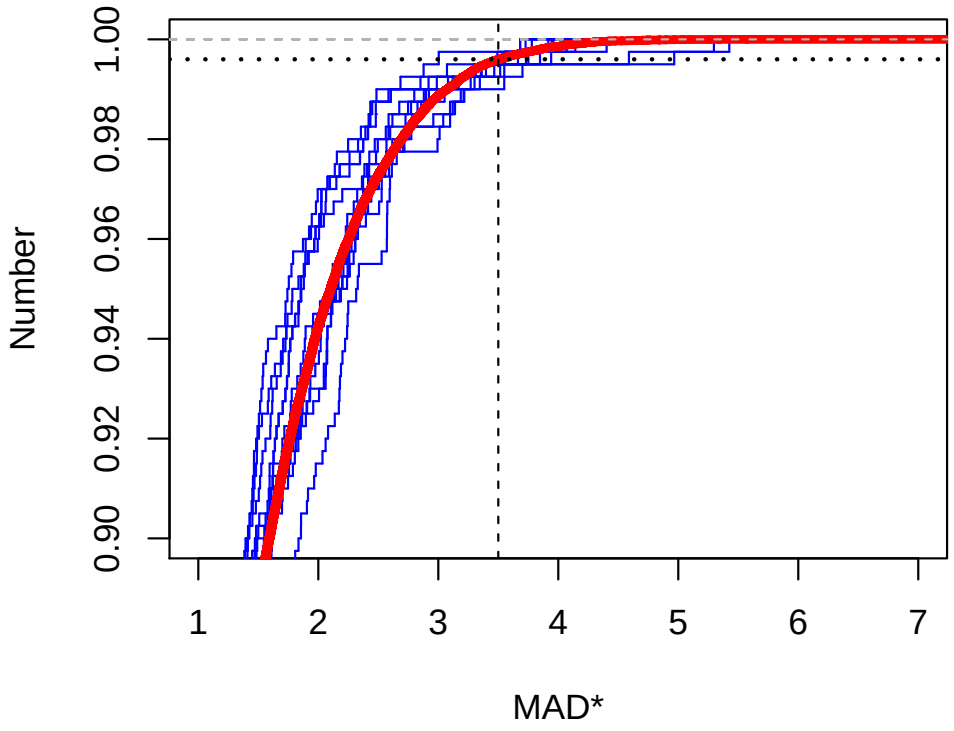

Figure 3.11: The median cumulative distributions of the normalized significance for under-sampled data with different number of data points in the light-curve (blue thin lines). The red thick line represents the distribution from our final sample, while the horizontal dashed and dotted line represents the statistical significance of 100% and 99.65%, respectively. The vertical line is our 3.5 σ threshold.

tion or misalignment of individual exposures. All these factors may introduce false variability. Following this procedure, we classified all the variable sources into three categories. Sources with clear variability in their light curve, far from other sources with no artifacts or potential problems recorded and with accumulated significance higher than 99.9%, were assigned grade A (86 sources). Sources with minor problems that may affect the reliability were assigned a grade B (32 sources). This category includes sources that might have centring issues, caused by the extension of the object or that are too faint and dispersed and sources between 3.5 sigma and accumulated significance of 99.9%. Finally, all sources that were found to be affected by saturation, diffraction spikes, blending or other significant problems were assigned a grade C (69

sources).

3.2.3 Stars and supernovae

In order to separate AGN candidates from stars, we followed Rowan-Robinson et al. (2005) and Damen et al. (2011). According to Rowan-Robinson et al. (2005), stars can be distinguished from the extra-galactic objects, such as QSOs and very distant AGNs by their brightness in the r band (r<23 mag) and their position in the $3.6\mu m/r$ flux ratio versus the $r-i$ diagram (Figure 3.12, right). The two populations occupy different regions in the diagram and can be easily separated. This method was also used by Falocco et al. (2015) and Rowan-Robinson et al. (2013). On the other hand, Damen et al. (2011) excluded the stellar population using a colour cut-off ($[J-K](AB) < 0.04mag$) and applied certain quality criteria to their initial sample: signal-to-noise ratio in K band $(S/N)_K > 5$ and their relative weight in the K band versus the z- band, $wK > 0.5$. We cross matched our initial catalogue of 21,647 sources

Table 3.3:: Catalogue of confirmed SNe identified in our survey.

ID	RA (J2000)	Dec (J2000)	N_p	T_{bas} (years)	<F850LP> (mag)	MAD* (σ)
7343	53.07570	-27.73630	8	0.14	24.10	11.1
9581	53.10564	-27.75084	17	2.51	22.71	4.72
14446	53.15638	-27.77966	6	0.18	24.97	4.20

with the SIMPLE data (Sec. 3.1.2) to obtain the colours for our sources and applied the above diagnostics. Figure 3.12 shows the $[J-K]$ vs. $3.6\mu m$ and the $3.6\mu m/r$ vs. $[r-i]$ diagrams with the sources colour coded by the `CI`. The open black circles presented in the plot are used to show the variable sources in each diagram. Both diagnostics indicated eight classified variable sources to be stars. All of them are grade C variable sources, as six were saturated and two were blended sources. We therefore identify no high-confidence candidate variables among the foreground stars.

For the identification of SNe, we relied on visual inspection of the light curves and the corresponding images. We found three sources with light curves of Grade A resembling SNe (ID 7343, 9581 & 14446), which have all been previously reported in the literature by Strolger et al. (2004) and Riess et al. (2007). Their light curves and observational properties can be found in Figure 3.13 and Table 3.3. Out of the SNe catalogues, there are 13 more SNe that have a counterpart in our initial sample, but they are all below the variability threshold. Possible explanations could be the differences in the observation dates (the peak was not observed), or that our

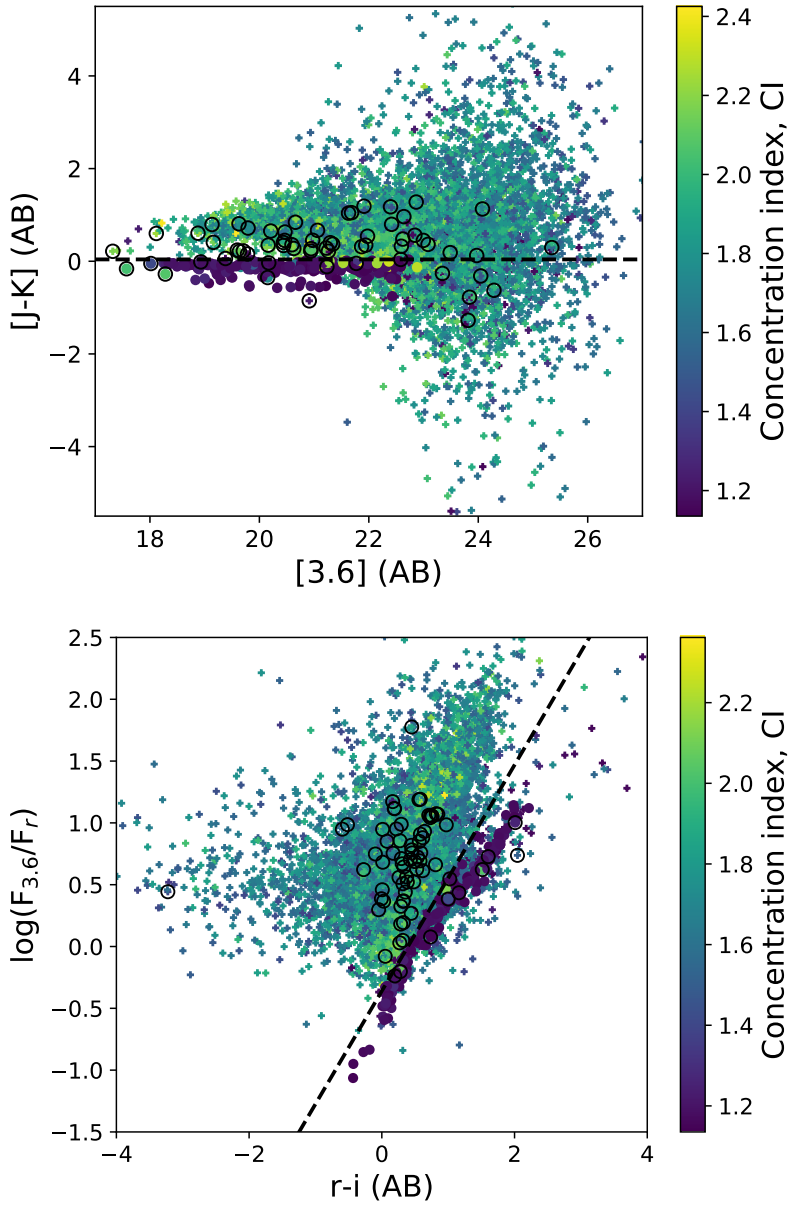

Figure 3.12: The $J-K$ *versus* $3.6\mu m$ diagram (upper) and the $3.6\mu m/r$ flux ratio versus $r-i$ diagram (lower). The crosses represent the common sources between our sample and the SIMPLE data. The filled circles are the sources classified as stars. All sources are colour coded by the CI. The open black circles indicate the variable sources.

variability algorithm could not detect variability if the number of the data points in the light curve that correspond to the peak was small and they were considered as outliers by MAD. For these sources, we also calculated the standard deviation, but

they were still below the threshold, thus the first case is more likely to happen.

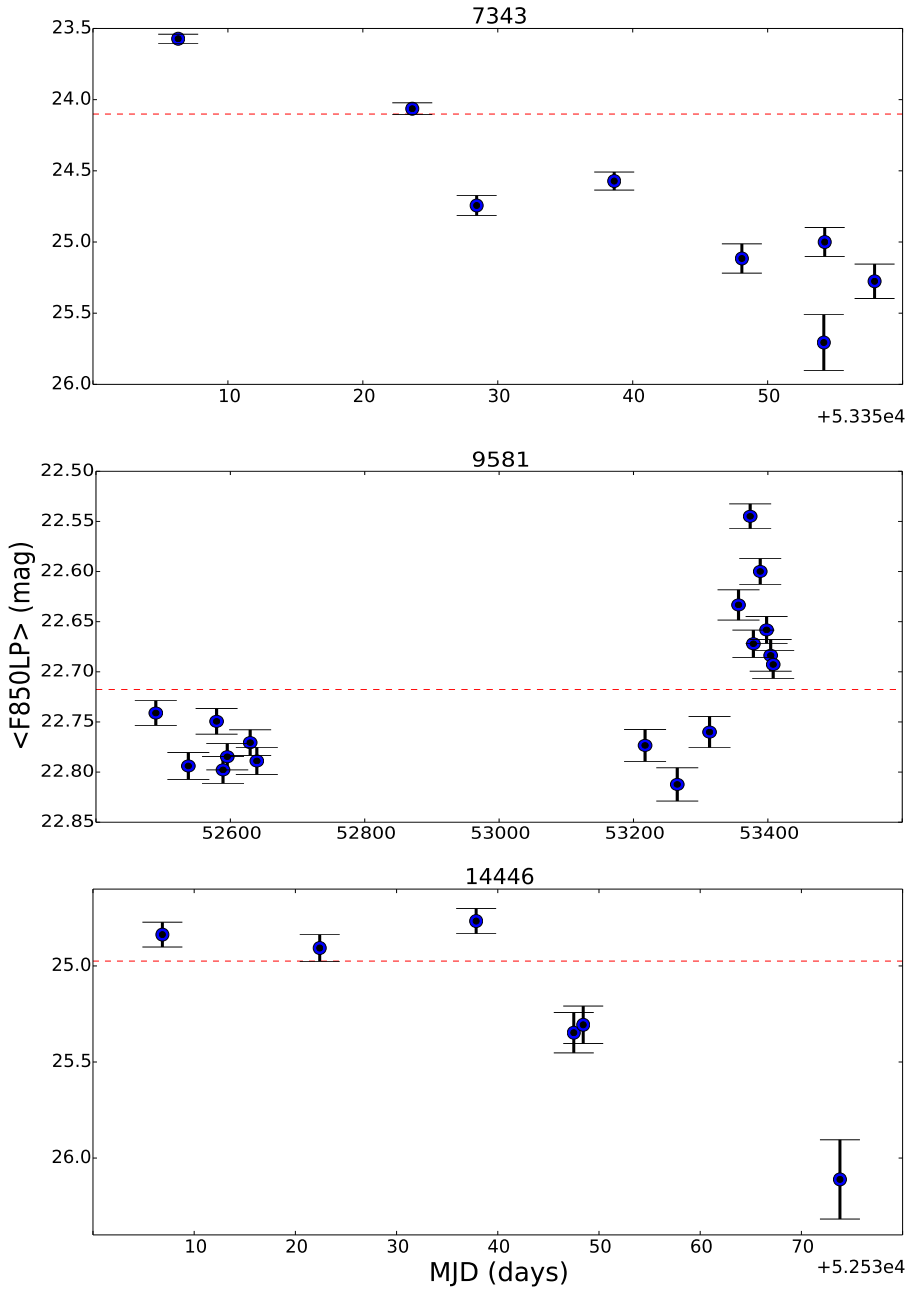

Figure 3.13: Light curves of the confirmed SNe identified in this study. The dashed line indicates the median magnitude and the number on the top of each plot indicates the identifier of the source.

In the next sections, we proceed with the analysis of the remaining 113 variable sources (10 point-like and 103 extended), which are presumed to be AGN candidates (Table 3.4). Figure 3.14 illustrates the positions of the variable sources on the sky,

while some examples of the AGN light curves can be found in Figure 3.15.

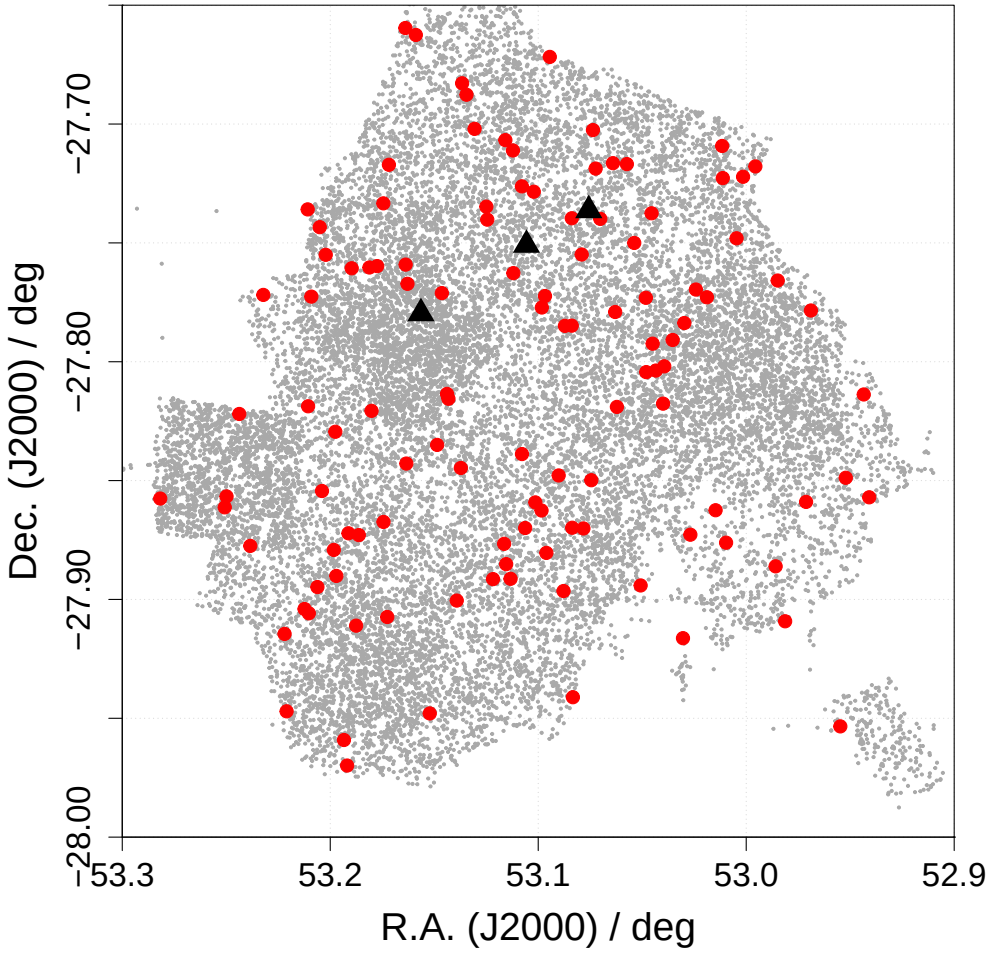

Figure 3.14: Spatial distribution of the AGN candidates (red circles). The confirmed SNe are shown with black triangles. The background grey points represent the whole sample consisting of 21,647 sources.

3.3 Properties of the AGN candidates

3.3.1 X-ray detections & upper limits

We cross-matched the final sample of the 113 AGN candidates with the four X-ray catalogues described in Section 3.1.2. We used a search radius of 2" as the maximal

Table 3.4:: Catalogue of the variable AGN candidates.

ID	Grade	RA (J2000)	Dec (J2000)	N_p	T_{bas} (years)	CI (mag)	<F850LP> (mag)	MAD* (σ)	z	z Ref.	F_x [0.5-8 keV] (ergs cm^{-2} s^{-1})
(1)	(2)	(3)	(4)	(5)	(6)	(7)	(8)	(9)	(10)	(11)	(12)
347	B	52.94086	-27.85703	5	9.1	2.22	22.56	5.93	0.58	3,c	<7.40E-16
398	A	52.94348	-27.81377	6	9.12	2.19	23.31	4.04	0.89	3,c	<4.86E-16
561	A	52.95213	-27.84881	8	9.11	1.7	24.55	10.6	0.2	3,g	<4.44E-16
615	A	52.95474	-27.95340	6	1.92	2.14	22.4	5.15	1.22	1,e	2.10E-015
1081	A	52.96888	-27.77844	5	8.18	2.01	22.03	5.91	0.67	1,a	3.17E-015
1181	B	52.97121	-27.85896	5	9.11	2.03	24.32	3.71	1.3	3,c	<2.40E-16
1560	B	52.98128	-27.90919	5	9.13	1.64	25.67	3.64	0.95	3,c	<4.65E-16
1749	A	52.98486	-27.76583	6	1.95	1.57	23.14	36.9	4.83	3,c	<2.72E-16
1799	A	52.98585	-27.88607	6	9.11	2.26	22.31	6.71	0.24	1,c	<1.31E-16
2300	B	52.99559	-27.71783	6	8.3	2.28	23.77	6.72	1.03	3,d	<3.05E-16
2644	A	53.00151	-27.72218	9	2.51	1.28	22.23	7.5	1.04	1,a	1.46E-014
2816	A	53.00463	-27.74807	9	8.46	1.29	25.43	4.23	0.66	3,a	<2.01E-16
3129	A	53.00967	-27.87611	5	9.14	1.47	23.78	3.67	1.43	1,a	1.06E-015
3240	A	53.01125	-27.72273	9	8.58	1.69	25.76	4.54	2.17	3,b	<1.92E-16
3268	A	53.01156	-27.70921	7	8.58	1.64	25.65	3.63	2.9	3,b	<4.20E-16
3485	B	53.01471	-27.86247	5	9.14	2.17	23.65	6.03	1.33	3,d	<3.52E-16
3753	A	53.01887	-27.77287	6	8.46	1.57	26.16	3.88	1.16	3,b	<2.98E-16
4080	A	53.02418	-27.76962	7	1.06	1.56	25.86	4.19	1.3	3,b	<1.44E-16
4210	A	53.02684	-27.87276	5	9.14	2.01	24.59	4.08	2.33	3,c	<3.02E-16
4388	B	53.02974	-27.78371	5	8.03	1.66	25.89	3.71	3.67	3,b	<1.67E-16
4422	A	53.03039	-27.91629	5	8.99	2.16	24.08	4.89	1.14	3,c	<2.66E-16
4757	A	53.03535	-27.79084	5	9.07	1.68	25.92	4.41	3.08	3,d	<1.38E-15
4949	A	53.03939	-27.80194	16	9.58	1.18	20.47	7.73	2.81	1,a	6.51E-015
4981	A	53.03997	-27.81762	5	1.11	1.73	26.3	5.87	0.3	3,b	<1.65E-16
5182	A	53.04340	-27.80370	5	0.9	1.57	26.02	5.06	1.47	3,b	<1.59E-16
5281	A	53.04498	-27.79240	19	9.58	1.99	24.9	3.99	0.81	3,b	<9.88E-17
5322	A	53.04550	-27.73754	11	8.59	1.26	22.42	3.78	1.62	1,a	1.95E-014
5497	A	53.04805	-27.80435	14	9.57	1.86	21.84	4.63	0.54	1,a	3.78E-017
5510	B	53.04824	-27.77309	11	9.44	2.21	23.47	5.06	1.21	2,b	<7.72E-16
5664	A	53.05076	-27.89412	5	9.19	2.08	23.75	7.13	1.1	3,c	<1.82E-16
5856	B	53.05383	-27.75002	22	2.52	2.13	24.34	3.77	1.2	2,b	<2.87E-16
6061	B	53.05739	-27.71684	5	2.5	1.69	25.73	3.64	1.55	3,b	<2.74E-16
6381	A	53.06216	-27.81900	12	9.39	1.79	25.06	3.73	1.05	3,b	<9.72E-17
6446	A	53.06299	-27.77906	34	9.33	2.06	24.39	5.04	0.96	2,b	<5.29E-17
6515	A	53.06407	-27.71645	12	8.59	1.82	24.62	4.27	2.55	3,d	<1.45E-16
6932	B	53.07015	-27.73988	5	2.44	1.62	25.48	3.6	0.76	3,b	<2.17E-16
7112	B	53.07239	-27.71873	14	8.59	2.33	22.89	4.79	0.64	1,b	<6.74E-15
7224	A	53.07367	-27.70253	10	8.59	2.05	23.66	4.43	1.18	1,d	<2.06E-16
7270	A	53.07447	-27.84984	17	9.51	2.39	20.91	5.53	0.12	1,a	1.58E-016
7531	B	53.07825	-27.87013	14	9.64	2.17	23.99	4.77	0.66	1,d	<2.67-E16
7588	A	53.07909	-27.75488	12	9.33	1.86	25.43	3.92	1.18	3,b	<1.89E-16
7906	B	53.08332	-27.94113	5	3.82	1.85	23.19	4.88	0.65	3,b	<1.46E-16
7924	A	53.08366	-27.86983	6	9.51	1.78	25.16	4.77	0.73	1,c	<1.24E-16
7938	A	53.08386	-27.73963	20	2.51	2.26	23.86	3.77	1.21	1,a	1.46E-016
7947	B	53.08388	-27.78481	5	9.08	1.44	25.77	3.79	2.3	3,b	<1.47E-16
8184	A	53.08716	-27.78490	18	9.33	2.14	22.31	5.26	0.66	1,a	4.15E-017
8240	A	53.08781	-27.89646	7	3.98	1.58	25.98	3.8	4.33	3,b	<1.32E-16
8413	A	53.09017	-27.84784	20	9.64	2.19	24.18	3.56	1.03	3,c	3.75E-017
8728	A	53.09443	-27.67175	8	2.6	1.9	24.9	4.46	1.35	3,c	<3.54E-16
8850	A	53.09608	-27.88041	15	9.11	1.51	25.1	3.86	0.02	3,d	<3.08E-16
8917	A	53.09674	-27.77237	26	9.33	1.93	24.73	3.51	0.6	2,b	<1.76E-16
9014	B	53.09825	-27.77718	5	2.21	2.14	24.22	3.63	0.42	1,f	<1.74E-16

Note. – (1): Identifier. (2): Quality grade. (3): Right ascension. (4): Declination. (5): Number of data points in the light curve. (6): Time baseline. (7): Concentration index. (8): Median magnitude in the F850LP filter. (9): Normalized MAD. (10): Redshift. (11): Method used to compute z (1: spectroscopy, 2: grism and 3: photometry), while the letter refers to the paper where the redshift obtained (a: Luo et al. (2017), b: Momcheva et al. (2016), c: Cardamone et al. (2011), d: Straatman et al. (2017), e: Xue et al. (2016), f: Taylor et al. (2009) and g: Wolf et al. (2008)). (12): Flux in the X-ray [0.5-8 keV] band. The '<' symbol represent the flux upper limit.

Table 3.4:: (Cont.)

ID	Grade	RA (J2000)	Dec (J2000)	N_p	T_{bas} (years)	CI (mag)	<F850LP> (mag)	MAD* (σ)	z	z Ref.	F_x [0.5-8 keV] (ergs cm^{-2} s^{-1})
(1)	(2)	(3)	(4)	(5)	(6)	(7)	(8)	(9)	(10)	(11)	(12)
9021	A	53.09840	-27.86258	7	9.08	1.62	25.68	4.47	1.12	3,b	<1.17E-16
9239	A	53.10137	-27.85917	6	9.08	1.56	25.74	4.51	0.9	3,b	<1.45E-16
9288	B	53.10213	-27.72846	5	2.26	1.74	25.25	3.79	1.08	1,f	<1.96E-16
9630	B	53.10628	-27.86994	5	2.25	1.92	25.11	4.82	1.33	3,d	<2.41E-16
9757	A	53.10780	-27.83883	32	9.64	2.25	23.57	3.54	1.09	1,a	3.75E-017
9764	A	53.10784	-27.72622	15	8.59	1.8	24.47	3.69	1.21	1,a	9.52E-017
10122	B	53.11194	-27.76271	8	8.86	1.98	25.17	5.34	1.3	1,d	<1.49E-16
10144	A	53.11215	-27.71111	12	8.59	2.27	23.79	11.2	1.6	2,b	<3.22E-16
10240	A	53.11330	-27.89131	26	9.11	1.89	24.62	3.56	2.19	2,b	<1.28E-16
10426	A	53.11540	-27.88511	5	3.72	1.52	25.9	4.16	1.29	3,b	<1.88E-16
10463	A	53.11578	-27.70676	11	8.59	1.43	25.19	4.67	0.12	3,d	<1.78E-16
10511	A	53.11638	-27.87660	14	9.32	2.21	22.52	5.78	0.38	1,a	<8.85E-17
10928	B	53.12174	-27.89144	24	9.11	2.23	24.24	4.92	1.03	3,d	<2.70E-16
11168	A	53.12448	-27.74021	10	2.52	2.31	19.55	5.51	0.07	1,a	6.95E-016
11213	A	53.12494	-27.73476	5	2.27	2.35	19.03	7.07	0.07	1,a	5.12E-016
12113	A	53.13448	-27.68765	11	2.66	2.1	24.69	4.32	0.96	2,b	3.61E-016
12311	B	53.13659	-27.68284	12	2.66	1.9	24.78	4.39	0.67	3,d	<4.09E-16
12361	A	53.13720	-27.84469	22	9.33	2.04	23.46	4.36	2.03	1,a	8.05E-017
12540	A	53.13916	-27.90047	26	9.12	1.93	24.34	5.03	1.33	2,b	<5.83E-17
12911	A	53.14316	-27.81556	28	8.73	1.91	24.85	3.91	4.14	1,b	<1.35E-16
12977	A	53.14385	-27.81352	52	8.73	2.28	21.11	4.02	0.2	3,b	<2.06E-16
13240	B	53.14633	-27.77111	8	2.29	2.21	24.73	3.88	1.31	1,d	<1.32E-16
13505	A	53.14860	-27.83498	7	8.47	1.96	25.09	3.74	0.06	3,b	<1.67E-16
13941	B	53.15214	-27.94796	12	3.91	2.24	21.29	3.74	0.12	1,c	<2.92E-16
14752	A	53.15884	-27.66252	12	2.55	1.18	20.49	3.59	0.84	1,a	4.63E-014
15280	A	53.16286	-27.76722	82	8.87	1.23	21.32	3.3	1.22	1,a	7.93E-015
15342	A	53.16340	-27.84283	13	8.85	1.57	24.98	3.89	0.13	3,b	<2.63E-16
15390	B	53.16373	-27.75912	94	8.86	1.98	24.37	4.82	1.03	3,d	<2.51E-16
15405	A	53.16386	-27.65959	8	2.54	1.71	25.25	5.68	1.1	3,b	<1.44E-15
16363	B	53.17179	-27.71713	5	2.28	1.75	25.3	4.68	1.28	3,b	<2.54E-16
16466	A	53.17258	-27.90738	11	2.5	1.51	26.41	4.3	0.08	3,b	<2.99E-16
16705	A	53.17438	-27.86740	13	9.12	1.23	22.37	4.33	3.61	1,a	5.74E-015
16721	A	53.17445	-27.73336	22	8.85	1.34	24.9	4.13	2.57	1,a	2.68E-015
17058	A	53.17742	-27.75976	10	7.29	1.62	26.14	4.19	2.51	3,b	<1.42E-16
17370	A	53.18014	-27.82066	15	8.86	1.3	22.82	13.33	1.92	1,a	9.28E-015
17472	B	53.18116	-27.76034	5	6.9	1.71	26.28	3.57	2.62	3,b	<1.20E-16
17999	A	53.18626	-27.87292	28	4.06	1.92	24.52	4.6	2.05	1,b	<1.17E-16
18125	A	53.18755	-27.91102	23	9.12	2.39	21.07	3.6	0.45	1,a	2.07E-016
18467	A	53.19124	-27.87216	14	9.12	2	24.21	4.23	0.98	2,b	<3.50E-16
18541	A	53.19188	-27.96988	6	2.73	1.61	24.79	5.96	0.21	3,c	<6.89E-16
18687	B	53.19341	-27.95913	6	0.85	1.96	22.05	4.29	0.65	3,c	<5.09E-16
19006	B	53.19706	-27.89010	16	9.12	1.99	24.67	3.92	1.29	2,b	<2.42E-16
19047	A	53.19754	-27.82945	6	2.69	1.55	25.67	3.55	0.24	3,b	<1.16E-16
19102	A	53.19828	-27.87916	12	9.13	1.25	25.61	4.32	1.04	3,b	<3.02E-16
19429	B	53.20216	-27.75500	5	8.6	1.9	25.3	3.8	2.19	3,d	<1.78E-16
19579	A	53.20396	-27.85437	21	9.12	2.16	24.33	6.32	1.37	2,b	<1.76E-16
19673	A	53.20503	-27.74339	12	8.57	2.24	21.95	3.76	0.21	1,a	1.71E-016
19762	B	53.20616	-27.89478	5	0.61	1.68	25.93	3.97	1.45	3,b	<5.02E-16
19976	A	53.20908	-27.77260	7	7.29	1.48	26.42	3.51	5	3,b	<1.43E-16
20057	A	53.21029	-27.90583	15	3.98	2.28	20.99	4	0.12	1,b	<3.90E-16
20076	A	53.21064	-27.81873	7	8.35	1.52	26.22	3.52	2.84	3,b	<4.87E-17
20085	A	53.21084	-27.73590	6	8.57	1.72	24.92	3.75	1.08	3,b	<2.36E-16
20190	A	53.21235	-27.90401	24	3.98	2.04	24.68	4.45	1.68	2,b	<3.47E-16
20698	A	53.22099	-27.94706	6	0.85	1.51	23.61	25.1	0.35	3,c	<4.47E-16
20760	B	53.22195	-27.91449	5	2.5	1.77	25.65	3.5	0.85	3,d	<2.57E-15
21288	A	53.23217	-27.77188	6	8.71	1.75	24.74	4.67	0.58	3,c	<2.16E-16
21541	A	53.23844	-27.87746	10	9.08	2.07	24.7	4.09	0.77	2,b	<3.49E-16
21733	A	53.24374	-27.82197	14	1.04	1.53	26.07	3.69	0.95	3,g	<2.07E-16
21944	B	53.24986	-27.85666	24	8.98	2.03	25.04	3.68	1.25	3,d	<2.74E-16
21983	B	53.25070	-27.86125	27	8.98	2.27	21.57	6.16	0.01	2,b	<5.51E-16
22884	A	53.28173	-27.85756	9	8.81	1.24	22.38	13.02	1.61	1,a	2.07E-014

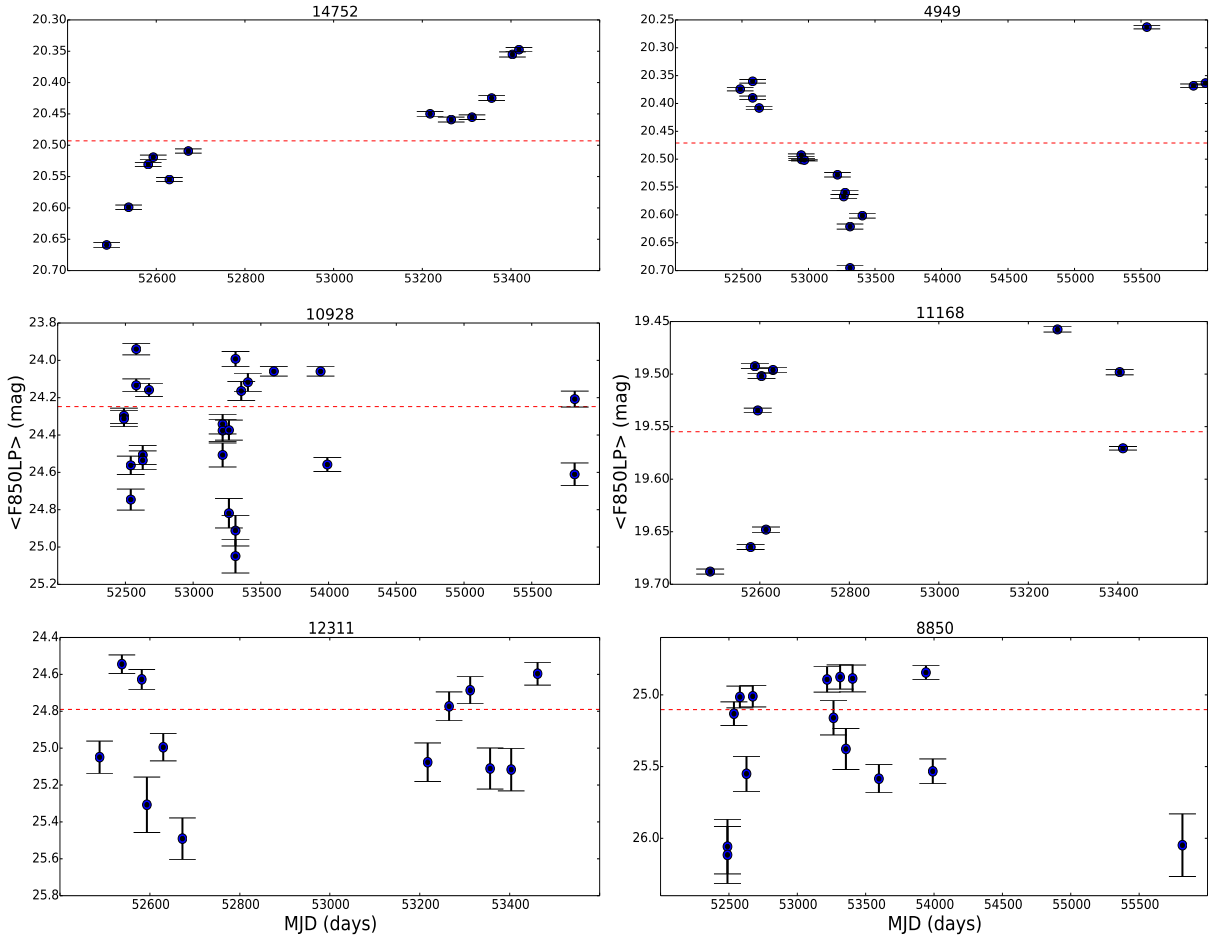

Figure 3.15: Example light curves of the AGN candidates. The dashed line indicates the median magnitude and the number on the top of each plot indicates the identifier of the source.

positional error of the X-ray sources reaches values of ∼1.8" that corresponds to high off-axis angles. The positional errors of our optically variable sources are less than 0.1". In order to check if the X-ray counterparts are the correct ones, we visually checked both optical and X-ray images. We excluded two X-ray counterparts that corresponded to neighbouring sources, resulting in a total of 26 AGN candidates with X-ray emission. The counterparts in the 7 Ms catalogue include all the sources from the lower depth catalogues, except for two sources detected in the 250 ks and 4 Ms catalogues. According to Luo et al. (2017), they do not exist in the 7 Ms catalogue, because they are variable sources or they are spurious detections resulting from background fluctuations or they did not pass the binomial no-source probability threshold used. The number of the X-ray counterparts is listed in Table 3.2 and increases with depth, as expected. All the variable point-like sources, except for two (ID: 2816 and

19102 with optical magnitude greater than 25 mag), have X-ray counterparts and also have been identified as QSOs or AGNs in other studies, including Villforth et al. (2010), Trevese et al. (2008) and Sarajedini et al. (2011). It is worth noting that four optically variable AGN candidates (ID 7270, 11168, 11213 & 19673) have been selected as X-ray variable sources in Young et al. (2012), while two out of those (ID 11168 & 11213) are present also in the variability-selected LLAGN catalogue of Ding et al. (2018).

A well-known diagnostic to identify AGNs is the F_X/F_{opt} diagram (Maccacaro et al. 1988; Barger et al. 2003; Hornschemeier et al. 2003), where F_X and F_{opt} are the X-ray and optical flux, respectively. The conventional AGN population lies in the area between $\log(F_X/F_{opt}) = \pm 1$, while spectroscopically confirmed AGN have been reported up to $\log(F_X/F_{opt}) = \pm 2$. The normal galaxies are expected to have $\log(F_X/F_{opt}) \leqslant -2$. In Figure 3.16, we plot the optical flux (F850LP) as a function of the X-ray (0.5-8 keV) flux of our optically variable AGNs compared with the normal galaxy (filled green squares) and AGN (open black squares) populations from Luo et al. (2017). The optically variable AGNs with X-ray detections (filled red circles) lie over the whole area within $F_X/F_{opt} = \pm 2$. We could be quite confident that sources with $F_X/F_{opt} > -1$ are AGNs, while between -2 and -1 their flux ratio is still consistent with AGNs, but their nature is confirmed by the combination of variability with X-ray emission.

The flux upper limits (open blue circles) are consistent with AGNs according to their F_X/F_{opt} ratio, though deeper X-ray images are needed to detect them. In particular, the majority of the flux upper limits lie below the average $F_X/F_{opt} = 0$ line, indicating that these AGNs are mostly X-ray weak. Concerning the sources that overlap with the normal galaxies, Luo et al. (2017) mentioned that a fraction of the normal galaxy population may also include LLAGNs. For the sources detected only in the soft or hard band, we transformed the fluxes into the [0.5-8 keV] band using the `WebPIMMS`[6] `v4.8d` software, assuming the photon index $\Gamma = 1.4$ and the Galactic HI column density $n_H = 10^{20}\mathrm{cm}^{-2}$. The same transformations were applied to the broad band $(0.5 - 7$ keV) of Luo et al. (2017).

To further understand the nature of these sources, we cross-matched our AGN candidates with the catalogue of Momcheva et al. (2016) to associate each source with the corresponding redshift of the host galaxy. Their catalogue provides the best redshift among grism, ground-based spectroscopic or photometric redshifts (Skelton et al. 2014). For the candidates with X-ray counterparts, we used the spectroscopic redshifts provided by Luo et al. (2017). The redshifts of some sources that did not

[6] https://heasarc.gsfc.nasa.gov/docs/software/tools/pimms.html

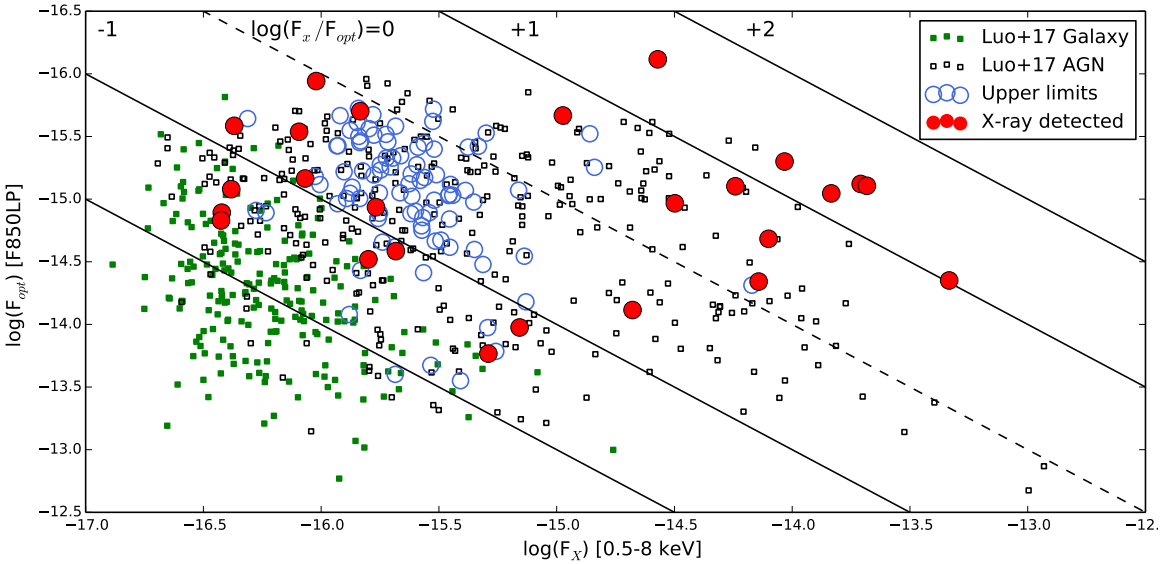

Figure 3.16: Broad (0.5-8 keV) X-ray vs. optical (<F850LP>) flux for the 26 AGN candidates with X-ray counterparts (red circles). Open blue circles represent those sources for which only upper limits were derived. The open black and filled green squares in the background represent the sources classified as AGN or normal galaxies in Luo et al. (2017), respectively. The dashed line indicates the $\log(F_{\rm X}/F_{\rm opt}) = 0$ and the solid lines from left to right correspond to $\log(F_X/F_{\rm opt}) = -2, -1, +1, +2$, respectively. The fluxes are given in units of ergs cm^{-2} s^{-1}.

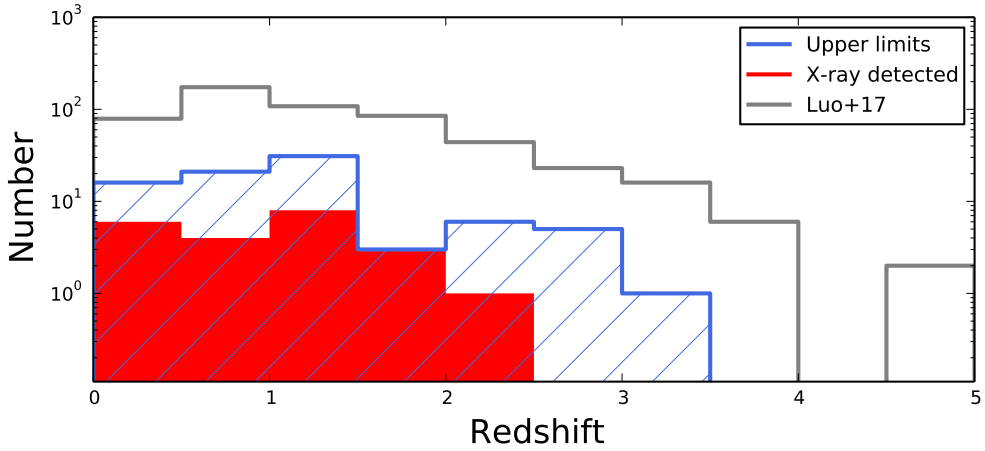

Figure 3.17: Redshift distribution for the candidate AGN with (filled red) and without (hatch-filled blue) X-ray counterparts. The grey histogram indicates all the X-ray sources with optical counterparts in GOODS-S.

have a match in the previous catalogues, were recovered from Straatman et al. (2017), Cardamone et al. (2011), Taylor et al. (2009) and Wolf et al. (2008). We found

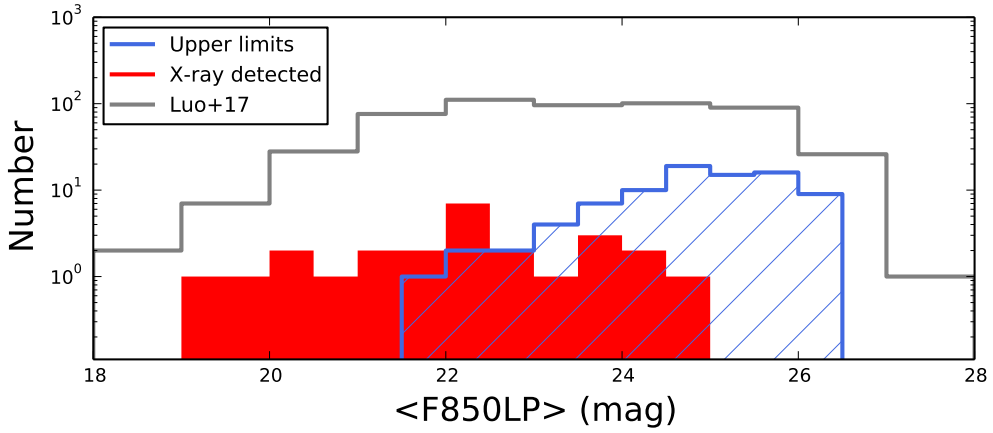

Figure 3.18: Median F850LP magnitude distribution for the candidate AGN with (red filled) and without (blue hatch-filled) X-ray counterparts. The grey histogram indicates all the X-ray sources with optical counterparts in GOODS-S.

published redshifts for all the variability-selected AGN candidates: 63 sources have photometric redshifts, while for the remaining 60 sources the redshifts were derived from spectra.

Even though the available spectra from Momcheva et al. (2016) and the other catalogues are capable to provide secure redshifts, the width of the lines is too noisy for the classification of our optically faint AGN sample (broad or narrow lines). The redshift distribution for the AGN candidates is presented in Figure 3.17 with the distribution of all the X-ray sample of the 7 Ms CDF-S catalogue that have an optical counterpart in GOODS-S for comparison. The AGNs with not yet detected X-ray emission extend to higher redshifts.

Figure 3.18 shows the magnitude distribution of the candidate AGNs and also the magnitude distribution of the X-ray sample reported in Luo et al. (2017) with an optical counterpart in GOODS-S (both AGNs and normal galaxies). It is very clear that the sample with X-ray upper limits is optically fainter than the AGN candidates with X-ray detections. The redshift and magnitude distributions suggest that the optical surveys, such as HST, may be able to identify faint high-redshift AGNs through variability. These AGNs would have been missed by current X-ray studies. Since faint nuclear emission can be observed in the optical, there are no obscuration at all or very weak obscuration effect by dust, thus these AGNs are likely LLAGNs. Their position in the $F_{\rm X}/F_{\rm opt}$ diagram suggests that these high-redshifted intrinsically X-ray weak AGNs lie below the conventional AGN population (around $F_{\rm X}/F_{\rm opt} = 0$), and thus, the dependence on redshift and X-ray flux should be considered when working with $F_{\rm X}/F_{\rm opt}$ diagrams.

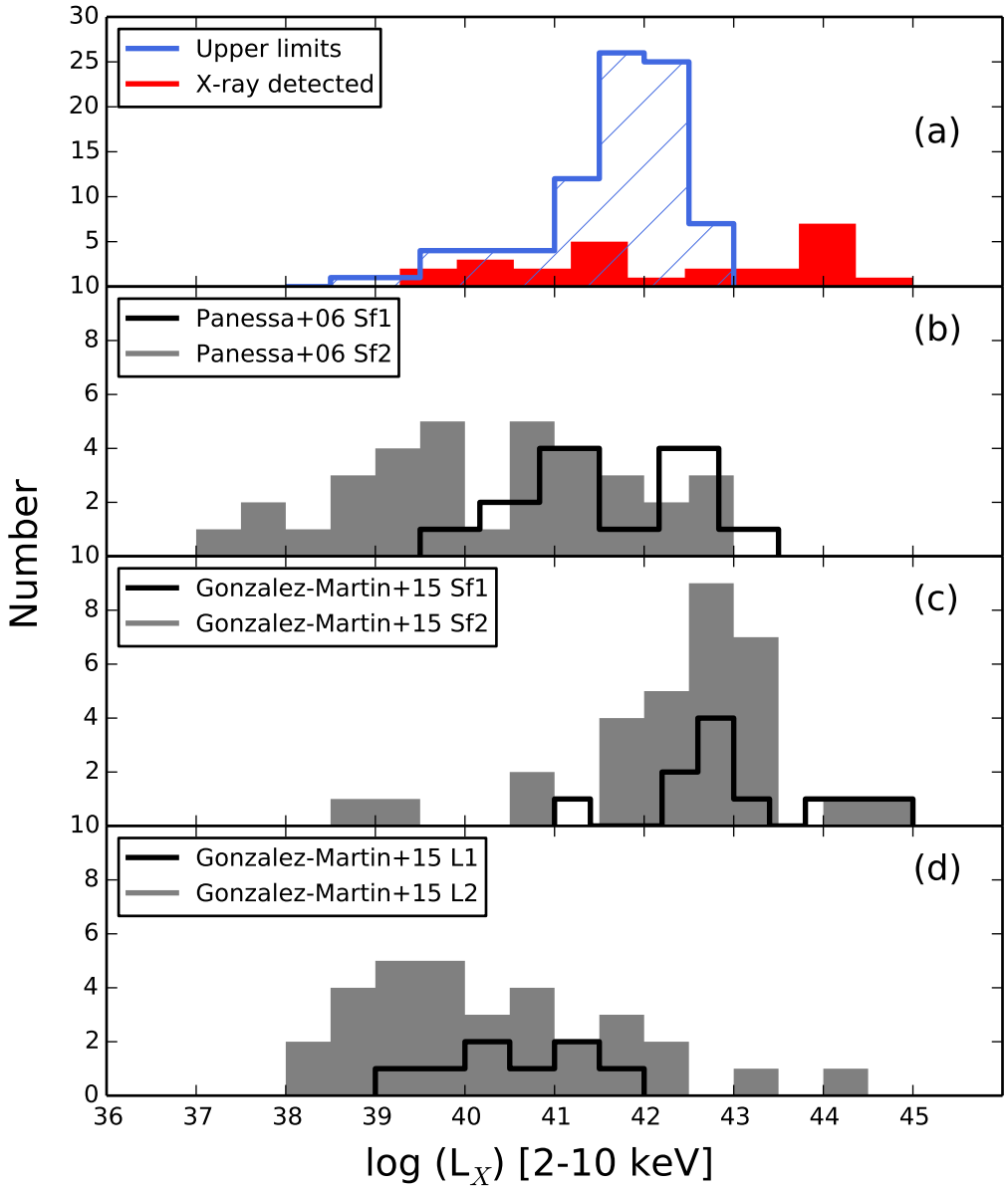

Figure 3.19: X-ray luminosities in the [2-10 keV] band (panel a) for the AGN candidates, with (red filled) and 3σ upper limits (blue hatch-filled) X-ray counterparts. In panel (b) the luminosity distributions of Seyfert galaxies are shown from Panessa et al. (2006). Panel (c) and (d) represent the galaxy population of Seyferts and LINERs derived from González-Martín et al. (2015). The black and shaded grey histograms indicate the type I and II, respectively.

We next estimated the X-ray luminosity [2-10 keV] of all the AGN candidates. We found the sample of variable sources with X-ray detections and upper limits

to be distributed over ∼5.5 and ∼4.5 orders of luminosity, from $10^{39.5}$ to 10^{45} ergs s^{-1} and $10^{38.5}$ to 10^{43} ergs s^{-1}, respectively, with mean values of 1.77×10^{42} and 4.57×10^{41} ergs^{-1} s^{-1}. In Figure 3.19, we compare our luminosity distribution with the distribution of different populations of AGNs located in the nearby universe (z∼0): Seyfert galaxies (Panessa et al. 2006) and LLAGNs (González-Martín et al. 2015) that include type I and II of LINERs and Seyferts. The luminosities of the AGN candidates detected here on the basis of optical variability lie within the range of the latter sub-classes of AGNs, denoting further evidence of AGN activity even at these low X-ray luminosities.

3.3.2 Mid-infrared selected AGN

In addition to studying their X-ray properties, we explore whether our optically variable AGN candidates show evidence of accretion onto a supermassive black hole via their infrared emission. The mid-IR emission from AGNs, in particular after the advent of sensitive spectrographs in space telescopes such as *ISO* and *Spitzer*, has proven extremely useful in revealing the presence of an AGN and characterising whether it is of type I or type II (Clavel et al. 2000; Verma et al. 2005; Weedman et al. 2005; Wu et al. 2009; Alonso-Herrero et al. 2016). It is now widely accepted that the AGN continuum emission appears as a power law from the 3 to 10 μm range, since the strong UV and X-ray radiation destroys the molecules responsible for the Polycyclic Aromatic Hydrocarbon (PAH) emission, while heating the surrounding dust particles in thermal equilibrium to near dust sublimation temperatures. The mid-IR AGN spectrum may also display absorption features with variable strength (due to astronomical silicates at 9.7 and 18μm) depending on the geometry of the obscuring dust as well as the luminosity of the active nucleus compared with the host galaxy (Nenkova et al. 2008a,b). Even when mid-IR spectra are not available, one may use mid-IR broad-band colours to trace this slope. A number of such diagnostics have been proposed using the IRAC instrument (Fazio et al. 2004) on board the *Spitzer* Space Telescope (Werner et al. 2004) which provided imaging at 3.6, 4.5, 5.8 and 8.0 μm for a large sample of galaxies. These include the "Lacy wedge" (Lacy et al. 2004, 2007; Sajina et al. 2005), the "Stern wedge" (Stern et al. 2005) and more recently the "Donley wedge" (Donley et al. 2007, 2012). Similar methods have also been proposed for sources observed with WISE (Stern et al. 2012; Assef et al. 2013; Mateos et al. 2012). We examine our candidates using the diagnostic of Donley et al. (2012), which has proven to be the most robust for a rather wide redshift range. The criteria by Lacy et al. (2007) are also used, for comparison.

We used the SIMPLE data mentioned in Section 3.1.2. This sample is photomet-

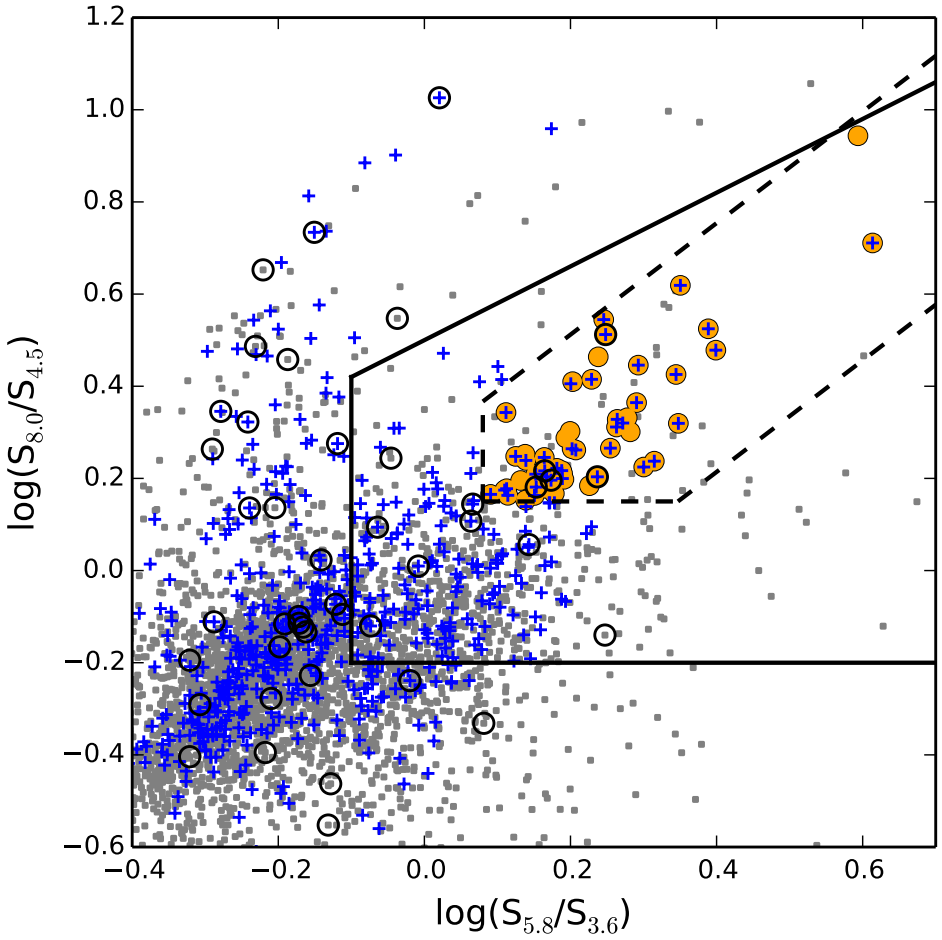

Figure 3.20: IRAC colour-colour diagram of the IR sample (gray points). The Lacy IR AGNs defined by the solid line. The Donley IR AGNs are those inside the dashed line and follow an IR power-law (filled orange circles). The optically variable and the X-ray selected AGN samples are represented by open circles and blue crosses, respectively.

rically complete at 5 μJy, where there is a turn-over in the number density plot of the fluxes in the [5.8] band. Furthermore, we restricted our analysis to 3,904 mid-IR sources (IR sample) that have detections at all four IRAC channels as well as an optical HST counterpart with five or more data points in the light curve identified by our survey. Out of the IR sample, there are 41 optically variable sources. Following the AGN selection criteria by Donley et al. (2012):

$x > 0.08$ and $y > 0.15$

$y > (1.21 * x) - 0.27$ and $y < (1.21 * x) + 0.27$

$f[4.5] > f[3.6]$ and $f[5.8] > f[4.5]$ and $f[8.0] > f[5.8]$,

where x=log(f[5.8]/f[3.6]), y=log(f[8.0]/f[4.5]) and f[band] is the flux of the corresponding band, we found 53 sources (hereafter, Donley IR AGNs). Out of those, 37 have X-ray counterparts, while five sources are optical variables. The latter five sources have also been detected in X-rays (in the 7Ms image) and are classified as QSOs in the literature. The optical variability can be explained by their QSO nature; i.e. direct view to the central source. At the same time the powerful AGN heats the dusty torus (seen face on) and its reprocessed emission dominates the infrared emission from the host galaxy.

Lacy et al. (2007) used a similar mid-IR colour-colour diagram with somewhat relaxed limits and without the power law condition:

$x > -0.1$ and $y > -0.2$

$y > (0.8 * x) - 0.5$.

Among the 770 sources that fulfill these criteria (hereafter, Lacy IR AGNs), there are 188 X-ray detections and 13 optically variable AGNs according to our analysis. The Lacy IR AGNs contains all 53 Donley IR AGNs. Figure 3.20 shows the IRAC 4-band colour-colour plot for the IR sample. The lines represent the wedges as defined in Lacy et al. (2007) and Donley et al. (2012). We also over-plotted the optically variable, Donley IR and the X-ray selected AGNs.

3.4 Discussion

3.4.1 Comparison with previous variability studies

We compared our variable sources with other variability studies of GOODS-S, including Villforth et al. (2010) and Sarajedini et al. (2011), who also searched for optical variability in this field. Out of the 88 variable sources reported by Villforth et al. (2010), 86 sources were included in our initial sample of 21,647 sources. Out of these, $\sim 8\%$ were identified as variable with our method. Similarly, out of the 42 variable sources of Sarajedini et al. (2011) in common with our initial sample, we recovered $\sim 17\%$. In a larger field of view, Trevese et al. (2008) found 132 variable sources, 23 of which lie in the area studied in this work and are included in our survey; we find eight sources to be variable in our catalogue. Regarding the sample of Falocco

et al. (2015), there is only one common source with our survey, which is classified as non-variable by our variability detection algorithm.

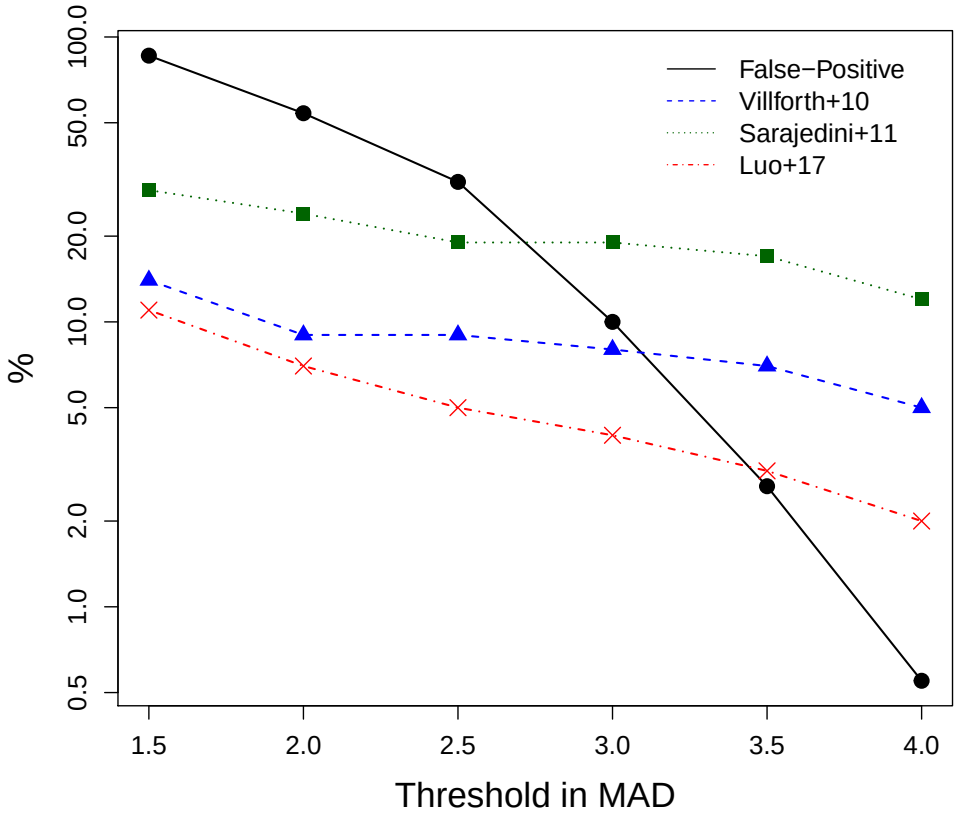

Figure 3.21: Percentage of false positive rate (black circles), recovery rate of variable sources identified by Villforth et al. (2010) (blue triangles) and Sarajedini et al. (2011) (green squares) and percentage of X-ray sources by Luo et al. (2017) (red crosses) identified as variables in this study as a function of different values of thresholds. The y-axis is in logarithmic scale.

The main differences between our study and the studies of Villforth et al. (2010) and Sarajedini et al. (2011) lie in the source detection algorithm and the larger amount of data. Our approach to identifying variable objects among a set of light curves is similar to the one used by Sarajedini et al. (2011) with two important modifications: 1) we used MAD as the measure of the light-curve scatter to filter out individual outliers and 2) we used the median instead of mean to determine the expected value of scatter in a given magnitude bin. Villforth et al. (2010) used C statistics that rely mostly on the estimated photometric uncertainties to select variables, while Sarajedini et al. (2011) used the classic standard deviation on V-band imaging data. Both

used a 3σ vs. a more secure threshold of 3.5σ employed in this work. In order to check the dependence of the recovery rate and the false-positive contamination by the adopted variability threshold, we calculated the recovery rate of both studies and also the percentage of the false positive rate out of the variable sources (as described in Section 3.2.2) for different values of the threshold. In Figure 3.21, we plot the results. By relaxing the threshold to lower values (MAD$\simeq$2.5), the recovery rate remains almost the same for both studies (1-2% difference), though the false positive rate rapidly increases. The threshold of 3.5 that we have adopted ensured that the false-positive contamination was kept below 5%.

The larger amount of data are due to the larger area included in this work, which doubled the number of sources, and the longer time baseline of the light curves. In particular, we used observations spanning up to ten years, instead of six months, increasing the number of points in the light curves, so we expect to detect new sources with higher sensitivity at longer timescales. Furthermore, the data reduction – source detection and photometry – differs from that employed in the previous studies. We used SExtractor, since it is better suited for detecting extended sources compared to IRAF. Moreover, we used images from the latest HLA data release, which is the first one to take into account the misalignments between both single exposures and filters[7]. Thus, the quality of the images used in this work and, consequently, the reliability of our photometry are supposed to be much higher than previous studies.

3.4.2 X-ray, mid-IR and optical variability selected AGNs

To facilitate a direct comparison and present the various selection methods in a uniform manner, we selected the Donley IR, Lacy IR and X-ray detected AGNs that lie inside the area of GOODS-S along with the optical variable AGN candidates. In Figure 5.14, we demonstrate the overlapping of the optical variability (113), Donley IR (53), Lacy IR (770) and X-ray selected (825) AGN samples with a Venn diagram.

The deepest available X-ray catalogue contains 825 sources in the area of GOODS-S. 621 sources have optical counterparts with five or more data points in their light curve, while 587 have both optical and IR detections. We found $\sim$3.5% of the X-ray sources having significant optical variability (Figure 3.21 shows also this percentage as a function of the variability threshold). On the other hand, among the 113 optical variable AGN candidates, 26 have X-ray counterparts ($\sim$23%). Optical variability could identify AGNs through a wide range of magnitudes and, especially, the AGN

[7] http://hla.stsci.edu/hla_faq.html

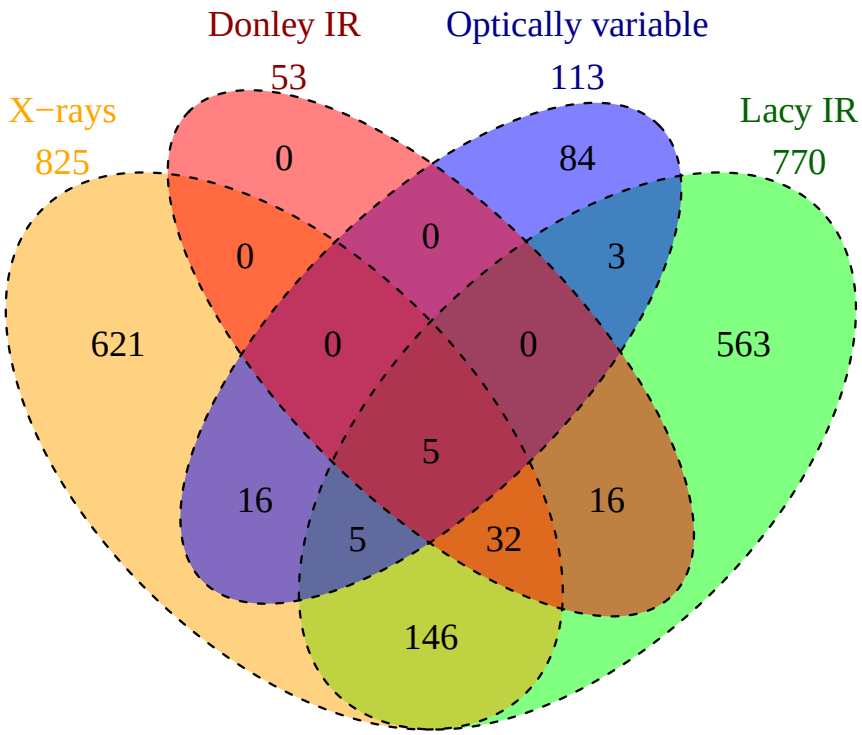

Figure 3.22: Venn diagram of the AGN samples selected through optical variability (blue), X-rays (orange), Donley et al. (2012) (red) and Lacy et al. (2007) (green) IR criteria.

population that is missed by X-rays (∼75%). This result comes from current X-ray survey depths. To visually demonstrate this dependence, in Figure 3.23 we show the fraction of variable sources that are X-ray detected in the four catalogues with various depths, divided into different magnitude bins. For the magnitude bins in the bright end, the fraction reaches values of about ∼70%, while at fainter magnitude bins there are no X-ray detections. Villforth et al. (2012) and Trevese et al. (2008) found similar results, while Sarajedini et al. (2011) had a higher rate of variable sources with X-ray detections. Out of the variable sample of Falocco et al. (2015), less than 10% had X-ray counterparts, and in the COSMOS field, De Cicco et al. (2015) reached a high percentage, up to ∼75%. However, their sample had a magnitude limit in the r band at $r \leq 23$ mag. Given the same limits in the magnitude, we derive almost the same completeness with respect to X-rays (Figure 3.23).

Furthermore, in this work we set a 3.5-σ cut-off in MAD to identify variables. Given a less conservative value of the cut-off, the percentage of X-ray detected sources in the variable sample increases. In particular, a 3-σ cut-off increases the X-ray de-

tected sources to 30%. However, at the same time the false positive variability rate also increases significantly. To avoid a high incidence of false variables, we necessarily miss a population of X-ray detected AGNs which display lower optical variability. Future surveys with higher sensitivities and better sampled data with longer time baselines will allow us to identify individually variable objects and fully characterize their variability properties without taking into account the whole population statistics. In that case, variability will be able to recover the X-ray detected AGN population with low significance (either low redshifted or high luminous AGNs).

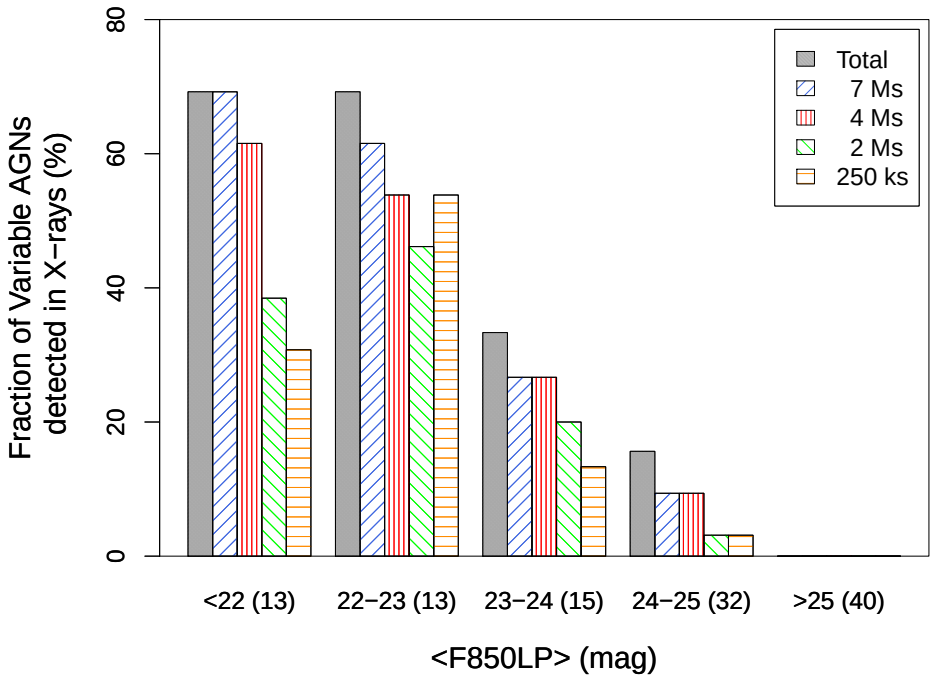

Figure 3.23: The fraction of AGNs selected through optical variability divided into five magnitude bins that are X-ray detected in catalogues of different depths. The number of optically variable AGNs in each bin are shown in the parentheses.

Regarding the IR selected AGNs, the Lacy et al. (2007) method selected a large number of AGN candidates through colour-colour criteria (770), comparable to that of X-ray AGNs. 25% of these are X-ray detected, while the majority of the X-ray sources fall outside the Lacy wedge (Fig. 3.20). Despite the large number of AGN candidates, the contamination of star-forming galaxies is expected to be as high as 80% (Donley et al. 2012), as the sensitivity limit of our IR sample is at 5 μJy. Donley et al. (2012) studied the star-forming contamination of the IR selected AGNs defined by Lacy et al. (2007) and Stern et al. (2005) for samples with different depths and

revised these criteria by adding an additional power law criterion. Thus, the Donley IR sample of 53 sources is expected to only have ∼10% contamination as stated by Donley et al. (2012). Out of those, 37 have X-ray emission (∼70%) and all of them are included in the Lacy IR sample. It is noteworthy to say that the Donley wedge contains sources that are selected by the Lacy et al. (2007) criteria, but fail the power law criterion of Donley et al. (2012). One third of the variable sample had detections at all four IRAC bands (41/113). The percentage of the variable sources common between the Donley and Lacy IR AGNs is ∼12% and ∼32%, respectively, while the majority of the variable sources fall outside both wedges (Figure 3.20) compared to previous ground-based variability studies (Falocco et al. 2016). This implies that the optical variability based on HST observations is capable to identify AGNs deep into the IR region where other selection methods fail.

It is obvious that different methods are at some level sensitive to different types of objects (different luminosities, different redshifts, different dust content along the line of sight, etc.). X-ray selection is by far the most robust technique resulting in a high number of AGNs. However, there is a large fraction of optically variables and IR selected AGNs that are not detected in X-rays. These sources are likely highly obscured or low-luminosity AGNs. The Lacy et al. (2007) diagnostic also returns a large sample of AGN candidates, but the contamination from star-forming galaxies is very high considering the depth of this study. At shallower depths, the contamination is minimized (Donley et al. 2012). On the other hand, the AGN sample selected by Donley et al. (2012) is highly complete and reliable having no contamination. However, it picks only a small sample of luminous, unobscured and obscured AGNs and misses the LLAGNs. Finally, optical variability returns a large sample of AGNs less obscured, moderate luminosity and redshift and is capable of identifying LLAGNs, which are missed by the other methods due to the currently survey depths.

Chapter 4

Hubble Catalogue of Variables: identification of AGN candidates in the CANDELS and Frontier Fields

As mentioned in the previous sections, an alternative method to identify AGN is through variability. The importance of the method was demonstrated in the previous section by its ability to identify low-luminosity AGN in the GOODS-field that even the deepest (currently available) X-ray observations would have missed. In order to search for AGN through variability, fields that have been observed multiple times are needed for the variability, but also observations with long exposure times for the AGN search. The HCV catalog contains many groups with deep observations obtained over multiple visits, making them appropriate for identifying variable AGN (spanning the range from the most luminous point-like quasars to the low-luminosity AGN). Such fields are the CANDELS and Frontier fields. CANDELS contains five deep fields that initially were observed with many filters that cover the whole electromagnetic spectrum to search for AGN. On the other hand, the Frontier Fields were observed to find galaxies in the early Universe and study the magnification due to clusters with high gravitational potentials. In this chapter, the HCV project will be presented with its main results along with the identification of AGN candidates in the aforementioned fields. Figure 4.1 shows the location of these fields in the sky.

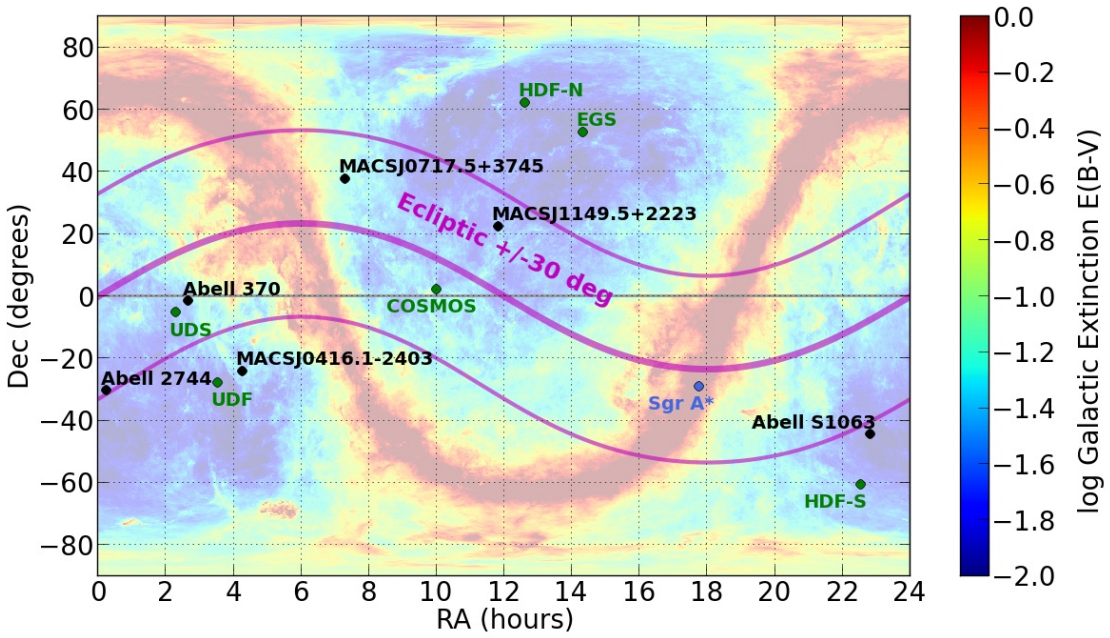

Figure 4.1: Location of the CANDELS and Frontier fields in the sky. The map is colour-coded with the Galactic extinction, e(B-V). Image credits: NASA/ESA.

4.1 Hubble catalogue of variables

The Hubble Catalogue of Variables (HCV) (Bonanos et al. 2019) was a 4-year project funded by the European Space Agency (ESA) based in the National Observatory of Athens in Greece and led by Dr. A. Z. Bonanos. It aimed to identify all the variable sources (point-like and extended) from the Hubble Space Catalogue (HSC, Lubow & Budavári 2013; Whitmore et al. 2016) using a magnitude depended thresholding in median absolute deviation. The HSC catalogue aims to optimize and enhance the scientific results of the Hubble Space Telescope (HST). This is done by combining all the HST visit-based source lists from the publicly available images in the Hubble Legacy Archive (HLA). The tens of thousands source lists that created using the SExtractor software (Bertin & Arnouts 1996b) were combine into one single master catalogue, the HSC. The HCV catalogue used the version 3 of the HSC that includes more than 500 millions detections that correspond to more than 100 million unique sources. All the HSC v.3 data were produced by the HLA data release 10 with observation up to October 2017 using the ACS, WFC3 and WFPC2 cameras on board HST. The area covered in these 23 years was approximately 40 square degrees (∼0.1% of the sky) and was observed with 108 filters from UV to IR regimes.

4.1.1 Data processing & Variability Analysis

The variability method relies on the assumption that the majority of the sources in a field are not variable, while a small fraction that stand out in the variability indices are considered as variables. Each field in the HSC catalogue and thus in the HCV catalogue is defined by the parameter GroupID that indicates a group of overlapping images. GroupIDs were used to gather all observations of the sources in a specific field. To have samples that are statistically complete, the HCV rejected fields that have less than 300 sources and sources with less than five data points in the light curve in a specific instrument and filter. In order to search for variability in the light curves, first it is necessary to have a clean sample of measurements. The HCV team before applying the variability algorithm created the pre-processing pipeline. The purpose of this was to remove the bad measurements and artifacts and correct for possible systematic effects. The first step of this procedure was to use the HSC flags to remove cosmic rays, diffused or saturated objects, diffraction spikes, other PSF features or to reject sources that are blended or suffer by the edge effect (Whitmore et al. 2016). Furthermore, a number of cut-offs were applied to assure the quality of the data. Such are a cut-off in the Concentration Index (CI<5.0), magnitude cuts (MagAper2<31.0 and MagAuto<35.0 mag) to avoid unphysical measurements and also cut in the photometric error (MagerrAper2<0.2 mag) to remove uncertain measurements. Next, the HCV team instead of using the classic photometric errors that may be underestimated (but not overestimated), computed a synthetic error to evaluate each of the measurements within a light curve. The synthetic error takes into account the concentration index, the difference between the circular MagAper2 and elliptical MagAuto apertures, the photometric error MagerrAper2 and the offset distance D that it is an indicator of the misalignment between images. This synthetic error in addition to outlier rejection processes (e.g. outlier of linear fit) managed to remove the majority of bad measurements. The final step of the HCV pre-processing was to compute the local (within a radius of 20") zero-point corrections to remove all the photometric zero-point variations. Before the variability algorithm, the HCV team constructed the light curves of all the sources in each field with accurate and reliable magnitudes and errors

As mentioned in the previous chapter, there are two methods to quantify the variability of a source: the scatter-based indices and those that quantify the smoothness of a light curve. Sokolovsky et al. (2017) compared and tested in total 18 variability indices in different data sets from ground-based observations, while they used simulated data to test the performance of the indices in light curves with different number of data points. Additional tests and simulations were performed in Bonanos et al. (2019) and Pouliasis et al. (2019), specifically for the HSC data. According

to these results, the HCV catalogue was based on the Median Absolute Deviation (MAD) variability index. A cut-off of 5σ was used in MAD and sources above this were considered as variable. Moreover, a complementary threshold in χ^2 statistics (3σ) was applied to reject sources with high photometric errors.

4.1.2 Validation algorithm

The evaluation the variable sources selected by the aforementioned process, and consequently the verification of the variability algorithm, the HCV team followed two procedures. The first one was directly output of the data processing pipeline through a validation algorithm, while the other method was the expert validation, a visually inspection of the quality of the candidate variables. The validation algorithm using several criteria assigned to each source a variability quality flag. The latter consists of five letters, each one corresponding to different quality criteria, and could be A for high, B for medium and C for low quality. The criteria used were: a) the concentration index, b) the difference MagAper2-MagAuto, c) the photometric error, d) the offset distance, D, and e) the peak-to-peak value. For a specific source, the quality flag depends on the deviation of these parameters from the average of the whole population in the field. Furthermore, except the quality flags, the validation algorithm classified the sources as single-filter variable candidates (SFVC) or multi-filter variable candidates (MFVC) depending on the number of filters the source stood out as variable. The SFVC may include both sources that have been observed only in one filter and also sources that may have observations in other filters too but appear not variable. Thus, the MFVC are considered as more reliable than the SFVC.

Concerning the expert validation, "expert" users evaluated individually the variable selected sources. They used the expert validation interface that was designed for this purpose. This software actually creates diagrams, such as the MAD versus the magnitude for the entire group or other parameters (D and CI) as a function of time. Moreover, the cut-out images for the sources were available in order to visually inspect the quality of the data. All the MFVC were evaluated by the experts, while due to the time constraints of the project and the large number of sources, the SFVC were evaluated for random fields. This expert validation quality flag could be: "0" if the variable candidate is not validated by the expert, "1" for the high confidence variables, "2" for the probable variable sources and "4" for possible artifacts. The majority of the rejected sources were mainly sources near bright stars or their diffraction spikes, diffuse sources with misalignment issues or blended objects.

4.1.3 HCV main results

In total, out of 15,160 GroupID's included in the HSC v.3 catalogue, 250 GroupdID's passed the HCV data processing pipeline. These consist of ∼3.7 million sources out of the initial 108 millions. The HCV identified 84,428 variable candidates (2.3% of the sources passed the selection criteria). 73,317 (87% of the total) variable sources were selected through a single filter, while the rest 11,115 (13% of the total) sources stood out as variables in more than one filters (multi-filter variables). In order to test the reliability of the HCV catalogue, the expert validation was applied in 16% of the total variable candidates, in almost half of the multi-filter and in 11% of the single-filter variable sources. The expert validation resulted in 40% high-confidence variables, 41% probable variables and 19% possible artifacts with much higher values concerning the multi-filter variable sources. Thus, the reliability (true variable sources) for the whole HCV catalogue is expected to be 81% for both single- and multi-filter variable candidates. Specifically, the percentage increases up to 84% for the multi-filter variables. The number of data points in the light-curves depends on the GroupID's and the different filters and may vary from 5-120 data-points, while the time baseline of the observations could be less than a day up to 15 years in some cases. The depth of the HSC catalogue compared to ground-based telescopes and its high number of sources make the HCV catalogue one of the largest databases of variable sources with magnitudes reaching 27 mag in the V filter. The release date of the HCV catalogue was in September 24th of 2019, and the HCV is available through the ESA Hubble Science Archive (eHST) at ESAC and MAST at STScI, while the data can be explored easily using the HCV Explorer, a visualization tool. The detailed description of the pre-processing analysis, the validation of the variable sources and the HCV results are presented in Bonanos et al. (2019).

4.2 Results

4.2.1 CANDELS fields

Variability is a basic characteristic of AGN at all wavelengths, appearing over periods of hours to years (Ulrich et al. 1997). Optical variability has therefore been used as a method to identify AGN (Pouliasis et al. 2019; Sarajedini et al. 2011; Villforth et al. 2010, 2012; De Cicco et al. 2015; Falocco et al. 2016); the importance of the method is demonstrated by its ability to identify low-luminosity AGN that even the deepest (currently available) X-ray observations would have missed. The HCV catalog contains many groups with deep observations obtained over multiple visits, making

them appropriate for identifying variable AGN (spanning the range from the most luminous point-like quasars to the low-luminosity AGN). Here, we demonstrate the power of the HCV catalog in the "Cosmic Assembly Near-IR Deep Extragalactic Legacy Survey" fields (CANDELS; Koekemoer et al. 2011; Grogin et al. 2011). The HCV catalog contains 621 variable candidates (179 MFVCs and 442 SFVCs) in the five CANDELS fields (GOODS South, GOODS North, COSMOS, EGS, and UDS). Following the expert validation of the sources, we excluded the sources classified as "possible artifacts", resulting in 171 variable candidates.

We cross-matched our variable sources with the SIMBAD database (using a radius of 1") to validate their nature. Table 4.1 presents the results for the different fields. Excluding the stellar population, 75% and ∼45% of the "high-confidence" and "probable" variable sources, respectively, are confirmed AGN or quasars. Regarding the rest of the sources showing variability, but which are classified as 'normal' galaxies in SIMBAD and do not show any X-ray emission, the aforementioned studies have shown that these extended sources are consistent with low-luminosity AGN (LLAGN), which would have been missed by the current depths of X-ray surveys, but are important to complete the AGN demographics. In Figure 4.2, we present three example light curves of variable sources in the CANDELS fields that are classified via spectroscopy as AGN or quasars. `MatchID`=45511920 is reported to be variable for the first time. We thus demonstrate the photometric quality of extended sources and, in particular, variable AGN in the HCV catalog.

Table 4.1:: HCV variables in the CANDELS fields.

Item	GOODS-N 1084534	GOODS-S 1084533	COSMOS 1081922	EGS 1045196	UDS 1036556	Total
Pipeline class. MFVCs/SFVCs	75/143 (218)	90/164 (254)	2/52 (54)	10/50 (60)	2/33 (35)	179/442 (621)
Expert validated MFVCs/SFVCs	58/- (58)	28/17 (45)	2/- (2)	6/31 (37)	-/28 (28)	95/76 (171)
AGN / Seyfert 1 / Seyfert 2	11	13	-	16	-	40
Quasars	11	10	-	3	2	26
Stars	19	10	1	-	-	30
Normal galaxies (LLAGN)	18	10	1	6	13	48
Total classified sources (SIMBAD)	59	43	2	25	15	144

Note. – `GroupIDs` are listed under the field name. Numbers in parentheses indicate the total number of both MFVCs and SFVCs.

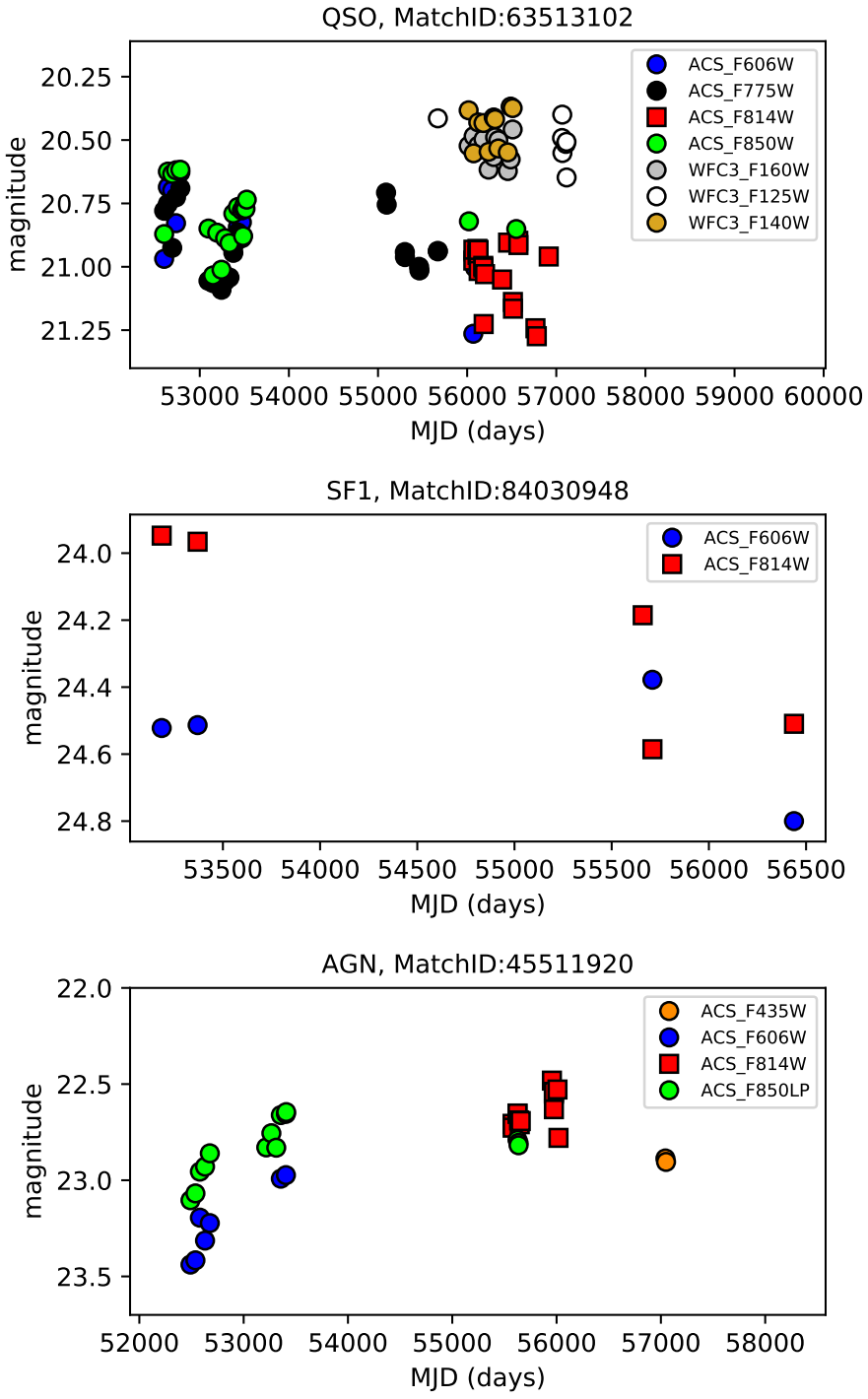

Figure 4.2: Examples of three variable sources in the CANDELS fields: a quasar in GOODS-North (*upper panel*), a Seyfert-1 in GOODS-South (*middle panel*), and a new variable AGN in EGS (*lower panel*).

4.2.2 Frontier Fields

The Hubble Frontier Fields consist of six deep fields centered in very strong lensing galaxy clusters and six parallel fields that are located near the cluster fields. The clusters that have been drown from the cluster catalogues of Abell et al. (1989) and Ebeling et al. (2001) are the Abell 370, Abell 2744, Abell s1063, MACSJ0416.1-2403, MACSJ0717.5+3746 and MACSJ1149.5+2223. Table 4.2 presents the the basic observational properties of the fields and the number of the HCV sources in each.

4.2.2.1 HCV variable sources

The HCV[1] explorer was used to retrieve all the variable sources in the Frontier Fields. The catalogues of the variable sources include information of the number of filters they stand out, number of data points in the light curves, mean magnitudes derived from the HCV and also the HSC catalogue and the variability indices used (MAD and χ^2). Furthermore, it includes a column with the expert validation flag as described in the previous section. By selecting all the variable sources except those with flag=4, we ended up with a clean sample of variable sources. Figure refmad1 shows the distribution of MAD as a function of magnitude for the Abell 2744 cluster field. The corresponding diagrams for all the cluster and parallel fields are presented in Appendix A. In the HSC catalogue and consequently in the HCV catalogue, the cluster and parallel fields are treated as separated GroupIDs. Exceptions to this are the MACS 0717 and MACS 1149, where the cluster and parallel fields are treated as one single GroupID.

4.2.2.2 AGN candidates

Following similar procedure as in Chapter 3, the identification of the AGN candidates is based on the extension and the variability of the sources. The extended and variable sources indicate AGN activity, since normal galaxies (extended) are not expected to be variable. On the other hand, quasars could be selected from the point-like variable sources after removing the stellar or the SNe populations. In order to separate the point-like and the extended sources, the concentration index was used as defined in Chapter 3. High values of the CI correspond to extended sources, while low values to point-like sources. For example, we present in Figure 4.4 the CI distribution for the GroupID 66095 (MACS 1149) derived from the filter ACS_F814W. The separation

[1] http://hst.esac.esa.int/hcv-explorer/

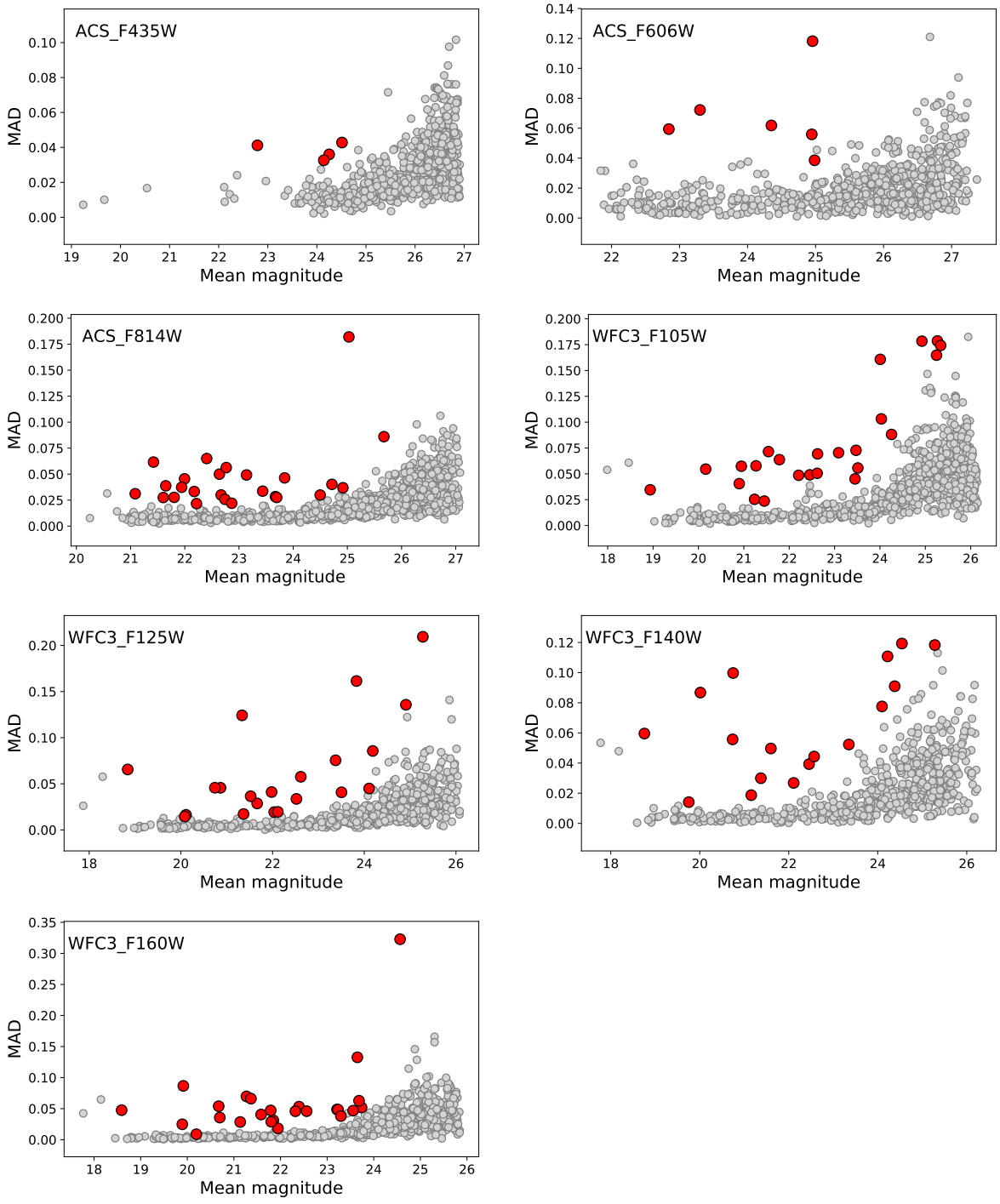

Figure 4.3: The MAD as a function of the mean magnitude for different filters as indicated in ABELL 2744 cluster field. All the sources in the field are shown with grey small circles, while the HCV variable sources are shown with red circles.

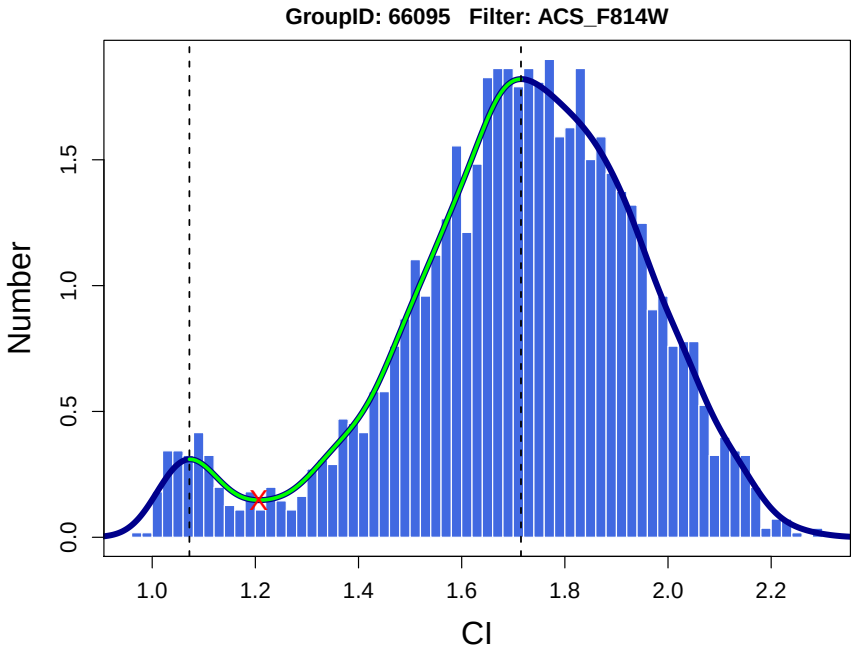

Figure 4.4: The concentration index distribution. The dashed vertical lines indicate the peaks of the two well separated point-like and extended distributions, while the red cross shows the separation point between them.

point (red cross) was defined as the minimum point (red cross) between the peaks (dashed lines) of the two well-defined distributions of the point-like and extended sources. Since the different filters may have slightly different CI separation points, the latter were derived from the filters that have the highest number of sources in the field. In total, there are 463 variable candidates in all the fields (Table 4.2). The average number of variables in the parallel fields is 20.6 variables per field (18-28), while for the cluster fields the average increases to 56.5 variables per field (29-75). Out of 463 variable candidates, 302 (65%) are extended sources and are expected to AGN candidates. For the point-like sources, further diagnostic criteria are required in order to separate the QSOs from the stellar population or SNe. All the variable sources (extended and point-like) from all the cluster and parallel fields are listed in the Appendix A.

4.2.2.3 Infrared selected AGN

For three of the cluster fields (Abell 370, Abell s1063 and Abell 2744), there are infrared broad-band photometric data from the Spitzer/IRAC camera in all four

Table 4.2:: HCV variables in the Frontier Fields.

HCV/HSC GroupID	Name	RA (h m s)	Dec (h m s)	$N_{sources}$	$N_{variables}$	$N_{extended}$	$N_{point\text{-}like}$
62353	MACS 0717 clu	07 17 34.00	+37 44 49.00	2,162	61 (2.82%)	32 (9/23)	29 (20/9)
62353	MACS 0717 par	07 17 32.63	+37 44 59.70	1,460	24 (1.64%)	6 (3/3)	18 (16/2)
66095	MACS 1149 clu	11 49 35.43	+22 23 44.63	2,137	29 (1.35%)	16 (9/7)	13 (5/8)
66095	MACS 1149 par	11 49 40.46	+22 18 01.53	1,494	20 (1.38%)	9 (6/3)	11 (10/1)
1042781	MACS 0416 clu	04 16 8.38	-24 04 20.80	1,830	75 (4.10%)	58 (39/19)	17 (8/9)
1040153	MACS 0416 par	04 16 33.40	-24 06 49.10	1,404	18 (1.28%)	18 (8/10)	–
1033838	Abell 370 clu	02 39 52.80	-01 34 36.00	2,053	66 (3.22%)	58 (30/28)	8 (2/6)
1083558	Abell 370 par	02 40 13.51	-01 37 34.00	1,455	18 (1.24%)	12 (3/9)	6 (1/5)
1043761	Abell 2744 clu	00 14 21.20	-30 23 50.10	1,688	45 (2.67%)	32 (27/5)	13 (8/5)
1042688	Abell 2744 par	00 13 53.27	-30 22 47.80	1,495	16 (1.07%)	7 (6/1)	9 (5/4)
1042675	Abell s1063 clu	22 48 44.30	-44 31 48.40	1,768	63 (3.56%)	42 (24/18)	21 (11/10)
1075304	Abell s1063 par	22 49 17.80	-44 32 43.30	1,434	28 (1.95%)	12 (10/2)	16 (7/9)
Total:				463		302 (174/128)	161 (93/68)

Note. – `GroupIDs` are listed under the field name. Numbers in parentheses indicate the total number of both MFVCs and SFVCs.

bands (3.6, 4.5, 5.8 and 8.0 μm). Thus, the diagnostics of Donley et al. (2012) and Lacy et al. (2007) were used to explore whether the optically variable AGN candidates show evidence of AGN activity in the mid-IR wavelengths and also to identify new AGN. The data were taken from the HFF-DeepSpace photometric catalogues (Shipley et al. 2018). These catalogues include photometric data from UV to mid-IR regime when available for all the cluster and parallel fields. Before applying the IR AGN criteria, first we restricted our analysis to mid-IR sources that have detections at all four IRAC channels and also signal-to-noise ratio higher than three (SNR>3). Furthermore, we used the flags by Shipley et al. (2018) to exclude bad photometric data. We then cross-matched these catalogues with the HCV data with five or more data points in the light curve identified by our survey. Below, we describe the results for each of these three clusters:

Abell 370: Out of the IR sample (6,798), there are 1630 HCV sources with more than five data points in their light curves. Applying SNR cut-offs and following the AGN selection criteria by Donley et al. (2012), we found 10 sources (hereafter, Donley IR AGNs). Out of those, one source is optically variable. Lacy et al. (2007) used a similar mid-IR colour-colour diagram with somewhat relaxed limits and without the power law condition. Among the 81 sources that fulfill these criteria (hereafter, Lacy IR AGNs), three are optically variable AGNs according to our analysis. The Lacy IR AGNs contains all Donley IR AGNs. Figure 4.5 shows the IRAC 4-band colour-colour plot of the IR sample. The lines represent the wedges as defined in Lacy et al. (2007) and Donley et al. (2012). We also over-plotted the optically variable sources.

Abell 2744: The HFF-DeepSpace catalogue consists of 9,390 sources in this cluster field. By cross-matching with the HCV sources, there are 1,535 sources with both IRAC and HST data with at least five data points in the light curves. Requiring, though detections at all four IRAC bands with high SNR, the remaining sources are 339 and 215, respectively. Among the 215 sources, there are only 6 out of all the 45 variable AGN candidates. In Figure 4.6, we plot the 4-band colour-colour diagram with the IR AGN criteria by Donley et al. (2012) and Lacy et al. (2007). The number of sources selected as AGN by the latter criteria is 10 and 73, respectively. The sources inside the wedge defined by Donley et al. (2012) are 36, but only ten (squares) following also the power-law. Three of the six variable sources (blue circles) are found inside the Lacy wedge and one of them also in Donley wedge. The rest sources lie outside the wedges having bluer colours.

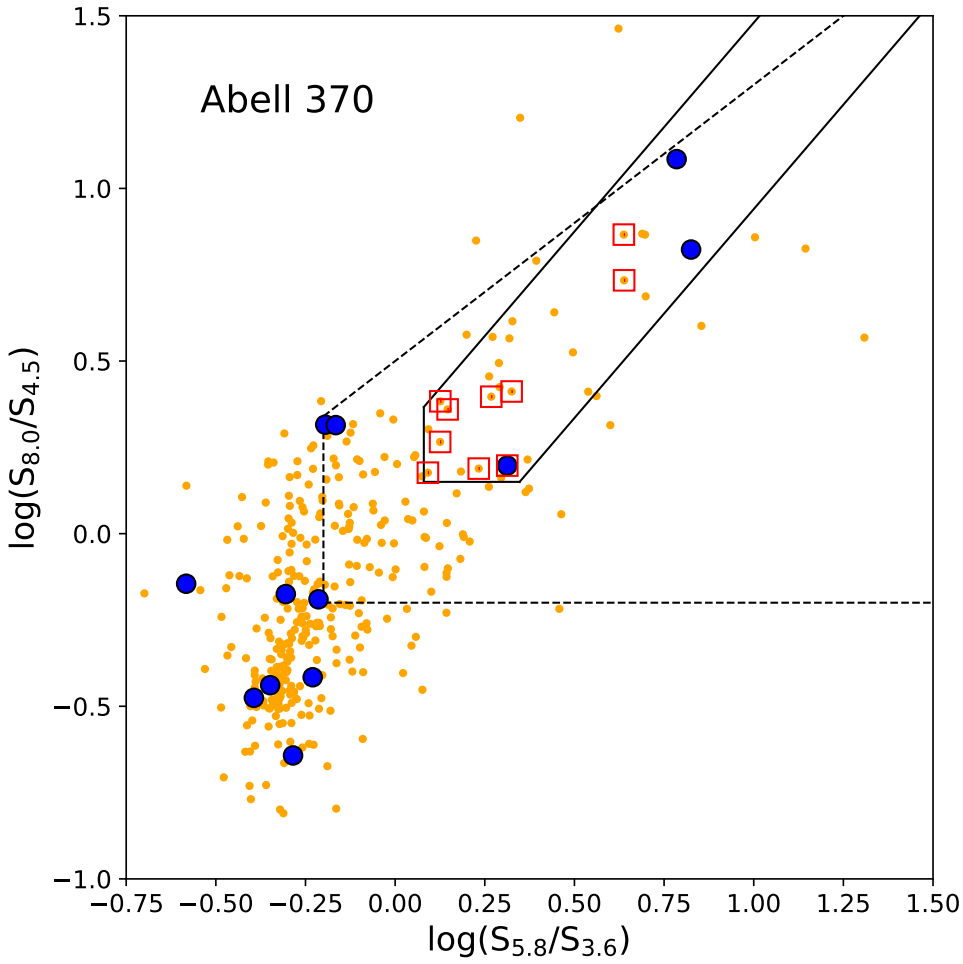

Figure 4.5: IRAC colour-colour diagram of the IR sample (orange points) in Abell 370 cluster field. The Lacy and Donley IR AGN are defined by the dashed and solid lines, respectively. The HCV optically variable AGN are represented by blue circles, while the Donley IR sources following a power-law are indicated with open squares.

Abell s1063: This cluster contains 7,611 sources in Shipley et al. (2018). Applying the SNR cut-offs, there are 178 sources with high statistical significance. Out of the 1,630 sources in the HCV catalogue, 131 have IR counterparts. The IR selection criteria of Lacy et al. (2007) and Donley et al. (2012) suggest 69 and 10 AGN candidates, respectively (Fig. 4.7). Among the nine variable HCV sources, two fall inside the Lacy edge, while the rest show no IR excess.

Regarding the IR selected AGNs, the Lacy et al. (2007) method selected a large number of AGN candidates through colour-colour criteria (223) in the three cluster

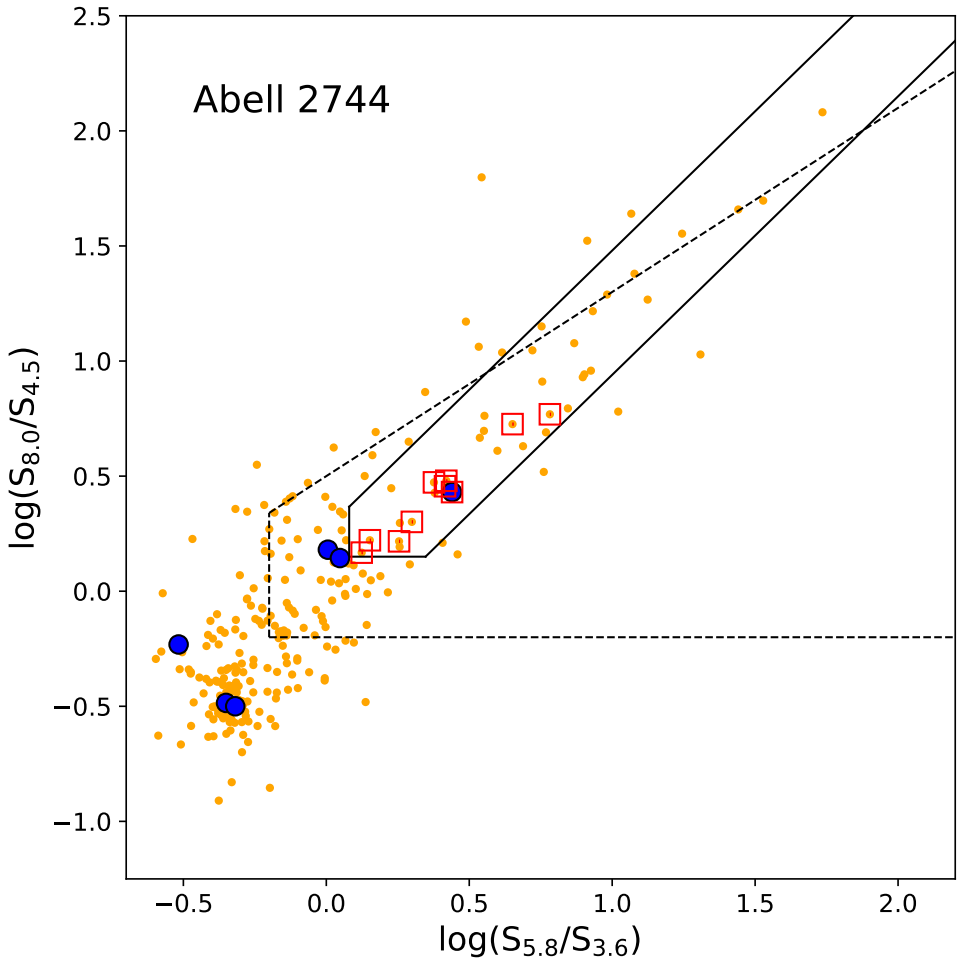

Figure 4.6: IRAC colour-colour diagram of the IR sample (orange points) in Abell 2744 cluster field. The Lacy and Donley IR AGN are defined by the dashed and solid lines, respectively. The HCV optically variable AGN are represented by blue circles, while the Donley IR sources following a power-law are indicated with open squares.

fields. Despite the large number of AGN candidates, the contamination of star-forming galaxies is expected to be as high as 80% (Donley et al. 2012), as the sensitivity limit of this IR sample is less than 5 μJy. Donley et al. (2012) studied the star-forming contamination of the IR selected AGNs defined by Lacy et al. (2007) and Stern et al. (2005) for samples with different depths and revised these criteria by adding an additional power law criterion. Thus, the Donley IR sample of 30 sources is expected to only have ∼10% contamination as stated by Donley et al. (2012). From the HCV variable sample, only a small percentage had detection at all four IRAC bands. The majority of those fall outside both wedges compared to previous

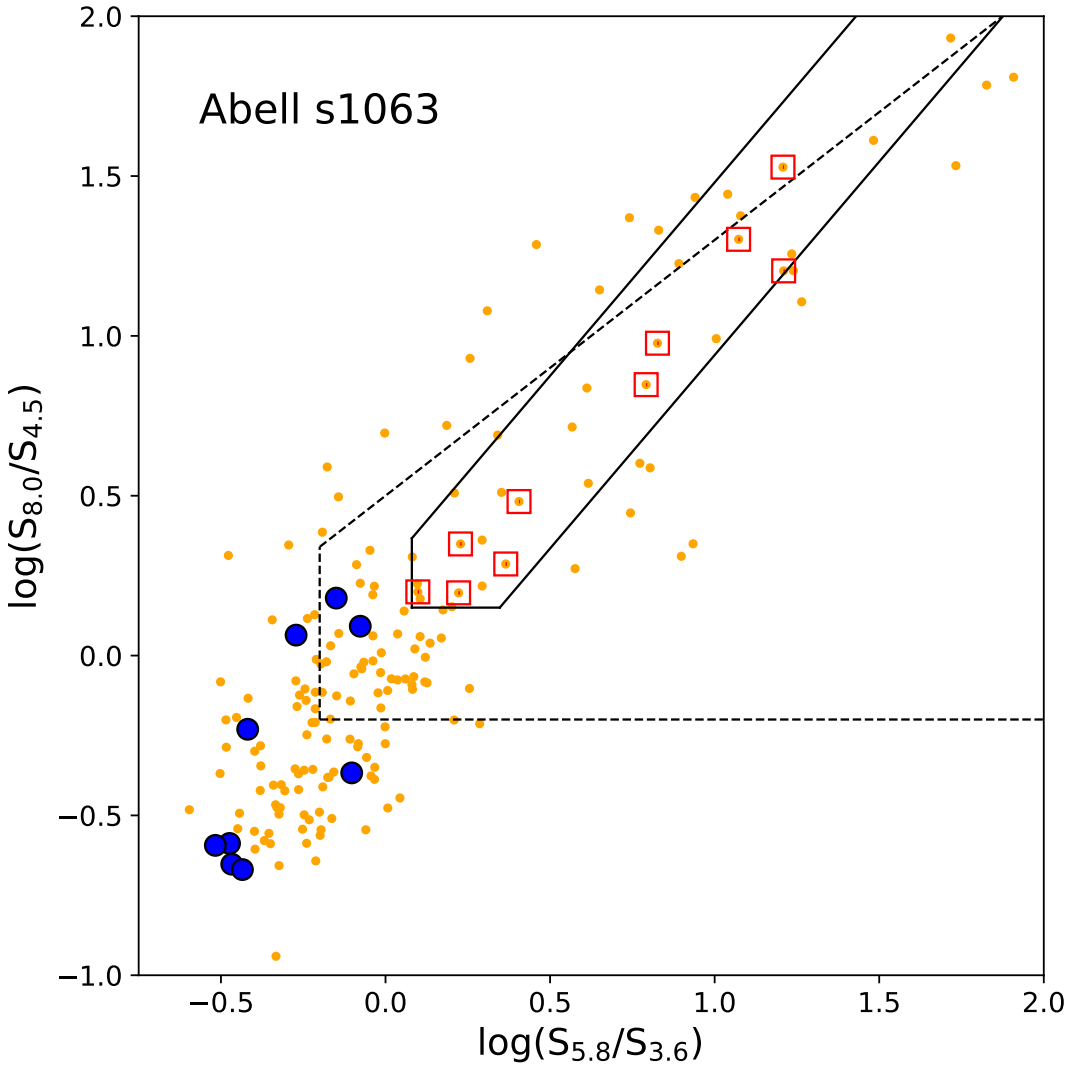

Figure 4.7: IRAC colour-colour diagram of the IR sample (orange points) in Abell s1063 cluster field. The Lacy and Donley IR AGN are defined by the dashed and solid lines, respectively. The HCV optically variable AGN are represented by blue circles, while the Donley IR sources following a power-law are indicated with open squares.

ground-based variability studies (Falocco et al. 2016). This implies that the optical variability based on HST observations is capable to identify AGNs deep into the IR region where other selection methods fail.

Chapter 5

An obscured AGN population hidden in the VIPERS field: identification through SED decomposition

To investigate any parallel evolution between galaxies and AGN, as well as to examine whether and how AGN feedback affects the evolution of galaxies, observations in infrared (IR), optical wavelengths and X-rays are required (Hopkins et al. 2006; Bower et al. 2006). The properties of galaxies hosting a black hole can be studied using optical and near-IR observations, while the absorbed AGN properties can be investigated in both X-rays and mid-IR regime (Hickox & Alexander 2018, and references therein). When the radiation of AGN dominates, X-ray emission is capable of penetrating large amounts of dust and gas without being absorbed. Consequently, X-rays are one of the most efficient methods of detecting AGNs nearly independent of obscuration (Luo et al. 2008). However, even hard X-rays can be obscured in the presence of huge amounts of dust and gas (Gilli et al. 2007; Fiore et al. 2008; Treister et al. 2009; Akylas et al. 2012).

Mid-IR selection techniques offer a powerful tool to separate AGNs from stars and galaxies. This is achieved by separating the (approximately) power law AGN spectrum from the black body stellar spectrum of galaxies. Thus, another way of detecting AGNs is through mid-IR observations, which has the advantage of being affected less by extinction. Mid-IR broad-band colour selection criteria have been proven extremely useful in revealing the presence of an AGN (Lacy et al. 2007; Stern et al. 2012; Mateos et al. 2012; Donley et al. 2012; Assef et al. 2013) based on obser-

vations made by the *Wide-field Infrared Survey Explorer* (*WISE*; Wright et al. 2010) and the *Spitzer* Space telescope (Werner et al. 2004). Furthermore, many studies used the IR selection criteria in combination with X-ray or optical photometric and spectroscopic data to uncover absorbed AGN (e.g. Rovilos et al. 2014; Hainline et al. 2014; Assef et al. 2015; Hviding et al. 2018; Glikman et al. 2019). However, IR selection techniques are biased against low-luminosity AGNs (Barmby et al. 2006; Georgantopoulos et al. 2008). SED decomposition can alleviate this problem by utilizing large wavelength range and properly disentangle accretion from star formation (e.g. Ciesla et al. 2015). SED decomposition can therefore provide a complementary tool to the X-ray and IR selection techniques, revealing weaker AGN systems with lower luminosities by reliably quantifying the host galaxy contribution to mid-IR colours.

This work focuses on selecting AGNs through SED modelling and fitting techniques in a sample of galaxies from the VIPERS survey (Guzzo, L. et al. 2014; Garilli, B. et al. 2014). We aim to find an AGN population with intermediate/high obscuration, which would be missed from current X-ray surveys and simple mid-IR colour cuts. The optical, near-IR and mid-IR data used for the SEDs along with ancillary data (spectroscopic data, X-ray catalogues, etc.) are presented in Section 5.1, while in Section 5.2, we describe the methods we used to construct and model the SEDs and also a Bayesian approach to select AGNs. In Section 5.3, we explore the optical spectra, demonstrate the properties of the SED selected AGNs in the mid-IR and X-ray regimes and we focus on the obscuration of these sources by applying different diagnostic tests. Finally, in Section 5.4, we discuss these properties along with the differences between SED, mid-IR and X-ray selected AGNs. Throughout the work, we assumed a ΛCDM cosmology with H_o=75 km s^{-1} Mpc^{-1}, Ω_M=0.3 and Ω_Λ=0.7.

5.1 Data

The selection of obscured AGNs through SED fitting analysis requires secure redshifts and available optical and IR photometry for the SED construction. For that purpose, we used data from the VIMOS Public Extragalactic Redshift Survey (VIPERS) in the Canada-France-Hawaii Legacy Survey (CFHTLS) W1 field that contains rich multi-wavelength data from X-rays to the mid-IR bands.

5.1.1 VIPERS

The VIPERS survey used the VIsible MultiObject Spectrograph (Le Fèvre, O. et al. 2013, VIMOS) to perform deep optical spectroscopy within the CFHTLS W1 field.

Follow-up spectroscopic targets were selected to the magnitude limit i'= 22.5 from the CFHTLS catalogues (Guzzo, L. et al. 2014), while an optical colour pre-selection excluded galaxies at z< 0.5 (Le Fèvre et al. 2013). Comparing with a sample of VVDS-Deep and VVDS-Wide surveys, the selection criteria yielded 100% completeness for z> 0.6 (Fig.4, Scodeggio et al. 2018). In our analysis, we use the Public Data Release 2 (PDR-2, Scodeggio et al. 2018) of the VIPERS survey, which consists of 86,775 galaxies with available spectra and their corresponding optical photometric data in the u, g, r, i and z bands from the CFHTLS T0007 data release (Hudelot et al. 2012). Each spectrum is assigned a quality flag. In this work, we use sources with flags higher than 2 (confidence level of redshift measurement higher than 90% based on more than one spectral features) that are considered as the most reliable (Garilli, B. et al. 2014; Scodeggio et al. 2018). In total, 45,180 galaxies meet this criterion within $0.5 < z < 1.2$.

5.1.2 VISTA-VHS

The VISTA Hemisphere Survey (VHS, McMahon et al. 2013) is one of the six large surveys that are coordinated by the Visible and Infrared Survey Telescope for Astronomy (VISTA, Emerson et al. 2006) to observe the entire sky in the southern hemisphere, covering 20,000 sq. degrees. The data used in this work are from the Data Release 6 that produced by the VISTA Science Archive (VSA). VSA handles all the data products generated by the VISTA Infrared CAMera (VIRCAM). The depth of the VHS observations is higher than other near infrared surveys, such as UKIDSS-LAS (Lawrence et al. 2007), 2MASS (Skrutskie et al. 2006) or DENIS (Epchtein et al. 1994), and the magnitude limits are 20.6, 19.8 and 18.5 mag (Vega) for the J, H and Ks band, respectively.

5.1.3 AIIWISE

The usage of mid-IR photometry, in our analysis, is twofold: First, its inclusion in the SED fitting process allow us to identify AGN candidates (see Section 3). Second, mid-IR photometry has been proven very efficient in detecting AGNs, since it is less affected by extinction. We, thus, compare our SED derived AGN candidates with those selected by IR colours (see Section 4). Launched by NASA, *WISE* mapped the whole sky in the mid-IR regime with its four band-passes: W1=3.4 μm, W2=4.6 μm, W3=12 μm and W4=22μm and reached 5σ depths of 16.5, 15.5, 11.2, and 7.9 mag in Vega system, respectively. The AllWISE source catalogue (Cutri & et al. 2013) consists of more than 700 million objects with signal-to-noise ratio higher than 5 in

at least one band in the combined images.

5.1.4 XMM-XXL

XMM-XXL field (Pierre et al. 2017) covers an area of ∼50 deg^2 with an exposure time of about 10 ks per *XMM-Newton* pointing. The survey is split into two approximately equal fields. In the analysis, we use data from the equatorial sub-region of the field (XMM-XXL-North; XXL-N) that overlaps with the CFHTLS W1 field and covers an area of about 25 deg^2. We make use of the most recent X-ray catalogue of Chiappetti et al. (2018), which consists of 14,168 X-ray sources in the northern XMM-XXL field.

5.1.5 Final sample

The VIPERS catalogue with spectroscopic redshfits and optical photometry was cross-matched with the list of mid-IR AllWISE and the near-IR VHS sources at the same time using the `xmatch` tool from the `astromatch`[1] package that uses different statistical methods for cross-matching of astronomical catalogues. This tool matches symmetrically a set of catalogues and gives the Bayesian probabilities of the associations or non-associations (Pineau et al. 2017). To properly perform `xmatch`, all the cross-matched catalogues must cover the same footprint. As AllWISE is an all-sky survey and the VHS data cover the entire VIPERS field, we selected only the IR sources that lie in the footprint of the VIPERS survey. After the cross-match with `xmatch`, we kept only sources with a high probability of association (>68%). When one source was associated with several counterparts, we selected the association with the highest probability. We then filtered out sources with signal-to-noise ratio lower than three in the near-IR and mid-IR bands to better constrain the SED fitting in the IR regime. The resulted catalogue of 6,860 sources was used as the parent sample (hereafter as VIPERS sample). In Figure 5.1, we show the optical, near-IR and mid-IR (from top to bottom) magnitude distributions of our final sources with signal-to-noise ratio higher than three, while in Figure 5.2 we present their corresponding redshifts (blue histogram). All the mid-IR (*WISE*) magnitudes were measured with profile-fitting photometry, since all the sources are point-like (ext_*flg*=0) in the mid-IR images, which may be due to the low angular resolution of *WISE* telescope (e.g. ∼6.1" for W1 band). The shape of the magnitude distributions in the optical and near-IR bands (Fig. 5.1) is Gaussian-like, while the mean magnitude value becomes brighter from the u band (24.3 mag) to Ks band (17.4 mag). This is consistent with

[1] https://github.com/ruizca/astromatch

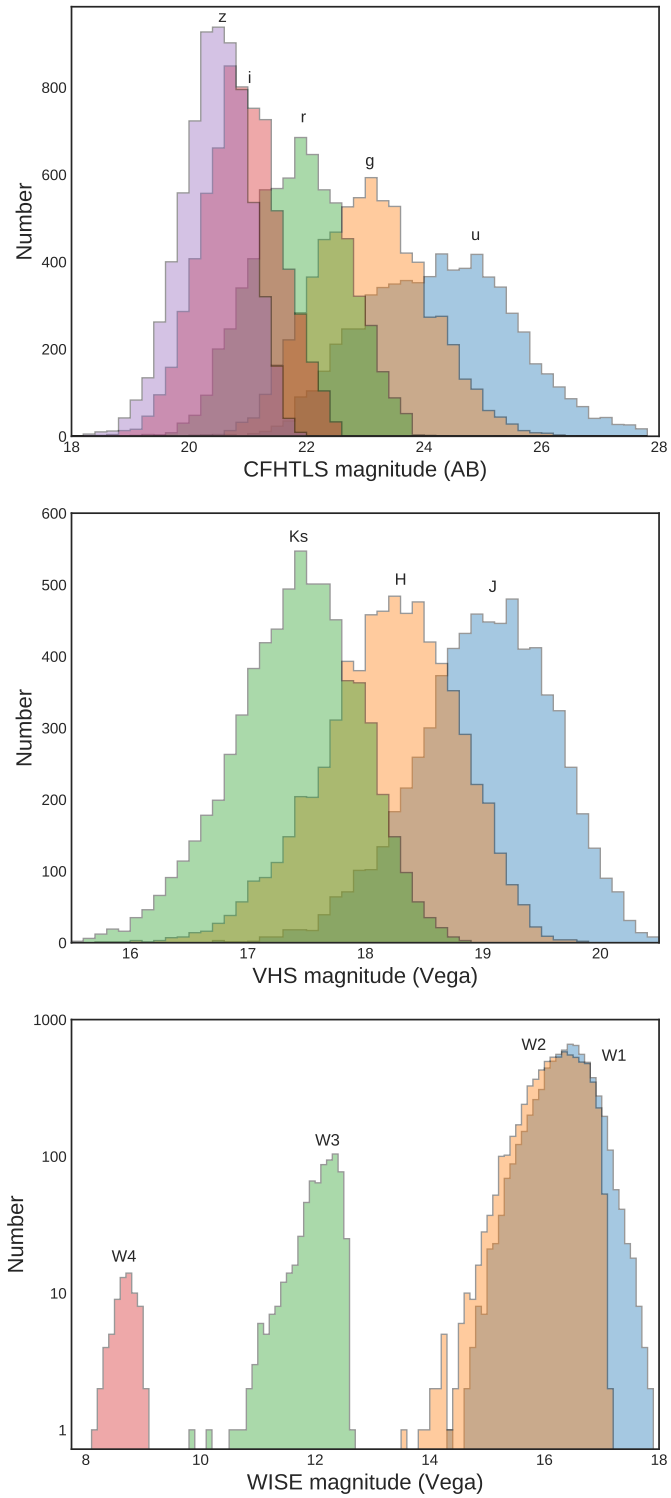

Figure 5.1: The magnitude distributions of our initial sample of 6,860 sources for the CFHTLS optical bands u, g, r, i and z (top), the VHS near-IR bands J, H and Ks (middle) and the *WISE* mid-IR bands W1, W2, W3 and W4 in Vega system (bottom) with signal-to-noise ratio higher than three.

the expected magnitudes of the underlying host galaxy SEDs. In the mid-IR bands, there is a degeneracy at W3 and W4 bands, since the AllWISE W3 and W4 bands have much lower sensitivities compared to W1 and W2 bands.

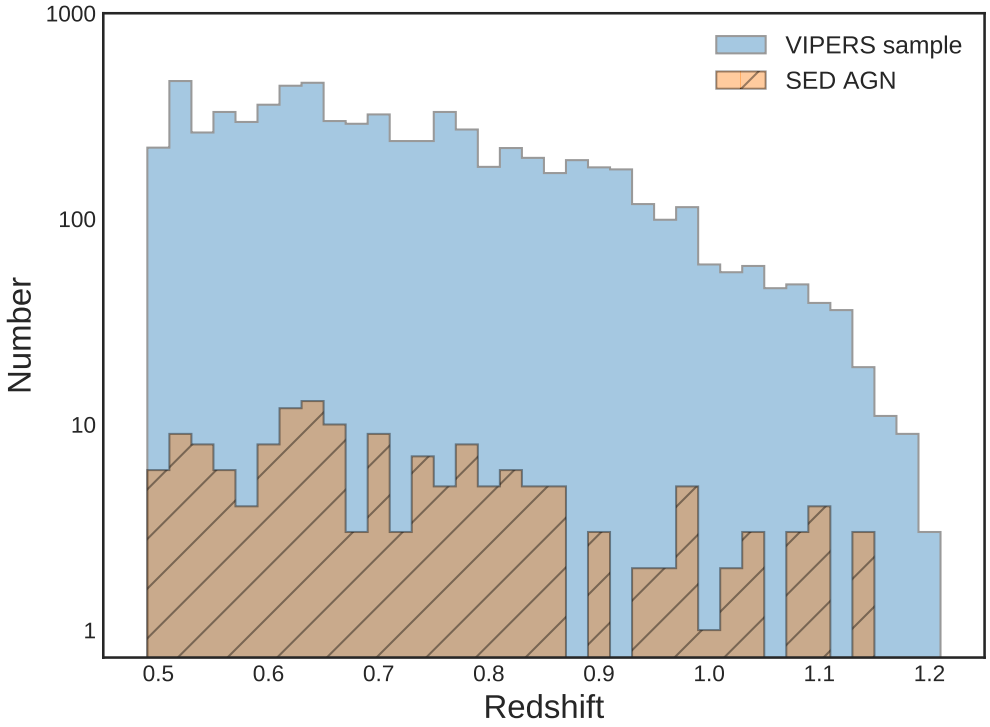

Figure 5.2: Redshift distribution for all sources in the initial sample (blue) and for the 160 high-confidence SED selected AGNs (orange-hatched).

5.2 Analysis

In this Section, we present the templates and parameter space used to fit the SEDs of the sources and the Bayesian methodology applied to select AGNs among these sources. We performed SED analysis using all the available optical (CFHTLS), near-IR (VHS) and mid-IR photometry (*WISE*), using `X-CIGALE` (Yang et al. 2020) that is the latest version of the Code Investigating GALaxy Emission (`CIGALE`, Noll et al. 2009; Ciesla et al. 2015; Boquien et al. 2019). This allows us to estimate the physical parameters of the sources. In particular, we are interested in the fraction of the IR luminosity originating from the AGN to the total IR luminosity of the galaxy, which is used as a proxy of the AGN activity (Ciesla et al. 2015). The SEDs were first fitted with a) a galaxy template and b) a galaxy plus an AGN component. For each case, we obtained the best-fitting solution provided by `X-CIGALE`, and used

the Bayesian Information Crirerion (BIC, Schwarz 1978) to quantify which template (galaxy/galaxy+AGN) provides the best fit for each source and the highest probability to host an AGN. We describe the analysis steps in detail below.

5.2.1 SED analysis with CIGALE

The `X-CIGALE` algorithm fits the observational multi-wavelength data with a grid of theoretical models and returns the best-fitted values for the physical parameters. The results are based on the energy balance, i.e., the energy absorbed by dust in UV/optical is re-emitted after heating at longer wavelengths, such as the mid-IR and far-IR. In this work, we built a grid of models including different stellar populations, dust attenuation properties, dust emission, star formation history and AGN emission. In particular, the models and the parameter space covered by these components are described below:

- To convolve the star formation histories of our sample, we used the double-exponentially-decreasing model (2τ-dec). This model, provides the best stellar mass and star formation rates of the sources, at the expense of unrealistic galaxy ages (Ciesla et al. 2015). Using a different model, e.g., 1τ-dec, delayed SFR, does not affect our measurements, as shown in Mountrichas et al. (2019).

- For the simple stellar population, we used the synthesis models of Bruzual & Charlot (2003), assuming the Initial Mass Function by Salpeter. We adopted a constant, solar metallicity of $Z = 0.02$, and a separation age between the young and the old stellar populations within the range of 1.5-1000 Myrs. A constant metallicity for all sources prevents long time consuming calculations, but also it does not affect significantly the shape of the SEDs compared to the observed ones and the derived properties (Yuan et al. 2018; Hunt et al. 2019).

- For the attenuation due to absorption and scatter of the stellar and nebular emission by interstellar dust, we utilized the attenuation law by Calzetti et al. (2000).

- The emission by dust in the IR regime was modelled by the semi-empirical Dale et al. (2014) templates. The parameter that describes them is the power-law slope of the dust mass distribution over heating intensity, α. These templates are strongly correlated to the adopted attenuation models through the dust luminosity that is the outcome of the energy balance that `X-CIGALE` is based on.

Table 5.1:: Models and the values for their free parameters used by `X-CIGALE` for the SED fitting of our initial sample (6,860 sources).

Parameter	Value
Star formation history: double-exponentially-decreasing (τ-dec) model	
Age of the main stellar population	0.5, 1.0, 3.0, 5.0, 7.0, 9.0, 11.0, 13.0
τ_{main}	0.1, 0.5, 1.0, 3.0, 5.0, 10.0, 20.0
age_{burst}	0.1, 0.2, 0.4, 0.5
Stellar population synthesis model	
Single Stellar Population Library	Bruzual & Charlot (2003)
Initial Mass Function	Salpeter
Metallicity	0.02 (Solar)
Nebular emission	
Ionization parameter ($logU$)	-2.0
Fraction of Lyman continuum escaping the galaxy (f_{esc})	0.0
Fraction of Lyman continuum absorbed by dust (f_{dust})	0.0
Line width in km/s	300.0
Dust attenuation: Calzetti et al. (2000)	
Colour excess of stellar continuum light for young stars E(B-V)	0.05, 0.1, 0.2, 0.3, 0.35, 0.4, 0.5, 0.6
Reduction factor for the E(B-V) of the old stars compared to the young ones	0.44
Dust template: Dale et al. (2014)	
IR power-law slope	2.0
AGN models from Fritz et al. (2006)	
Ratio between outer and inner radius of the torus (r_{ratio})	60.0
Optical depth at 9.7 μm (τ)	0.1, 1.0, 6.0, 10.0
Parameter linked to the radial dust distribution in the torus (β)	-0.5
Parameter linked to the angular dust distribution in the torus (γ)	4.0
Angular opening angle of the torus (θ)	100.0
Angle with line of sight (ψ)	0.001, 50.100, 89.990
AGN fraction	0.1, 0.2, 0.3, 0.5, 0.7, 0.9
Extinction in polar direction, E(B-V)	0.0, 0.05, 0.1, 0.15, 0.2, 0.3, 1.0
Emissivity of the polar dust	1.6
Temperature of the polar dust (K)	100.0

Note. – τ_{main} is the e-folding time of the main stellar population model in Gyr, age is the age of the main stellar population in the galaxy in Gyr (the precision is 1 Myr), and age_{burst} is the age of the late burst in Gyr (the precision is 1 Myr). β and γ are the parameters used to define the law for the spatial behaviour of the torus density. The functional form of the latter is $\rho(r,\theta) \propto r\beta e^{-\gamma|cos\theta|}$, where r and θ are the radial distance and the polar distance, respectively. θ is the opening angle and ψ the viewing angle of the torus. Type-2 AGNs have $\psi = 0.001$ and Type-1 AGNs have $\psi = 89.990$, while values equal to $\psi = 50.100$ are for intermediate type of AGN. The extinction in polar direction, E(B-V), included in the AGN module, accounts for the possible extincion in type-1 AGN, due to polar dust. The AGN fraction is measured as the AGN emission relative to IR luminosity (1–1000 μm).

- The AGN emission was modelled using the Fritz et al. (2006) template that includes both the emission from the central AGN and also the re-emitted radiation from the dusty torus heated by the central engine at longer wavelengths. Additionally, this latest version of the `X-CIGALE` code introduces polar-dust extinction to account for the possible extinction in type-1 AGN (Yang et al. 2020).

Table 5.1 presents the models and the values of their free parameters, used in the fitting process.

5.2.2 Best model selection - Bayesian factor

In Bayesian statistics, the choice of the model that fits best to the data is achieved through the Bayes Factor, **BF**, that is the ratio of the posteriori to a priori complementary probabilities (or the so-called evidence ratio). Let's assume that two models ($\mathbf{m_1}$, $\mathbf{m_2}$) have to be compared to a specific data set $\mathbf{y}$ and $\mathbf{p_1}$, $\mathbf{p_2}$ their parameters, respectively. Applying the Bayes theorem, the posteriori probabilities for the two models are:

$$f(\mathbf{m_1}|\mathbf{y}) = \frac{f(\mathbf{m_1})f(\mathbf{y}|\mathbf{m_1})}{\sum_{i=1}^{2} f(\mathbf{m_i})f(\mathbf{y}|\mathbf{m_i})} \quad \text{and} \quad f(\mathbf{m_2}|\mathbf{y}) = 1 - f(\mathbf{m_1}|\mathbf{y}). \tag{5.1}$$

Then, we calculate the ratio of the posteriori complementary probabilities of the two models (posterior odds, $\mathbf{PO} = \frac{f(\mathbf{m_1}|\mathbf{y})}{f(\mathbf{m_2}|\mathbf{y})}$) and also the Bayes factor of model $\mathbf{m_1}$ against model $\mathbf{m_2}$:

$$\mathbf{BF} = \frac{f(\mathbf{m_1}|\mathbf{y})/f(\mathbf{m_2}|\mathbf{y})}{f(\mathbf{m_1})/f(\mathbf{m_2})}$$

$$= [\mathrm{f}(\mathbf{m_1})\mathrm{f}(\mathbf{y}—\mathbf{m_1}) \frac{}{\sum_{i=1}^{2} f(\mathbf{m_i})f(\mathbf{y}|\mathbf{m_i})]/[\frac{f(\mathbf{m_2})f(\mathbf{y}|\mathbf{m_2})}{\sum_{i=1}^{2} f(\mathbf{m_i})f(\mathbf{y}|\mathbf{m_i})}]} \frac{}{f(\mathbf{m_1})/f(\mathbf{m_2}) = \frac{f(\mathbf{y}|\mathbf{m_1})}{f(\mathbf{y}|\mathbf{m_2})}}, \tag{5.2}$$

where $f(\mathbf{y}|\mathbf{m_i})$ is the marginal likelihood (or the so-called evidence) of the i model and is calculated by integrating with respect to parameters of each model:

$$f(\mathbf{y}|\mathbf{m_i}) = \int f(\mathbf{y}|\mathbf{k_i}, \mathbf{m_i}) f_i(\mathbf{p_i}) d\mathbf{p_i}, \quad i = 1, 2. \tag{5.3}$$

Table 5.2:: Explanation of Bayes Factor and ΔBIC values according to Kass & Raftery (1995) and selection of high-confidence SED AGNs compared to mid-IR and X-ray selected samples.

ΔBIC (2*log(BF))	BF	Evidence in favor of model m	AGN Probability (%)	Number of SEDs (6,860)	mid-IR AGN (52/35)	X-ray AGN (116)	X-ray & mid-IR AGN (17/14)
>10	>150	very strong	0.08	2,346	0/0	5	0/0
(6-10)	(3,20)	strong	2.50	2,053	1/0	29	0/0
(2-6)	(1,3)	little	11.35	1,894	5/3	40	2/2
(-2-2)	(<1)	equal for both	43.00	407	2/0	8	0/0
(-6,-2)	(3,20)	little	84.30	87	7/2	6	1/0
(-10,-6)	(20,150)	strong	97.62	17	7/5	4	3/2
<-10	>150	very strong	99.89	56	30/25	24	11/10
<-2	**>3**	**strong**	**91.21**	**160**	**44/32**	**34**	**15/12**

Note. – For positive values of 2log(BF) the best model, m, is assumed to be this with only galaxy templates, while for negative values m represents the model when an AGN component is included. Thus, the evidence in each case refers to model m. The AGN probabilities are the average of each bin and refer to the model with AGN templates: high values indicate AGN activity. The number of SEDs refers to the number of sources in each ΔBIC bin. The last three columns give the number of mid-IR, X-ray and both mid-IR and X-ray selected AGNs in these bins. In mid-IR AGN and the last columns, the two numbers correspond to selection criteria of Assef et al. (2013) with reliability of 75% and 90%, respectively. The last row corresponds to our AGN selection criteria with $\Delta BIC < -2$.

The value of the Bayes factor determines the rejection or not of the initial assumption with high values (>1) indicating evidence in favor of that model. In practice, the Bayes factor is a measure of the weight of the information that is included in the data in a favor of one model against an other. It can be used as a relative measurement for the comparison of the two models. Kass & Raftery (1995) gave the possible explanation of the Bayes factor for the comparison between two models that are shown in Table 5.2. Alternative methods are required when the BF is calculated with not enough information for the a priori probabilities. Information Criteria, such as the Akaike Information Criterion (Akaike 1974, AIC) or the Bayesian Information criterion (Schwarz 1978, BIC), are applied, since they are capable of calculating an approximation of the BF in the absence of priori distributions. This is achieved, by taking into account the complexity of the models, in addition to the goodness of fit. In this work, we used BIC, since it evaluates the true model among all possible and alternative hypotheses, while it is more conservative in the parameter impact on the selection compared to AIC. It favors models with small number of parameters, while by increasing the parameter space, it penalizes more the model. The values of BIC for a model are given by:

$$BIC = -2 * ln(L) + 2 * p * ln(N), \tag{5.4}$$

where p and N are the number of parameters and the number of observations, respectively, while L is the maximum likelihood of the model. To compare two models and select the best one, we calculate the difference of the information of the two models:

$$\Delta BIC = -2 * ln(L_1/L_2) - (p_2 - p_1) * ln(N), \tag{5.5}$$

where the first term of this equation gives the ratio of the likelihoods of the two models and (p_2-p_1) is the difference of the parameters used in each model. It can be shown that the difference in BIC values for two models, ΔBIC, are related to BF, and in this case the latter can be calculated approximately by:

$$BF = exp(-\Delta BIC/2). \tag{5.6}$$

We further consider the Schwarz weights (Burnham & Anderson 2002):

$$weight = \frac{exp(-\Delta BIC_j/2)}{\sum_{n=1}^{2} exp(-\Delta BIC_n/2)}. \tag{5.7}$$

These weights indicate the relative preference between two candidate models (n=1,2) and also provide a method to combine a parameter when using multiple model averaging. In other words, they express a probability that favours one model (in this case

j) against the other. In Table 5.2, we give the interpretation for each value of ΔBIC and we select the best model according to ΔBIC values and the posteriori probability of each model.

5.3 Results

5.3.1 SED selected AGNs

To identify AGN candidates, we constructed and modelled the SEDs of all the 6,860 sources in the VIPERS sample. Each SED was fitted twice. In the first run, we used only galaxy model templates. In the second run, we used both galaxy and AGN templates. For each case, we obtained the best fitting model and we calculated the BIC values (Eq. 5.4). Based on the difference, ΔBIC (Eq. 5.5), and its interpretation (Table 5.2), we classified the sources into samples with different evidence ratio (or AGN probability). Following Del Moro et al. (2016), we adopted a threshold of ΔBIC< -2 to select AGN candidates. This results to 160 galaxies ($\sim$2.3% of the initial sample) with probabilities hosting an AGN higher than 73% (the mean value is equal to 91.20%) and evidence that favors the model when including the AGN templates. These sources also have lower values of the reduced χ^2 in the model fitting when adding an AGN component. Figure 5.3 shows the ΔBIC distribution for the VIPERS sample (blue histogram). The vertical dashed line denotes the threshold used in this work.

In Figure 5.4, we present the SEDs with and without AGN templates (lower and upper panels, respectively) for a source classified as AGN, with probability of 99.99%. When an AGN component is added to the fitting process, the fit is significantly improved and the relative residual fluxes are minimized, as shown at the bottom of each panel. In Table 5.3, we list the properties of the 160 SED selected AGNs, while Figure 5.2 shows their redshift distribution (orange-hatched histogram). We, further, explored whether the availability of photometry at different wavelengths affects the AGN selection method. In particular, we tested whether the omission of (i) near-IR photometry, (ii) the longest mid-IR photometric bands and (iii) the addition of far-IR data, affects the AGN selection method. Towards, this end we followed the procedure described in Section 5.2:, i.e., we compared the δBIC values assuming that the real AGNs are those defined with the highest number of bands used.

Our analysis revealed, that the absence of the near-IR data results in a high number of false positive AGN identifications. This is probably due to the fact that in these bands the AGN and galaxy SEDs are almost equal in fluxes. Thus, we

Table 5.3:: Catalogue of the 160 SED selected AGNs.

VIPERS ID (1)	RA (J2000) (2)	DEC (J2000) (3)	z (4)	L_{IR} (erg s^{-1}) (5)	L_X (erg s^{-1}) (6)	mid-IR AGN (7)	Broad lines (8)	[NeV] emission (9)	MEx AGN (10)	TBT AGN (11)	SED AGN type (12)	r–W2 (Vega) (13)
101128062	30.44515	-5.94690	0.652	43.93	<43.68	0	0	0	0	1	2.0	4.76
101143290	30.65517	-5.87594	0.736	44.07	<43.68	0	0	0	0	1	2.0	4.94
101145879	31.06676	-5.85939	0.529	43.51	<42.89	0	0	0	0	1	2.0	4.93
101166083	30.97806	-5.76278	0.516	43.46	<42.70	0	0	0	0	0	2.0	4.63
101167170	30.61551	-5.75817	1.029	45.06	<43.68	0	0	0	0	0	2.0	6.64
101171205	30.42398	-5.74079	0.986	44.86	<43.92	0	1	1	0	1	1.0	4.92
101175047	30.91564	-5.72366	0.549	43.77	<43.28	0	0	0	0	1	1.5	5.99
101183266	31.14391	-5.68359	0.690	44.26	<43.68	0	0	0	0	1	1.5	5.75
101184375	30.53652	-5.68232	0.655	43.93	<43.65	0	0	0	0	0	2.0	4.85
101199625	30.43171	-5.60912	0.530	43.30	<43.92	0	0	0	1	1	2.0	5.39
102121299	32.02825	-5.96117	0.538	44.33	43.84	1	0	0	1	1	2.0	6.02
102129812	31.40485	-5.92148	0.817	43.95	<43.42	0	0	0	0	0	1.5	6.63
102133752	31.33519	-5.90048	0.537	44.04	43.89	0	0	0	1	0	1.0	5.36
102138525	31.56050	-5.87794	0.797	44.57	<43.60	0	0	0	1	1	1.5	6.22
102178761	31.22399	-5.67968	0.689	43.68	<43.54	0	0	1	0	1	2.0	4.70
102183859	31.62379	-5.65619	0.599	43.69	<43.09	0	0	0	0	0	2.0	5.09
103134908	32.21963	-5.97658	0.644	44.37	<43.13	0	0	0	1	1	1.5	4.84
103143919	32.29891	-5.93776	0.773	44.76	43.78	1	1	1	0	1	1.0	7.63
103151883	32.35777	-5.90568	0.636	45.12	43.80	1	1	1	0	0	1.0	5.29
103180263	32.25861	-5.78499	0.644	44.71	43.68	0	1	0	0	1	1.0	5.14
103180825	32.77869	-5.78191	0.748	44.73	43.77	0	1	0	0	1	1.5	5.19
103197293	32.67400	-5.71261	0.664	43.52	<43.30	0	0	1	0	1	2.0	5.76
104170739	33.70780	-5.90915	0.715	43.80	<43.26	0	0	0	1	1	2.0	4.22
104236309	33.97194	-5.65539	0.546	43.85	<43.03	0	0	0	0	0	1.0	6.34
105139296	34.09171	-5.95674	1.048	44.14	<43.88	0	0	1	0	1	2.0	6.88
105145409	34.09651	-5.93140	1.095	44.51	<43.71	0	0	1	0	1	2.0	6.54
105152074	34.22651	-5.90089	0.697	44.63	<43.13	0	0	1	1	1	1.0	5.11
105189949	34.16295	-5.72786	0.643	43.55	<43.16	0	0	0	1	1	2.0	6.01
105201540	34.64631	-5.67718	0.851	44.58	<43.63	0	0	0	0	1	1.0	5.37
105211420	34.71244	-5.62929	0.643	44.19	<42.69	0	0	0	1	1	1.0	5.88
105216790	34.47889	-5.60829	0.843	44.39	<43.43	1	0	0	1	0	1.5	7.61
106158702	35.13075	-5.87612	0.599	45.02	43.58	0	1	0	0	1	1.5	4.72
106164318	35.79339	-5.85072	0.506	44.50	<42.87	1	0	0	1	1	2.0	6.06
106204876	35.60449	-5.66945	1.078	44.44	<44.20	1	0	1	0	0	2.0	6.94
106208862	35.82120	-5.65156	0.802	43.88	<43.50	0	0	0	0	1	2.0	5.95
107161301	36.85607	-5.65162	1.077	44.57	<43.72	1	0	1	0	1	2.0	7.15
108114624	37.12663	-5.97348	0.553	43.55	<43.46	0	0	0	1	1	2.0	5.36
108120334	37.46318	-5.94224	0.955	45.12	<43.94	1	0	1	0	1	2.0	7.86
108137534	37.02236	-5.85604	0.778	44.70	43.88	1	1	1	0	1	2.0	5.40
108163578	37.59208	-5.70686	0.716	44.68	<43.53	1	0	0	1	1	1.0	5.67
108167635	37.26583	-5.68088	1.043	44.87	<43.77	1	1	1	0	1	1.0	6.05
108168148	37.07837	-5.68167	0.626	43.93	<43.56	0	0	0	1	1	1.5	6.10
109130669	38.48938	-5.91916	0.554	43.99	<42.89	0	0	0	1	1	2.0	4.74
109161838	38.20769	-5.76429	1.102	44.28	<43.76	0	0	1	0	1	2.0	6.44
109164682	38.43727	-5.74709	0.825	44.42	<43.14	0	0	0	0	0	1.0	6.70
109179237	38.46824	-5.67911	0.593	43.44	<43.06	0	0	0	1	1	2.0	3.86
110043474	31.13770	-5.43120	0.666	44.55	<43.55	1	0	1	1	1	1.0	5.63
110054196	31.15407	-5.37707	0.596	44.77	<43.38	0	1	0	0	1	1.0	5.02
110066563	30.80605	-5.31692	0.696	43.82	<43.04	0	0	0	0	1	2.0	5.78
110072899	30.28438	-5.28715	0.776	44.51	<43.95	1	0	1	1	1	1.5	6.81
110078074	30.76310	-5.26278	0.512	43.66	<43.09	0	0	0	0	1	2.0	5.64
110100629	30.69404	-5.15765	0.859	44.09	44.22	0	1	0	0	1	1.0	6.01
110133664	30.77885	-5.00982	0.507	43.67	<43.11	0	0	0	1	1	2.0	6.06
110180344	30.94828	-4.79023	0.617	44.02	<43.31	0	0	0	1	1	1.5	5.92
110202029	30.44836	-4.68994	0.558	43.96	<43.55	0	0	0	0	1	2.0	5.46

Note. – (1): Identifier. (2): Right ascension. (3): Declination. (4): Redshift. (5): Infrared AGN luminosity. (6): X-ray [2-10 keV] luminosity. The '<' symbol represent the upper limit. (7): "1" ("0") if AGN is (is not) selected through mid-IR colours. (8): "1" ("0") for existence (absence) of broad lines. (9), (10), (11): "1" ("0") if AGN is (is not) selected via [NeV] emission, MEx and TBT diagrams, respectively. (12): AGN type derived from the SED fitting results (ψ value). (13): r–W2 colour (Yan et al. 2013).

Table 5.3:: *continued*

VIPERS ID (1)	RA (J2000) (2)	DEC (J2000) (3)	z (4)	L_{IR} (erg s^{-1}) (5)	L_X (erg s^{-1}) (6)	mid-IR AGN (7)	Broad lines (8)	[NeV] emission (9)	MEx AGN (10)	TBT AGN (11)	SED AGN type (12)	r–W2 (Vega) (13)
110204490	30.46040	-4.67859	0.764	44.08	<43.81	1	0	1	1	1	2.0	5.60
111063425	31.62215	-5.31458	0.613	43.91	<42.98	0	0	0	0	1	1.5	5.69
111076897	31.61439	-5.24968	0.963	44.37	43.86	0	1	1	1	1	1.0	5.59
111108509	31.47468	-5.10136	1.135	44.53	<44.06	0	0	0	0	0	2.0	6.62
111117682	31.51571	-5.05702	1.084	45.27	<44.21	1	0	1	0	1	1.5	7.51
111120886	31.32135	-5.04079	0.516	43.90	<43.12	0	0	0	0	1	2.0	5.26
111153701	31.84755	-4.88503	0.704	44.30	<43.37	1	0	1	1	1	1.5	6.38
111157163	31.98383	-4.86751	0.557	43.73	<42.71	0	0	0	1	1	2.0	5.36
111161925	31.35488	-4.84550	1.093	44.70	<43.57	0	0	1	0	0	2.0	7.30
111192162	31.88525	-4.70298	0.500	44.42	42.92	0	0	0	0	0	1.5	5.33
112032836	32.35279	-5.47099	0.649	44.21	<43.52	0	0	0	0	1	1.0	4.95
112071341	32.94422	-5.28638	0.789	44.49	<43.71	1	0	1	1	1	1.5	6.83
112089875	32.39088	-5.19864	0.620	43.74	<43.21	0	0	0	0	1	2.0	5.27
112100049	33.02364	-5.15279	1.035	44.87	<43.83	0	0	0	0	0	2.0	7.58
112105956	32.70154	-5.12298	0.565	43.95	<43.33	0	0	0	0	0	1.0	4.80
112130497	32.44284	-5.01467	0.983	44.58	<44.03	0	0	1	0	1	2.0	7.47
112141684	33.06693	-4.96233	0.983	44.77	44.36	1	0	0	0	0	2.0	7.69
112155596	32.76740	-4.89028	0.524	45.33	<43.80	1	1	0	0	1	1.5	4.94
112163489	33.00277	-4.85407	0.754	44.40	<43.35	1	0	0	1	1	1.5	7.42
112167778	32.26360	-4.83555	0.843	44.86	<43.37	1	0	0	1	1	1.5	6.47
112169655	32.31060	-4.82707	0.655	44.23	<43.18	1	0	0	0	1	1.0	7.05
112173291	33.05381	-4.81045	0.507	43.44	<43.18	0	0	0	1	1	2.0	5.41
112196243	32.45579	-4.70356	0.701	43.85	<43.25	0	0	0	0	1	2.0	5.35
113037156	33.96294	-5.45440	0.641	44.36	<43.22	0	0	0	1	0	1.0	6.48
113044521	33.32085	-5.42048	1.014	44.86	44.48	0	1	1	0	1	1.0	6.09
113051150	33.34912	-5.38764	0.697	45.32	43.87	1	1	0	0	1	1.5	5.23
113064992	33.13933	-5.32305	0.540	43.27	<43.16	0	0	0	1	1	2.0	5.05
113092199	33.45236	-5.19618	0.585	43.95	<43.03	0	0	0	1	1	2.0	5.42
113110546	33.99779	-5.11639	0.500	44.10	43.35	1	0	0	1	1	2.0	6.66
113169191	33.07584	-4.85186	0.742	43.53	<43.16	0	0	0	0	0	2.0	4.73
113180911	33.82514	-4.80045	0.624	43.68	<43.06	0	0	0	0	0	2.0	5.18
113206860	33.08376	-4.67540	0.807	43.97	<43.85	0	0	0	0	1	2.0	5.37
114073711	34.67060	-5.31094	0.659	44.23	<43.29	0	0	0	1	1	2.0	6.44
114082043	34.38863	-5.26415	0.599	44.36	44.03	0	0	0	0	0	1.0	5.66
114108550	34.74651	-5.16858	0.753	44.65	<43.24	1	0	0	1	1	1.0	6.70
114131874	34.58537	-5.07403	0.649	44.52	44.17	1	1	0	0	1	1.5	6.32
114139331	34.32735	-5.04438	0.823	44.98	43.63	0	1	1	0	1	1.0	4.68
114161732	34.28235	-4.95660	1.092	44.61	<43.95	0	0	0	0	1	1.0	6.98
115027291	35.78914	-5.49197	0.626	44.26	43.46	1	0	0	1	1	2.0	5.59
115115472	35.66146	-5.06443	0.907	44.05	43.58	0	1	1	0	1	1.0	7.31
115122976	35.65010	-5.02796	0.845	44.24	44.12	0	0	1	1	1	2.0	7.63
115135448	35.82728	-4.97046	0.828	44.41	43.88	1	0	0	1	1	1.0	7.91
116014737	36.78589	-5.55085	0.553	44.16	<43.32	0	0	0	1	1	1.0	6.18
116032161	36.57659	-5.45495	0.770	43.68	<43.80	0	0	1	1	1	2.0	5.65
116042241	36.60305	-5.40163	1.000	44.76	<44.39	0	0	1	0	1	2.0	6.63
116046207	36.75194	-5.38182	0.870	45.31	<43.87	0	1	1	0	1	1.5	4.88
116085907	36.02205	-5.18092	0.649	43.69	<42.54	0	0	0	0	1	1.0	6.67
116099542	36.73734	-5.11584	0.704	43.58	<43.27	0	0	1	1	1	2.0	5.74
116150199	36.37517	-4.87492	0.629	43.72	<43.03	0	0	0	0	1	2.0	5.43
116167222	36.39511	-4.79289	0.854	44.17	<43.40	1	0	1	1	1	2.0	6.68
116192311	35.95629	-4.66974	0.622	44.21	43.51	0	0	0	1	1	2.0	5.84
117010534	37.79089	-5.57627	0.986	45.13	<44.44	1	0	0	0	1	1.5	8.43
117027325	37.62852	-5.49188	0.784	43.88	<43.44	0	0	0	0	1	2.0	5.54
117037264	37.08046	-5.44453	0.786	44.44	<43.46	1	0	0	1	1	2.0	7.08
117050860	36.96234	-5.37541	0.804	44.92	44.34	1	0	1	1	1	2.0	7.86

Note. – (1): Identifier. (2): Right ascension. (3): Declination. (4): Redshift. (5): Infrared AGN luminosity. (6): X-ray [2-10 keV] luminosity. The '<' symbol represent the upper limit. (7): "1" ("0") if AGN is (is not) selected through mid-IR colours. (8): "1" ("0") for existence (absence) of broad lines. (9), (10), (11): "1" ("0") if AGN is (is not) selected via [NeV] emission, MEx and TBT diagrams, respectively. (12): AGN type derived from the SED fitting results (ψ value). (13): r–W2 colour (Yan et al. 2013).

Table 5.3:: *continued*

VIPERS ID (1)	RA (J2000) (2)	DEC (J2000) (3)	z (4)	L_{IR} (erg s^{-1}) (5)	L_X (erg s^{-1}) (6)	mid-IR AGN (7)	Broad lines (8)	[NeV] emission (9)	MEx AGN (10)	TBT AGN (11)	SED AGN type (12)	r–W2 (Vega) (13)
117062279	37.26845	-5.31627	0.779	43.96	<43.54	0	0	0	0	1	2.0	5.85
117066130	37.84448	-5.29393	0.586	43.92	<43.37	0	0	0	1	1	2.0	5.09
117110515	37.15691	-5.09081	0.698	43.49	<43.03	0	0	0	0	1	2.0	5.04
117135140	37.13011	-4.97454	0.933	44.05	<43.71	0	0	0	0	0	2.0	4.99
117173795	37.68207	-4.76728	0.630	43.56	<43.37	0	0	0	0	1	2.0	4.17
117177187	37.35116	-4.75558	0.892	44.30	<43.49	1	0	0	0	1	2.0	7.08
117178247	37.36978	-4.74554	0.610	44.66	43.37	0	0	0	1	1	1.0	4.87
117186794	37.30807	-4.70517	0.662	43.91	43.76	0	1	0	0	1	1.5	5.81
118042646	38.32293	-5.41092	0.708	44.63	<43.34	0	1	1	0	1	1.0	5.79
118086325	38.44772	-5.18750	0.638	44.22	<44.14	1	0	0	1	1	1.0	5.72
118086892	38.49890	-5.18475	0.516	43.41	<43.97	0	0	0	0	0	2.0	5.61
118086923	38.28170	-5.18458	0.731	44.12	<43.10	0	0	1	1	1	1.0	6.38
118087346	38.60147	-5.18252	0.803	44.55	<43.83	1	0	0	0	0	1.5	6.74
118128010	38.48948	-4.98375	0.646	43.74	<43.46	0	0	0	1	1	2.0	5.38
118161115	38.01033	-4.80912	0.543	43.28	<42.83	0	0	0	1	1	2.0	5.13
118187397	38.10186	-4.67423	0.763	44.22	<43.28	1	0	0	1	1	2.0	7.06
119009735	30.37515	-4.64988	0.894	44.72	<44.70	1	0	1	0	1	2.0	6.72
119034376	30.75731	-4.53195	0.939	44.08	<43.56	0	0	0	0	1	2.0	6.54
119061358	30.48839	-4.39574	0.549	43.96	<43.81	1	0	0	0	0	1.5	7.23
119088613	31.14702	-4.26421	0.578	43.83	<42.87	0	0	0	0	1	2.0	4.61
119091830	30.98208	-4.25297	0.735	44.14	<43.34	0	0	0	0	0	2.0	5.74
119095831	30.75257	-4.22947	0.525	43.64	<42.92	0	0	0	0	0	2.0	5.17
120040724	31.90079	-4.52882	0.971	44.27	<43.85	0	1	0	0	1	1.0	5.52
120071991	31.39916	-4.39738	0.741	45.08	<43.50	1	0	0	1	1	1.0	7.19
120103089	31.84380	-4.27291	0.707	44.46	43.20	0	1	0	0	1	1.5	5.10
120114522	32.09921	-4.22791	0.745	44.39	<43.36	1	0	1	1	1	1.0	6.69
121034054	32.41920	-4.54024	0.591	43.62	<43.30	0	0	0	0	0	2.0	5.44
121043880	32.91610	-4.48952	0.851	44.38	<43.34	0	0	0	0	1	1.5	5.95
121046919	32.42821	-4.47505	0.533	44.81	43.96	1	1	0	0	1	1.5	4.82
121062481	32.42717	-4.40335	0.842	44.42	<43.51	0	0	0	0	0	1.5	7.13
121099761	32.53067	-4.24116	0.822	43.93	<43.40	0	0	1	1	1	2.0	5.56
121102071	32.87646	-4.23080	0.609	44.33	43.46	1	1	0	0	1	1.0	4.95
122022800	33.37111	-4.57965	0.674	44.64	43.60	0	1	1	0	1	1.0	5.43
122042685	33.50952	-4.48348	0.514	43.82	<43.06	0	0	0	1	1	1.0	4.12
122043807	33.72362	-4.47911	0.722	44.80	<43.67	0	0	0	0	1	2.0	5.86
122052858	33.11464	-4.43304	1.149	45.44	<44.08	1	1	0	0	0	1.0	5.31
122100077	33.17477	-4.21485	0.669	44.50	43.57	1	0	1	1	1	1.0	5.87
123021037	34.20095	-4.59600	0.502	43.27	<42.88	0	0	0	1	1	2.0	4.46
123057675	34.49237	-4.42283	0.646	44.43	43.89	0	0	1	1	1	1.0	5.08
123098574	34.78088	-4.24129	0.660	43.97	<43.00	0	0	0	0	1	2.0	5.14
124035576	35.84055	-4.52366	0.619	44.09	<43.16	0	0	0	0	0	1.5	4.82
124072245	35.24707	-4.36030	0.812	44.36	<43.20	0	0	0	0	0	1.0	5.36
124075097	35.57515	-4.34718	0.837	44.11	<43.24	0	0	0	0	1	1.0	7.06
124109737	35.53904	-4.19366	0.616	44.14	<43.13	0	0	0	0	1	2.0	5.32
125022958	36.15360	-4.58911	0.639	43.63	<43.04	0	0	0	0	0	2.0	4.44
125026840	36.42350	-4.57150	0.611	44.26	<43.04	0	1	0	0	1	1.5	5.78
127028630	38.34431	-4.55794	0.578	44.59	43.33	0	0	0	1	1	1.0	5.09
127061363	38.40941	-4.39736	0.753	44.71	44.09	1	0	0	1	1	1.0	5.76
127103639	38.46575	-4.21191	1.150	45.00	<43.70	1	0	1	0	0	1.5	6.16
127111323	38.32294	-4.17705	0.658	43.61	<43.11	0	0	0	0	1	2.0	5.63

Note. – (1): Identifier. (2): Right ascension. (3): Declination. (4): Redshift. (5): Infrared AGN luminosity. (6): X-ray [2-10 keV] luminosity. The '<' symbol represent the upper limit. (7): "1" ("0") if AGN is (is not) selected through mid-IR colours. (8): "1" ("0") for existence (absence) of broad lines. (9), (10), (11): "1" ("0") if AGN is (is not) selected via [NeV] emission, MEx and TBT diagrams, respectively. (12): AGN type derived from the SED fitting results (ψ value). (13): r–W2 colour (Yan et al. 2013).

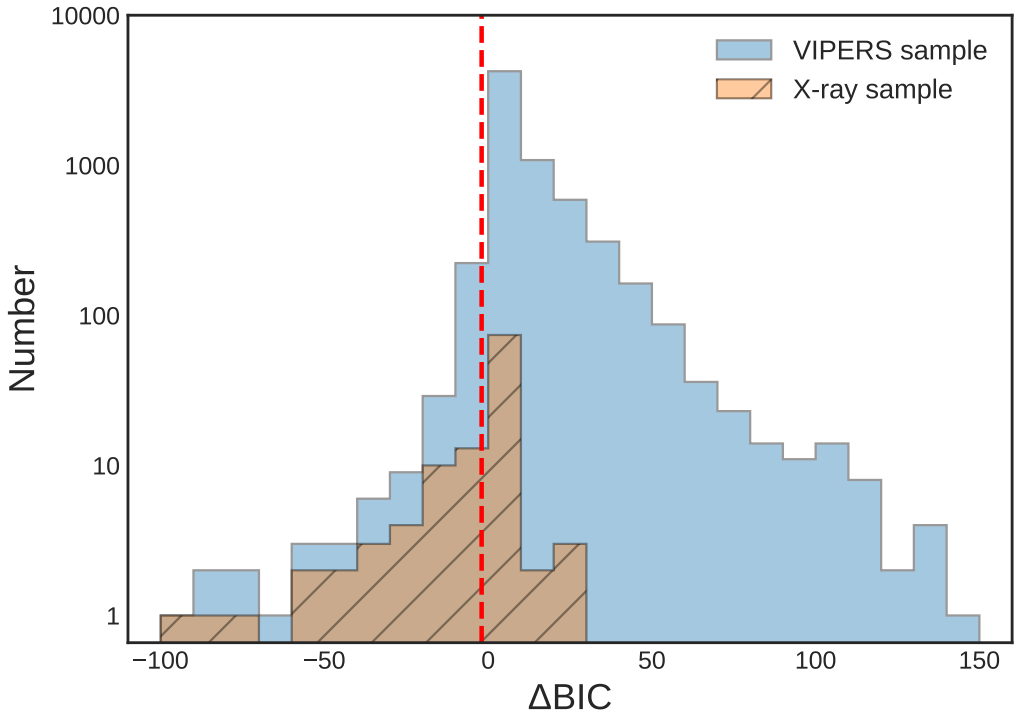

Figure 5.3: The distribution of ΔBIC for the VIPERS sample (blue). The orange-hatched histogram represents the distribution only for the X-ray sample. The vertical dashed line represents the threshold used in this work adopted by Del Moro et al. (2017) corresponding to evidence that favors the model when including the AGN template.

chose to include near-IR bands in our analysis to better constraint the SED fitting and increase the reliability of our method. Furthermore, we tested if the absence of both the W3 and W4 bands affects the reliability of the AGN selection method. Comparing the SED selected samples, we concluded that the absence of W3 and W4 bands resulted in 16% of false-positive AGN candidates. W3 and W4 photometric bands are available for 86% of the galaxies in the VIPERS sample. Thus, we expect $\sim 2\%$ of our SED selected AGN to be misclassified.

We also examined whether the addition of far-IR data affects the AGN selection method. For that purpose, we used the *Herschel* Multi-tiered Extragalactic Survey (HerMES) data (Oliver et al. 2012) that overlap with the VIPERS field. HerMES used PACS (Poglitsch et al. 2010) and SPIRE (Griffin et al. 2010) photometric data from the ESA *Herschel Space Observatory* (Pilbratt et al. 2010). We cross-matched the VIPERS sample with the far-IR sources as described in Section 5.1.5. For the 174 sources with *Herschel* data, we run the `X-CIGALE` code with and without AGN

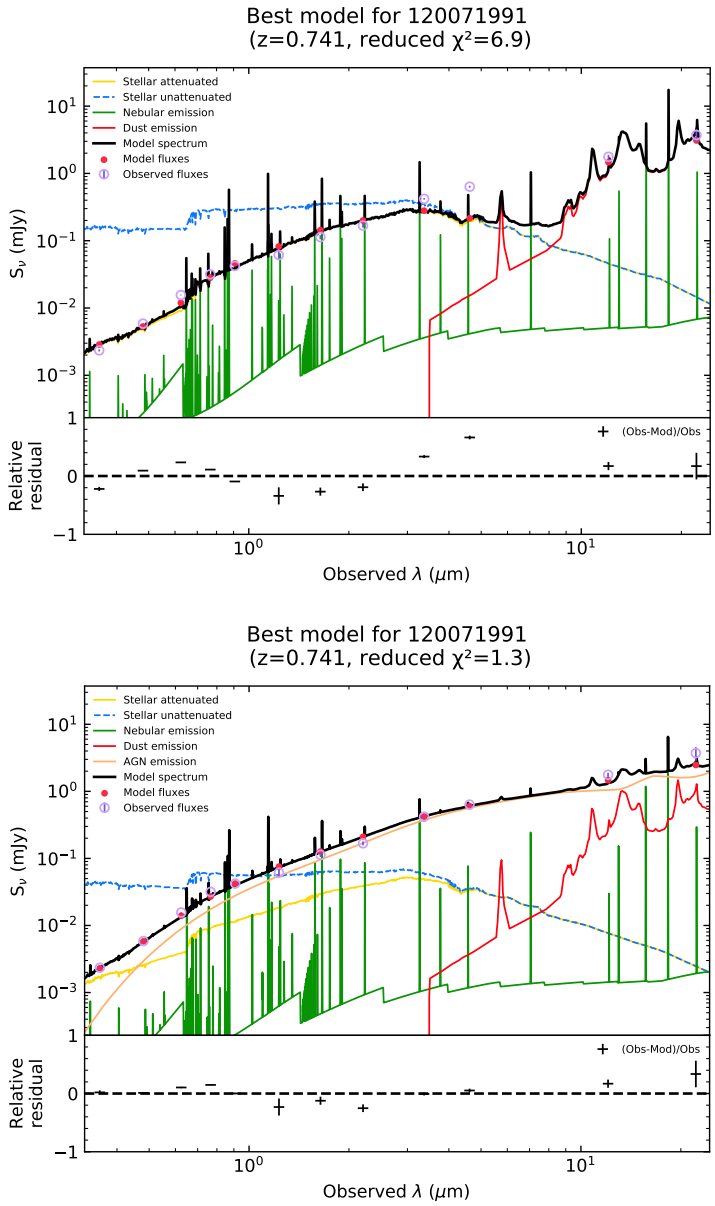

Figure 5.4: SED fitting example of a source classified as AGN with probability 99.99%. The upper and lower SEDs correspond to models without and with AGN templates, respectively. The dust emission is plotted in red, the AGN component in green, the attenuated (unattenuated) stellar component is shown with the yellow (blue) solid (dashed) line, while the orange lines shows the nebular emission. The total flux is represented with black colour. Below each SED, we plot the relative residual fluxes versus the wavelength.

templates. We, then, compared the SED selected AGNs and we found no statistical

differences between the results. Thus, in our analysis, we do not require far-IR photometry. This does not affect the reliability of our method, while it allows us to apply the methodology in a significantly larger galaxy sample.

According to the SED fitting results, 71% of the sources have inclination angle, ψ, values $\leq 50^o$. In particular, 46/160 (29%) and 81/160 (51%) have $\psi = 50^o$ and $\psi = 0^o$, respectively. ψ is defined as the angle between the equatorial AGN axis and the line of sight and is used as a proxy of obscuration. Specifically, $\psi = 90^o$ denotes type-1 AGN, whereas $\psi \leq 50^o$ indicates intermediate or type-2 AGN. Thus, the vast majority (70%) of our AGN candidates seem to present some level of obscuration. To further investigate the nature of the sources, in the next subsections we examine their optical spectra, their X-ray and mid-IR properties and we apply different obscuration diagnostics using optical and IR colours.

5.3.2 X-ray detections and upper limits

In this section, we explore the X-ray properties of our 160 SED selected AGN. We use the most recent available X-ray catalogue to search for counterparts, while for non detections we derive upper limits by constructing the X-ray mosaic using all available images in the field. Out of 14,168 X-ray sources in the northern XMM-XXL field (Chiappetti et al. 2018), 10,029 sources (∼70%) fall inside the field of view of the VIPERS pointings. Cross-matching this sample with the whole VIPERS catalogue using the `xmatch` software (see Section 5.1.5), there are 4,736 sources with high probability of association (68%). 359 of them have good quality spectroscopic redshifts (see Section 5.1.5) and are within the redshift range used in this study ($0.5 < z < 1.2$). 116/359 have optical, near-IR and mid-IR counterparts with a signal-to-noise ratio greater than three in the W1 and W2 *WISE* bands. The ΔBIC distribution of the 116 X-ray sources is shown in Figure 5.3. Out of these, 34 sources (∼30%) are also SED selected AGNs (ΔBIC>-2). This means that the remaining 70% is not selected with the SED fitting technique. These sources should be AGNs with small amount of dust in their torus (or dust-free) and/or low IR contribution to the total of their hosts making them difficult to identify in the mid-IR wavelengths. We examine the nature of the latter in the next sections.

For the 126 SED selected AGNs not detected in X-rays, we derived the upper limits in the soft [0.5-2 keV] and hard [2-8 keV] bands. First, we constructed the mosaics taking into account all the publicly available *XMM-Newton* observations (Jansen et al. 2001) covering the XMM-XXL northern field. The detailed imaging procedure is described in Ruiz & Georgakakis (in prep.). Briefly, we retrieved and processed the overlapping observations in the field from all detectors by following

the standard data reduction tasks of the *XMM-Newton* Scientific Analysis Software (Gabriel et al. 2004, SAS) and accounting for all the latest calibration files. `EPIC-pn` (Strüder et al. 2001) and both `MOS-1` and `MOS-2` (Turner et al. 2001) detectors were operated in full frame mode using the thin filter. The event files from all detectors were cleaned from hot pixels/columns and pixels at the edges of the cameras and were screened to remove high particle background and soft proton flares by setting `FLAG`=0 and selecting `pn` and `MOS` single events with 0<`PATTERN`<4 and `PATTERN`≤12, respectively. In a similar way, we built the combined mosaic with the exposure maps. The background mosaics were produced by masking the areas around the X-ray detections.

For the upper limits, we extracted the total counts around the sources within a circular region of radius equal to 15". For the background, we used a circular region centered on the target position with a radius of 30" and we normalized this to the area of the sources. Then, we used a Bayesian approach of 99.7% confidence level to derive upper limits (Kraft et al. 1991). To find the final count rates, we divided the upper limits with the exposure time and the encircled energy fraction (eef): $count\,rate = upper\,limit/eef/exposure\,time$. The exposure time was taken as the average value of the pixels in a circular region of 15", while we adopted eef=0.7 that corresponds to the radius used for the sources extraction counts. The count rates were converted to fluxes, using an energy conversion factor (ecf) calculated for each band. For the ecf calculation, we used the `webbPIMMS` site by assuming a power-law model with photon index of $\Gamma = 1.7$ (Nandra et al. 2005; Tozzi et al. 2006) and galactic absorption $N_H = 2.6 * 10^{20}\mathrm{cm}^{-2}$. We calculated separately the ecf for the `pn` and `MOS` thin filters and we took the average of them all. The final ecf used are equal to 2.58×10^{11} and 6.82×10^{10} ergs photon^{-1} for the soft and hard band, respectively. The luminosities were calculated using the following equation:

$$L_X = 4 * \pi * D_L^2 * F_X * (1+z)^{\Gamma-2}, \tag{5.8}$$

where L_X and F_X are the flux and luminosity in the hard band, respectively, D_L is the luminosity distance, z is the redshift and Γ is the photon index (Alexander et al. 2003; Xue et al. 2011). The units of L_X are given in erg s^{-1}.

5.3.3 Mid-IR selected AGNs

In addition to studying their X-ray properties, we explore whether the 160 SED selected AGNs could be characterized as AGN via simple mid-IR colour selection criteria. These criteria are based on the power-law that appears in the mid-IR bands (5-10 μm) when AGN luminosity is at least comparable with that of its host. A

number of diagnostics have been proposed using *WISE* data that provides imaging at 3.4, 4.6, 12 and 22 μm for a large sample of galaxies. These include a simple colour cut-off (W1–W2$\geq$0.8) defined by Stern et al. (2012) for bright sources (W2$\leq$15.05 mag), a more refined magnitude-dependent cut-off taking into account faint sources in the W2 band by Assef et al. (2013) and two wedges in W1–W2 vs. W2–W3 and W1–W2 vs. W3–W4 colour-colour diagrams suggested by Mateos et al. (2012) using three and four *WISE* bands, respectively. Similar methods have also been proposed for sources observed with the IRAC instrument (Fazio et al. 2004) on board the *Spitzer Space Telescope* (Werner et al. 2004) with observations at 3.6, 4.5, 5.8 and 8.0 μm filters. These are the "Lacy wedge" (Lacy et al. 2004, 2007; Sajina et al. 2005), the "Stern wedge" (Stern et al. 2005) and, more recently, the "Donley wedge" (Donley et al. 2007, 2012).

First, we examined the VIPERS sample using the diagnostics of Stern et al. (2012) and Assef et al. (2013). We used the AllWISE data mentioned in Section 5.1.3. This sample is photometrically complete at 16.8 mag (Vega), where there is a turn-over in the number density plot of the fluxes in the W2 band. Using the Stern et al. (2012) criteria, we selected 25 AGN with magnitude brighter than W2=15.05 mag. Since this method is not reliable for fainter objects, we utilised the AGN selection criteria by Assef et al. (2013):

$$\mathrm{y} > \alpha_\mathrm{r} * \exp(\beta_\mathrm{r} * (\mathrm{x} - \gamma_\mathrm{r})^2), \mathrm{x} > \gamma_\mathrm{r} \tag{5.9}$$

$$\mathrm{y} > \alpha_\mathrm{r}, \mathrm{x} \leq \gamma_\mathrm{r}, \tag{5.10}$$

where $x = W2$ and $y = W1 - W2$ and the revised constant values of $(\alpha_r, \beta_r, \gamma_r)$ given by Assef et al. (2018) are equal to $(0.650, 0.153, 13.86)$ and $(0.486, 0.092, 13.07)$ for the 90% and 75% reliability levels, respectively. We found 35 sources at 90% and 52 sources at 75% reliability. Figure 5.5 shows the *WISE* colour-magnitude (W1–W2 versus W2) plot for the VIPERS sample. The lines represent the wedges as defined in Assef et al. (2013) for both 90% and 75% reliability. We also over-plotted the 160 SED (ΔBIC$\leq$-2) and X-ray selected AGN samples. The shaded green area represents the Stern et al. (2012) threshold for AGN selection.

Additionally, we selected mid-IR AGNs through Mateos et al. (2012) colour selection criteria by using the colours (W2–W3) and (W1–W2). We do not apply the second diagnostic of Mateos et al. (2012) that utilizes four *WISE* bands as the inclusion of the W4 band with high signal-to-noise ratio reduces our sample to only 53 sources. There are 668/6,860 sources in our sample that have detections in all three bands (W1, W2 and W3) and signal-to-noise ratio greater than three. Following

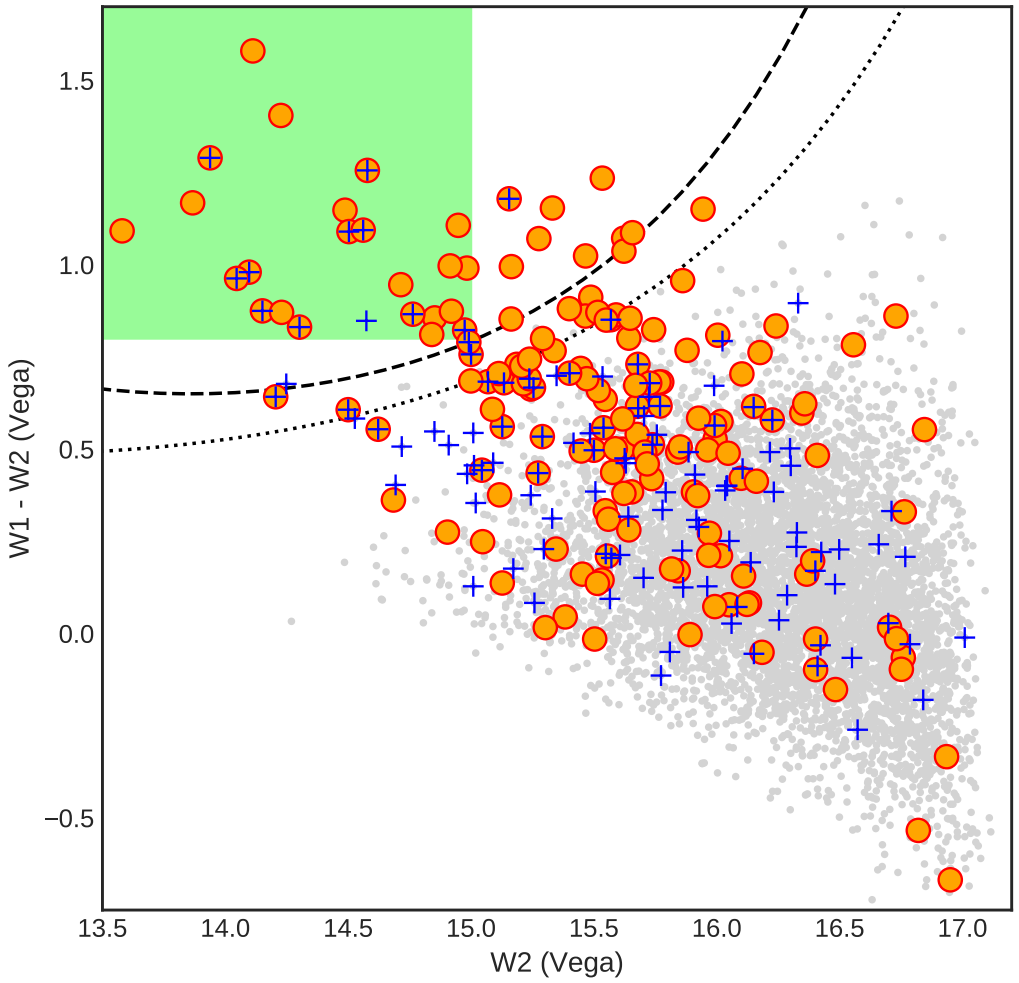

Figure 5.5: *WISE* magnitude-colour (W2, W1–W2) diagram for all 6,860 VIPERS sources (gray points). The dashed (dotted) line represents the Assef et al. (2013) selection threshold with reliability of 90% (75%). The orange circles and blue crosses represent the SED and X-ray selected AGNs, respectively. The shaded area indicates the AGN selection criteria by Stern et al. (2012)

Mateos et al. (2012)'s criteria:

$$W1 - W2 < 0.3150 \times (W2 - W3) + 0.796 \tag{5.11}$$

$$W1 - W2 > -3.172 \times (W2 - W3) + 7.624 \tag{5.12}$$

$$W1 - W2 > 0.3150 \times (W2 - W3) - 0.222 \tag{5.13}$$

we selected 31 mid-IR AGNs. All of them are SED selected AGN by our analysis, while 29 sources are also selected by the Assef criterion with 75% reliability. In Figure 5.6, we plot the (W2–W3) versus (W1–W2) colours. The dotted lines define the Mateos

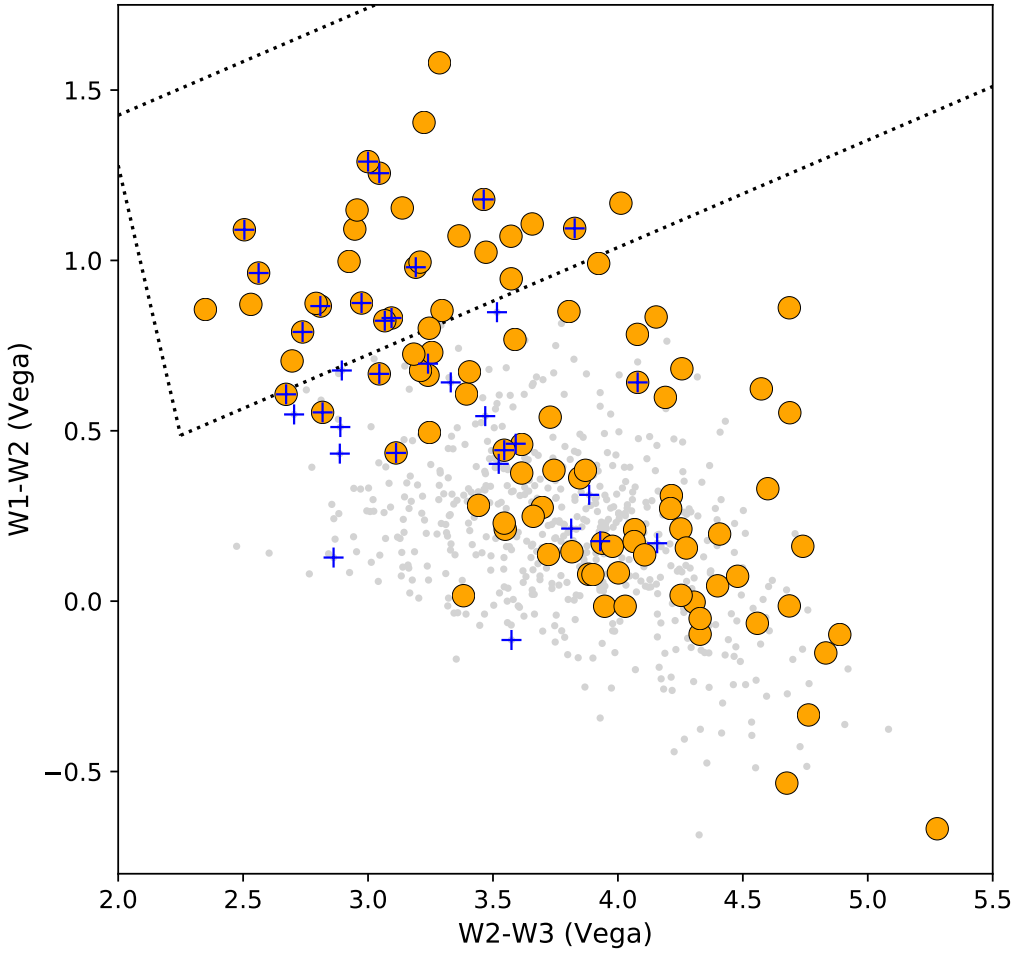

Figure 5.6: *WISE* colour-colour (W2–W3, W1–W2) diagram of the *VIPERS* sample with detections in all three bands (gray points) with the Mateos et al. (2012) selection wedge (dotted lines). The orange circles and blue crosses represent the SED and X-ray selected AGNs, respectively, with detections in W1, W2 and W3 bands.

et al. (2012) wedge. For reference, we plot the SED (orange circles) and X-ray (blue crosses) selected AGN samples. As illustrated in Figure 5.7, 54/160 of our AGN candidates are also mid-IR selected AGN, using at least one of the aforementioned criteria.

5.3.4 Optical spectroscopy

We further inspected the spectra of all the SED selected AGNs to check for any AGN signature in their emission lines. In particular, we searched for the [NeV] forbidden

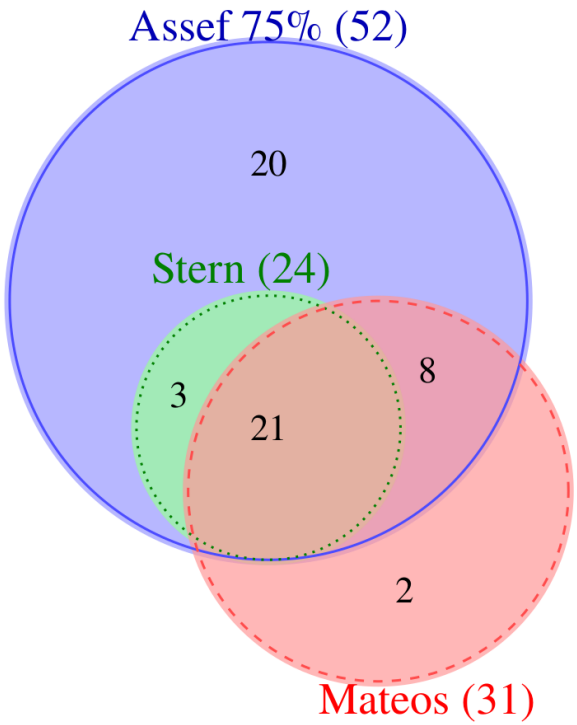

Figure 5.7: Venn diagram of the AGN samples selected through the mid-IR colour selection criteria defined by Mateos et al. (2012) (red-dashed), Assef et al. (2013) (blue-solid) and Stern et al. (2012) (green-dotted).

emission line at λ=3426 Å that is often used as a diagnostic tool to distinguish between AGN and star-forming galaxies (e.g. Schmitt 1998). Furthermore, we looked whether broad emission lines are present. Additionally, we used two optical emission line diagnostics to separate the AGN and star-forming populations: the Mass Excitation diagram (MEx, Juneau et al. 2011, 2014) and the colour excitation diagram (TBT, Trouille et al. 2011), that use the ([OIII], Hb) and ([NeIII], [OII]) emission line flux ratios, respectively. For this part of our analysis, we used the latest version of the `specutils`[2] packages in `PYTHON`.

5.3.4.1 [NeV] emitters and broad lines

Based on the information provided in the VIPERS spectroscopic catalogue, 27 out of the 160 SED selected AGN, present broad emission lines in their spectra. As already mentioned, the [NeV] emission line at λ=3426 Å is a good indicator of AGN activity

[2] https://specutils.readthedocs.io/en/stable/index.html

(Schmitt 1998; Gilli et al. 2010). Its high reliability is based on the fact that the energy needed to ionize [NeV] is 97 eV and may only come from high energy sources as opposed to, for example, stellar emission, since in the latter case the maximum emitted energy is lower than 55 eV (Haehnelt et al. 2001). The [NeV] at λ=3346 Å can also be used to identify AGN. However, it has less diagnostic power, as its intensity is significantly lower compared to [NeV] λ3426 Å (see e.g. Fig. 1 in Maddox 2018). Many previous studies have used the [NeV] emission to select a large number of AGNs. Mignoli et al. (2013) identified 94 type 2 [NeV] emitters and compared them to X-ray selected AGN and those from line ratio diagnostics. They concluded that the [NeV] emitters can identify low-luminosity and heavily obscured AGNs with increasing fraction to higher stellar masses. More recently, Vergani et al. (2018) studied the properties of the hosts of [NeV] AGNs, such as stellar masses, ages and colours. For the optical spectral coverage of VIPERS, the [NeV] line is accessible only for sources that lie at redshift higher than $z > 0.62$. There are 114 SED AGNs above this redshift limit. After removing objects with artefacts in their spectra and/or those with very low quality, we ended up with 42 [NeV] emitters. The vast majority of them have signal-to-noise ratio higher than five.

5.3.4.2 MEx and TBT diagram

For low redshifts $z < 0.5$, the classic emission line ratio diagnostic diagram usually used is the Baldwin, Phillips, & Terlevich diagram (BPT, Baldwin et al. 1981). In our case, the standard emission lines used in the BPT diagram lie outside the wavelength coverage of the optical spectrographs. For example, for redshifts higher than $z > 0.5$ the [NII] and Hα lines are redshifted to the observed near-IR regime. Thus, alternative indicators have been proposed in the literature, such as the rest-frame Bessel U-B galaxy colour (Yan et al. 2011, Colour Excitation diagram), H band absolute magnitude (Weiner et al. 2006), [OII]/Hβ (Lamareille 2010), Dn4000 break (Marocco et al. 2011), the stellar mass (MEx diagram) or the rest-frame colour (TBT diagram). All these replacements of the [NII]/Hα ratio are based on the correlation between the galaxy stellar mass and the gas phase metallicity or the rest-frame colours (depended on stellar mass; Kauffmann et al. 2003). In this work, we used the MEx and TBT diagrams.

MEx diagram avoids blending of lines in low-resolution spectra, by utilizing stellar mass and only two spectral lines, i.e., [OIII]5007 and Hβ. In our analysis, we used the calibrated diagram of Juneau et al. (2014) that is reliable to higher redshift (up to z$\sim$1). Using the flux ratio of [OIII] and Hβ and the stellar mass of a galaxy, we utilized the mass excitation diagram to classify a source as star-forming

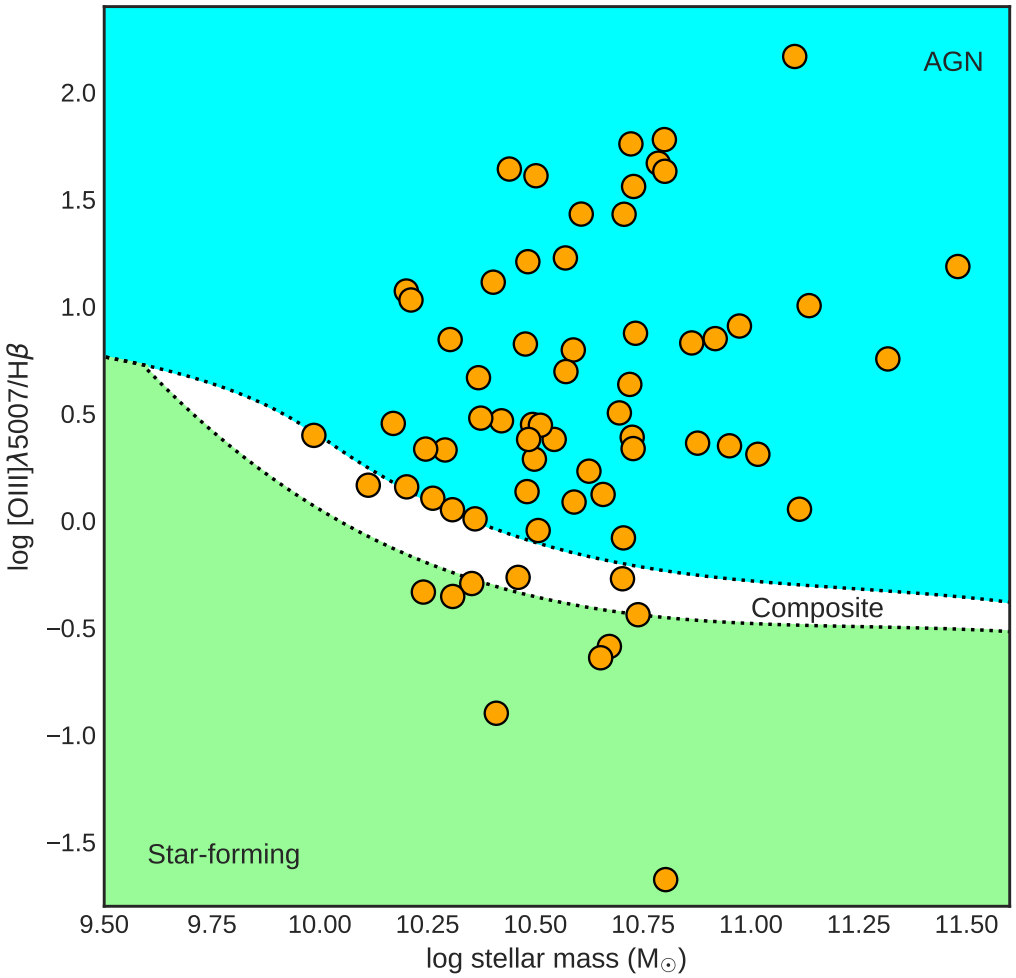

Figure 5.8: The Mass Excitation (MEx) diagram for the 66 SED selected AGNs that have significant both [OIII] and Hβ emission lines. The dotted lines separate the star-forming galaxies from the AGNs. AGNs are found above the upper line (blue region), while under the lowest line the star-forming galaxies lie (green shaded area). In between these lines, there is a composite population that consists of both AGN and star-forming systems.

galaxy, AGN or composite galaxy (i.e., both star-formation and AGN emission). To have both of the aforementioned lines present, we limited our sample to sources with $z \leq 0.9$, due to the VIPERS spectral coverage. Among our 160 SED selected AGNs, 66 sources have both [OIII] and Hβ lines with good quality spectra. In Figure 5.8, we present the MEx diagnostic plot, including the two empirically determined dividing lines of Juneau et al. (2014) that separate the pure star-forming (under), the galaxies with significant AGN emission (above) and the composite (in between) galaxies.

The masses were derived from the SED fitting technique described in the previous sections. The MEx diagnostic was calibrated by using the Chabrier (2003) IMF, thus we corrected the stellar masses of our sources as we assumed initially the Salpeter (1955) IMF when we modelled the SEDs. In particular, we multiplied our stellar masses by a factor of 0.62 as found in Zahid et al. (2012). At the end, according to MEx diagnostic, 53 sources (88%) lie in the AGN area, six sources in the composite region, while seven sources in the star-forming region.

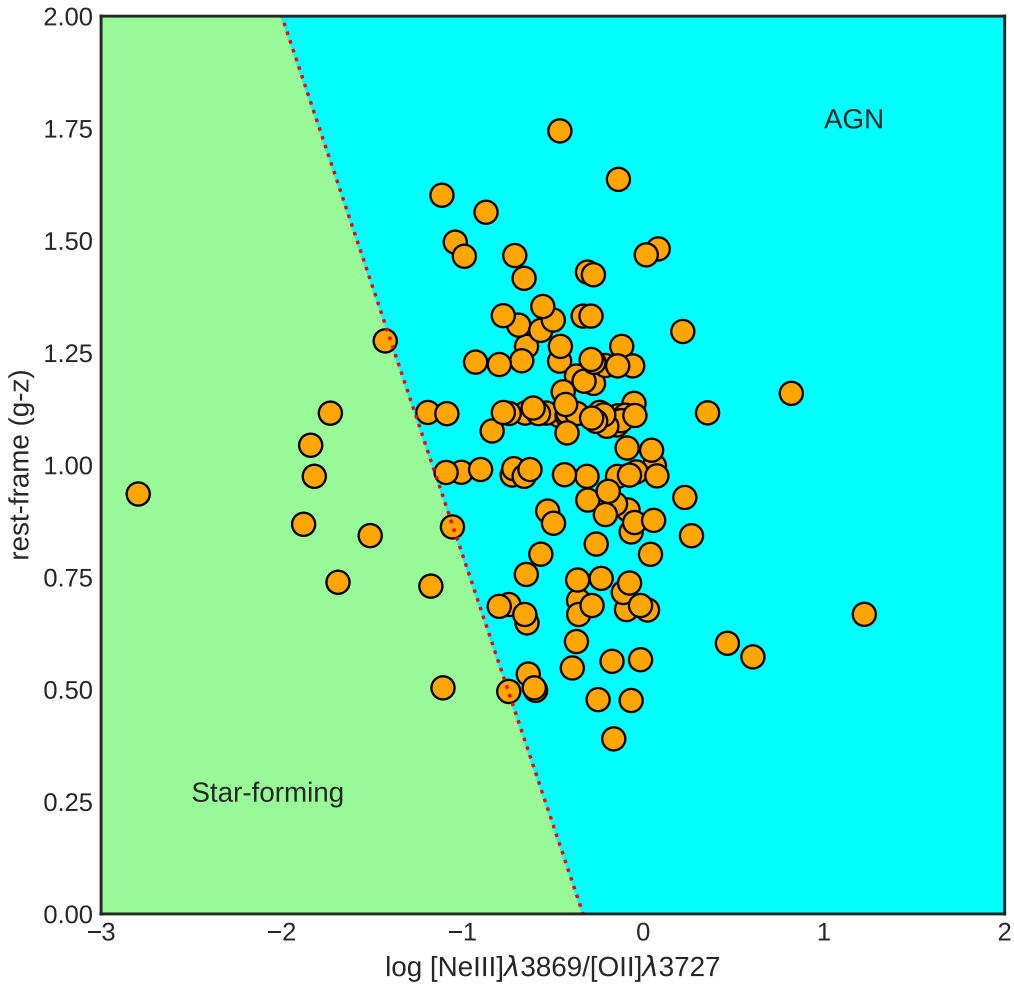

Figure 5.9: The TBT diagram for the 138 SED selected AGNs that have significant [NeIII] and/or [OII] emission lines. The dotted line separates the star-forming galaxies from the AGNs. The latter are found on the right part of this diagram (blue shaded region), while on the left side the star-forming galaxies exist (green shaded area).

The TBT diagram uses the rest frame colour $^{0.0}$(g-z) as a function of the ratio of the emission lines [NeIII] and [OII]. This method relies on the assumption that AGNs

are hosted by massive, fast-rotating galaxies and have high ionization lines compared to the star-forming galaxies (Zhang et al. 2019). Moreover, it is not affected by reddening, since these two lines are close to each other. An additional advantage of this method is that it can be used up to redhsift z∼1.4 for optical spectra. TBT diagram is able to disentangle the star-forming galaxies from AGNs, but not the composite galaxies. However, 70% of the composite galaxies fall inside the AGN area (Pons et al. 2016). In Figure 5.9, the TBT diagram is shown for the 138/160 sources that have good quality spectra. The separation line (dotted) is defined as follows:

$$^{0.0}(g - z) = -1.2 \times \log([\mathrm{NeIII}]/[\mathrm{OII}]) - 0.4. \quad (5.14)$$

126 sources (91%) fall inside the AGN area (shaded blue), while twelve sources in the star-forming region (shaded green). The MEx and TBT diagrams have classified seven and twelve of our SED selected AGN, as star-forming galaxies. However, 7/7 and 5/12 of these sources in the MEx and the TBT diagram, respectively, are selected as AGN through other methods (e.g. X-rays, mid-IR, [NeV] emission).

In total, optical spectroscopy confirms that 134/160 (∼84%) SED selected AGNs present signs of AGN activity. The remaining sources mainly have poor quality spectra, thus the above diagnostics could not be applied.

5.3.5 Intrinsic absorption estimation

SED fitting results revealed that 71% of the AGNs are obscured ($\psi \leq 70$ corresponding to AGNs of type 1.5 and 2), based on the estimated inclination angle (Section 5.3.1). However, in this section we also explore different diagnostic criteria of obscuration using optical and mid-IR colours or the X-ray to mid-IR relation.

5.3.5.1 Mildly obscured AGNs

Obscured sources are expected to be unbiased by dust in the mid-IR regime, while being absorbed in the optical bands. Yan et al. (2013) used a r–W2>6 mag cut-off along with the Stern criteria (W1–W2>0.8 and W2<15.2 mag) to select type II AGNs. LaMassa et al. (2016) used W1 instead of W2 band with a more relaxed threshold (r–W1>4 mag) in a sample of X-ray sources in Stripe 82 field and highlighted the power of this diagnostic to reveal obscured AGNs not detected through the classic W1–W2 colour criterion by Assef et al. (2013). In this work, we used the Yan et al. (2013) criteria. In Figure 5.10, we plot the r–W2 colour distribution for the 160 high-confidence SED selected AGNs and also the VIPERS sources classified as normal

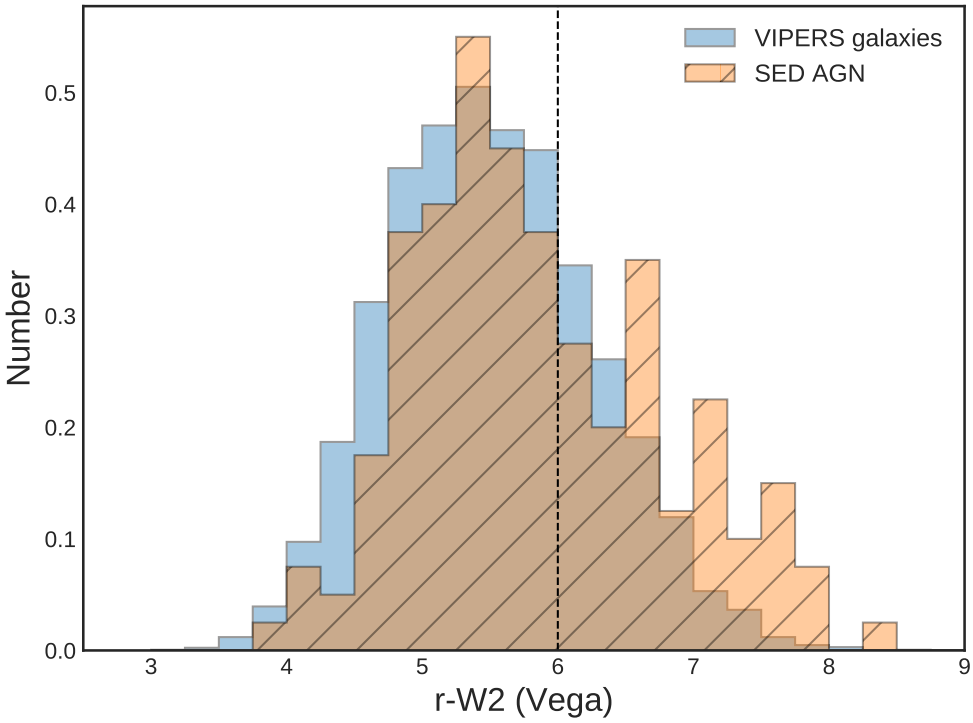

Figure 5.10: The normalized distribution of r–W2 colour for the VIPERS sample classified as normal galaxies (blue) and the SED selected AGNs (orange-hatched). The vertical dashed line represents the threshold used in Yan et al. (2013) to select obscured AGNs.

galaxies, for reference. To facilitate a better comparison, we converted the CFHTLS r band to r_{SDSS} Vega system to calculate the r–W2 colour as defined by Yan et al. (2013). Almost 40% of the AGNs have red colours ($r - W2 \geq 6$). Out of those, 43/61 have viewing angles (ψ) that indicate AGNs of type 1.5 and 2. The remaining 18 optical red, type 1 AGNs have $E(B-V) > 0.05$ while most of them have $E(B-V) \geq 0.3$, that indicates large amount of polar dust in these sources (Yang et al. 2020).

Hickox et al. (2017) explored the mid-IR colours and the SEDs of a large sample of type I and II quasars selected via SDSS spectroscopy. They showed that simple mid-IR colour cuts could identify the majority of luminous AGNs but may miss the most heavily obscured AGNs. On the other hand, r–W2 colour criteria might be biased against low redshift regimes (z<0.5). Thus, they defined a new optical-IR selection criterion that cleanly separates the unobsorbed and obscured AGNs: (u–W3[AB])>1.4×(W1–W2[Vega])+3.2. This is more effective as it uses the maximum baseline between optical and IR wavelength range. However, it requires detections (or upper limits) in all four bands u, W1, W2 and W3. In Figure 5.11, we plot the

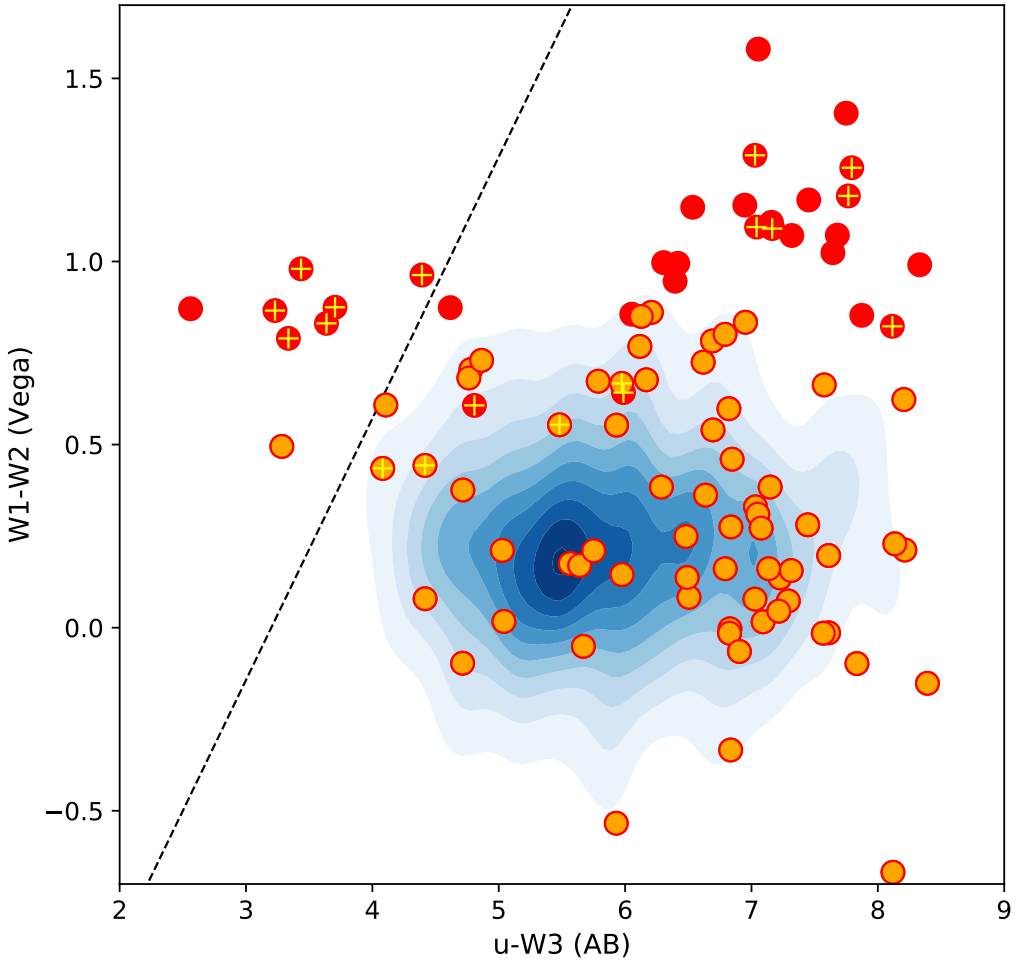

Figure 5.11: Optical-IR colour diagram for the 98 SED selected AGNs (filled circles). Hickox et al. (2017) selection relation is presented by the dashed line (see text for more details). Sources on the right side of this line are considered obscured. The density contours present the VIPERS sample, while the red filled circles and the crosses show the mid-IR and X-ray selected AGNs.

W1–W2 versus the u–W3 colours for all the sources in the VIPERS sample requiring detections in all four bands with a minimal signal-to-noise ratio greater than two as in Hickox et al. (2017), resulting in 98 SED selected AGNs. For reference, we over-plot the AGN samples selected through mid-IR (red circles) and X-ray (crosses) selection techniques. More than 90% of the SED selected AGNs lie in the area characterized by obscuration. As expected all the sources near and on the left side of the line are unobscured broad-line AGNs.

5.3.5.2 Highly obscured AGNs

To search for sources with extreme intrinsic absorption in our sample, we used the relation of their IR and X-ray luminosity. It is well known that the mid-IR luminosity

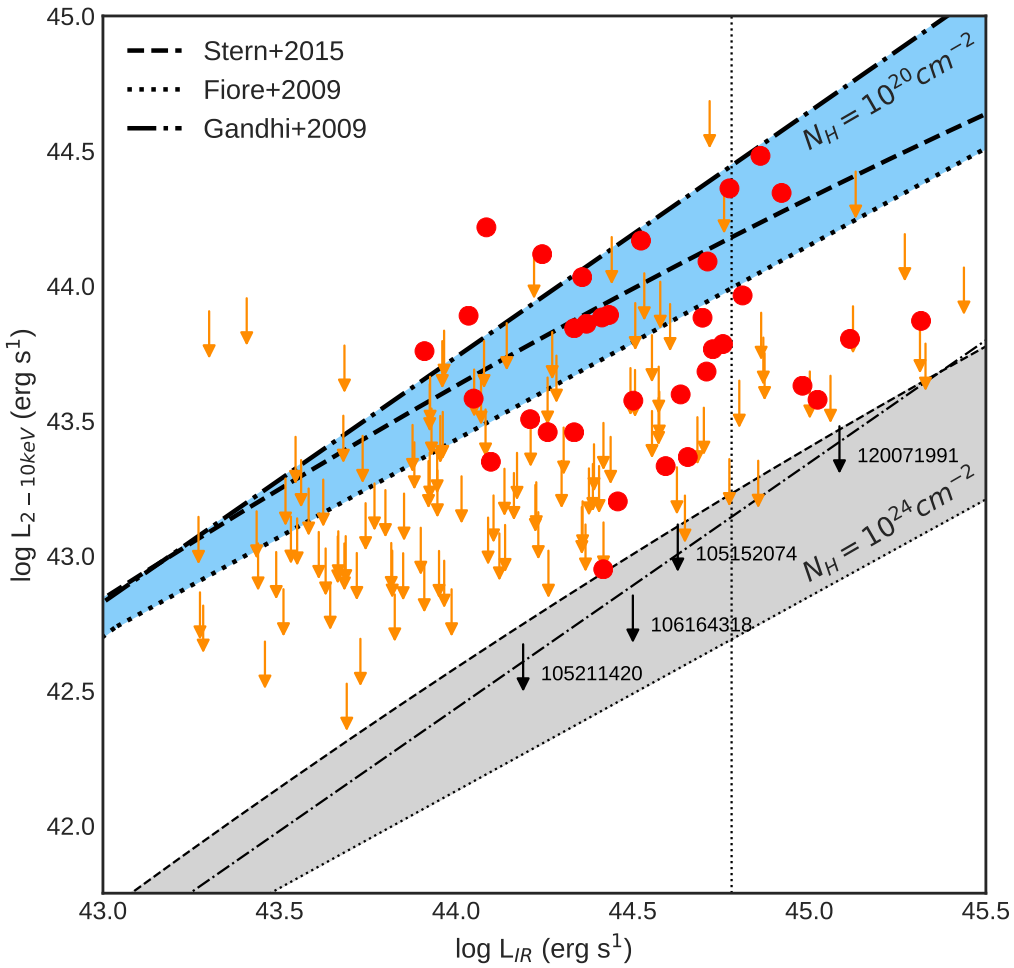

Figure 5.12: The X-ray luminosity in the [2-10 kev] band as a function of the IR luminosity of the SED selected AGNs with (red circles) and without (orange arrows) X-ray detections. The thick lines represent the correlation derived by (Stern 2015), Fiore et al. (2009) and Gandhi et al. (2009) for unabsorbed AGNs. The lower thinner lines are for obscured ($N_H = 10^{24}$cm^{-2}) AGNs, assuming X-ray suppression with a factor of 20. The shaded areas correspond to the scatter of the relations derived in the aforementioned studies. The vertical line at $L_{IR}>6\times10^{44}$ erg s^{-1} corresponds to our threshold for luminous sources. The thick black arrows indicate the most heavily obscured AGNs according to this plot.

is correlated with the unabsorbed X-ray emission in the AGNs for a wide range of

luminosities (Lutz et al. 2004; Gandhi et al. 2009; Mateos et al. 2015; Stern 2015). The mid-IR emission provides a good measurement of the AGN luminosity regardless obscuration. On the other hand, the X-ray emission is expected to be suppressed at some level with increasing HI column densities (Alexander et al. 2005, 2008). Thus, the X-ray to mid-IR luminosity ratio constitutes another measurement of obscuration. In Figure 5.12, we plot the X-ray luminosity in the hard band as a function of the AGN mid-IR luminosity derived by `X-CIGALE`. To facilitate comparison with previous studies, we transformed the luminosities from [2-8 keV] band into the [2-10 keV] band using the `WebPIMMS`[3] `v4.8d` software, assuming a photon index of $\Gamma = 1.7$ and the Galactic HI column density $N_H = 10^{20}\mathrm{cm}^{-2}$. The dashed bold line in the plot represents the relation derived from Stern (2015) from an unabsorbed AGN sample distributed over several orders of magnitude. For reference, we plot the relations given by Fiore et al. (2009) and Gandhi et al. (2009). The bottom lines indicate the corresponding relation for obscured sources with $N_H = 10^{24}\mathrm{cm}^{-2}$. For the latter, we assumed that the X-ray emission is suppressed by a factor of 20 (Lansbury et al. 2015).

The majority of the sources lie below the Stern (2015) relation, suggesting that these are obscured AGNs. Four sources (thick black arrows in Fig. 5.12) lie in the Compton-Thick (CT) regime, that suggests they may have column densities $N_H \geq 10^{24}\mathrm{cm}^{-2}$ (but see, Georgantopoulos et al. 2011, for possible contaminants). Figure 5.13 presents the SEDs of these four sources.

5.4 Discussion

The identification of AGNs in a specific wavelength regime depends strongly on the physical and observational properties of the sources, such as the luminosity, redshift, absorption and black hole mass. Thus, different selection techniques are more sensitive to different AGN populations and the overlapping among them is affected by the completeness and reliability along with the depth of each survey. To compare the various selection methods used in this work in a uniform manner, we selected the X-ray detected AGNs that have a counterpart in our initial VIPERS catalogue (with optical, near-IR and mid-IR counterparts). The Venn diagram, in Figure 5.14, presents the overlap of the SED (160), mid-IR (54) and X-ray (116) selected AGN samples. The numbers in the parenthesis indicate the number of confirmed AGN through optical spectroscopy ([NeV] emission, MEx and TBT diagrams). In total, 139/160 (∼87%)

[3] https://heasarc.gsfc.nasa.gov/docs/software/tools/pimms.html

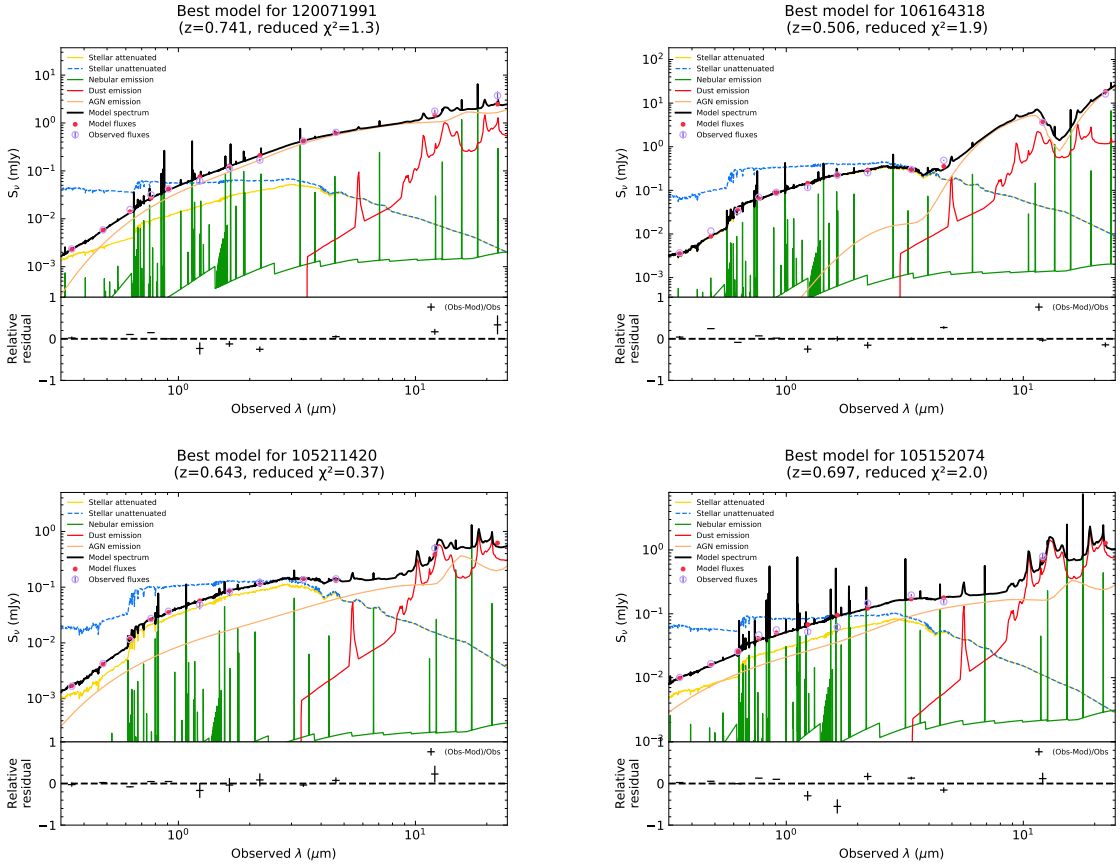

Figure 5.13: SEDs of the four AGNs with extreme obscuration according to the L_X–L_{IR} relation. The dust emission is plotted in red, the AGN component in green, and the attenuated (unattenuated) stellar component is shown with the yellow (blue) solid (dashed) line, while the orange lines shows the nebular emission. The total flux is represented with black colour. Below each SED, we plot the relative residual fluxes versus wavelength.

of the SED selected AGNs revealed by our analysis, are also classified as AGN in at least one of the different AGN selection methods presented in the literature.

Specifically, all the mid-IR selected AGN (Mateos et al. 2012; Stern et al. 2012) are classified as AGN via our SED fitting technique. Regarding AGNs selected by the Assef et al. (2013) criteria (Section 5.3.3), 32 (44) out of 35 (52) sources with a reliability of 90% (75%), were also characterised as AGN, by our SED fitting criteria. This corresponds to a percentage of 91.5% (84.6%). The mid-IR sources not selected in our analysis have values of ΔBIC lower than the threshold adopted in this work. To better understand the behaviour of ΔBIC in this colour diagnostic and check if the latter sources are real AGNs, we plotted the populations defined in Table 5.2 in

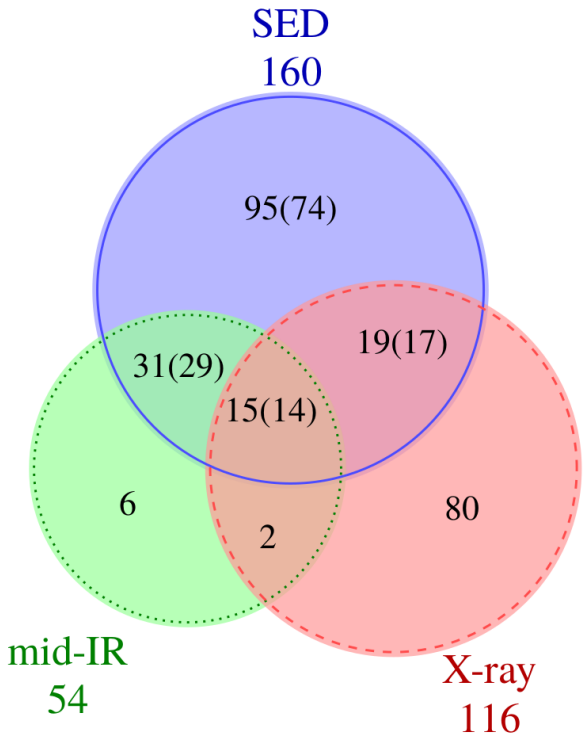

Figure 5.14: Venn diagram of the AGN samples selected through SED decomposition (blue-solid), X-ray detection (red-dashed) and mid-IR criteria (green-dotted). These samples consists of sources that fall inside the VIPERS field, have spectroscopic redshifts from VIPERS in the range [0.5,1.2] and have optical, near-IR and mid-IR counterparts. The numbers inside parenthesis are the confirmed SED selected AGNs through optical spectroscopy.

the Assef et al. (2013) diagram (Fig. 5.16). Starting from the upper left panel to the lower right, ΔBIC is decreasing, while the probability of the sources hosting an AGN is increasing. The normal galaxy population with values ΔBIC>2 (upper left and middle panels) is consistent with the mid-IR colours and all lie outside the wedges of Assef et al. (2013). In cases where it is uncertain which model describes better the observed SEDs (upper right) and the probability is 50-50, the majority of this population lies still below the lines. Increasing the probability of a source to host an AGN (the observed data fit better models with galaxy and AGN templates), it moves towards the mid-IR AGN wedges defined by Assef et al. (2013) (lower panels). Despite the relaxed threshold adopted in this work, there is a large population that would not be selected through simple colour-colour cuts. This SED selected population is twice the number of the AGN selected through the Assef et al. (2013) criteria. Figure 5.16 shows the robustness of the latter diagnostic criteria, but also the importance of selecting AGNs via SED decomposition techniques, as they are able to identify a much

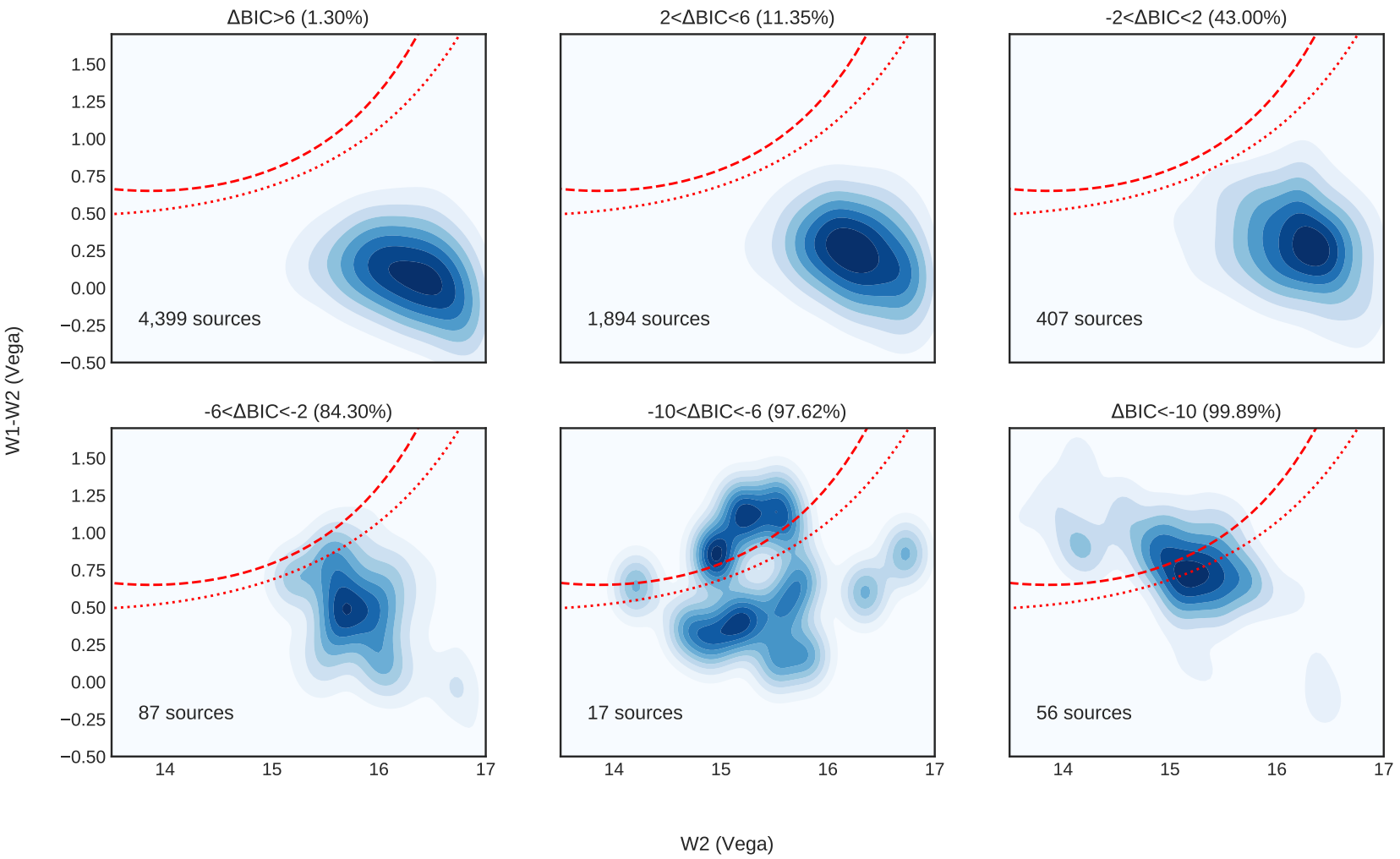

Figure 5.15: Density plots of the VIPERS sample in the W2, W1–W2 magnitude-colour diagram separated into bins with different ΔBIC values (AGN probabilities). Above each panel, we label the range of ΔBIC and in the parenthesis the average probability of the sources hosting an AGN. The dashed and dotted lines represent the AGN selection criteria defined by Assef et al. (2013) with 90% and 75% reliability, respectively.

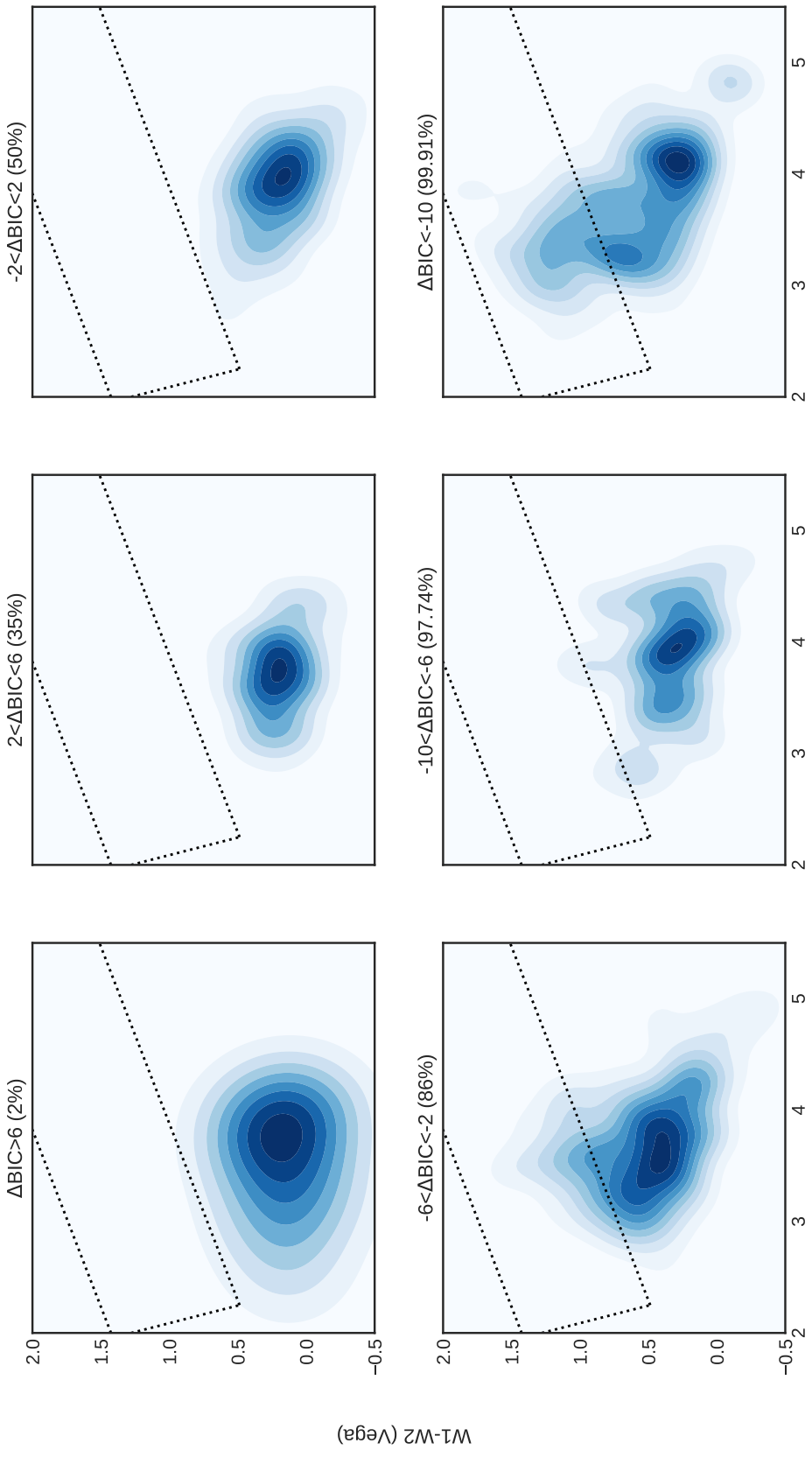

Figure 5.16: Density plots of the VIPERS sample in the W2–W3, W1–W2 magnitude-colour diagram separated into bins with different ΔBIC values (AGN probabilities). Above each panel, we label the range of ΔBIC and in the parenthesis the average probability of the sources hosting an AGN. The dotted lines represent the AGN selection criteria defined by Mateos et al. (2012).

larger AGN population. SED fitting may better separate the mid-IR AGN emission from their host galaxy. In Figure 5.17, we plot the colour-magnitude diagram for the 160 SED selected AGNs colour-coded based on the r–W2 colour. Larger symbols correspond to higher AGN IR luminosities, derived by the SED fitting. It is evident that while the method of Assef et al. (2013) selects the brightest and most optical red AGNs, SED decomposition allows us to identify less luminous AGNs with bluer colours.

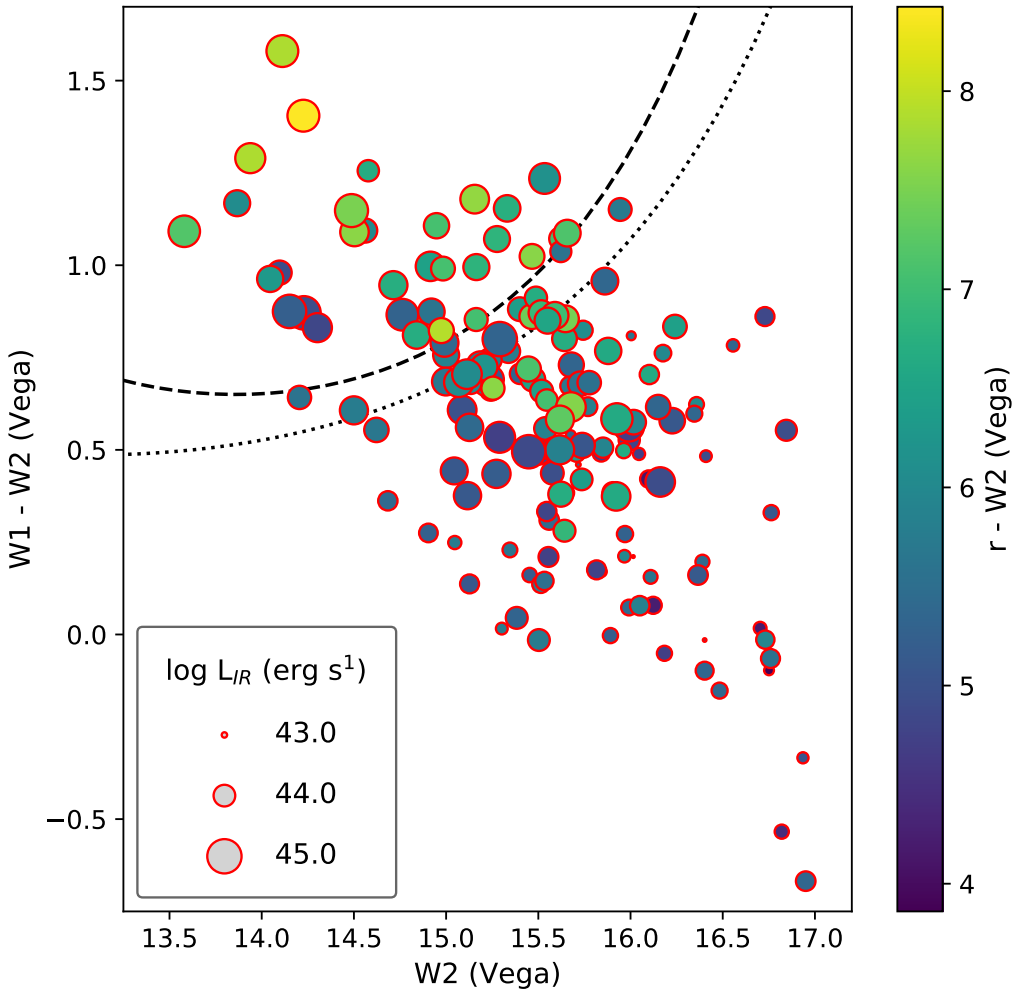

Figure 5.17: *WISE* magnitude-colour (W2, W1–W2) diagram for the 160 SED selected AGNs colour-coded based on their optical colour (r–W2). The size of the circles corresponds to the IR luminosity as indicated in the legend. The dashed (dotted) line represents the Assef et al. (2013) selection threshold with reliability of 90% (75%).

Furthermore, among the Assef et al. (2013) selected AGNs with reliability 75%

and 90%, 17 (∼33%) and 14 (∼40%) sources have X-ray emission, respectively. Mendez et al. (2013) showed that the percentage of mid-IR selected AGNs that have X-ray detections depends strongly on the depths of the surveys and ranges between 45% to 90%. When the depth of the IR surveys increases, this fraction decreases. On the other hand, increasing the X-ray depth increases the fraction of mid-IR AGNs that are X-ray detected. For example, Pouliasis et al. (2019) found that ∼70% of mid-IR AGNs have X-ray detections in the ∼7 Ms *Chandra* Deep Field South (CDFS) image. Our results agree well with those of Mendez et al. (2013) for shallow depth X-ray surveys (in this work the average is ∼20 ks) and low sensitivity limits in the IR bands. The majority of the X-ray sources lie outside the mid-IR wedges (Fig. 5.5). This could be due to the fact that these sources may be less luminous in mid-IR or that the relative emission from the host galaxy overpower this from the AGN. Sources inside the Assef et al. (2013) wedge with no X-ray counterparts are expected to be luminous obscured AGNs. Out of these, 12/37 (∼33%) have [NeV] emission in their optical spectra while the vast majority have red colours.

Finally, 30% of the X-ray population is selected as AGN via SED decomposition with high significance. On the other hand, we found that ∼21% of the SED selected AGNs have X-ray emission. As shown in Table 5.2, the majority of the X-ray sources have low AGN probabilities, based on our Bayesian analysis. One possible explanation is that these sources do not have large enough amount of dust around their black hole to overpower the host galaxy luminosity. Indeed, the average IR AGN luminosity for the X-ray sources not selected through SED decomposition is almost 0.5 dex lower compared to SED selected AGNs. To investigate this scenario, in Figure 5.18, we plot the stacked SEDs for AGN samples identified via different combinations of AGN selections methods. AGNs selected through the SED fitting technique, mid-IR colours and are detected in X-rays (upper right panel) are in general AGN-dominated systems. Furthermore, the median AGN emission extends to the optical wavelengths which indicates that these are less obscured sources. In the case of AGN that are SED and mid-IR selected (upper left panel) the AGN component is dominant but the AGNs are more obscured. Similarly, the SED-only selected sample (bottom left panel) consists of obscured AGNs, though with less dominant AGN component. In contrast, the X-ray only selected AGNs (lower right panel) comprise of systems that the host galaxy component dominates the SED. The scatter in the AGN emission in those stacked SEDs, especially in the optical regime of the spectrum, is mostly due to the different types of AGN (obscured, unobscured, intermediate type).

Taking into account only sources with high mid-IR luminosity, 7 out of 21 sources (∼34%) have an X-ray counterpart. The luminosity cut at $L_{IR}>6\times10^{44}$ erg s^{-1} (vertical line in Fig. 5.12) was defined in Del Moro et al. (2016) and corresponds to the

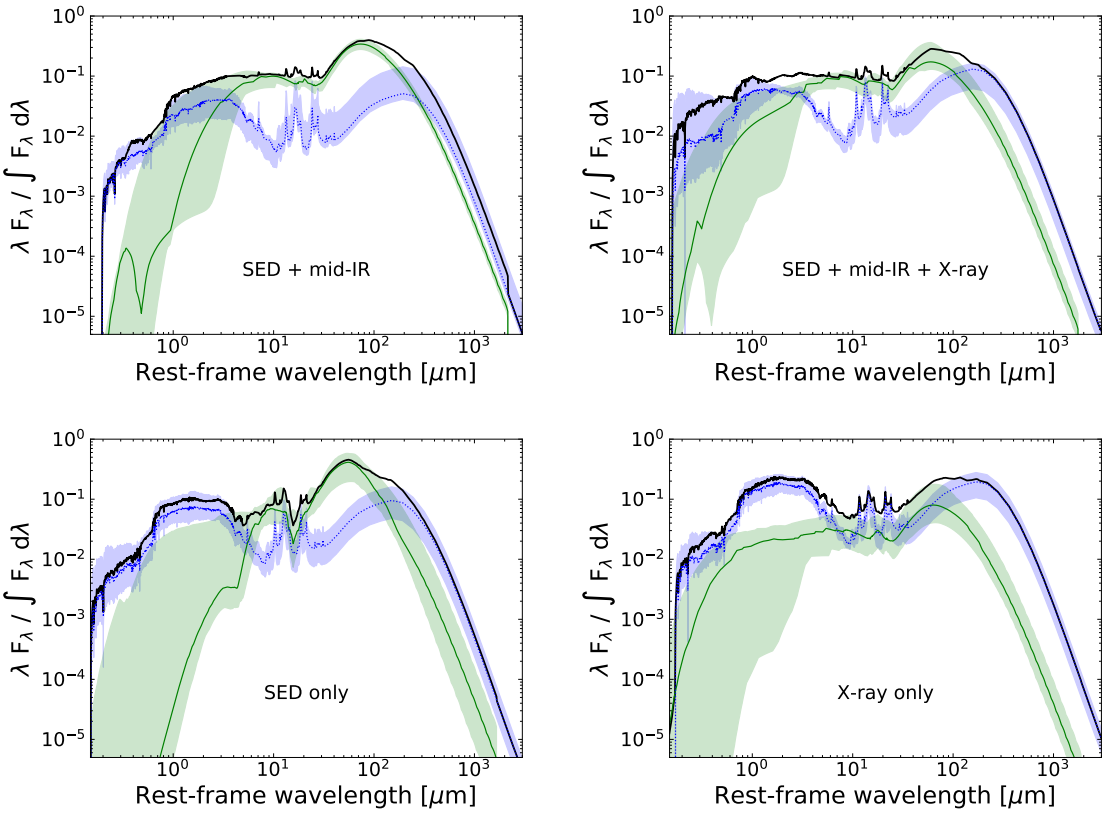

Figure 5.18: Stacked SEDs at rest-frame for AGN samples selected through different selection methods as indicated. The median SEDs of the host galaxy emission and the AGN components are plotted with blue dotted and green solid lines, respectively. The black thick line shows the median total flux, while the shaded areas correspond to 15$^{\rm th}$ up to 75$^{\rm th}$ percentiles at each wavelength.

X-ray quasar regime according to the L_X-L_{IR} relation. Del Moro et al. (2016) found that 70% of mid-IR luminous AGNs in the redshift range $1< z <3$ is detected in the X-rays. This discrepancy comes partially from the different redshift regime and mostly from the depth of their X-ray observations (2 and 4 Ms) *Chandra* X-ray observations compared to the *XMM-Newton* observations used in this study with much lower exposure times (∼20 ks). In Mountrichas et al. (2017), the obscured fraction among a sample of type I AGNs (average redshift equal to 2.3) with luminosities higher than $L_{IR}>1.6\times10^{46}$ erg s^{-1} was found ∼10%. This indicates a higher number of obscured sources at higher redshifts and type I AGNs. Finally, 10/21 of these sources are also [NeV] emitters, while the majority of them are classified as optically red (r–W2≥6). Example SEDs of the luminous mid-IR AGNs with and without X-ray detections are shown in Figure 5.19 and Figure 5.20, respectively.

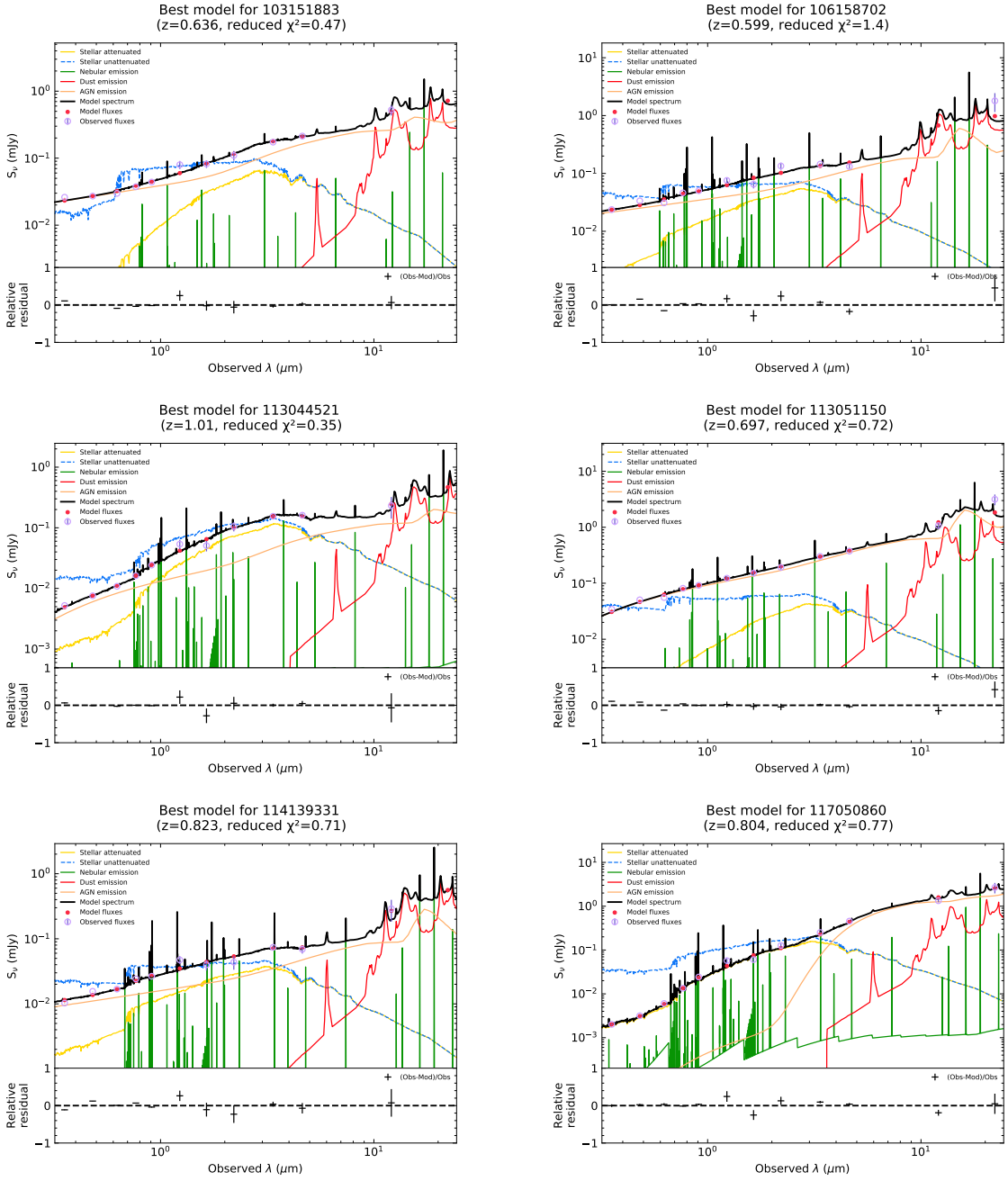

Figure 5.19: Six example SEDs of luminous AGNs (L_{IR}>6×10^{44} erg s^{-1}) with X-ray detections. The dust emission is plotted in red, the AGN component in green, and the attenuated (unattenuated) stellar component is shown with the yellow (blue) solid (dashed) line, while the orange lines shows the nebular emission. The total flux is represented with black colour. Below each SED, we plot the relative residual fluxes versus wavelength.

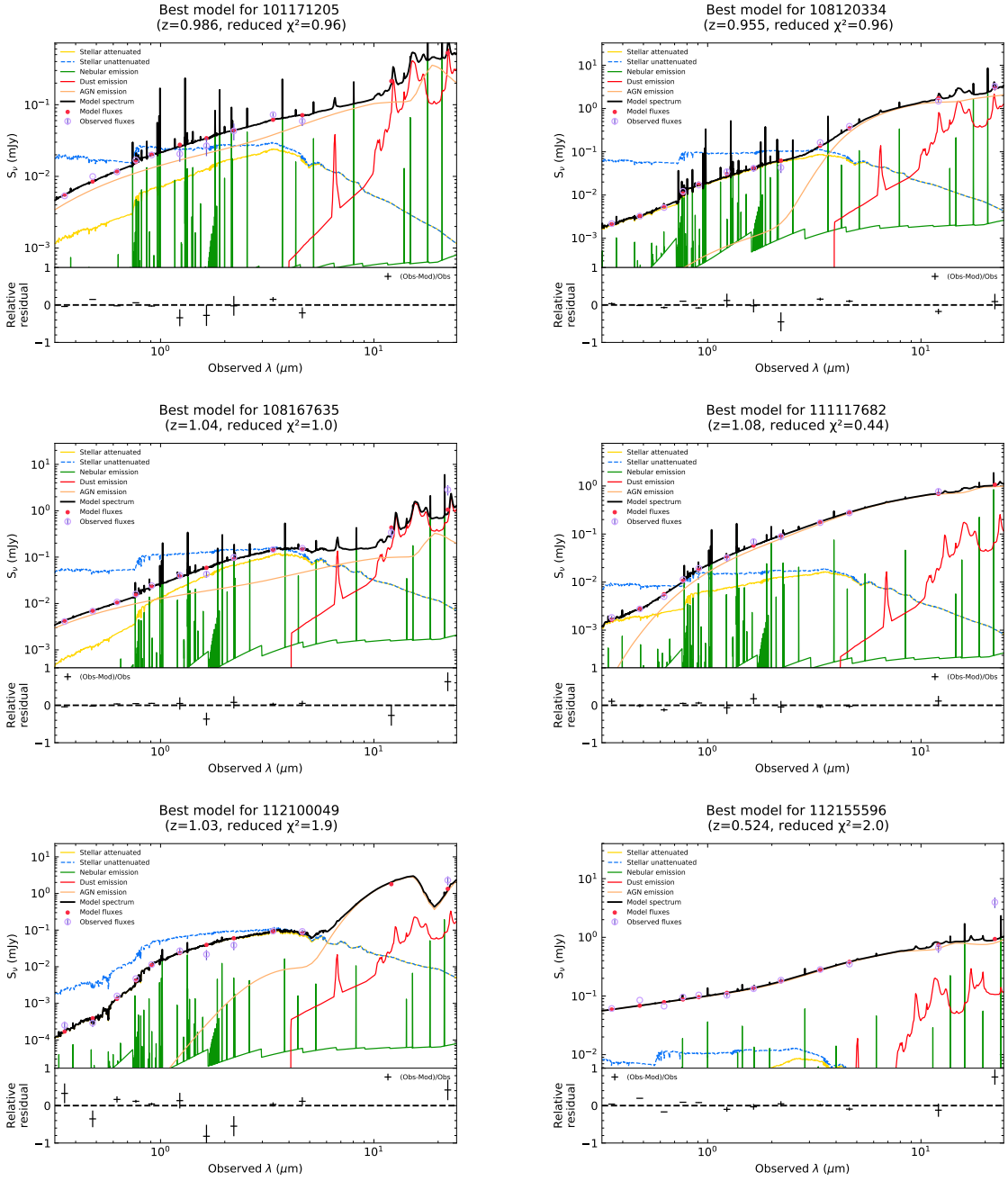

Figure 5.20: Six example SEDs of luminous AGNs (L_{IR}>6×10^{44} erg s^{-1}) without X-ray detections. The dust emission is plotted in red, the AGN component in green, and the attenuated (unattenuated) stellar component is shown with the yellow (blue) solid (dashed) line, while the orange lines shows the nebular emission. The total flux is represented with black colour. Below each SED, we plot the relative residual fluxes versus wavelength.

Chapter 6

Summary & Conclusions

In this work, different selection techniques were used to identify AGN based on photometric and spectroscopic data from different wavelength regimes of the electromagnetic spectrum (optical, infrared, X-rays) as well as techniques that are based on flux variability. The main purpose is to enhance the reliability and completeness of the existing methods, but also to apply and test new ones. The thesis comprises of two main parts, AGN identification through variability and through SED decomposition. Optical variability was used in the first two Chapters. In GOODS-S field, it was used in order to constrain the significance and reliability of the method compared to other selection methods using X-ray and IR data. The results of the latter were applied in the CANDELS and Frontier Fields. The second part uses SED fitting techniques with a Bayesian analysis, in order to search for obscured AGN in the VIPERS field. The advantages and limitations are discussed in detail, while the results are compared and validated through spectroscopic analysis and AGN selected in the X-ray and mid-IR regimes. Below, I summarize the main results of this thesis:

GOODS South field: Variability is a basic property of AGNs and has been proven to be a reliable method to reveal non-obscured LLAGNs. Many studies assembled multi-epoch data and used variability to identify AGNs. The need, though, for highest photometric accuracy and long-term observational monitoring impose limits on the completeness of such surveys. Previously in the GOODS South field, Villforth et al. (2010, 2012) and Sarajedini et al. (2003, 2011) used a five epoch dataset (i- and z-band, respectively) spanning six months. In a larger area and from ground-based telescopes, Falocco et al. (2015) used, also, a six month baseline, while Trevese et al. (2008) used a longer time baseline of two years.

In this work, we substantially increased the time baseline by up to ten years using deep HST observations (z-band).We created a new catalogue of optically variable

AGN candidates in the GOODS-S. We used SExtractor to construct the light curves of ∼22,000 sources. The Median Absolute Deviation was utilized to search for variability as it has the highest performance among the other variability indices in the presence of outliers. A 3.5σ cut-off was applied to identify variable sources. Our results can be summarized as follows:

- We identified 116 high confidence variable sources. After removing three known Supernovae, we ended up with 113 AGN candidates (103 extended and ten point-like).
- We explored the mid-IR properties of our AGN candidates. 41 sources have been detected in all four *Spitzer*/IRAC bands and, out of those, 13 and five sources are classified as AGNs through the colour selection adopted by Lacy et al. (2007) and Donley et al. (2012), respectively. Also, the space observations compared to ground-based studies identify AGNs deep into the IR region when other methods fail.
- We cross-matched our AGN sample with the published X-ray catalogues (CDF-S 2, 4 & 7 Ms and ECDFS 250 ks) and found 26 variable sources with X-ray counterparts. This corresponds to ∼23% (26/113).
- For all the sources without X-ray detections, we used the 7 Ms image in CDF-S and estimated the flux upper limits using a confidence level of 99.7%. These sources are optically fainter with higher redshifts up to z=4.
- The X-ray to optical flux ratios revealed that the variable sources are consistent with the AGN population, as they lie within the area of $-2 < \log(F_X/F_{\rm opt}) < +2$, but their average $\log(F_{\rm X}/F_{\rm opt})$ ratio suggests that high-redshifted intrinsically X-ray weak AGNs lie below the conventional $\log(F_{\rm X}/F_{\rm opt}) = 0$ area.
- The X-ray luminosities of our variable AGN candidates are comparable to those of LLAGNs in the Local Universe (Panessa et al. 2006; González-Martín et al. 2015). Hence, the variability in deep optical photometric data is a promising method of finding optically low luminosity AGNs, which the X-ray observations may miss.

CANDELS & Frontier fields: The Hubble catalogue of variables is a project aimed to identify all the variable sources from Hubble Source Catalogue. It provides a unique opportunity to search for objects that vary from days up to more than ten years. The list of variable sources could consist of SNe, Cepheids, fast transients and also AGN. In this work, we used the HCV data to identify AGN candidates in the

CANDELS and Frontier fields. These fields are appropriate to search for AGN as they consists of multiple observations with long exposure times. The main results can be summarized as follows:

- In the CANDELS fields, the HCV catalogue resulted in 621 variable sources, 179 multi-filter variable candidates (MFVC) and 442 single-filter variable candidates (SFVC). Out of those, 171 were evaluated by the expert validation and considered as high-confidence or probable variable sources.
- Using the Simbad database and excluding the stellar population, 75% and 45% of the high-confidence and probable variable sources, respectively, are confirmed AGN or quasars. The remaining extended sources are expected to be low-luminosity AGN.
- In the Frontier fields, we identified 463 variable sources in twelve cluster and parallel fields. Out of those, 302 (174 MFVC & 128 SFVC) are extended and 161 (93 MFVC & 68 SFVC) point-like sources.
- The fraction of the variable sources to the total number of sources is generally higher for the cluster fields (2.95%) rather than the parallel fields (1.42%).
- We explored the mid-IR selected AGN in three of the cluster with available data using the selection criteria of Lacy et al. (2007) and Donley et al. (2012). In total, there are 223 sources inside the Lacy wedge, while 30 sources follwing the criteria of Donley et al. (2012). The majority of the variable sources fall outside these wedges. Due to their extension and their position in the diagram, they are expected to be low-luminosity AGN.

VIPERS field: AGN selection based on X-ray emission is by far the most reliable and effective tool to select a large number of AGNs. However, it is biased against the most obscured ones. SED fitting techniques in the mid-IR regime are able to disentangle the IR emission coming from the torus, which is heated by the central engine from the host galaxy, and identify these populations that X-ray selection misses. In this work, we built and modelled the SEDs of 6,860 sources in the CFHTLS W1 field, using the `X-CIGALE` software. All sources in this sample have spectroscopic redshifts from the VIPERS survey and have been observed in optical (CFHTLS), near-IR (VHS) and mid-IR (*WISE*) photometric bands. We fitted these SEDs with galaxy only templates and in a second run we combined both galaxy and AGN templates. Using a Bayesian approach, we compared these two fits and selected the objects in which the addition of an AGN component provides higher statistically confidence level. We ended up

with 160 sources with high AGN probability. Our main results can be summarized as follows:

- Exploring their optical spectra, there are 27 broad line AGNs, while 42/114 (37%) inside the spectral coverage have [NeV] emission. Using the MEx and TBT diagrams, 90% of our SED selected AGNs, with the corresponding emission lines detected, fall inside the AGN or composite areas in these diagrams. In total, 134/160 (84%) of our SED selected sources are confirmed AGNs, by these robust diagnostic tools.

- 34/160 (21%) of the SED selected AGNs have X-ray emission. On the other hand, among the X-ray selected AGNs, 34/116 (30%) sources are selected through our SED analysis method. The remaining X-ray population not selected though SED fitting has host-galaxy dominated systems.

- To compare our SED decomposition technique with mid-IR selection methods that identify AGN, we applied the selection criteria of Assef et al. (2013), Stern et al. (2012) and Mateos et al. (2012). Our analysis, revealed that the SED method recovers the mid-IR AGN population with high completeness. Furthermore, we demonstrated the power of the SED decomposition in finding AGNs with lower luminosities and less AGN-dominated systems, that mid-IR colour techniques fail to uncover. ∼30% of the mid-IR AGNs have X-ray emission, while almost 33% of the remaining sources have in addition [NeV] emission. These numbers are in agreement with those found among the SED selected AGN.

- According to the SED fitting results, the vast majority (∼70%) of the AGNs have inclination angles of view $\psi \leq 50$ indicating some level of obscuration (type 1.5 and 2). To quantify this obscuration, we used a variety of diagnostics.

- We, first, used optical and mid-IR colour selection criteria. 61 sources (∼40%) are classified as optical red AGN according to Yan et al. (2013). Then, we explored the colour criteria proposed by Hickox et al. (2017). Out of 98 sources with high signal-to-ratio in the u and W3 bands, the vast majority lie in the area of obscured AGNs.

- To search for sources with high intrinsic absorption, we used the X-ray to IR luminosity ratio. For non-detections in the X-rays, we derived the upper limits using a confidence level of 99.7%. The position of the sources in the L_X-L_{IR} diagram suggests moderate obscuration, while four sources lie in the area with $N_H = 10^{24}\text{cm}^{-2}$ indicating that these sources could be Compton Thick candidates.

- Finally, there are 21 luminous SED selected AGNs ($L_{IR}>6\times10^{44}$ erg s^{-1}), of which seven have X-ray emission. The remaining sources are also classified as AGNs by both the criteria of Assef et al. (2013) and Mateos et al. (2012) and they are characterized by red colours (r–W2>6).

We conclude that the different methods (SED decomposition, mid-IR colours, X-ray emission or variability) used to identify AGNs are complementary to each other and equally important to constrain the full picture of the AGN demographics. In particular, optical variability is able to identify a large number of LLAGNs even at high redshifts, where the other methods fail. These are critical for studying the faint end of the AGN luminosity function and it might be the key between normal galaxies and AGNs. The completeness of this method compared to the X-ray selected AGN is dependent on the depth of the survey. In deep (mag< 26.5) surveys like in GOODS-S, it is about 25%, while going to shallower depths (mag<23) the percentage reaches up to 70%. Another key factor in optical variability is the threshold used. More restrict cut-offs result in low completeness, but high reliability. The optical variability, further, is able to identify AGN that lie in the IR colour colour diagrams outside the selection criteria. These AGN are extended sources with low luminosity. The variability detection technique used in this work may be applied not only to HST observations but also to other surveys such as the Large Synoptic Survey Telescope (Ivezić et al. 2008, LSST). On the other hand, SED decomposition technique is able to identify a large number of obscured AGNs that the X-ray surveys miss and the simple mid-IR colour cuts do not select. These are critical for studying the AGN population with high obscuration at host-galaxy dominated systems and it might be the key between the connection of normal galaxies and AGNs.

Appendix A

Additional Figures & Tables - Frontier Fields

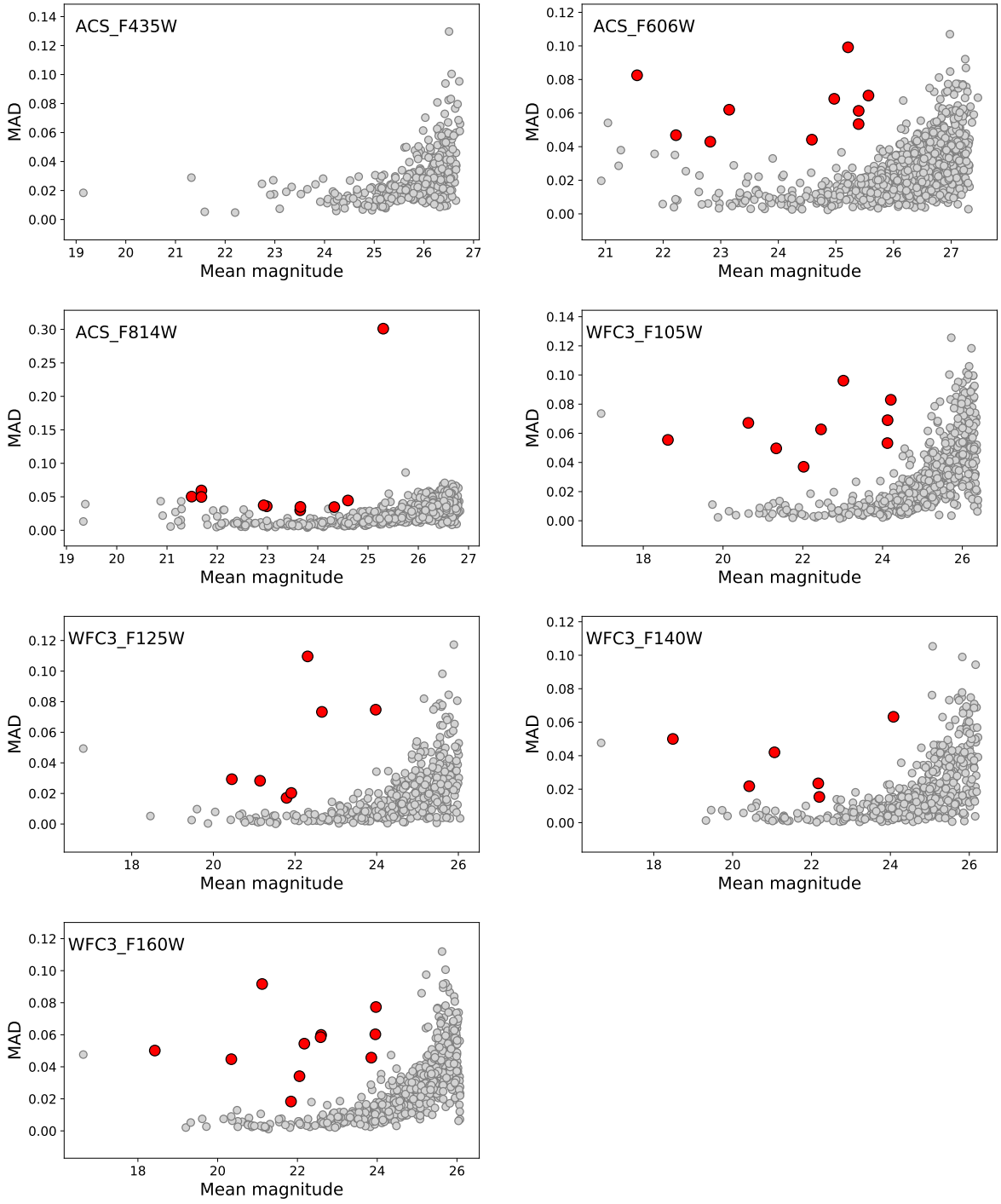

Figure A.1: The MAD as a function of the mean magnitude for different filters as indicated in ABELL 2744 parallel field. All the sources in the field are shown with grey small circles, while the HCV variable sources are shown with red circles.

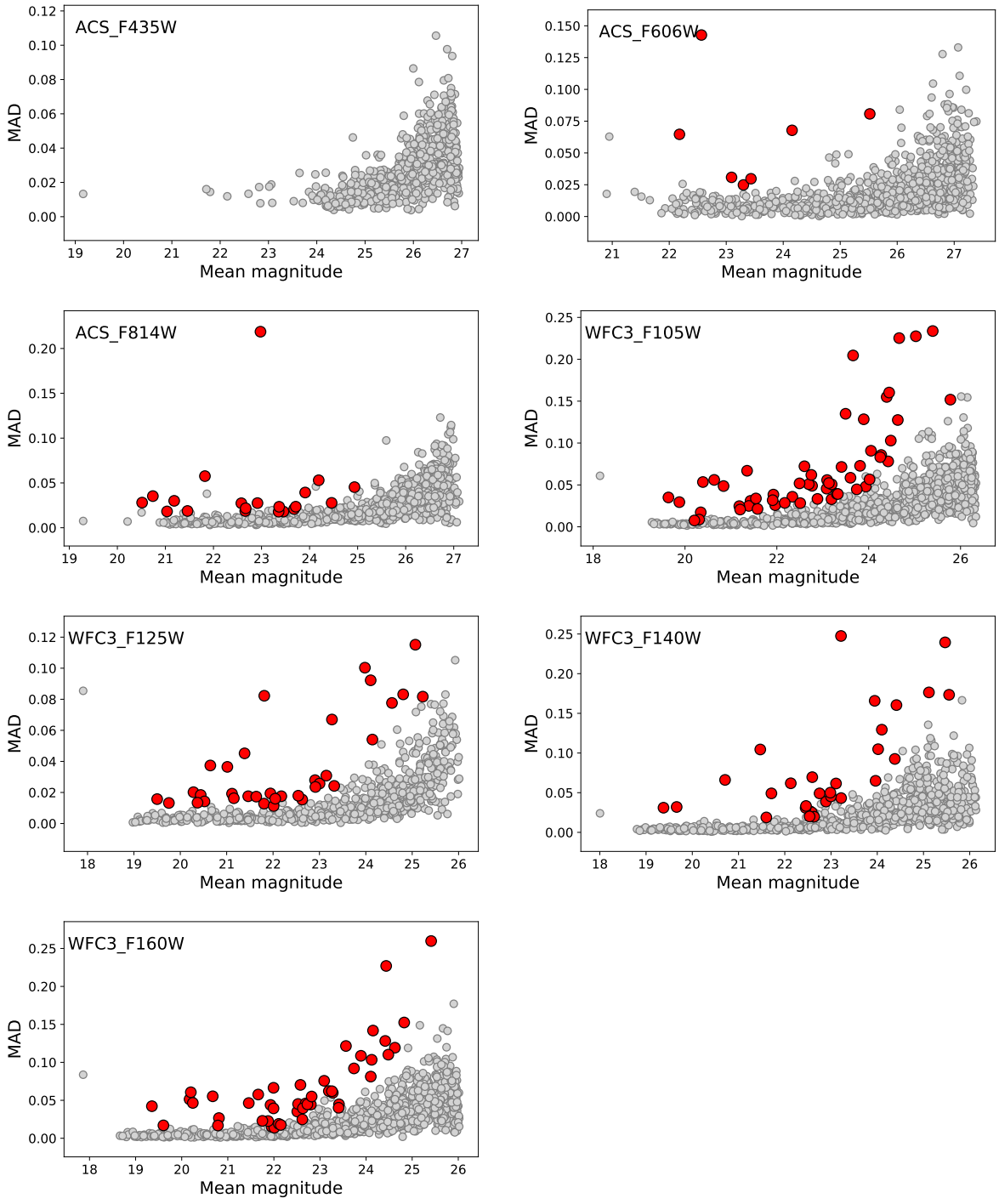

[MAD vs. magnitude in ABELL 370 cluster field.]The MAD as a function of the mean magnitude for different filters as indicated in ABELL 370 cluster field. All the sources in the field are shown with grey small circles, while the HCV variable sources are shown with red circles.

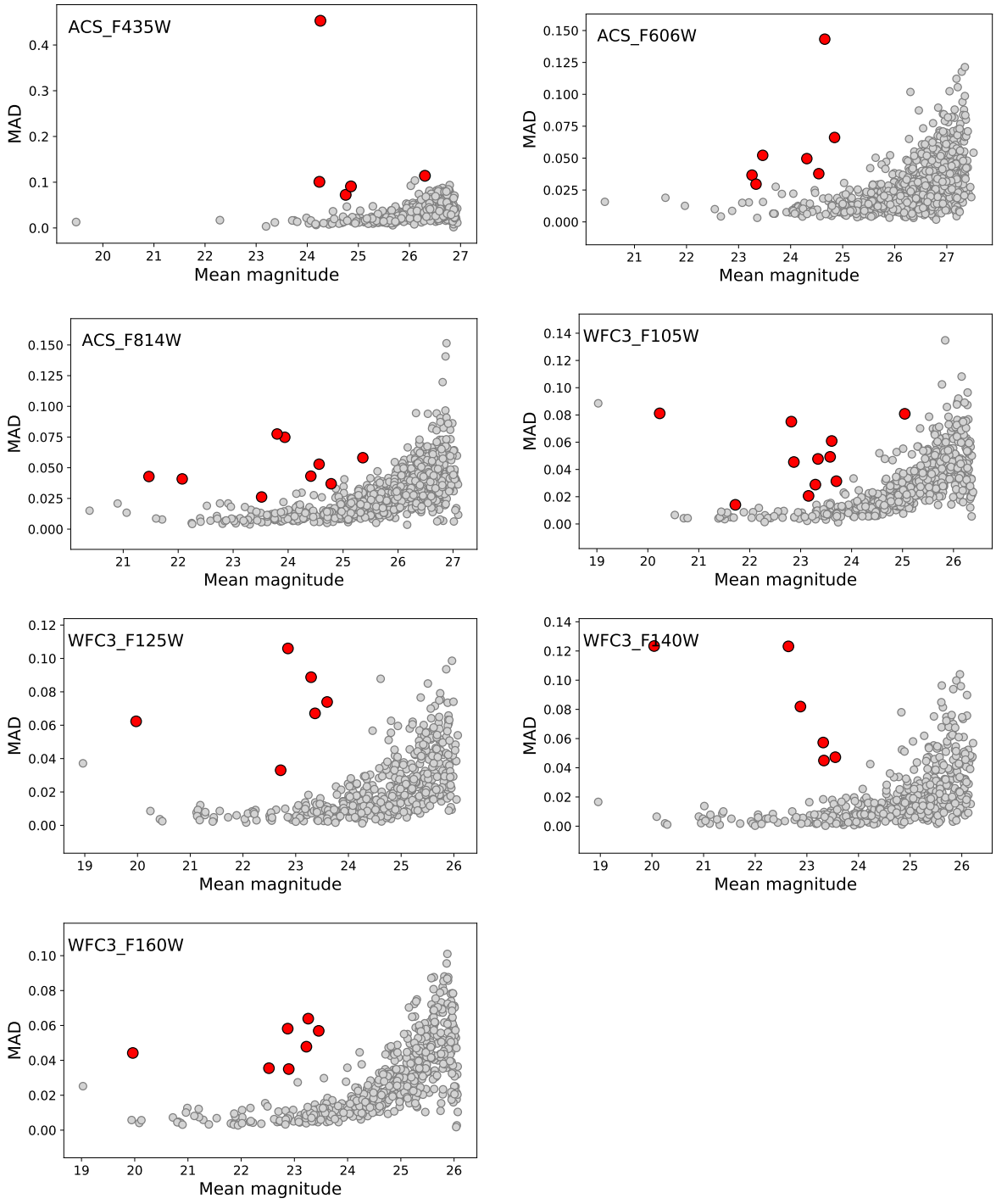

[MAD vs. magnitude in ABELL 370 parallel field.]The MAD as a function of the mean magnitude for different filters as indicated in ABELL 370 parallel field. All the sources in the field are shown with grey small circles, while the HCV variable sources are shown with red circles.

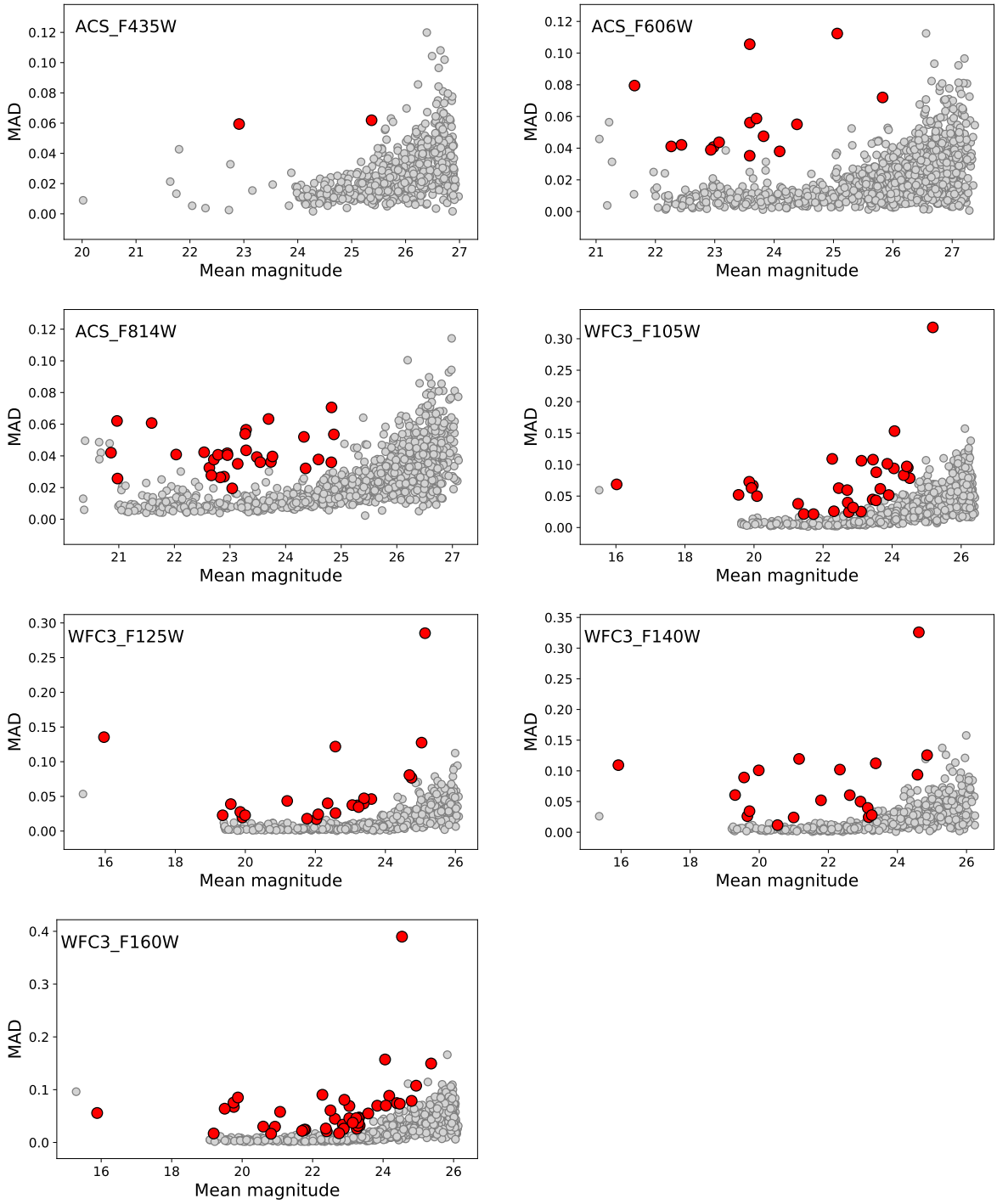

[MAD vs. magnitude in ABELL S1063 cluster field.]The MAD as a function of the mean magnitude for different filters as indicated in ABELL S1063 cluster field. All the sources in the field are shown with grey small circles, while the HCV variable sources are shown with red circles.

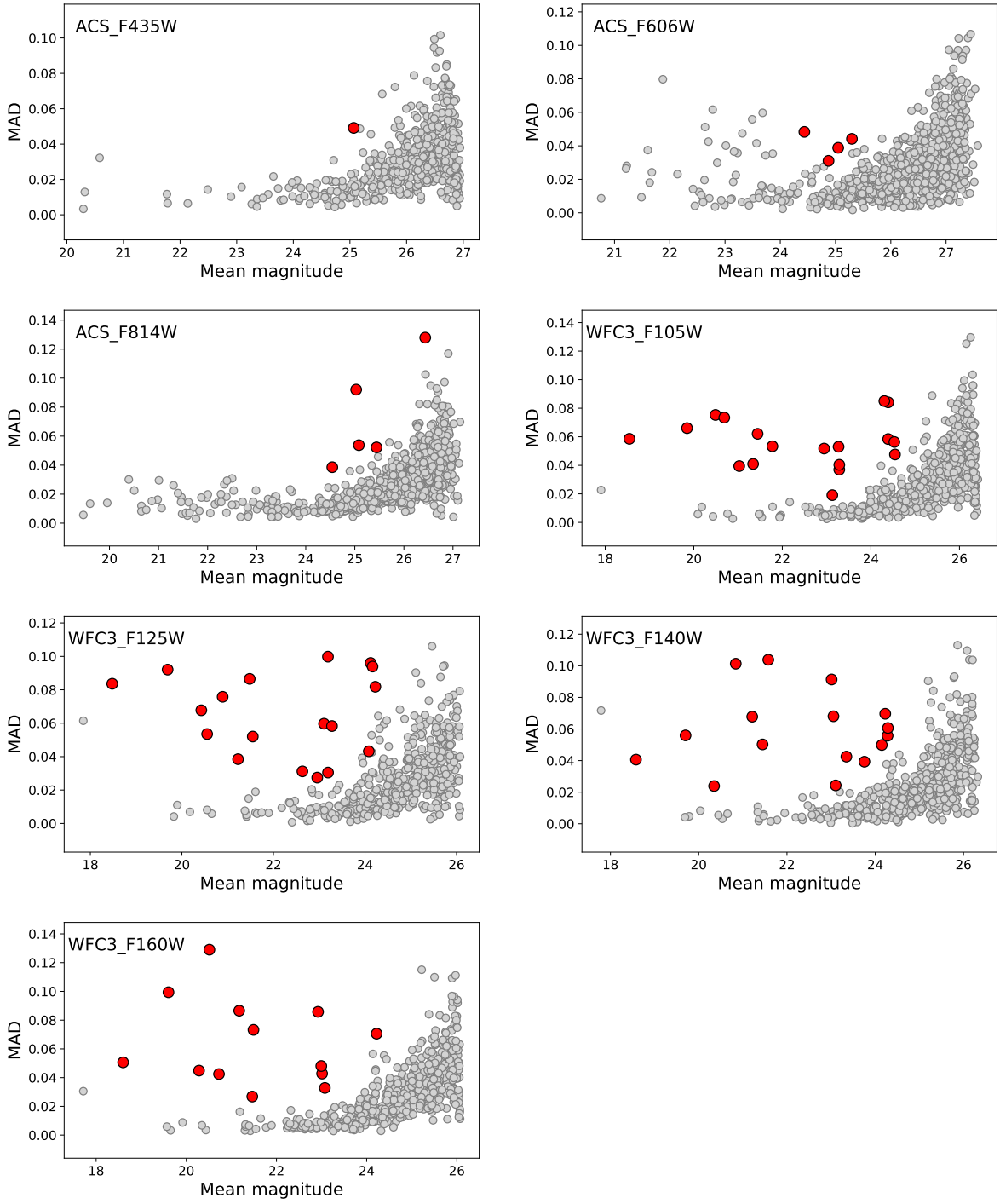

Figure A.2: The MAD as a function of the mean magnitude for different filters as indicated in ABELL S1063 parallel field. All the sources in the field are shown with grey small circles, while the HCV variable sources are shown with red circles.

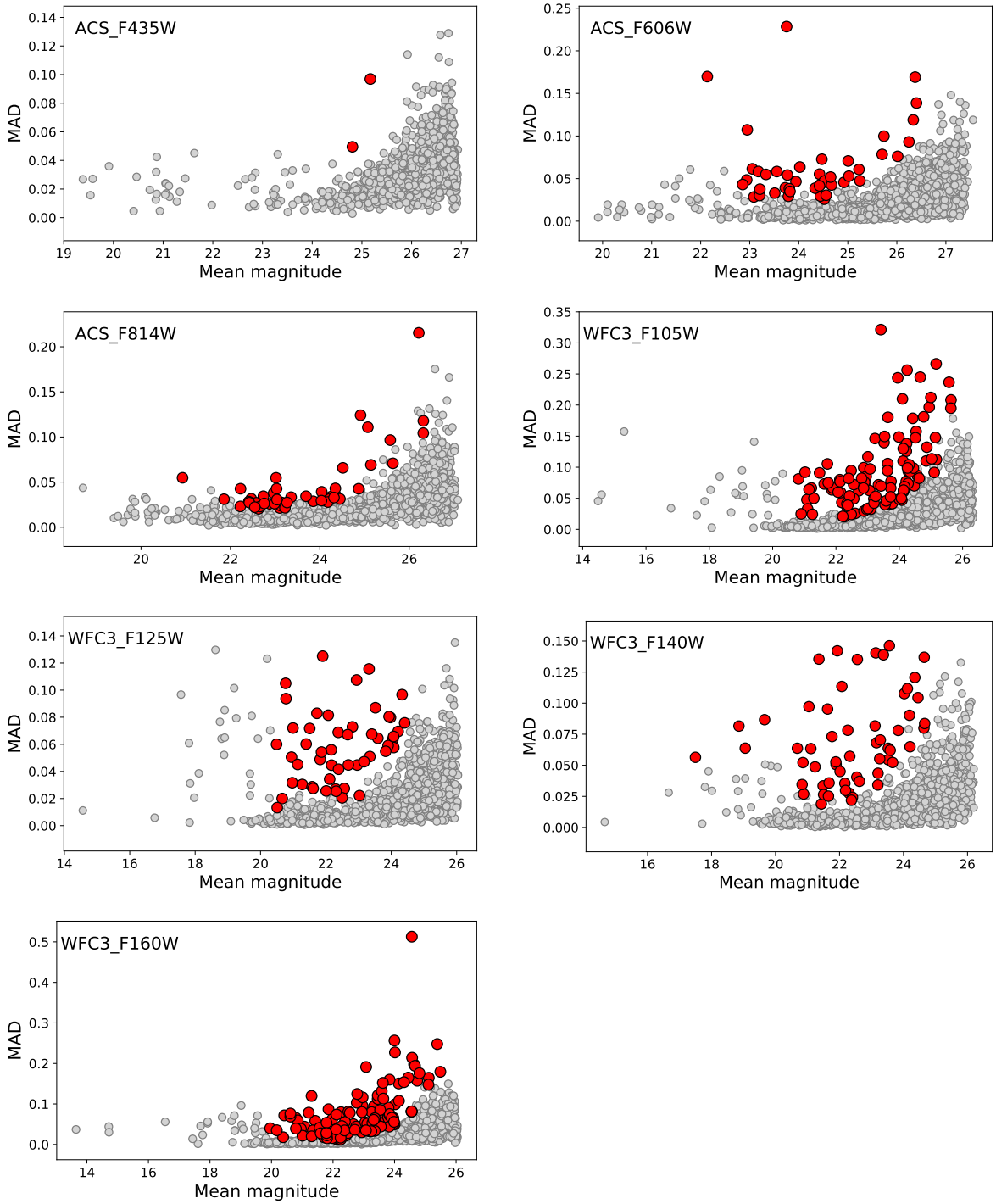

Figure A.3: The MAD as a function of the mean magnitude for different filters as indicated in the combined cluster and parallel field of MACS 0717. All the sources in the field are shown with grey small circles, while the HCV variable sources are shown with red circles.

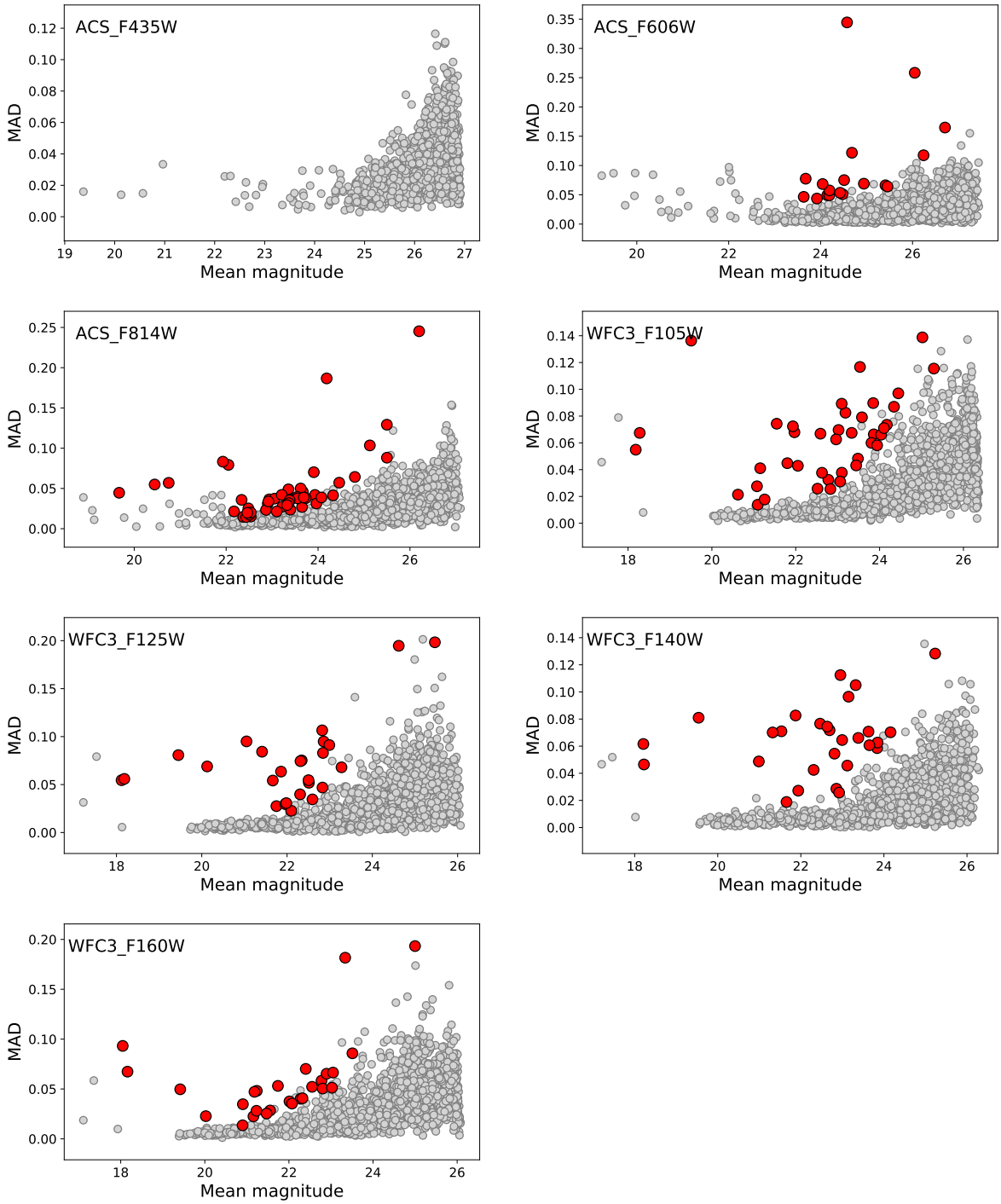

Figure A.4: The MAD as a function of the mean magnitude for different filters as indicated in the combined cluster and parallel field of MACS 1149. All the sources in the field are shown with grey small circles, while the HCV variable sources are shown with red circles.

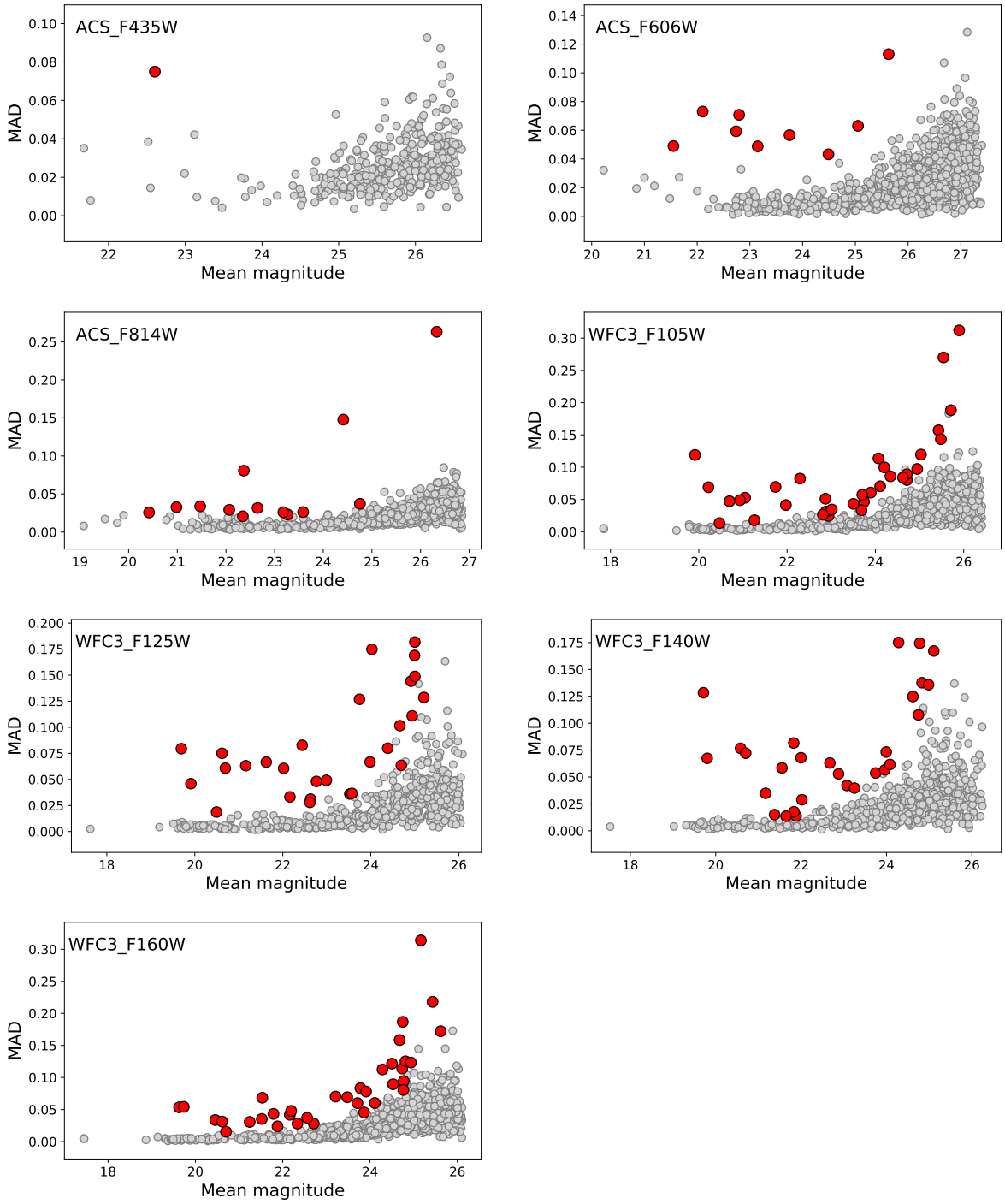

Figure A.5: The MAD as a function of the mean magnitude for different filters as indicated in MACS 0416 cluster field. All the sources in the field are shown with grey small circles, while the HCV variable sources are shown with red circles.

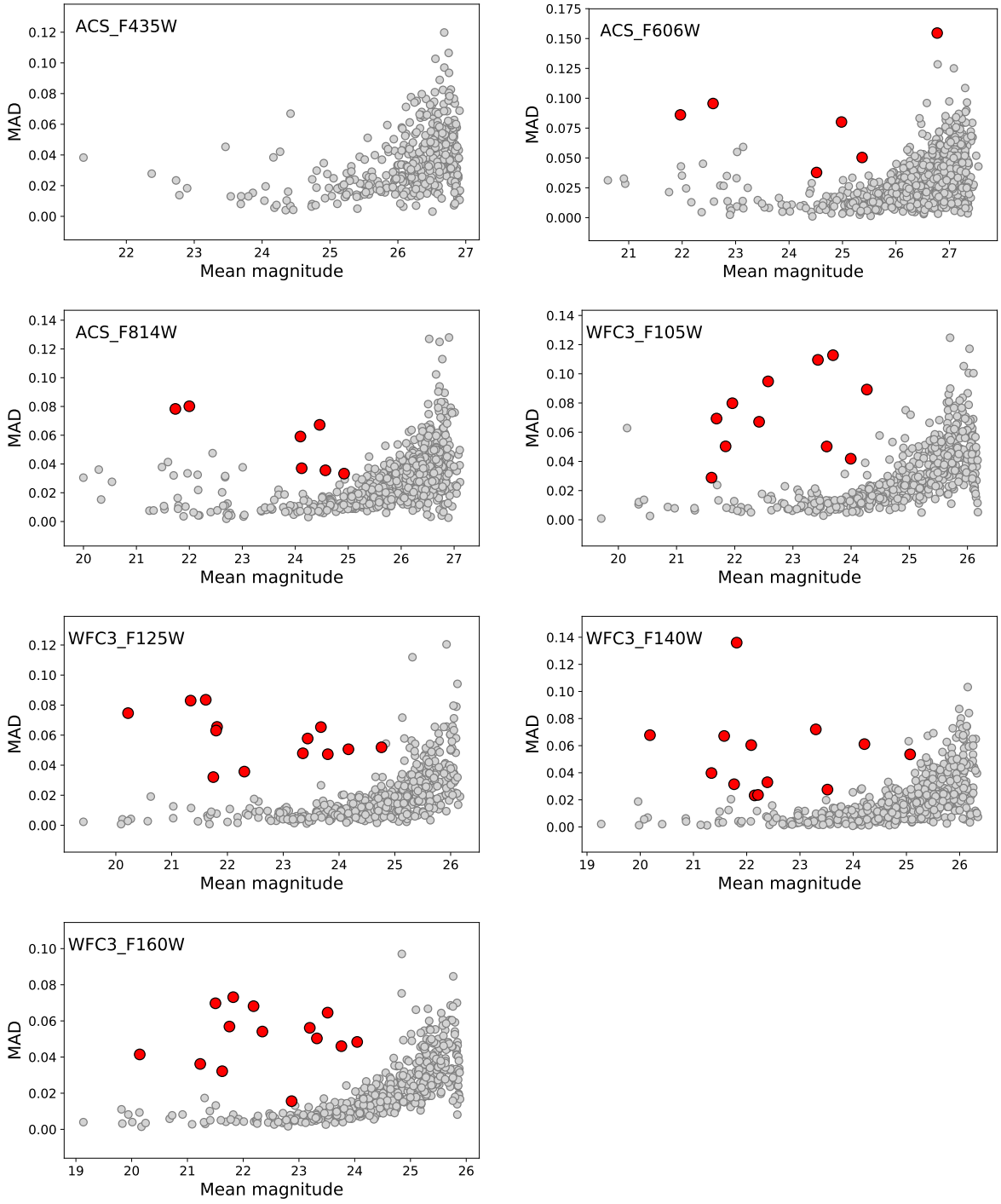

Figure A.6: The MAD as a function of the mean magnitude for different filters as indicated in the MACS 0416 parallel field. All the sources in the field are shown with grey small circles, while the HCV variable sources are shown with red circles.

Table A.1:: HCV variables in the Abell 2744 cluster field.

MatchID (1)	RA(J2000) (2)	Dec(J2000) (3)	Classification (4)	Extent (5)
692509	3.57406	-30.41466	1	ext
6778541	3.58896	-30.39379	1	ext
7943923	3.59876	-30.38799	1	ext
8241307	3.57665	-30.39133	1	pl
8844948	3.60268	-30.39756	1	ext
9902975	3.58876	-30.39969	1	ext
10388358	3.60110	-30.41762	1	ext
12728150	3.59203	-30.40493	1	ext
14594175	3.60341	-30.41674	1	ext
18581918	3.57632	-30.39830	2	pl
24793983	3.60246	-30.39763	2	ext
25368868	3.59275	-30.39150	2	pl
25710098	3.61036	-30.41497	1	pl
30314944	3.58655	-30.39935	1	ext
33259574	3.57443	-30.39989	2	pl
33619012	3.59478	-30.39729	1	ext
34374779	3.56409	-30.38424	1	ext
36461830	3.59632	-30.39635	1	pl
39505133	3.60821	-30.40985	1	pl
40540160	3.61508	-30.40436	1	pl
40979110	3.60840	-30.38764	2	pl
45290870	3.60997	-30.38198	2	ext
45363767	3.59619	-30.41614	1	pl
45998828	3.58727	-30.39364	1	ext
46109413	3.60128	-30.37455	1	ext
47796850	3.58624	-30.40017	1	ext
49318778	3.56563	-30.38841	1	pl
56673718	3.59303	-30.39669	1	ext
60168076	3.58436	-30.40285	1	ext
61758295	3.59031	-30.40038	1	ext
62183545	3.58445	-30.40007	2	ext
64373499	3.57894	-30.39731	2	ext
70050143	3.56957	-30.41212	1	ext
72039034	3.60590	-30.41780	1	ext
72053578	3.59491	-30.39719	1	ext
73227542	3.60228	-30.37357	1	pl
75771799	3.60079	-30.41800	1	ext
78443879	3.58701	-30.39992	1	ext
80288909	3.57875	-30.39684	1	ext
86696348	3.60767	-30.41970	1	ext
88328791	3.59854	-30.40885	1	ext
94123226	3.54569	-30.39186	1	ext
96850626	3.58471	-30.39979	1	ext
97578329	3.58067	-30.38572	2	pl
103945900	3.58390	-30.39856	2	ext

Note. – (1): HSC/HCV unique identifier, (2) & (3): Coordinates in degrees, (4): 1/2 for single/multiple filter variable candidates, (5): Extended or point-like sources.

Table A.2:: HCV variables in the Abell 2744 parallel field.

MatchID (1)	RA(J2000) (2)	Dec(J2000) (3)	Classification (4)	$N_{filtersV}$ (5)	Extent (6)
907438	3.47007	-30.36489	2	2	ext
8096553	3.47508	-30.35122	1	1	ext
21454115	3.45843	-30.39207	2	3	pl
22583503	3.45767	-30.38062	1	1	ext
23770057	3.48787	-30.38744	2	5	pl
27600811	3.48809	-30.39783	1	1	ext
36117588	3.46038	-30.37973	1	1	ext
38189944	3.47217	-30.35269	1	1	pl
42746308	3.43844	-30.38022	1	1	pl
56251568	3.48702	-30.38791	2	5	pl
59972327	3.47526	-30.38434	1	1	ext
86086361	3.48748	-30.35977	1	1	pl
87433341	3.49655	-30.36974	1	1	pl
91072089	3.45927	-30.39983	1	1	ext
95696232	3.49127	-30.38431	2	4	pl
100391260	3.46308	-30.41002	1	1	pl

Note. – (1): HSC/HCV unique identifier, (2) & (3): Coordinates in degrees, (4): 1/2 for single/multiple filter variable candidates, (5): Number of filters the source stands out as variable and (6): Extended or point-like sources.

Table A.3:: HCV variables in the Abell s1063 cluster field.

MatchID (1)	RA(J2000) (2)	Dec(J2000) (3)	Classification (4)	$N_{filtersV}$ (5)	Extent (6)
838226	342.18393	-44.52541	2	2	ext
3442322	342.21103	-44.52812	1	1	pl
6736675	342.18964	-44.49502	1	1	pl
9554085	342.16031	-44.52845	2	2	ext
11255816	342.18179	-44.51085	1	1	ext
11480425	342.21088	-44.51326	2	2	ext
14070739	342.15610	-44.51225	1	1	pl
15280900	342.15891	-44.50998	2	2	ext
16534520	342.20178	-44.55086	1	1	ext
17594998	342.15634	-44.52028	1	1	pl
21891980	342.19836	-44.54879	1	1	ext
26573558	342.17386	-44.53216	2	2	ext
31169078	342.18484	-44.51831	1	1	ext
31175632	342.20242	-44.51145	2	2	pl
31600167	342.16211	-44.53030	1	1	ext
31811774	342.17438	-44.53293	1	1	ext
33191088	342.18219	-44.56053	1	1	pl
33988028	342.19296	-44.52818	1	1	ext
34205524	342.16147	-44.54476	2	3	pl
36164356	342.18405	-44.53621	2	2	ext
36166763	342.20746	-44.51925	1	1	ext
36334581	342.18469	-44.53621	2	2	ext
37539935	342.17407	-44.53259	1	1	ext
38181514	342.19754	-44.54528	2	2	ext
40596658	342.19827	-44.51236	2	4	pl
41154468	342.18454	-44.52932	1	1	ext
43219232	342.21127	-44.51367	1	1	ext
43772354	342.17661	-44.55478	1	1	pl
44707071	342.14273	-44.53134	1	1	ext
49980831	342.19278	-44.55453	1	1	ext
53011330	342.18292	-44.53048	1	1	ext
56603798	342.17545	-44.54553	2	2	ext
60631824	342.18182	-44.52734	2	4	pl
62976579	342.22211	-44.52158	1	1	pl
63847983	342.18903	-44.53005	2	2	ext
64444520	342.18033	-44.54417	1	1	ext
66610743	342.16354	-44.51472	2	2	ext

Note. – (1): HSC/HCV unique identifier, (2) & (3): Coordinates in degrees, (4): 1/2 for single/multiple filter variable candidates, (5): Number of filters the source stands out as variable and (6): Extended or point-like sources.

Table A.3:: (Cont.)

MatchID (1)	RA(J2000) (2)	Dec(J2000) (3)	Classification (4)	$N_{filtersV}$ (5)	Extent (6)
68176033	342.16711	-44.53131	2	5	pl
68342662	342.18851	-44.51138	1	1	ext
69306964	342.18359	-44.51648	1	1	pl
70454135	342.18478	-44.53154	2	4	ext
72844120	342.18625	-44.54606	2	5	pl
76224156	342.17639	-44.51143	1	1	ext
81265969	342.20880	-44.53342	2	2	ext
82939089	342.17645	-44.53350	1	1	ext
83905644	342.20975	-44.52500	1	1	ext
84141537	342.17166	-44.51953	2	5	pl
86079523	342.17969	-44.56190	1	1	pl
86340048	342.17456	-44.53317	1	1	ext
90452701	342.18564	-44.53127	2	3	ext
92129319	342.22089	-44.52777	1	1	pl
92795438	342.18570	-44.53053	2	2	ext
94042309	342.16107	-44.51305	1	1	pl
96168312	342.17404	-44.52747	1	1	ext
100533563	342.18347	-44.50200	1	1	ext
101266666	342.21167	-44.51506	2	2	ext
102270835	342.18307	-44.53312	1	1	ext
102536861	342.16980	-44.53532	2	3	ext
102923568	342.21130	-44.51328	2	2	ext
104159066	342.18665	-44.52250	1	1	ext
104704736	342.20248	-44.51619	2	4	pl
105019919	342.20062	-44.54132	2	2	pl
106498270	342.20181	-44.53158	2	5	pl

Note. – (1): HSC/HCV unique identifier, (2) & (3): Coordinates in degrees, (4): 1/2 for single/multiple filter variable candidates, (5): Number of filters the source stands out as variable and (6): Extended or point-like sources.

Table A.4:: HCV variables in the Abell s1063 parallel field.

MatchID (1)	RA(J2000) (2)	Dec(J2000) (3)	Classification (4)	$N_{filtersV}$ (5)	Extent (6)
2353714	342.32465	-44.54847	1	1	ext
2641267	342.30481	-44.56335	2	4	pl
7533906	342.29730	-44.54961	1	1	pl
9867598	342.33499	-44.55937	2	4	pl
11077429	342.33478	-44.56030	1	1	ext
22901690	342.32718	-44.55894	2	4	pl
23601803	342.32956	-44.52567	1	1	pl
25105715	342.31442	-44.57813	1	1	ext
25893904	342.32385	-44.55164	1	1	ext
36717656	342.34750	-44.52958	1	1	pl
38577887	342.32190	-44.53877	1	1	ext
39960828	342.33630	-44.56089	2	4	pl
44343386	342.31934	-44.56168	2	3	pl
52946733	342.31213	-44.52988	2	3	pl
60908446	342.34100	-44.53011	1	1	pl
63144071	342.33667	-44.53211	2	3	ext
65916223	342.36078	-44.53982	1	1	ext
74368271	342.31149	-44.51663	1	1	ext
74606711	342.32547	-44.55471	2	4	pl
79469135	342.32285	-44.52694	1	1	pl
81014990	342.32941	-44.55159	1	1	ext
83297743	342.33136	-44.53493	2	2	ext
87028495	342.33667	-44.53214	1	1	pl
87655494	342.34244	-44.54065	1	1	pl
97181858	342.30472	-44.53804	2	3	pl
100549522	342.33551	-44.55980	1	1	ext
101725318	342.31912	-44.53971	2	2	pl
103381132	342.31262	-44.52837	1	1	ext

Note. – (1): HSC/HCV unique identifier, (2) & (3): Coordinates in degrees, (4): 1/2 for single/multiple filter variable candidates, (5): Number of filters the source stands out as variable and (6): Extended or point-like sources.

Table A.5:: HCV variables in the Abell 370 cluster field.

MatchID (1)	RA(J2000) (2)	Dec(J2000) (3)	Classification (4)	$N_{filtersV}$ (5)	Extent (6)
879322	39.99565	-1.59685	1	1	pl
3316565	39.96335	-1.56593	1	1	ext
6368635	39.98987	-1.56865	1	1	ext
6757167	39.97391	-1.58733	2	4	pl
8081859	39.96373	-1.56145	2	6	ext
8491399	39.96891	-1.59804	2	2	pl
9566034	39.97340	-1.59883	2	2	pl
11848627	39.95662	-1.58940	2	2	ext
12435124	40.00108	-1.59449	1	1	ext
12767611	39.97830	-1.57410	2	2	ext
16965253	39.97669	-1.56010	2	3	ext
17936779	39.98467	-1.57247	2	2	ext
18484411	39.96152	-1.59319	1	1	ext
21102961	39.97183	-1.57956	1	1	ext
21323138	39.97186	-1.58000	2	2	ext
21606441	39.98576	-1.57473	1	1	ext
21734934	39.98566	-1.57427	2	2	ext
22019244	39.96991	-1.57137	2	2	ext
22732326	39.98194	-1.58893	2	4	pl
24222859	39.97754	-1.58450	1	1	ext
26589970	39.97408	-1.58436	2	2	ext
27317518	39.96566	-1.58934	1	1	ext
31340773	39.96786	-1.55810	2	3	ext
31853471	39.95363	-1.57331	1	1	pl
33266031	39.97046	-1.58239	2	3	ext
34445582	39.96590	-1.58963	1	1	ext
34963360	39.96877	-1.57424	2	2	ext
38689491	39.97058	-1.59731	2	4	pl
39010992	39.96475	-1.58016	2	3	ext
39405402	39.98164	-1.56816	1	1	ext
40758432	39.97242	-1.58459	1	1	ext
42837739	39.98114	-1.56361	2	2	ext
49257603	39.98157	-1.57066	2	2	ext
51247974	39.97019	-1.58364	2	2	ext
52826078	39.97345	-1.58446	2	2	ext
53383517	39.95830	-1.57103	1	1	ext
54419217	39.97254	-1.58390	2	2	ext
54544874	39.96572	-1.58950	1	1	ext
54974990	39.98592	-1.57464	2	2	ext
54975407	39.97218	-1.58226	1	1	ext
64868580	39.98602	-1.57421	1	1	ext
65036658	39.95887	-1.57087	1	1	ext
65368334	39.96427	-1.59122	1	1	ext
66634420	39.97424	-1.58409	1	1	ext
68789060	39.96932	-1.58964	1	1	ext
69550184	39.97163	-1.55645	1	1	ext
69991461	39.99079	-1.59258	1	1	ext

Note. – (1): HSC/HCV unique identifier, (2) & (3): Coordinates in degrees, (4): 1/2 for single/multiple filter variable candidates, (5): Number of filters the source stands out as variable and (6): Extended or point-like sources.

Table A.5:: (Cont.)

MatchID (1)	RA(J2000) (2)	Dec(J2000) (3)	Classification (4)	$N_{filtersV}$ (5)	Extent (6)
70654911	39.97704	-1.55998	2	3	ext
71956573	39.96978	-1.57364	2	2	ext
72289751	39.98570	-1.57398	1	1	ext
72902400	39.97826	-1.57466	2	2	ext
76948047	39.97099	-1.58580	1	1	ext
79160238	39.97322	-1.58419	1	1	ext
82277699	39.97240	-1.56181	1	1	ext
84384241	39.95680	-1.59849	2	2	pl
87744413	39.96882	-1.57810	1	1	ext
89571512	39.97240	-1.58920	1	1	ext
91268620	39.96811	-1.57112	1	1	ext
91577992	39.97406	-1.58422	2	4	ext
93444096	39.97274	-1.58478	2	2	ext
95031997	39.98626	-1.57453	2	2	ext
95795321	39.98586	-1.57502	2	3	ext
97122284	39.97363	-1.58430	2	2	ext
100412836	39.98579	-1.57414	1	1	ext
102769545	39.96555	-1.58964	2	2	ext
106571850	39.97555	-1.56673	1	1	ext

Note. – (1): HSC/HCV unique identifier, (2) & (3): Coordinates in degrees, (4): 1/2 for single/multiple filter variable candidates, (5): Number of filters the source stands out as variable and (6): Extended or point-like sources.

Table A.6:: HCV variables in the Abell 370 parallel field.

MatchID (1)	RA(J2000) (2)	Dec(J2000) (3)	Classification (4)	$N_{filtersV}$ (5)	Extent (6)
919661	40.07555	-1.64492	1	1	ext
15818075	40.05115	-1.65553	2	2	ext
19939957	40.07381	-1.63169	2	2	ext
22604027	40.06208	-1.64049	2	4	pl
28811365	40.07081	-1.61755	1	1	ext
38631361	40.06853	-1.63340	2	4	pl
38841123	40.07380	-1.63170	2	2	ext
46522067	40.04993	-1.62973	2	4	pl
49464850	40.05803	-1.64093	2	4	ext
50076621	40.06690	-1.63496	2	4	pl
55543821	40.03679	-1.62971	1	1	ext
69316778	40.07449	-1.61748	2	5	pl
70064209	40.05642	-1.61417	2	2	ext
73655116	40.05376	-1.64691	1	1	ext
83241083	40.05071	-1.63065	1	1	ext
94488496	40.06388	-1.61360	1	1	ext
95357550	40.02787	-1.61546	1	1	ext
99505670	40.07534	-1.63219	1	1	pl

Note. – (1): HSC/HCV unique identifier, (2) & (3): Coordinates in degrees, (4): 1/2 for single/multiple filter variable candidates, (5): Number of filters the source stands out as variable and (6): Extended or point-like sources.

Table A.7:: HCV variables in the MACS 0416 cluster field.

MatchID (1)	RA(J2000) (2)	Dec(J2000) (3)	Classification (4)	$N_{filtersV}$ (5)	Extent (6)
24889653	64.05386	-24.08234	2	5	pl
25051475	64.04522	-24.07147	1	1	ext
25125549	64.03560	-24.08945	2	3	ext
27650138	64.03965	-24.06665	2	3	ext
30116717	64.03784	-24.06901	1	1	ext
30758126	64.03014	-24.08640	1	1	ext
32516277	64.00482	-24.06756	1	1	pl
33850795	64.03749	-24.06601	2	3	ext
35817963	64.04497	-24.07988	2	6	pl
36165214	64.05838	-24.06283	1	1	ext
37692016	64.02873	-24.09069	1	1	ext
38508017	64.03964	-24.06718	2	4	ext
39392695	64.02928	-24.08772	1	1	ext
42443039	64.05669	-24.06615	2	3	pl
42494382	64.03893	-24.06576	1	1	ext
46514445	64.02685	-24.07009	1	1	ext
48302590	64.05953	-24.06675	1	1	ext
50194698	64.02703	-24.11039	1	1	ext
50868785	64.03750	-24.07318	1	1	ext
50928059	64.05558	-24.06077	2	2	ext
55423828	64.03259	-24.07755	1	1	ext
55472809	64.03064	-24.08355	1	1	ext
55501522	64.03573	-24.06539	2	4	pl
59000900	64.05881	-24.08962	1	1	pl
59860098	64.03322	-24.07607	1	1	ext
62948819	64.01800	-24.07261	1	1	ext
63422019	64.02284	-24.10249	1	1	pl
64769386	64.03106	-24.07857	2	2	ext
65953382	64.03784	-24.06617	2	3	ext
71325825	64.05847	-24.06615	1	1	ext
71872755	64.04338	-24.08930	1	1	ext
72868851	64.04450	-24.09518	1	1	ext
74482060	64.02392	-24.08432	1	1	ext
78414034	64.02802	-24.06106	1	1	ext
79178207	64.03862	-24.06995	1	1	ext
79310709	64.06181	-24.05238	1	1	pl
81190799	64.02932	-24.08184	1	1	ext
82042598	64.03687	-24.06632	1	1	ext
84546446	64.04437	-24.09132	1	1	ext
87553287	64.04483	-24.06984	1	1	ext
88436710	64.01915	-24.07085	2	3	ext

Note. – (1): HSC/HCV unique identifier, (2) & (3): Coordinates in degrees, (4): 1/2 for single/multiple filter variable candidates, (5): Number of filters the source stands out as variable and (6): Extended or point-like sources.

Table A.7:: (Cont.)

MatchID (1)	RA(J2000) (2)	Dec(J2000) (3)	Classification (4)	$N_{filtersV}$ (5)	Extent (6)
90995412	64.03906	-24.07024	1	1	ext
91437859	64.02984	-24.09032	1	1	ext
91899656	64.03006	-24.05746	2	5	pl
91927516	64.03359	-24.05287	1	1	ext
92203284	64.02638	-24.07022	1	1	ext
92832771	64.02566	-24.08537	2	2	ext
95171719	64.06063	-24.09209	1	1	pl
95335384	64.03056	-24.08270	1	1	ext
96350121	64.01868	-24.09335	1	1	pl
97127294	64.03580	-24.06970	2	2	ext
97257508	64.05067	-24.08191	1	1	ext
99846082	64.03490	-24.06538	2	4	pl
100353822	64.03239	-24.09055	2	4	pl
100797955	64.02741	-24.08662	1	1	ext
103548890	64.04189	-24.06285	1	1	ext
106816496	64.03634	-24.06750	2	2	ext

Note. – (1): HSC/HCV unique identifier, (2) & (3): Coordinates in degrees, (4): 1/2 for single/multiple filter variable candidates, (5): Number of filters the source stands out as variable and (6): Extended or point-like sources.

Table A.8:: HCV variables in the MACS 0416 parallel field.

MatchID (1)	RA(J2000) (2)	Dec(J2000) (3)	Classification (4)	$N_{filtersV}$ (5)	Extent (6)
875	64.14967	-24.11035	2	3	ext
4646279	64.11713	-24.12443	2	4	ext
12223486	64.14335	-24.11442	1	1	ext
13406887	64.12636	-24.12599	2	3	ext
19436335	64.12134	-24.12610	1	1	ext
22065380	64.13908	-24.10785	1	1	ext
27244267	64.14034	-24.11016	1	1	ext
38218832	64.15081	-24.13325	1	1	ext
38429062	64.14671	-24.13632	2	5	ext
51746684	64.15908	-24.12066	1	1	ext
54858760	64.14082	-24.13509	2	4	ext
65860823	64.13188	-24.12536	2	5	ext
83104740	64.12878	-24.12868	1	1	ext
85983960	64.11938	-24.13118	1	1	ext
87738834	64.13542	-24.09222	2	5	ext
96632970	64.12532	-24.12008	2	5	ext
97504891	64.14389	-24.13145	2	3	ext
107875132	64.12132	-24.12610	2	3	ext

Note. – (1): HSC/HCV unique identifier, (2) & (3): Coordinates in degrees, (4): 1/2 for single/multiple filter variable candidates, (5): Number of filters the source stands out as variable and (6): Extended or point-like sources.

Table A.9:: HCV variables in the MACS 1149 cluster field.

MatchID (1)	RA(J2000) (2)	Dec(J2000) (3)	Classification (4)	$N_{filtersV}$ (5)	Extent (6)
1380201	177.39359	22.41070	1	1	ext
3293755	177.40614	22.38770	2	3	pl
3752266	177.42577	22.39002	1	1	pl
5344151	177.39313	22.41131	1	1	ext
7485061	177.41287	22.39119	2	5	pl
11749434	177.40387	22.38908	1	1	ext
15599497	177.38629	22.41184	1	1	ext
19632734	177.39272	22.40308	2	2	ext
28201030	177.41928	22.39329	2	5	pl
28224254	177.39534	22.41005	2	2	pl
39451157	177.38720	22.40294	1	1	ext
48514708	177.40314	22.39587	2	2	pl
48661867	177.39658	22.41332	1	1	ext
55288322	177.38144	22.39702	2	2	ext
57761614	177.41490	22.38938	2	4	pl
57897576	177.38756	22.38519	1	1	ext
60982023	177.39339	22.41134	2	2	ext
63143451	177.38527	22.41575	1	1	pl
67836193	177.40237	22.40738	1	1	pl
69527533	177.42566	22.41250	1	1	pl
71214923	177.40020	22.39793	2	3	ext
71655609	177.37590	22.40138	1	1	pl
80898049	177.39717	22.37266	2	2	pl
86739409	177.40381	22.38647	2	3	ext
89886768	177.37971	22.39509	1	1	ext
97031037	177.39142	22.39064	2	3	ext
97035204	177.37373	22.40464	1	1	ext
100282660	177.38788	22.38489	2	4	pl
107706149	177.39906	22.39715	2	2	ext

Note. – (1): HSC/HCV unique identifier, (2) & (3): Coordinates in degrees, (4): 1/2 for single/multiple filter variable candidates, (5): Number of filters the source stands out as variable and (6): Extended or point-like sources.

Table A.10:: HCV variables in the MACS 1149 parallel field.

MatchID (1)	RA(J2000) (2)	Dec(J2000) (3)	Classification (4)	$N_{filtersV}$ (5)	Extent (6)
3729932	177.40840	22.32272	1	1	ext
4202613	177.44601	22.30402	1	1	pl
5616090	177.40533	22.32485	1	1	ext
9203794	177.41838	22.31075	2	4	ext
10141936	177.39435	22.28629	1	1	pl
15611329	177.39350	22.30791	1	1	pl
16983552	177.40780	22.28416	2	3	pl
26176306	177.40080	22.27786	1	1	pl
34140531	177.41585	22.27222	1	1	pl
40020973	177.40854	22.29168	1	1	ext
42794849	177.41820	22.27805	1	1	ext
51068124	177.38124	22.29695	1	1	ext
52342758	177.40286	22.28731	2	2	ext
61568900	177.39726	22.29225	1	1	pl
69158740	177.40236	22.31312	2	2	ext
78413887	177.42581	22.27007	1	1	pl
82012655	177.45421	22.30090	1	1	pl
88773642	177.43054	22.29186	1	1	pl
89088888	177.42345	22.32076	1	1	pl
105561340	177.41443	22.31483	1	1	ext

Note. – (1): HSC/HCV unique identifier, (2) & (3): Coordinates in degrees, (4): 1/2 for single/multiple filter variable candidates, (5): Number of filters the source stands out as variable and (6): Extended or point-like sources.

Table A.11:: HCV variables in the MACS 0717 cluster field.

MatchID (1)	RA(J2000) (2)	Dec(J2000) (3)	Classification (4)	$N_{filtersV}$ (5)	Extent (6)
5218913	109.42713	37.75298	2	2	ext
5630522	109.37001	37.77449	1	1	pl
7162567	109.38953	37.73839	2	2	ext
11080194	109.40484	37.74646	1	1	ext
12030863	109.40487	37.75976	2	2	ext
14278683	109.41834	37.76634	1	1	pl
15225427	109.41152	37.73474	1	1	pl
15697698	109.40464	37.73800	2	3	ext
18933245	109.39228	37.76167	2	4	pl
24287330	109.37428	37.76110	1	1	ext
26324887	109.41484	37.73937	2	4	ext
27575415	109.38058	37.74106	2	2	ext
29027780	109.39383	37.74008	1	1	pl
29881241	109.38427	37.72869	1	1	pl
32760903	109.40319	37.74377	2	4	pl
36990211	109.37029	37.72679	1	1	pl
37151887	109.38416	37.73939	2	4	pl
37451459	109.40480	37.73834	2	2	ext
37965595	109.38614	37.75498	1	1	pl
38365615	109.40418	37.73992	2	2	ext
41543856	109.40464	37.74684	1	1	pl
41716144	109.38055	37.74681	2	2	ext
46322406	109.37255	37.73832	2	4	pl
48467472	109.39294	37.73522	2	2	pl
48783299	109.38628	37.75470	1	1	pl
49978712	109.40595	37.73920	2	3	ext
50848363	109.39366	37.76445	2	3	ext
53480207	109.40586	37.74097	2	2	ext
55820850	109.37509	37.77152	1	1	pl
56188797	109.38332	37.74125	2	2	ext
56380757	109.39761	37.75423	2	2	ext
56955337	109.38558	37.74241	1	1	ext
57350619	109.37758	37.76899	1	1	pl
59813220	109.41251	37.74731	1	1	pl
59897224	109.39713	37.74161	1	1	ext
60744585	109.36733	37.74102	2	4	pl
61162590	109.39287	37.73505	2	3	ext
61333594	109.39127	37.75858	1	1	ext
62791557	109.39534	37.74116	1	1	ext
62934248	109.39201	37.74584	1	1	pl
64265754	109.40577	37.74214	2	2	ext
66277550	109.37101	37.72306	1	1	pl
67702898	109.42416	37.74346	1	1	pl

Note. – (1): HSC/HCV unique identifier, (2) & (3): Coordinates in degrees, (4): 1/2 for single/multiple filter variable candidates, (5): Number of filters the source stands out as variable and (6): Extended or point-like sources.

Table A.11:: (Cont.)

MatchID (1)	RA(J2000) (2)	Dec(J2000) (3)	Classification (4)	$N_{filtersV}$ (5)	Extent (6)
70236916	109.36700	37.72420	1	1	pl
73733996	109.40356	37.74931	1	1	ext
74612703	109.35226	37.72675	1	1	pl
75631337	109.38609	37.74201	1	1	ext
76393846	109.41692	37.73809	2	2	ext
78374402	109.39318	37.73793	2	2	pl
82597575	109.40505	37.74144	2	3	ext
83642035	109.39703	37.74680	2	2	ext
89092034	109.40676	37.71720	1	1	pl
92841518	109.36501	37.74339	2	2	ext
95506191	109.39914	37.74557	2	2	ext
96149091	109.39723	37.75571	2	2	ext
99327866	109.40411	37.76167	1	1	pl
99731405	109.37582	37.77249	1	1	pl
100361039	109.40984	37.74124	2	3	pl
103820450	109.40575	37.76043	2	5	pl

Note. – (1): HSC/HCV unique identifier, (2) & (3): Coordinates in degrees, (4): 1/2 for single/multiple filter variable candidates, (5): Number of filters the source stands out as variable and (6): Extended or point-like sources.

Table A.12:: HCV variables in the MACS 0717 parallel field.

MatchID (1)	RA(J2000) (2)	Dec(J2000) (3)	Classification (4)	$N_{filtersV}$ (5)	Extent (6)
7992501	109.31236	37.84636	1	1	ext
11534129	109.33879	37.79954	1	1	pl
15213304	109.34684	37.80142	1	1	pl
16395473	109.31015	37.85638	1	1	pl
16811230	109.32856	37.81173	1	1	pl
23786927	109.31892	37.81180	1	1	pl
24327210	109.31632	37.80862	2	2	ext
28757980	109.31941	37.83679	2	3	pl
29791906	109.34039	37.81163	1	1	pl
32153739	109.35046	37.81288	1	1	pl
40406335	109.30841	37.84161	1	1	ext
51300245	109.29572	37.81115	1	1	pl
71628798	109.34300	37.85218	1	1	pl
72964819	109.29227	37.83275	2	2	ext
73203564	109.31303	37.80143	1	1	ext
75733212	109.36103	37.83635	1	1	pl
75758936	109.33723	37.80740	1	1	pl
77073293	109.31369	37.84740	2	4	pl
82144750	109.32584	37.81934	2	2	ext
86560405	109.36253	37.83349	1	1	pl
99326192	109.35912	37.84475	1	1	pl
101568166	109.33392	37.84006	1	1	pl
102494313	109.34426	37.84352	1	1	pl
107667671	109.35230	37.81035	1	1	pl

Note. – (1): HSC/HCV unique identifier, (2) & (3): Coordinates in degrees, (4): 1/2 for single/multiple filter variable candidates, (5): Number of filters the source stands out as variable and (6): Extended or point-like sources.

Appendix B

Miscellaneous

B.1 List of publications

- **Pouliasis, E.** et al. An obscured AGN population hidden in the XMM-XXL field: identification through SED decomposition. Submitted in Monthly Notices of the Royal Astronomical Society.
- Bonanos, A. Z. et al. (incl. **Pouliasis, E.**) 2019. The Hubble Catalog of Variables (HCV). Astronomy and Astrophysics 630, A92.
- Yang, M. et al. (incl. **Pouliasis, E.**) 2019. Evolved massive stars at low-metallicity. I. A source catalog for the Small Magellanic Cloud. Astronomy and Astrophysics 629, A91.
- **Pouliasis, E.** et al. 2019. Robust identification of active galactic nuclei through HST optical variability in GOODS-S: comparison with the X-ray and mid-IR-selected samples. Monthly Notices of the Royal Astronomical Society 487, 4285.
- Spetsieri, Z. T. et al. (incl. **Pouliasis, E.**) 2018. Massive star population of the Virgo Cluster galaxy NGC4535. Discovery of new massive variable candidates with the Hubble Space Telescope. Astronomy and Astrophysics 618, A185.
- **Pouliasis, E.**, Di Matteo, P., Haywood, M. 2017. A Milky Way with a massive, centrally concentrated thick disc: new Galactic mass models for orbit computations. Astronomy and Astrophysics 598, A66.
- Sokolovsky, K. V. et al. (incl. **Pouliasis, E.**) 2017. Comparative performance of selected variability detection techniques in photometric time series data. Monthly Notices of the Royal Astronomical Society 464, 274.

B.2 List of Conferences/Workshops attended

- "The 14th Hellenic Astronomical Conference" (Talk), 08-11/07/2019, Volos, Greece
- "Super-massive Black Holes: Environment and Evolution" (Talk), 19-22/06/2019, Corfu, Greece
- "Unveiling the Physics Behind Extreme AGN Variability" (Poster), 10-14/07/2017, St Thomas, U.S. Virgin Islands
- "The X-ray Universe 2017", 06-09/06/2017 (Talk), Rome, Italy
- "The 13th Hellenic Astronomical Conference" (Talk), 02-06/07/2017, Heraklion, Greece
- 2nd Hel.A.S. Astrophysics Summer School: "Nuclear Activity in Galaxies" (+Talk), 11-15/07/2015, Athens, Greece
- LOC member in European Week of Astronomy & Space Science by EAS, 03-10/07/2016, Athens, Greece
- "AGN: What's in a name" by ESO, 27/06-01/07/2016 (Poster), Garching, Germany
- 1st ASTERICS Virtual Observatory school by ESA (+Talk), 12-17/12/2015, Madrid, Spain

B.3 Other activities

- Support astronomer in Aristarchos Telescope, (6-7/10/2015, 25-26/07/2016, 5-6/10/2016), Helmos Observatory, Greece
- Scientific visits to STScI for the "Hubble Catalogue of Variables" project, 2 weeks (12/2016), Baltimore, USA
- Tutoring in Astronomy summer school organized by National Observatory of Athens, years: 2017, 2018 and 2019, Greece
- Organizer/coordinator of workshops on Visual Observatory tools (TOPCAT, Aladin, VOSA, etc.) in National and Kapodistrian University of Athens & the National Observatory of Athens, 02/03/2016, 01-08/04/2016 and 05/2019, Greece

- Junior member of the Hellenic Astronomical Society
- Organizer of the weekly Astronomy & Astrophysics Club, 2017-2018, National Observatory of Athens, Greece
- Tutoring/mentoring of three undergraduate students during their 3-month internships

References

Abell, G. O., Corwin, Harold G., J., & Olowin, R. P. 1989, ApJS, 70, 1

Abramowicz, M. A., Czerny, B., Lasota, J. P., & Szuszkiewicz, E. 1988, ApJ, 332, 646

Afanasiev, V. L., Dodonov, S. N., Khrapov, S. S., Mustsevoi, V. V., & Moiseev, A. V. 2007, Astrophysical Bulletin, 62, 15

Akaike, H. 1974, IEEE Transactions on Automatic Control, 19, 716

Akylas, A., Georgakakis, A., Georgantopoulos, I., Brightman, M., & Nandra, K. 2012, A&A, 546, A98

Alexander, D. M., Bauer, F. E., Chapman, S. C., et al. 2005, ApJ, 632, 736

Alexander, D. M., & Hickox, R. C. 2012, , 56, 93

Alexander, D. M., Bauer, F. E., Brandt, W. N., et al. 2003, The Astronomical Journal, 125, 383

Alexander, D. M., Chary, R. R., Pope, A., et al. 2008, ApJ, 687, 835

Alexander, T. 1995, MNRAS, 274, 909

Alonso-Herrero, A., Rieke, M. J., Rieke, G. H., & Shields, J. C. 2000, ApJ, 530, 688

Alonso-Herrero, A., Esquej, P., Roche, P. F., et al. 2016, MNRAS, 455, 563

Anderson, J. M., Ulvestad, J. S., & Ho, L. C. 2004, ApJ, 603, 42

Antonucci, R. 1993, ARA&A, 31, 473

Antonucci, R. R. J. 1984, ApJ, 278, 499

Antonucci, R. R. J., & Miller, J. S. 1985, ApJ, 297, 621

Arnaud, K. A., Branduardi-Raymont, G., Culhane, J. L., et al. 1985, MNRAS, 217, 105

Assef, R. J., Stern, D., Noirot, G., et al. 2018, ApJS, 234, 23

Assef, R. J., Stern, D., Kochanek, C. S., et al. 2013, ApJ, 772, 26

Assef, R. J., Eisenhardt, P. R. M., Stern, D., et al. 2015, ApJ, 804, 27

Bañados, E., Venemans, B. P., Decarli, R., et al. 2016, ApJS, 227, 11

Bañados, E., Venemans, B. P., Mazzucchelli, C., et al. 2018, Nature, 553, 473

Bahcall, J. N., Kozlovsky, B.-Z., & Salpeter, E. E. 1972, ApJ, 171, 467

Balbus, S. A., & Hawley, J. F. 1991, ApJ, 376, 214

Baldassare, V. F., Geha, M., & Greene, J. 2018, ArXiv e-prints, arXiv:1808.09578

Baldwin, J. A., Phillips, M. M., & Terlevich, R. 1981, PASP, 93, 5

Baloković, M., Comastri, A., Harrison, F. A., et al. 2014, ApJ, 794, 111

Barger, A. J., Cowie, L. L., Capak, P., et al. 2003, AJ, 126, 632

Barmby, P., Alonso-Herrero, A., Donley, J. L., et al. 2006, ApJ, 642, 126

Barr, P., White, N. E., & Page, C. G. 1985, MNRAS, 216, 65P

Barth, A. J., Ho, L. C., Rutledge, R. E., & Sargent, W. L. W. 2004, ApJ, 607, 90

Barth, A. J., & Shields, J. C. 2000, PASP, 112, 753

Barthel, P. 1989, Scientific American, 260, 20

Barvainis, R. 1987, ApJ, 320, 537

Baskin, A., & Laor, A. 2018, MNRAS, 474, 1970

Bauer, A., Baltay, C., Coppi, P., et al. 2009, ApJ, 696, 1241

Beckmann, V., Courvoisier, T. J. L., Gehrels, N., et al. 2009, in American Institute of Physics Conference Series, Vol. 1126, American Institute of Physics Conference Series, ed. J. Rodriguez & P. Ferrando, 141–144

Beckmann, V., & Shrader, C. R. 2012, Active Galactic Nuclei

Begelman, M. C., & Cioffi, D. F. 1989, ApJ, 345, L21

Bentz, M. C., & Katz, S. 2015, PASP, 127, 67

Bentz, M. C., Denney, K. D., Grier, C. J., et al. 2013, ApJ, 767, 149

Bershady, M. A., Trevese, D., & Kron, R. G. 1998, ApJ, 496, 103

Bertin, E., & Arnouts, S. 1996a, A&AS, 117, 393

—. 1996b, A&AS, 117, 393

—. 2010, SExtractor: Source Extractor, Astrophysics Source Code Library, ascl:1010.064

Bianchi, S., Guainazzi, M., Matt, G., Fonseca Bonilla, N., & Ponti, G. 2009, A&A, 495, 421

Blandford, R., Meier, D., & Readhead, A. 2019, ARA&A, 57, 467

Blandford, R. D. 1990, in Active Galactic Nuclei, ed. R. D. Blandford, H. Netzer, L. Woltjer, T. J. L. Courvoisier, & M. Mayor, 161–275

Blandford, R. D., & Rees, M. J. 1978, Phys. Scr, 17, 265

Blandford, R. D., & Znajek, R. L. 1977, MNRAS, 179, 433

Bloom, S. D., & Marscher, A. P. 1996, ApJ, 461, 657

Boella, G., Butler, R. C., Perola, G. C., et al. 1997, A&AS, 122, 299

Bonanos, A. Z., Yang, M., Sokolovsky, K. V., et al. 2019, A&A, 630, A92

Bondi, H. 1952, MNRAS, 112, 195

Boquien, M., Burgarella, D., Roehlly, Y., et al. 2019, A&A, 622, A103

Boroson, T. A., & Green, R. F. 1992, ApJS, 80, 109

Boula, S., Kazanas, D., & Mastichiadis, A. 2019, MNRAS, 482, L80

Boulade, O., Charlot, X., Abbon, P., et al. 2000, Society of Photo-Optical Instrumentation Engineers (SPIE) Conference Series, Vol. 4008, Development of MegaCam, the next-generation wide-field imaging camera for the 3.6-m Canada-France-Hawaii Telescope, ed. M. Iye & A. F. Moorwood, 657–668

Bower, G. A., Wilson, A. S., Heckman, T. M., & Richstone, D. O. 1996, AJ, 111, 1901

Bower, R. G., Benson, A. J., Malbon, R., et al. 2006, MNRAS, 370, 645

Brandt, W. N., & Alexander, D. M. 2010, Proceedings of the National Academy of Science, 107, 7184

—. 2015, A&A Rev., 23, 1

Brightman, M., & Nandra, K. 2011, MNRAS, 413, 1206

Brinkman, A., Aarts, H., den Boggende, A., et al. 1998, in Science with XMM, 2

Brinkman, B. C., Gunsing, T., Kaastra, J. S., et al. 2000, Society of Photo-Optical Instrumentation Engineers (SPIE) Conference Series, Vol. 4012, Description and performance of the low-energy transmission grating spectrometer on board Chandra, ed. J. E. Truemper & B. Aschenbach, 81–90

Brotherton, M. S., Wills, B. J., Francis, P. J., & Steidel, C. C. 1994, ApJ, 430, 495

Bruzual, G., & Charlot, S. 2003, MNRAS, 344, 1000

Burnham, K. P., & Anderson, D. R. 2002, Ecological Modelling. Springer Science & Business Media, New York, New York, USA

Burtscher, L., Jaffe, W., Raban, D., et al. 2009, ApJ, 705, L53

Burtscher, L., Meisenheimer, K., Tristram, K. R. W., et al. 2013, A&A, 558, A149

Calzetti, D., Armus, L., Bohlin, R. C., et al. 2000, ApJ, 533, 682

Canizares, C. R., Davis, J. E., Dewey, D., et al. 2005, PASP, 117, 1144

Capetti, A., Verdoes Kleijn, G., & Chiaberge, M. 2005, A&A, 439, 935

Cappelluti, N., Predehl, P., Böhringer, H., et al. 2011, Memorie della Societa Astronomica Italiana Supplementi, 17, 159

Cardamone, C. N., van Dokkum, P. G., Urry, C. M., et al. 2011, VizieR Online Data Catalog, 218

Carilli, C. L., Perley, R. A., Dhawan, V., & Perley, D. A. 2019, ApJ, 874, L32

Cecil, G., Greenhill, L. J., DePree, C. G., et al. 2000, ApJ, 536, 675

Cerruti, M., Zech, A., Boisson, C., & Inoue, S. 2015, MNRAS, 448, 910

Chabrier, G. 2003, ApJ, 586, L133

Chandrasekhar, S. 1931, MNRAS, 91, 456

Chartas, G., Kochanek, C. S., Dai, X., Poindexter, S., & Garmire, G. 2009, ApJ, 693, 174

Chatterjee, R., Roychowdhury, A., Chandra, S., & Sinha, A. 2018, ApJ, 859, L21

Chiaberge, M. 2004, in Multiwavelength AGN Surveys, ed. R. Mújica & R. Maiolino, 217–226

Chiappetti, L., Fotopoulou, S., Lidman, C., et al. 2018, A&A, 620, A12

Ciesla, L., Charmandaris, V., Georgakakis, A., et al. 2015, A&A, 576, A10

Clavel, J., Reichert, G. A., Alloin, D., et al. 1991, ApJ, 366, 64

Clavel, J., Schulz, B., Altieri, B., et al. 2000, A&A, 357, 839

Comastri, A., Iwasawa, K., Gilli, R., et al. 2010, ApJ, 717, 787

Corbett, E. A., Robinson, A., Axon, D. J., & Hough, J. H. 2000, MNRAS, 311, 485

Courvoisier, T. J. L., & Türler, M. 2005, A&A, 444, 417

Crenshaw, D. M., & Kraemer, S. B. 2007, ApJ, 659, 250

Crenshaw, D. M., Kraemer, S. B., Schmitt, H. R., et al. 2009, ApJ, 698, 281

Cristiani, S., Trentini, S., La Franca, F., & Andreani, P. 1997, A&A, 321, 123

Cristiani, S., Vio, R., & Andreani, P. 1990, AJ, 100, 56

Croton, D. J. 2006, MNRAS, 369, 1808

Curtis, H. D. 1918, Publications of Lick Observatory, 13, 9

Cutri, R. M., & et al. 2013, VizieR Online Data Catalog, 2328

Dadina, M. 2007, A&A, 461, 1209

—. 2008, A&A, 485, 417

Dale, D. A., Helou, G., Magdis, G. E., et al. 2014, ApJ, 784, 83

Damen, M., Labbé, I., van Dokkum, P. G., et al. 2011, ApJ, 727, 1

Dasyra, K. M., Ho, L. C., Netzer, H., et al. 2011, ApJ, 740, 94

Dasyra, K. M., Ho, L. C., Armus, L., et al. 2008, ApJ, 674, L9

Dasyra, K. M., Peterson, B. M., Tacconi, L. J., et al. 2010, in IAU Symposium, Vol. 267, Co-Evolution of Central Black Holes and Galaxies, ed. B. M. Peterson, R. S. Somerville, & T. Storchi-Bergmann, 172–176

Davidson, K., & Netzer, H. 1979, Reviews of Modern Physics, 51, 715

Davis, S. W., & Laor, A. 2011, ApJ, 728, 98

De Cicco, D., Paolillo, M., Covone, G., et al. 2015, A&A, 574, A112

De Cicco, D., Paolillo, M., Falocco, S., et al. 2019, A&A, 627, A33

de Diego, J. A. 2010, AJ, 139, 1269

de Rosa, A., Panessa, F., Bassani, L., et al. 2012, MNRAS, 420, 2087

de Vries, W. H., Becker, R. H., White, R. L., & Loomis, C. 2005, AJ, 129, 615

Del Moro, A., Alexander, D. M., Bauer, F. E., et al. 2016, MNRAS, 456, 2105

Del Moro, A., Alexander, D. M., Aird, J. A., et al. 2017, ApJ, 849, 57

den Herder, J. W., Brinkman, A. C., Kahn, S. M., et al. 2001, A&A, 365, L7

Denney, K. D., De Rosa, G., Croxall, K., et al. 2014, ApJ, 796, 134

Dermer, C. D., & Schlickeiser, R. 1993, ApJ, 416, 458

di Clemente, A., Giallongo, E., Natali, G., Trevese, D., & Vagnetti, F. 1996, ApJ, 463, 466

Di Matteo, T., Springel, V., & Hernquist, L. 2005, Nature, 433, 604

Ding, N., Luo, B., Brandt, W. N., et al. 2018, ApJ, 868, 88

Dokuchaev, V. I., Eroshenko, Y. N., & Rubin, S. G. 2007, arXiv e-prints, arXiv:0709.0070

Donati, J. F. 2003, Astronomical Society of the Pacific Conference Series, Vol. 307, ESPaDOnS: An Echelle SpectroPolarimetric Device for the Observation of Stars at CFHT, ed. J. Trujillo-Bueno & J. Sanchez Almeida, 41

Donati, J.-F., Kouach, D., Lacombe, M., et al. 2018, SPIRou: A NIR Spectropolarimeter/High-Precision Velocimeter for the CFHT, 107

Dong, X., Wang, T., Yuan, W., et al. 2007, ApJ, 657, 700

Donley, J. L., Rieke, G. H., Pérez-González, P. G., Rigby, J. R., & Alonso-Herrero, A. 2007, ApJ, 660, 167

Donley, J. L., Koekemoer, A. M., Brusa, M., et al. 2012, ApJ, 748, 142

Dopita, M. A., & Sutherland, R. S. 1995, ApJ, 455, 468

Dower, R. G., Bradt, H. V., Doxsey, R. E., Johnston, M. D., & Griffiths, R. E. 1980, ApJ, 235, 355

Dressler, A. 1989, in IAU Symposium, Vol. 134, Active Galactic Nuclei, ed. D. E. Osterbrock & J. S. Miller, 217

Drissen, L., Martin, T., Rousseau-Nepton, L., et al. 2019, MNRAS, 485, 3930

Ebeling, H., Edge, A. C., & Henry, J. P. 2001, ApJ, 553, 668

Eddington, A. S. 1916, MNRAS, 77, doi:10.1093/mnras/77.1.16

Edge, D. O., Shakeshaft, J. R., McAdam, W. B., Baldwin, J. E., & Archer, S. 1959, MmRAS, 68, 37

Efstathiou, A., Christopher, N., Verma, A., & Siebenmorgen, R. 2013, MNRAS, 436, 1873

Efstathiou, A., & Rowan-Robinson, M. 1995, MNRAS, 273, 649

Ehman, J. R., Dixon, R. S., & Kraus, J. D. 1970, AJ, 75, 351

Einstein, A. 1916, Annalen der Physik, 354, 769

Ekers, J. A. 1969, Australian Journal of Physics Astrophysical Supplement, 7, 3

Elvis, M., Maccacaro, T., Wilson, A. S., et al. 1978, MNRAS, 183, 129

Emerson, J., McPherson, A., & Sutherland, W. 2006, The Messenger, 126, 41

Epchtein, N., de Batz, B., Copet, E., et al. 1994, Ap&SS, 217, 3

Eracleous, M., & Halpern, J. P. 2001, ApJ, 554, 240

Esposito, V., & Walter, R. 2016, A&A, 590, A49

Event Horizon Telescope Collaboration, Akiyama, K., Alberdi, A., et al. 2019, ApJ, 875, L1

Fabian, A. C. 2006, in ESA Special Publication, Vol. 604, The X-ray Universe 2005, ed. A. Wilson, 463

Fabian, A. C., & Ross, R. R. 2010, Space Sci. Rev., 157, 167

Fabian, A. C., Zoghbi, A., Ross, R. R., et al. 2009, Nature, 459, 540

Falcke, H., Nagar, N. M., Wilson, A. S., & Ulvestad, J. S. 2000, ApJ, 542, 197

Falocco, S., Paolillo, M., Covone, G., et al. 2015, A&A, 579, A115

Falocco, S., De Cicco, D., Paolillo, M., et al. 2016, The Universe of Digital Sky Surveys, 42, 275

Fanaroff, B. L., & Riley, J. M. 1974, MNRAS, 167, 31P

Fanidakis, N., Baugh, C. M., Benson, A. J., et al. 2011, MNRAS, 410, 53

Fath, E. A. 1909a, Lick Observatory Bulletin, 149, 71

—. 1909b, PASP, 21, 138

—. 1909c, Popular Astronomy, 17, 504

—. 1913, ApJ, 37, 198

Fazio, G. G., Hora, J. L., Allen, L. E., et al. 2004, ApJS, 154, 10

Feltre, A., Charlot, S., & Gutkin, J. 2016, MNRAS, 456, 3354

Ferrarese, L., & Ford, H. 2005, Space Sci. Rev., 116, 523

Ferrarese, L., & Merritt, D. 2000, ApJ, 539, L9

Ferreira Lopes, C. E., & Cross, N. J. G. 2016, A&A, 586, A36

—. 2017, A&A, 604, A121

Filho, M. E., Barthel, P. D., & Ho, L. C. 2002, A&A, 385, 425

Filho, M. E., Fraternali, F., Markoff, S., et al. 2004, A&A, 418, 429

Filippenko, A. V. 1993, in The Nearest Active Galaxies, ed. J. Beckman, L. Colina, & H. Netzer, 99

Filippenko, A. V., & Ho, L. C. 2003, ApJ, 588, L13

Filippenko, A. V., & Terlevich, R. 1992, ApJ, 397, L79

Finke, J. D. 2013, ApJ, 763, 134

Finke, J. D., & Becker, P. A. 2014, ApJ, 791, 21

Fiore, F., Grazian, A., Santini, P., et al. 2008, ApJ, 672, 94

Fiore, F., Puccetti, S., Brusa, M., et al. 2009, ApJ, 693, 447

for the Advancement of Science., B. A. 1845, Report of the British Association for the Advancement of Science., Vol. 15th Meeting (1845) (London.), 536, https://www.biodiversitylibrary.org/bibliography/2276 — 1831-1938 [L] ; 1864, 1886-1918, 1933[T]. — Continued as: Advancement of Science

Ford, H. C., Bartko, F., Bely, P. Y., et al. 1998, in Proc. SPIE, Vol. 3356, Space Telescopes and Instruments V, ed. P. Y. Bely & J. B. Breckinridge, 234–248

Friedman, H., & Byram, E. T. 1967, Science, 158, 257

Fritz, J., Franceschini, A., & Hatziminaoglou, E. 2006, MNRAS, 366, 767

Fruchter, A. S., & Hook, R. N. 2002, PASP, 114, 144

Gabriel, C., Denby, M., Fyfe, D. J., et al. 2004, in Astronomical Society of the Pacific Conference Series, Vol. 314, Astronomical Data Analysis Software and Systems (ADASS) XIII, ed. F. Ochsenbein, M. G. Allen, & D. Egret, 759

Galeev, A. A., Rosner, R., & Vaiana, G. S. 1979, ApJ, 229, 318

Gallimore, J. F., Baum, S. A., & O'Dea, C. P. 1997, Ap&SS, 248, 253

Gallimore, J. F., Elitzur, M., Maiolino, R., et al. 2016, ApJ, 829, L7

Gallo, E., Treu, T., Marshall, P. J., et al. 2010, ApJ, 714, 25

Gandhi, Horst, H., Smette, A., et al. 2009, A&A, 502, 457

García, J., & Kallman, T. R. 2010, ApJ, 718, 695

García, J. A., Kara, E., Walton, D., et al. 2019, ApJ, 871, 88

García-Burillo, S., Combes, F., Ramos Almeida, C., et al. 2016a, ApJ, 823, L12

—. 2016b, ApJ, 823, L12

García-González, J., Alonso-Herrero, A., Pérez-González, P. G., et al. 2014, in Highlights of Spanish Astrophysics VIII, Proc. of the XI Scientific Meeting of the Spanish Astronomical Society, arXiv:1411.7556

Garilli, B., Guzzo, L., Scodeggio, M., et al. 2014, A&A, 562, A23

Garmire, G. P., Bautz, M. W., Ford, P. G., Nousek, J. A., & Ricker, Jr., G. R. 2003, in Proc. SPIE, Vol. 4851, X-Ray and Gamma-Ray Telescopes and Instruments for Astronomy., ed. J. E. Truemper & H. D. Tananbaum, 28–44

Gebhardt, K., Bender, R., Bower, G., et al. 2000, ApJ, 539, L13

Genzel, R., Thatte, N., Krabbe, A., Kroker, H., & Tacconi-Garman, L. E. 1996, ApJ, 472, 153

Georgantopoulos, I., Georgakakis, A., Rowan-Robinson, M., & Rovilos, E. 2008, A&A, 484, 671

Georgantopoulos, I., Rovilos, E., Akylas, A., et al. 2011, A&A, 534, A23

George, I. M., & Fabian, A. C. 1991, MNRAS, 249, 352

Ghez, A. M., Klein, B. L., Morris, M., & Becklin, E. E. 1998, ApJ, 509, 678

Giacconi, R., Gursky, H., Paolini, F. R., & Rossi, B. B. 1962, Phys. Rev. Lett., 9, 439

Giavalisco, M., Ferguson, H. C., Koekemoer, A. M., et al. 2004, ApJ, 600, L93

Gilli, R., Comastri, A., & Hasinger, G. 2007, A&A, 463, 79

Gilli, R., Vignali, C., Mignoli, M., et al. 2010, A&A, 519, A92

Giveon, U., Maoz, D., Kaspi, S., Netzer, H., & Smith, P. S. 1999, MNRAS, 306, 637

Glikman, E., Lacy, M., LaMassa, S., et al. 2019, in American Astronomical Society Meeting Abstracts, Vol. 233, American Astronomical Society Meeting Abstracts #233, 134.01

Goad, M., & Wanders, I. 1996, ApJ, 469, 113

González-Martín, O., Masegosa, J., Márquez, I., et al. 2015, A&A, 578, A74

Goodrich, R. W., Veilleux, S., & Hill, G. J. 1994, ApJ, 422, 521

Gower, J. F. R., Scott, P. F., & Wills, D. 1967, MmRAS, 71, 49

Graham, A. W., & Driver, S. P. 2007, ApJ, 655, 77

Graham, M. J., Djorgovski, S. G., Drake, A. J., et al. 2014, MNRAS, 439, 703

Granato, G. L., De Zotti, G., Silva, L., Bressan, A., & Danese, L. 2004, ApJ, 600, 580

Gravity Collaboration, Sturm, E., Dexter, J., et al. 2018, Nature, 563, 657

Greene, J. E., & Ho, L. C. 2004, ApJ, 610, 722

—. 2005a, ApJ, 627, 721

—. 2005b, ApJ, 630, 122

—. 2007, ApJ, 670, 92

Greene, J. E., Ho, L. C., & Barth, A. J. 2008, ApJ, 688, 159

Greenstein, J. L. 1963, Nature, 197, 1041

Griffin, M. J., Abergel, A., Abreu, A., et al. 2010, A&A, 518, L3

Grogin, N. A., Kocevski, D. D., Faber, S. M., et al. 2011, ApJS, 197, 35

Gu, M. F., & Li, S.-L. 2013, A&A, 554, A51

Gültekin, K., Richstone, D. O., Gebhardt, K., et al. 2009, ApJ, 698, 198

Gursky, H., Kellogg, E. M., Leong, C., Tananbaum, H., & Giacconi, R. 1971, ApJ, 165, L43

Guzzo, L., Scodeggio, M., Garilli, B., et al. 2014, A&A, 566, A108

Haardt, F., & Maraschi, L. 1991, ApJ, 380, L51

—. 1993, ApJ, 413, 507

Haardt, F., Maraschi, L., & Ghisellini, G. 1994, ApJ, 432, L95

Haehnelt, M. G., Madau, P., Kudritzki, R., & Haardt, F. 2001, ApJ, 549, L151

Hainline, K. N., Hickox, R. C., Carroll, C. M., et al. 2014, ApJ, 795, 124

Häring, N., & Rix, H.-W. 2004, ApJ, 604, L89

Harrison, C. 2014, PhD thesis

Harrison, F. A., Craig, W. W., Christensen, F. E., et al. 2013, ApJ, 770, 103

Hasinger, G., Burg, R., Giacconi, R., et al. 1998, A&A, 329, 482

Hawkins, M. R. S. 1993, Nature, 366, 242

Hazard, C., Gulkis, S., & Bray, A. D. 1967, ApJ, 148, 669

Hazard, C., Mackey, M. B., & Shimmins, A. J. 1963, Nature, 197, 1037

Heckman, T. M. 1980, A&A, 500, 187

Helfand, D. J., Stone, R. P. S., Willman, B., et al. 2001, AJ, 121, 1872

Herschel, W. 1786, Philosophical Transactions of the Royal Society of London Series I, 76, 457

—. 1789, Philosophical Transactions of the Royal Society of London Series I, 79, 212

—. 1800, Proceedings of the Royal Society of London Series I, 1, 98

—. 1802, Philosophical Transactions of the Royal Society of London Series I, 92, 477

Hickox, R. C., & Alexander, D. M. 2018, ARA&A, 56, 625

Hickox, R. C., Myers, A. D., Greene, J. E., et al. 2017, ApJ, 849, 53

Ho, L. C. 1999, ApJ, 516, 672

—. 2002, ApJ, 564, 120

Ho, L. C., Filippenko, A. V., & Sargent, W. L. 1995, ApJS, 98, 477

Ho, L. C., Filippenko, A. V., & Sargent, W. L. W. 1993, ApJ, 417, 63

—. 1997, ApJS, 112, 315

Ho, L. C., Feigelson, E. D., Townsley, L. K., et al. 2001, ApJ, 549, L51

Hönig, S. F. 2019, ApJ, 884, 171

Hönig, S. F., Beckert, T., Ohnaka, K., & Weigelt, G. 2006, A&A, 452, 459

Hönig, S. F., & Kishimoto, M. 2010, A&A, 523, A27

—. 2017, ApJ, 838, L20

Hönig, S. F., Kishimoto, M., Antonucci, R., et al. 2012, ApJ, 755, 149

Hönig, S. F., Kishimoto, M., Tristram, K. R. W., et al. 2013, ApJ, 771, 87

Hook, I. M., McMahon, R. G., Boyle, B. J., & Irwin, M. J. 1994, MNRAS, 268, 305

Hoormann, J. K., Martini, P., Davis, T. M., et al. 2019, MNRAS, 487, 3650

Hopkins, P. F., Hernquist, L., Cox, T. J., et al. 2006, ApJS, 163, 1

Hopkins, P. F., Hernquist, L., Cox, T. J., & Kereš, D. 2008, ApJS, 175, 356

Hornschemeier, A. E., Bauer, F. E., Alexander, D. M., et al. 2003, AJ, 126, 575

Houck, J. R., Roellig, T. L., Van Cleve, J., et al. 2004, Society of Photo-Optical Instrumentation Engineers (SPIE) Conference Series, Vol. 5487, The infrared spectrograph on the Spitzer Space Telescope, ed. J. C. Mather, 62–76

Hoyle, F., & Fowler, W. A. 1963, MNRAS, 125, 169

Hu, C., Wang, J.-M., Ho, L. C., et al. 2008, ApJ, 683, L115

Hubble, E. P. 1926, ApJ, 64, 321

Hudelot, P., Cuillandre, J. C., Withington, K., et al. 2012, VizieR Online Data Catalog, II/317

Hunt, L. K., De Looze, I., Boquien, M., et al. 2019, A&A, 621, A51

Hviding, R. E., Hickox, R. C., Hainline, K. N., et al. 2018, MNRAS, 474, 1955

Imanishi, M., Nakanishi, K., & Izumi, T. 2016, ApJ, 822, L10

Ishibashi, W., & Courvoisier, T. J. L. 2009, A&A, 495, 113

Ives, J. C., Sanford, P. W., & Penston, M. V. 1976, ApJ, 207, L159

Ivezić, Ž., Kahn, S. M., Tyson, J. A., et al. 2008, ArXiv e-prints, arXiv:0805.2366

Jaffe, W., Meisenheimer, K., Röttgering, H. J. A., et al. 2004, Nature, 429, 47

Jansen, F., Lumb, D., Altieri, B., et al. 2001, A&A, 365, L1

Jansky, K. G. 1932, Proceedings of the Institute of Radio Engineers, 20, 1920

—. 1933, Nature, 132, 66

Juneau, S., Dickinson, M., Alexander, D. M., & Salim, S. 2011, ApJ, 736, 104

Juneau, S., Bournaud, F., Charlot, S., et al. 2014, ApJ, 788, 88

Kaiser, C. R., & Alexander, P. 1997, MNRAS, 286, 215

Kant, I. 1755, Allgemeine Naturgeschichte und Theorie des Himmels

Kapahi, V. K., & Saikia, D. J. 1982, Journal of Astrophysics and Astronomy, 3, 465

Kasliwal, V., Vogeley, M., & T. Richards, G. 2015, Monthly Notices of the Royal Astronomical Society, 451, doi:10.1093/mnras/stv1230

Kaspi, S., Smith, P. S., Netzer, H., et al. 2000, ApJ, 533, 631

Kass, R. E., & Raftery, A. E. 1995, Journal of the American Statistical Association, 90, 773

Katz, J. I. 1977, ApJ, 215, 265

Kauffmann, G., Heckman, T. M., Tremonti, C., et al. 2003, MNRAS, 346, 1055

Kawaguchi, T., Mineshige, S., Umemura, M., & Turner, E. L. 1998, ApJ, 504, 671

Keeler, J. 1900, The Spiral Nebula H.1.55 Pegasi (University of Chic. Press)

Kelly, B. C., Bechtold, J., & Siemiginowska, A. 2009, ApJ, 698, 895

Kelly, B. C., Becker, A. C., Sobolewska, M., Siemiginowska, A., & Uttley, P. 2014, ApJ, 788, 33

Kerr, R. P. 1963, Phys. Rev. Lett., 11, 237

Kewley, L. J., Groves, B., Kauffmann, G., & Heckman, T. 2006, MNRAS, 372, 961

Kewley, L. J., Maier, C., Yabe, K., et al. 2013, ApJ, 774, L10

Kim, J., Karouzos, M., Im, M., et al. 2018, ArXiv e-prints, arXiv:1809.01350

King, A., & Pounds, K. 2015, ARA&A, 53, 115

Kishimoto, M., Hönig, S. F., Antonucci, R., et al. 2011, A&A, 536, A78

Koekemoer, A. M., Faber, S. M., Ferguson, H. C., et al. 2011, ApJS, 197, 36

Komossa, S. 2015, Journal of High Energy Astrophysics, 7, 148

Kormendy, J., & Ho, L. C. 2013, ARA&A, 51, 511

Kormendy, J., & Kennicutt, Jr., R. C. 2004, ARA&A, 42, 603

Kormendy, J., & Richstone, D. 1995, ARA&A, 33, 581

Koss, M., Trakhtenbrot, B., Ricci, C., et al. 2017, ApJ, 850, 74

Kozlowski, S. 2016, Monthly Notices of the Royal Astronomical Society, 459, stw819

Kraft, R. P., Burrows, D. N., & Nousek, J. A. 1991, ApJ, 374, 344

Kristian, J. 1973, ApJ, 179, L61

Krolik, J. H. 1992, in American Institute of Physics Conference Series, Vol. 254, American Institute of Physics Conference Series, ed. S. S. Holt, S. G. Neff, & C. M. Urry, 473–485

Krolik, J. H. 1999, ApJ, 515, L73

Krolik, J. H., & Begelman, M. C. 1988, ApJ, 329, 702

Kubota, A., & Done, C. 2018, MNRAS, 480, 1247

Lacy, M., Petric, A. O., Sajina, A., et al. 2007, AJ, 133, 186

Lacy, M., Storrie-Lombardi, L. J., Sajina, A., et al. 2004, ApJS, 154, 166

Lamareille, F. 2010, A&A, 509, A53

LaMassa, S. M., Civano, F., Brusa, M., et al. 2016, ApJ, 818, 88

Lansbury, G. B., Gandhi, P., Alexander, D. M., et al. 2015, ApJ, 809, 115

Laplace, P. S. 1796, Exposition du systeme du monde [microform] / par Pierre-Simon Laplace (De l'Imprimerie du Cercle-Social Paris), 2 v. ;

Lasker, B. M., Lattanzi, M. G., McLean, B. J., et al. 2008, AJ, 136, 735

Lauer, T. R., Faber, S. M., Richstone, D., et al. 2007, ApJ, 662, 808

Lawrence, A. 1991, MNRAS, 252, 586

Lawrence, A., & Elvis, M. 1982, ApJ, 256, 410

Lawrence, A., & Papadakis, I. 1993, ApJ, 414, L85

Lawrence, A., Warren, S. J., Almaini, O., et al. 2007, MNRAS, 379, 1599

Le Fèvre, O., Cassata, P., Cucciati, O., et al. 2013, A&A, 559, A14

Le Fèvre, O., Cassata, P., Cucciati, O., et al. 2013, A&A, 559, A14

Leftley, J. H., Tristram, K. R. W., Hönig, S. F., et al. 2018, ApJ, 862, 17

Lehmann, I., Hasinger, G., Schmidt, M., et al. 2001, A&A, 371, 833

Li, S.-L., & Cao, X. 2008, MNRAS, 387, L41

Li, Z., Zhou, H., Hao, L., et al. 2015, ApJ, 812, 99

Lípari, S., Mediavilla, E., Garcia-Lorenzo, B., et al. 2004, MNRAS, 355, 641

López-Gonzaga, N., Burtscher, L., Tristram, K. R. W., Meisenheimer, K., & Schartmann, M. 2016, A&A, 591, A47

Lubow, S., & Budavári, T. 2013, Astronomical Society of the Pacific Conference Series, Vol. 475, Hubble Source Catalog, ed. D. N. Friedel, 203

Luo, B., Bauer, F. E., Brandt, W. N., et al. 2008, ApJS, 179, 19

Luo, B., Brandt, W. N., Xue, Y. Q., et al. 2017, ApJS, 228, 2

Lusso, E., & Risaliti, G. 2016, ApJ, 819, 154

Lutz, D., Maiolino, R., Spoon, H. W. W., & Moorwood, A. F. M. 2004, A&A, 418, 465

Lynden-Bell, D. 1969, Nature, 223, 690

Maccacaro, T., Gioia, I. M., Wolter, A., Zamorani, G., & Stocke, J. T. 1988, ApJ, 326, 680

MacLeod, C. L., Ivezić, , Kochanek, C. S., et al. 2010, The Astrophysical Journal, 721, 1014

MacLeod, C. L., Ivezić, Ž., Sesar, B., et al. 2012, ApJ, 753, 106

Maddox, N. 2018, MNRAS, 480, 5203

Magorrian, J., Tremaine, S., Richstone, D., et al. 1998, AJ, 115, 2285

Maiolino, R., Salvati, M., Bassani, L., et al. 1998, A&A, 338, 781

Maoz, D., Koratkar, A., Shields, J. C., et al. 1998, AJ, 116, 55

Maoz, D., Nagar, N. M., Falcke, H., & Wilson, A. S. 2005, ApJ, 625, 699

Maraschi, L., Ghisellini, G., & Celotti, A. 1992, ApJ, 397, L5

Marconi, A., & Hunt, L. K. 2003, ApJ, 589, L21

Marconi, A., Risaliti, G., Gilli, R., et al. 2004, MNRAS, 351, 169

Marocco, J., Hache, E., & Lamareille, F. 2011, A&A, 531, A71

Marshall, F. E., Boldt, E. A., Holt, S. S., et al. 1980, ApJ, 235, 4

Marshall, N., Warwick, R. S., & Pounds, K. A. 1981, MNRAS, 194, 987

Marziani, P., Calvani, M., & Sulentic, J. W. 1997, Astronomical Society of the Pacific Conference Series, Vol. 121, On the Difference Between Radio Quiet and Radio Loud AGN, ed. D. T. Wickramasinghe, G. V. Bicknell, & L. Ferrario, 761

Mason, K. O., Puchnarewicz, E. M., & Jones, L. R. 1996, MNRAS, 283, L26

Mason, K. O., Breeveld, A., Much, R., et al. 2001, A&A, 365, L36

Mastichiadis, A. 2016, Galaxies, 4, 59

Mateos, S., Alonso-Herrero, A., Carrera, F. J., et al. 2012, MNRAS, 426, 3271

Mateos, S., Carrera, F. J., Alonso-Herrero, A., et al. 2015, MNRAS, 449, 1422

—. 2016, ApJ, 819, 166

Matt, G., Perola, G. C., & Piro, L. 1991, A&A, 247, 25

Matthews, T. A., Bolton, J. G., Greenstein, J. L., Münch, G., & Sandage, A. R. 1961, in , 148

Matthews, T. A., & Sandage, A. R. 1963, ApJ, 138, 30

Mayer, L., Kazantzidis, S., Escala, A., & Callegari, S. 2010, Nature, 466, 1082

Mazzucchelli, C., Bañados, E., Venemans, B. P., et al. 2017, ApJ, 849, 91

McHardy, I. 2010, X-Ray Variability of AGN and Relationship to Galactic Black Hole Binary Systems, ed. T. Belloni, Vol. 794, 203

McMahon, R. G., Banerji, M., Gonzalez, E., et al. 2013, The Messenger, 154, 35

Menci, N., Fiore, F., Puccetti, S., & Cavaliere, A. 2008, ApJ, 686, 219

Mendez, A. J., Coil, A. L., Aird, J., et al. 2013, ApJ, 770, 40

Merloni, A. 2004, MNRAS, 353, 1035

Michell, J. 1784, Philosophical Transactions of the Royal Society of London, 74, 35

Middei, R., Bianchi, S., Marinucci, A., et al. 2019, A&A, 630, A131

Middei, R., Vagnetti, F., Bianchi, S., et al. 2017, A&A, 599, A82

Mignoli, M., Vignali, C., Gilli, R., et al. 2013, A&A, 556, A29

Miller, J. S., Goodrich, R. W., & Mathews, W. G. 1991, ApJ, 378, 47

Miniutti, G., & Fabian, A. C. 2004, MNRAS, 349, 1435

Minkowski, R. 1960, ApJ, 132, 908

Momcheva, I. G., Brammer, G. B., van Dokkum, P. G., et al. 2016, ApJS, 225, 27

Mortlock, D. J., Warren, S. J., Venemans, B. P., et al. 2011, Nature, 474, 616

Mountrichas, G., Georgakakis, A., & Georgantopoulos, I. 2019, MNRAS, 483, 1374

Mountrichas, G., Georgantopoulos, I., Secrest, N. J., et al. 2017, MNRAS, 468, 3042

Müller-Sánchez, F., Prieto, M. A., Hicks, E. K. S., et al. 2011, ApJ, 739, 69

Murray, S. S., Austin, G. K., Chappell, J. H., et al. 2000, Society of Photo-Optical Instrumentation Engineers (SPIE) Conference Series, Vol. 4012, In-flight performance of the Chandra high-resolution camera, ed. J. E. Truemper & B. Aschenbach, 68–80

Mushotzky, R. F., Marshall, F. E., Boldt, E. A., Holt, S. S., & Serlemitsos, P. J. 1980, ApJ, 235, 377

Nandra, K., Laird, E. S., Adelberger, K., et al. 2005, MNRAS, 356, 568

Narayan, R., & Yi, I. 1994, ApJ, 428, L13

Nenkova, M., Elitzur, M., & Ivezič, Ž. 2001, Astronomical Society of the Pacific Conference Series, Vol. 247, Modeling AGN Dust Distributions with the Continuum Radiative Transfer Code DUSTY, ed. G. Ferland & D. W. Savin, 383

Nenkova, M., Sirocky, M. M., Ivezić, Ž., & Elitzur, M. 2008a, ApJ, 685, 147

Nenkova, M., Sirocky, M. M., Nikutta, R., Ivezić, Ž., & Elitzur, M. 2008b, ApJ, 685, 160

Netzer, H. 2013, The Physics and Evolution of Active Galactic Nuclei

—. 2015, ARA&A, 53, 365

Netzer, H., & Laor, A. 1993, ApJ, 404, L51

Nikutta, R., Elitzur, M., & Lacy, M. 2009, ApJ, 707, 1550

Nobuta, K., Akiyama, M., Ueda, Y., et al. 2012, ApJ, 761, 143

Noll, S., Burgarella, D., Giovannoli, E., et al. 2009, A&A, 507, 1793

Norman, C., Hasinger, G., Giacconi, R., et al. 2002, ApJ, 571, 218

Novikov, I. D., & Thorne, K. S. 1973, in Black Holes (Les Astres Occlus), 343–450

Oh, K., Yi, S. K., Schawinski, K., et al. 2015, ApJS, 219, 1

Oke, J. B., & Schmidt, M. 1963, AJ, 68, 288

Oliver, S. J., Bock, J., Altieri, B., et al. 2012, MNRAS, 424, 1614

Oppenheimer, J. R., & Snyder, H. 1939, Physical Review, 56, 455

Oppenheimer, J. R., & Volkoff, G. M. 1939, Physical Review, 55, 374

Orr, M. J. L., & Browne, I. W. A. 1982, MNRAS, 200, 1067

Osterbrock, D. E. 1977, ApJ, 215, 733

—. 1981, ApJ, 249, 462

Osterbrock, D. E., & Ferland, G. J. 2006, Astrophysics of gaseous nebulae and active galactic nuclei

Ostriker, J. P., Choi, E., Ciotti, L., Novak, G. S., & Proga, D. 2010, ApJ, 722, 642

Packham, C., Radomski, J. T., Roche, P. F., et al. 2005, ApJ, 618, L17

Padovani, P., Alexander, D. M., Assef, R. J., et al. 2017, A&A Rev., 25, 2

Page, M. J., Mason, K. O., McHardy, I. M., Jones, L. R., & Carrera, F. J. 1997, MNRAS, 291, 324

Panagiotou, C., & Walter, R. 2019, A&A, 626, A40

Panessa, F., Bassani, L., Cappi, M., et al. 2006, A&A, 455, 173

Paolillo, M., Schreier, E. J., Giacconi, R., Koekemoer, A. M., & Grogin, N. A. 2004, ApJ, 611, 93

Paolillo, M., Papadakis, I., Brandt, W. N., et al. 2017, MNRAS, 471, 4398

Park, J., & Trippe, S. 2017, ApJ, 834, 157

Penston, M. V., Penston, M. J., Selmes, R. A., Becklin, E. E., & Neugebauer, G. 1974, MNRAS, 169, 357

Peterson, B. M. 2006, The Broad-Line Region in Active Galactic Nuclei, ed. D. Alloin, Vol. 693, 77

Petropoulou, M., & Mastichiadis, A. 2012, MNRAS, 426, 462

Petrucci, P. O., & Henri, G. 1997, A&A, 326, 99

Petrucci, P. O., Ursini, F., De Rosa, A., et al. 2018, A&A, 611, A59

Petrucci, P. O., Paltani, S., Malzac, J., et al. 2013, A&A, 549, A73

Piccinotti, G., Mushotzky, R. F., Boldt, E. A., et al. 1982, ApJ, 253, 485

Pierre, M., Adami, C., Birkinshaw, M., et al. 2017, Astronomische Nachrichten, 338, 334

Pilbratt, G. L., Riedinger, J. R., Passvogel, T., et al. 2010, A&A, 518, L1

Pilkington, J. D. H., & Scott, J. F. 1965, MmRAS, 69, 183

Pineau, F. X., Derriere, S., Motch, C., et al. 2017, A&A, 597, A89

Poglitsch, A., Waelkens, C., Geis, N., et al. 2010, A&A, 518, L2

Pons, E., Elvis, M., Civano, F., & Watson, M. G. 2016, ApJ, 824, 51

Popović, L. Č. 2003, ApJ, 599, 140

Pouliasis, E., Georgantopoulos, I., Bonanos, A. Z., et al. 2019, MNRAS, 487, 4285

Pounds, K. A., Nandra, K., Stewart, G. C., George, I. M., & Fabian, A. C. 1990, Nature, 344, 132

Pravdo, S. H., Nugent, J. J., Nousek, J. A., et al. 1981, ApJ, 251, 501

Puget, P., Stadler, E., Doyon, R., et al. 2004, Society of Photo-Optical Instrumentation Engineers (SPIE) Conference Series, Vol. 5492, WIRCam: the infrared wide-field camera for the Canada-France-Hawaii Telescope, ed. A. F. M. Moorwood & M. Iye, 978–987

Radomski, J. T., Packham, C., Levenson, N. A., et al. 2008, ApJ, 681, 141

Ramos Almeida, C., & Ricci, C. 2017, Nature Astronomy, 1, 679

Reber, G. 1944, ApJ, 100, 279

Rees, M. J. 1978, in IAU Symposium, Vol. 77, Structure and Properties of Nearby Galaxies, ed. E. M. Berkhuijsen & R. Wielebinski, 237

Rees, M. J. 1984, ARA&A, 22, 471

Rees, M. J., Begelman, M. C., Blandford, R. D., & Phinney, E. S. 1982, Nature, 295, 17

Rees, M. J., Silk, J. I., Werner, M. W., & Wickramasinghe, N. C. 1969, Nature, 223, 788

Rees, M. J., & Volonteri, M. 2007, in IAU Symposium, Vol. 238, Black Holes from Stars to Galaxies – Across the Range of Masses, ed. V. Karas & G. Matt, 51–58

Ricci, C., Walter, R., Courvoisier, T. J. L., & Paltani, S. 2011, A&A, 532, A102

Ricci, C., Trakhtenbrot, B., Koss, M. J., et al. 2017, ApJS, 233, 17

Ricci, C., Ho, L. C., Fabian, A. C., et al. 2018, MNRAS, 480, 1819

Rieke, G. H., Young, E. T., Cadien, J., et al. 2004, Society of Photo-Optical Instrumentation Engineers (SPIE) Conference Series, Vol. 5487, On-orbit performance of the MIPS instrument, ed. J. C. Mather, 50–61

Riess, A. G., Strolger, L.-G., Casertano, S., et al. 2007, ApJ, 659, 98

Ross, R. R., & Fabian, A. C. 2005, MNRAS, 358, 211

Rosse, T. E. O. 1850, Philosophical Transactions of the Royal Society of London Series I, 140, 499

Rousseeuw, P. J., & Croux, C. 1993, Journal of the American Statistical Association, 88, 1273

Rovilos, E., Georgantopoulos, I., Akylas, A., et al. 2014, MNRAS, 438, 494

Rowan-Robinson, M. 1977, ApJ, 213, 635

Rowan-Robinson, M., Gonzalez-Solares, E., Vaccari, M., & Marchetti, L. 2013, Monthly Notices of the Royal Astronomical Society, 428, 1958

Rowan-Robinson, M., Babbedge, T., Surace, J., et al. 2005, AJ, 129, 1183

Ruiz, M., Rieke, G. H., & Schmidt, G. D. 1994, ApJ, 423, 608

Rybicki, G. B., & Lightman, A. P. 1979, Radiative processes in astrophysics

—. 1986, Radiative Processes in Astrophysics

Ryle, M., Smith, F. G., & Elsmore, B. 1950, MNRAS, 110, 508

Sajina, A., Lacy, M., & Scott, D. 2005, ApJ, 621, 256

Salpeter, E. E. 1955, ApJ, 121, 161

—. 1964, ApJ, 140, 796

Sandage, A. 1965, ApJ, 141, 1560

Sarajedini, V. L., Gilliland, R. L., & Kasm, C. 2003, ApJ, 599, 173

Sarajedini, V. L., Koo, D. C., Klesman, A. J., et al. 2011, ApJ, 731, 97

Sauty, C., & Tsinganos, K. 1994, A&A, 287, 893

Sauty, C., Tsinganos, K., & Trussoni, E. 1999, A&A, 348, 327

Schartmann, M., Meisenheimer, K., Camenzind, M., et al. 2008, A&A, 482, 67

Scheuer, P. A. G., & Readhead, A. C. S. 1979, Nature, 277, 182

Schmidt, M. 1963, Nature, 197, 1040

Schmidt, M., & Green, R. F. 1983, ApJ, 269, 352

Schmidt, M., Hasinger, G., Gunn, J., et al. 1998, A&A, 329, 495

Schmitt, H. R. 1998, The Astrophysical Journal, 506, 647

Schulze, A., & Wisotzki, L. 2010, A&A, 516, A87

Schwarz, G. 1978, The Annals of Statistics, 6, 461

Schwarzschild, K. 1916, Abh. Konigl. Preuss. Akad. Wissenschaften Jahre 1906,92, Berlin,1907, 1916, 189

Scodeggio, M., Guzzo, L., Garilli, B., et al. 2018, A&A, 609, A84

Seyfert, C. K. 1943, ApJ, 97, 28

Shakura, N. I. 1972, AZh, 49, 921

Shakura, N. I., & Sunyaev, R. A. 1973, A&A, 500, 33

Shapiro, S. L., Lightman, A. P., & Eardley, D. M. 1976, ApJ, 204, 187

Shapiro, S. L., & Teukolsky, S. A. 1983, Black holes, white dwarfs, and neutron stars : the physics of compact objects

She, R., Ho, L. C., & Feng, H. 2017, ApJ, 842, 131

Shields, J. C. 1992, ApJ, 399, L27

Shipley, H. V., Lange-Vagle, D., Marchesini, D., et al. 2018, ApJS, 235, 14

Silk, J., & Rees, M. J. 1998, A&A, 331, L1

Simm, T., Salvato, M., Saglia, R., et al. 2016, A&A, 585, A129

Simm, T., Saglia, R., Salvato, M., et al. 2015, A&A, 584, A106

Simpson, C. 2005, MNRAS, 360, 565

Singh, K. P., Garmire, G. P., & Nousek, J. 1985, ApJ, 297, 633

Singh, K. P., Rao, A. R., & Vahia, M. N. 1990, ApJ, 365, 455

Skelton, R. E., Whitaker, K. E., Momcheva, I. G., et al. 2014, ApJS, 214, 24

Skrutskie, M. F., Cutri, R. M., Stiening, R., et al. 2006, AJ, 131, 1163

Slipher, V. M. 1917, Lowell Observatory Bulletin, 3, 59

Smith, E. P., Heckman, T. M., Bothun, G. D., Romanishin, W., & Balick, B. 1986, ApJ, 306, 64

Sobolewska, M. A., & Papadakis, I. E. 2009, MNRAS, 399, 1597

Sokolovsky, K. V., Gavras, P., Karampelas, A., et al. 2017, MNRAS, 464, 274

Soltan, A. 1982, MNRAS, 200, 115

Stalevski, M., Asmus, D., & Tristram, K. R. W. 2017, MNRAS, 472, 3854

Stalevski, M., Fritz, J., Baes, M., Nakos, T., & Popović, L. Č. 2012, MNRAS, 420, 2756

Stern, D. 2015, The Astrophysical Journal, 807, 129

Stern, D., Moran, E. C., Coil, A. L., et al. 2002, ApJ, 568, 71

Stern, D., Eisenhardt, P., Gorjian, V., et al. 2005, ApJ, 631, 163

Stern, D., Assef, R. J., Benford, D. J., et al. 2012, ApJ, 753, 30

Storchi-Bergmann, T., Eracleous, M., Teresa Ruiz, M., et al. 1997, ApJ, 489, 87

Straatman, C. M. S., Spitler, L. R., Quadri, R. F., et al. 2017, VizieR Online Data Catalog, 183

Strateva, I. V., Strauss, M. A., Hao, L., et al. 2003, AJ, 126, 1720

Strolger, L.-G., Riess, A. G., Dahlen, T., et al. 2004, ApJ, 613, 200

Strüder, L., Briel, U., Dennerl, K., et al. 2001, A&A, 365, L18

Suganuma, M., Yoshii, Y., Kobayashi, Y., et al. 2006, ApJ, 639, 46

Suh, H., Hasinger, G., Steinhardt, C., Silverman, J. D., & Schramm, M. 2015, ApJ, 815, 129

Tadhunter, C., & Tsvetanov, Z. 1989, Nature, 341, 422

Tanaka, Y., Inoue, H., & Holt, S. S. 1994, PASJ, 46, L37

Tananbaum, H., Avni, Y., Branduardi, G., et al. 1979, ApJ, 234, L9

Taniguchi, Y., Shioya, Y., & Murayama, T. 2000, AJ, 120, 1265

Taylor, E. N., Franx, M., van Dokkum, P. G., et al. 2009, ApJS, 183, 295

Terashima, Y., Ho, L. C., & Ptak, A. F. 2000, ApJ, 539, 161

Terashima, Y., & Wilson, A. S. 2003, ApJ, 583, 145

Terlevich, R., Tenorio-Tagle, G., Franco, J., & Melnick, J. 1992, MNRAS, 255, 713

Toba, Y., Oyabu, S., Matsuhara, H., et al. 2014, ApJ, 788, 45

Tortosa, A., Bianchi, S., Marinucci, A., Matt, G., & Petrucci, P. O. 2018, A&A, 614, A37

Tozzi, P., Gilli, R., Mainieri, V., et al. 2006, A&A, 451, 457

Trakhtenbrot, B., & Netzer, H. 2012, MNRAS, 427, 3081

Tran, H. D. 2001, ApJ, 554, L19

Treister, E., & Urry, C. M. 2012, Advances in Astronomy, 2012, 516193

Treister, E., Urry, C. M., & Virani, S. 2009, ApJ, 696, 110

Tremaine, S., Gebhardt, K., Bender, R., et al. 2002, ApJ, 574, 740

Trevese, D., Boutsia, K., Vagnetti, F., Cappellaro, E., & Puccetti, S. 2008, A&A, 488, 73

Trevese, D., Kron, R. G., Majewski, S. R., Bershady, M. A., & Koo, D. C. 1994, ApJ, 433, 494

Tristram, K. R. W., Burtscher, L., Jaffe, W., et al. 2014, A&A, 563, A82

Tristram, K. R. W., Meisenheimer, K., Jaffe, W., et al. 2007, A&A, 474, 837

Trouille, L., Barger, A. J., & Tremonti, C. 2011, ApJ, 742, 46

Tsinganos, K., Sauty, C., & Trussoni, E. 2001, in American Institute of Physics Conference Series, Vol. 558, American Institute of Physics Conference Series, ed. F. A. Aharonian & H. J. Völk, 299–311

Turner, M. J. L., Abbey, A., Arnaud, M., et al. 2001, A&A, 365, L27

Turner, T. J., & Pounds, K. A. 1989, MNRAS, 240, 833

Ulrich, M.-H., Maraschi, L., & Urry, C. M. 1997, ARA&A, 35, 445

Ulvestad, J. S., & Ho, L. C. 2001, ApJ, 562, L133

Urry, C. M., & Padovani, P. 1995, PASP, 107, 803

Vagnetti, F., Middei, R., Antonucci, M., Paolillo, M., & Serafinelli, R. 2016, A&A, 593, A55

Valdes, F. G., Campusano, L. E., Velasquez, J. D., & Stetson, P. B. 1995, PASP, 107, 1119

van Dokkum, P. G. 2001, PASP, 113, 1420

Vanden Berk, D. E., Wilhite, B. C., Kron, R. G., et al. 2004, ApJ, 601, 692

Veilleux, S., & Osterbrock, D. E. 1987, ApJS, 63, 295

Vergani, D., Garilli, B., Polletta, M., et al. 2018, A&A, 620, A193

Verma, A., Charmandaris, V., Klaas, U., Lutz, D., & Haas, M. 2005, Space Sci. Rev., 119, 355

Vika, M., Driver, S. P., Graham, A. W., & Liske, J. 2009, MNRAS, 400, 1451

Villforth, C., Koekemoer, A. M., & Grogin, N. A. 2010, ApJ, 723, 737

Villforth, C., Sarajedini, V., & Koekemoer, A. 2012, MNRAS, 426, 360

Voges, W., Aschenbach, B., Boller, T., et al. 1999, A&A, 349, 389

Volonteri, M. 2010, A&A Rev., 18, 279

—. 2012, Science, 337, 544

Volonteri, M. 2014, in The First Billion Years of Galaxies and Black Holes, 21

Weedman, D. W. 1973, ApJ, 183, 29

Weedman, D. W., Hao, L., Higdon, S. J. U., et al. 2005, ApJ, 633, 706

Weiner, B. J., Willmer, C. N. A., Faber, S. M., et al. 2006, ApJ, 653, 1027

Weisskopf, M. C., Tananbaum, H. D., Van Speybroeck, L. P., & O'Dell, S. L. 2000, Society of Photo-Optical Instrumentation Engineers (SPIE) Conference Series, Vol. 4012, Chandra X-ray Observatory (CXO): overview, ed. J. E. Truemper & B. Aschenbach, 2–16

Werner, M. W., Roellig, T. L., Low, F. J., et al. 2004, ApJS, 154, 1

Wheeler, J. A. 1968, The American Scholar, 37, 248

Whitmore, B. C., Allam, S. S., Budavári, T., et al. 2016, AJ, 151, 134

Whitney, A. R., Shapiro, I. I., Rogers, A. E. E., et al. 1971, Science, 173, 225

Wilson, A. S., & Colbert, E. J. M. 1995, ApJ, 438, 62

Wolf, C., Hildebrandt, H., Taylor, E. N., & Meisenheimer, K. 2008, A&A, 492, 933

Woltjer, L. 1959, ApJ, 130, 38

Wright, E. L., Eisenhardt, P. R. M., Mainzer, A. K., et al. 2010, AJ, 140, 1868

Wright, T. 1750, An original theory or new hypothesis of the universe : founded upon general phaenomena of the visible creation; and particularly the Via the laws of nature, and solving by mathematical principles : the Lactea ...compris'd in nine familiar letters from the author to his friendand : illustrated with upward of thirty graven and mezzotinto plates ..., doi:10.3931/e-rara-28672

Wu, Y., Charmandaris, V., Huang, J., Spinoglio, L., & Tommasin, S. 2009, ApJ, 701, 658

Xue, Y. Q., Luo, B., Brandt, W. N., et al. 2016, ApJS, 224, 15

—. 2011, ApJS, 195, 10

Yan, L., Donoso, E., Tsai, C.-W., et al. 2013, AJ, 145, 55

Yan, R., Ho, L. C., Newman, J. A., et al. 2011, The Astrophysical Journal, 728, 38

Yang, G., Boquien, M., Buat, V., et al. 2020, MNRAS, 491, 740

Yaqoob, T., & Padmanabhan, U. 2004, ApJ, 604, 63

Young, M., Brandt, W. N., Xue, Y. Q., et al. 2012, ApJ, 748, 124

Yuan, F.-T., Argudo-Fernández, M., Shen, S., et al. 2018, A&A, 613, A13

Zahid, H. J., Dima, G. I., Kewley, L. J., Erb, D. K., & Davé, R. 2012, ApJ, 757, 54

Zappacosta, L., Comastri, A., Civano, F., et al. 2018, ApJ, 854, 33

Zdziarski, A. A., Fabian, A. C., Nandra, K., et al. 1994, MNRAS, 269, L55

Zel'dovich, Y. B. 1964, Soviet Physics Doklady, 9, 195

Zensus, J. A. 1997, ARA&A, 35, 607

Zhang, K., Schlegel, D. J., Andrews, B. H., et al. 2019, ApJ, 883, 63

Zubovas, K., & King, A. 2013, ApJ, 769, 51

Zuo, W., Wu, X.-B., Liu, Y.-Q., & Jiao, C.-L. 2012, ApJ, 758, 104